

Technische Universität München
Institut für Energietechnik

Lehrstuhl für Thermodynamik

Identification and Analysis of Nonlinear Heat Sources in Thermo-Acoustic Systems

Fatih Selimefendigil

Vollständiger Abdruck der von der Fakultät für Maschinenwesen der Technischen Universität München zur Erlangung des akademischen Grades eines

DOKTOR – INGENIEURS

genehmigten Dissertation.

Vorsitzender:

Univ.-Prof. Dr.-Ing. H. Baier

Prüfer der Dissertation:

1. Univ.-Prof. W. H. Polifke, Ph.D. (CCNY)

2. Prof. R. I. Sujith, Ph.D.,

Indian Institute of Technology, Madras, Indien

Die Dissertation wurde am 12. 04. 2010 bei der Technischen Universität München eingereicht und durch die Fakultät für Maschinenwesen am 23. 06. 2010 angenommen.

Acknowledgments

First of all, I would like to express my special thanks to Prof. Polifke, Ph.D., for offering me this PhD position and introducing me to the thermo-acoustic world. His continuous support and encouragement were key factors in the completion of this work. My special thanks go to Prof. R. I. Sujith from IIT Madras for valuable discussions, encouragement and especially for his hospitality during my visit to India in November 2007. I also would like to thank Prof. Dr. -Ing. Horst Baier for kindly accepting to chair the defense.

I am grateful to everyone I collaborated with, especially Priya Subramanian from IIT Madras and Stephan Föllner for their cooperation and helpful discussions.

I thank my office colleague Daniel Morgenweck for his sympathetic attitude and help in translating the abstract into German.

Many thanks to Mrs. Bassett and Mrs. Schulz-Reichwald for taking care of administrative tasks and answering all my endless questions. I would like to thank everyone at the Chair of Thermodynamics for contributing to the encouraging ambience.

My sincere thanks to my parents for their continued love and support in all my academic endeavors.

This project is funded by Deutsche Forschungsgemeinschaft (DFG) under the Project number Po710/6-1,2 and the Department of Science and Technology (DST) of India whose financial support are gratefully acknowledged.

Braunschweig, April 2010

Fatih Selimefendigil

Abstract

Amplitude prediction of nonlinear oscillations in thermo-acoustic systems is important since the detrimental effects of instabilities on the combustor lifetime and noise emissions depend on the limit cycle amplitude. In thermo-acoustics, the nonlinearity associated with the response of the heat source to a velocity perturbation is often dominant and controls the steady state oscillations. Therefore, it is crucial to have an accurate dynamic model of the heat source available, which can be used in the nonlinear regime for a range of operating conditions.

Different nonlinear system identification procedures have been used to obtain a dynamic model of the heat source that is valid for a range of amplitudes and frequencies. The identified nonlinear heat source in time domain is coupled to the time domain model of thermo-acoustic system. Higher order transfer functions are developed as the extension of the linear transfer functions to the nonlinear regime and used in the frequency domain to investigate the nonlinear heat source/linear acoustic interaction. A physics-based model for the dynamics of the heat source, based on Proper Orthogonal Decomposition (POD) method, is formulated as an alternative to system identification. In a multivariate approach, POD modes are constructed from Computational Fluid Dynamics (CFD) data, and subsequent projection of the governing system of equations onto the modes gives the reduced order model of the nonlinear heat source.

A frequency domain coupled modes system model is developed that takes into account the interaction of various modes through the higher order transfer functions of the nonlinear heat source. The various contributions of the coupling terms to the Rayleigh index is determined, and an energy balance between the modes is analyzed in the nonlinear regime.

Finally, a systematic approach is presented to study the non-modal stability of thermo-acoustics where the system has non-orthogonal eigenvectors. In this approach, the heat source is obtained from linear system identification, and

a full system is simulated in time domain using the Galerkin method. The approach is attractive inasmuch as it allows to consider realistic configurations of the heat source, even with large delay times.

Contents

1	Introduction	1
1.1	Thermo-Acoustic Instabilities	1
1.2	Nonlinear Effects in Thermo-Acoustic Systems	5
1.3	Non-Normality of Thermo-Acoustic Systems	8
1.4	Modeling Approaches of Thermo-Acoustic Systems	10
1.4.1	Time Domain System Models	10
1.4.2	Frequency Domain System Models	11
1.5	Thesis Overview and Contributions	13
2	Transient Simulation of the Heat Source	18
2.1	CFD Model of Heat Transfer of the Wire in Pulsating Flow	18
2.2	Numerical Simulation of Pulsating Flow with Wall Heat Transfer for a Heated Plate	20
2.3	Heat Transfer in Oscillatory Flow	22
2.4	Laminar Premixed Flame Configuration	28
3	Linear System Identification	30
3.1	Procedures and Model Structures used in Linear System Identifi- cation	31
3.2	Time Domain Identification using Correlation Analysis	33
3.3	Identification of a Simple Model ("King's law") for the Heat Source	35
3.4	Identification of the CFD Model Heat Source	37
3.5	Identification of a Laminar Premixed Flame Model	41
3.6	Discussions and Conclusions	43
4	Nonlinear System Identification	44

4.1	Nonlinear Transfer Function from Fast Fourier Transformation (FFT)	46
4.2	Nonlinear Identification Problem	49
4.3	Polynomial Identification	51
4.3.1	Derivation	51
4.3.2	Identification of the Heat Transfer of Wire in Pulsating Flow from Unsteady CFD	52
4.3.3	Nonlinear Transfer Function	57
4.3.3.1	Harmonic Balance	57
4.3.3.2	Harmonic Probing	59
4.4	Neural Network Identification	64
4.4.1	Extraction of Volterra Kernels in terms of Neural Network Weights	67
4.4.2	Higher Order Transfer Functions	70
4.4.3	Nonlinear Identification of the Wire in Pulsating Flow from CFD and Nonlinear Transfer Function	71
4.4.4	Nonlinear Identification of the Laminar Premixed Flame	73
4.5	Other Nonlinear Identification Strategies	76
4.5.1	Block Oriented Structures	76
4.5.2	Identification based on Fuzzy Logic	78
4.6	Discussions and Conclusions	86
5	Low Order Model of the Heat Source with POD	89
5.1	Low Order Model with Proper Orthogonal Decomposition	91
5.1.1	Computing POD Modes	91
5.1.2	Galerkin Projection	92
5.1.3	Incorporating the term related to the pressure	93
5.1.4	Incorporating the Inlet Boundary Condition	95
5.1.5	Multivariate Approach	97
5.2	Results	98
5.2.1	POD modes and eigenspectra at single harmonic excitation	98
5.2.2	Mono-variate model: constant amplitude or constant frequency	99
5.2.3	Bivariate model for a range of amplitudes and frequencies	103

5.2.4	Nonlinear transfer function of the heat source from low order model	105
5.3	Discussion and Conclusion	107
6	Prediction and Analysis of Thermo-Acoustic Limit Cycles	110
6.1	Galerkin Time Domain	114
6.1.1	Derivation	114
6.1.2	Stability Analysis of Nonlinear Dynamical System	116
6.1.3	Simulation with the CFD/SI Model of the Wire Heat Source	120
6.2	Describing Function	121
6.2.1	Describing Function of Cubic and Saturation Type Nonlinearity	125
6.2.2	Limit Cycle Calculation with Describing Function	127
6.3	Frequency Domain System Model with Coupled Modes	130
6.3.1	Derivation	131
6.3.2	Interpretation of Modal Coupling	134
6.3.3	Comparison with Time Domain Simulation and Describing Function	135
6.3.4	Rayleigh Index and Energy Balance in the Nonlinear Regime	137
6.4	Conclusions and Outlook	143
7	Non-Modal Analysis of Thermo-Acoustic Stability	145
7.1	Thermo-Acoustics as Delay Differential System	148
7.2	Elements of the Non-Modal Stability Analysis	151
7.2.1	Eigenvalues	151
7.2.2	Pseudo-spectra of the delay system	154
7.2.3	Maximum growth factor and Kreiss' theorem	155
7.3	Results	156
7.4	Discussions and Conclusions	159
8	Summary and Conclusions	162
A	System Properties	180
A.1	Linearity	180
A.2	Time Invariant	180

CONTENTS

A.3 Stability	181
A.4 Causality	182
B Describing Function Table	184
C Nonlinear Network Model	187

Nomenclature

Latin Characters

a	evolution coefficient of mode, modal coefficient
a_i	polynomial coefficients
A	flame surface area [m ²]
A	amplitude of forcing
A, B	fuzzy sets
A, B	system matrices
A_0, A_n, B_n	Fourier coefficients
A, B, C, D, F	polynomial representation of linear system identification
b	flame radius [m]
B_n	n th order Bernoulli number
c	speed of sound [m/s]
c	element of cluster centers vector
c_1, c_2	damping coefficients
c_i	polynomial coefficients
c_v	specific heat capacity at constant volume [J/kg-K]
C	vector of cluster centers
C	calibration matrix
C, D	modal coefficients in frequency domain
d	diameter [m]
D	domain
D	coefficient of the heat source
E	perturbation energy
f	frequency [Hz]
f	nonlinear function of state vectors

Nomenclature

f	tangent hyperbolic function
$f(t)$	forcing function at the inlet
f_{in}, f_{out}	static input/output nonlinearity
$f_{Nyquist}$	Nyquist frequency
F	nonlinear function
$F(\omega)$	frequency response
G	linear dynamic part
G	field property
$G(j\omega)$	linear acoustic transfer function
G_{max}	maximum growth factor
h	heat transfer coefficient [W/m ² -K]
h	unit impulse
h	partitioned delay
h_n	n th order Volterra kernel
H_n	n th order transfer function
i, j	imaginary unit
I	identity matrix
J	Jacobian matrix
k	heat transfer rate coefficient
$K(A, \omega)$	amplitude and frequency dependent gain
K_1, K_2	heat transfer rate constants
L	filter length
L	length [m]
L	solution operator
m	fuzziness exponent
M	matrix of cross products of modes
M	signal length
M	number of units of neural network topology
n	interaction index
n	normal
n	slope of the output curve in linear regime
N	length of the signal
N	length of the partitioned delay
N	inner domain

N	number of modes
$N(A, \omega)$	describing function
$N(s)$	Laplace transformed modal coefficient
N_u	number of past inputs
N_Q	number of past outputs
p	pressure [Pa]
po	polynomial order
P	unknown vector parameter
PM	partition matrix
q	data set
Q	heat transfer rate per unit area [W/m^2]
\hat{Q}	magnitude of heat release rate, interaction index
Q_1, Q_{-1}, Q_2, Q_{-2}	complex conjugate coefficients
r	threshold value for the liner regime
r	number of clusters
$r(t)$	external forcing
R	matrix of modes
R	rule
R_{Qu}	cross-correlation vector
R_{uu}	auto-correlation matrix
s	coefficient of system matrices
S	cross-section area of the duct [m^2]
S	matrix of velocity modes
S	matrix of data set
S_L	laminar flame speed [m/s]
T	period of oscillation [s]
T	temperature [K]
u, v	velocity [m/s]
U	matrix of inputs
v	additive noise
V	velocity perpendicular to flame [m/s]
V	cost function
w, x	state vectors
w, W	weights of neural network

x	antecedent
X	universe
x_f	heat source location [m]
X, Y	coordinate system aligned to flame [m]
y	consequent
y	output
$Q(s)$	Laplace transformed output
z	element of data set matrix
z	root, eigenvalue
Z	training data set

Greek Characters

α	flame inclination angle [deg]
β	degree of the fulfillment
β	coefficient of system matrices
γ	specific heat ratio [-]
Γ_1	inlet
δ	Kronecker delta
Δt	time step [s]
Δf	frequency resolution [Hz]
Δq_r	heat release per unit mass of mixture [J/kg]
$\Delta(z)$	characteristic equation
ϵ	perturbation amplitude
ζ	flame front position [m]
η	modal coefficient
θ	weights of neural network
λ	eigenvalue
λ	thermal conductivity [W/m-K]
Λ	pseudo-spectra
μ	dynamic viscosity [kg/m-s]
μ	membership function
ν	kinematic viscosity [m ² /s]

ξ	damping factor
ρ	density [kg/m ³]
σ	singular value
τ	time lag [s]
Φ	phase [deg]
φ	set of regressor
χ	state vectors of modal coefficients
ω	radial frequency [rad/s]
Ω	domain
Ω	partition of delay dimension

Indices

∞	free stream
$\rightarrow 0$	zero limit
a	air
approx	approximation
CFD	CFD
d	duct
d_1, d_2, d_3	modal indices
f	flame
m	model
max	maximum
min	minimum
NeuralNet	related to neural network
Nyquist	Nyquist
o	operating point
pred	prediction
Q	output
s, ss	steady state
u	input
uu, uQ	bilinear products
w	wire

Superscripts

'	fluctuating
\sim	dimensional
\rightarrow	vector
.	first order time derivative
..	second order time derivative
–	mean value
(1), (2)	includes first/second order spatial derivatives
N	up to time N
T	temperature component
T	transpose
u, v	velocity components

Non-Dimensional numbers

A	Velocity amplitude ratio [u' / \bar{u}]
Re	Reynolds number [$\mu \bar{u} / L$]
Pr	Prandtl number [$c_p \mu / \lambda$]
Ma	Mach number [\bar{u} / c]
Str	Strouhal number [$\omega L / \bar{u}$]
Nu	Nusselt number [$\alpha L / \lambda$]

Abbreviations

ARX	Auto Regressive with EXogenous Input
CFD	Computational Fluid Dynamics
DDE	Delay Differential Equation

FFT	Fast Fourier Transformation
FIR	Finite Impulse Response
HOTF	Higher Order Transfer Functions
LOM	Low Order Model
LTI	Linear Time Invariant
NARX	Nonlinear Auto Regressive with EXogenous Input
NFIR	Nonlinear Finite Impulse Response
NOE	Nonlinear Output Error
ODE	Ordinary Differential Equation
OE	Output Error
POD	Proper Orthogonal Decomposition
RI	Rayleigh Index
SI	System Identification
TS	Takagi - Sugeno fuzzy model

Operators

\Im	Imaginary part
\Re	Real part
∇	Nabla operator
Δ	Laplace operator
$\langle \cdot, \cdot \rangle$	Inner product
$\langle \dots \rangle$	Ensemble average
$\ \cdot \ $	Norm
D	Differential operator
\mathcal{L}	Laplace transformation
z	Shift operator
Z	Z-transformation

1 Introduction

1.1 Thermo-Acoustic Instabilities

Thermo-acoustic instabilities are a major concern in many power generation systems, gas turbines, rocket engines and industrial burners [89, 106]. In gas turbines, the establishment of stringent emission standards and regulations requires that they operate in lean premixed regimes. In this regime, the combustors are more prone to thermo-acoustic instabilities [82]. These instabilities are mainly a result of the interaction of acoustic waves and fluctuating heat release (other effects like the fluctuations of equivalence ratio and entropy can also affect the instability). As a result of this interaction, a self sustained feedback loop may be established. The resulting large amplitude pressure oscillations may cause structural damage to the mechanical parts, excessive heat transfer to the walls of the combustion chamber and increased noise emissions [38, 89, 106, 113]. Therefore, it is important to understand the nature of these oscillations along with adequate modeling strategies for better design and control.

If the heat release fluctuations are in phase with the pressure fluctuations, the acoustic oscillations acquire energy from the heat source. This criterion for the occurrence of the instabilities is known as "Rayleigh criterion", which has been stated by Lord Rayleigh as [115] :

“If heat be communicated to, and abstracted from, a mass of air vibrating (for example) in a cylinder bounded by a piston, the effect produced will depend upon the phase of the vibration at which the transfer of heat takes place. If heat be given to the air at the moment of greatest condensation, or be taken from it at the moment of greatest rarefaction, the vibration will be encouraged. On the other hand, if heat will be given at the moment of greatest rarefaction,

or abstracted at the moment of greatest condensation, the vibration will be discouraged”.

Mathematically, this relation can be represented as an index [113];

$$\text{RI} = \frac{1}{T} \int_0^T \int_V p'(x, t) Q'(x, t) dt dV, \quad (1.1)$$

for one cycle of the oscillation with period T , pressure fluctuation p' and heat release fluctuation Q' . The above integral relation is valid when the gas dynamics is linear and can be derived using linearized conservation equations [27, 46]. The Rayleigh criterion for nonlinear acoustics has been considered by Culick [30]. If $\text{RI} > 0$, then instability is enhanced. The Rayleigh criterion is a necessary but not sufficient condition for instability in the presence of losses of acoustic energy.

Let us assume the following forms for a resonator tube at open-open boundary conditions with a concentrated heat source for the pressure and the heat release oscillations,

$$p'(x, t) = \hat{P} \sin(\omega t) \sin\left(\frac{\pi}{L} x\right), \quad (1.2)$$

$$Q'(x, t) = f(u(t - \tau)) = \hat{Q} \sin(\omega(t - \tau)) \cos\left(\frac{\pi}{L} x\right) \delta(x - x_f), \quad (1.3)$$

where a compact heat source is located at position x_f for a tube length of L , and the chosen spatial ansatz ($\sin\left(\frac{\pi}{L} x\right)$) for the pressure oscillation p' satisfies the boundary condition. The spatial ansatz ($\cos\left(\frac{\pi}{L} x\right)$) for the acoustic velocity oscillation u' can be seen from the one-dimensional acoustic momentum equation involving the relation between the pressure and velocity. The heat release response is expressed as a linear function of acoustic velocity with a delay term τ . This, so-called “ $n - \tau$ ” model [29], is a widely used heat source model for combustion applications. Substituting the above expressions in the Rayleigh index, we obtain the following simplified form,

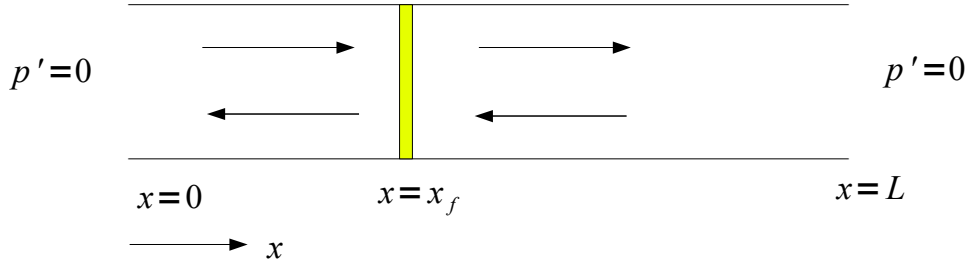


Figure 1.1: A resonator tube of length L at open-open boundary conditions with a concentrated heat source at position $x = x_f$

$$\text{RI} = \frac{\hat{P}\hat{Q}}{4} \cos(\omega\tau) \sin\left(2\frac{\pi}{L}x_f\right). \quad (1.4)$$

The above expression becomes greater than zero if the conditions $\cos(\omega\tau) > 0$ and $\sin\left(\frac{2\pi}{L}x\right) > 0$ or if $\cos(\omega\tau) < 0$ and $\sin\left(\frac{2\pi}{L}x\right) < 0$ are satisfied simultaneously. This implies the following relation for the Rayleigh index to be positive for the delay term τ and heat source location x_f

$$0 < x_f < \frac{L}{2}, \quad 0 < \tau < \frac{T}{4} \quad \text{or} \quad \frac{3T}{4} < \tau < T, \quad (1.5)$$

$$\frac{L}{2} < x_f < L, \quad \frac{T}{4} < \tau < \frac{3T}{4}. \quad (1.6)$$

A graphical representation of the above relationship, which represents the regions of potential instability (“stability map”), is shown in Fig. 1.2.

Now let us assume the heat release oscillation as a nonlinear function (for a nonlinear relation, the method of superposition does not apply, see Appendix A for a definition of the linearity) of the acoustic velocity as,

$$Q'(x, t) = \left(\hat{Q} \sin(\omega(t - \tau)) \cos\left(\frac{\pi}{L}x\right) + \epsilon \left(\hat{Q} \sin(\omega(t - \tau)) \cos\left(\frac{\pi}{L}x\right) \right)^3 \right) \delta(x - x_f). \quad (1.7)$$

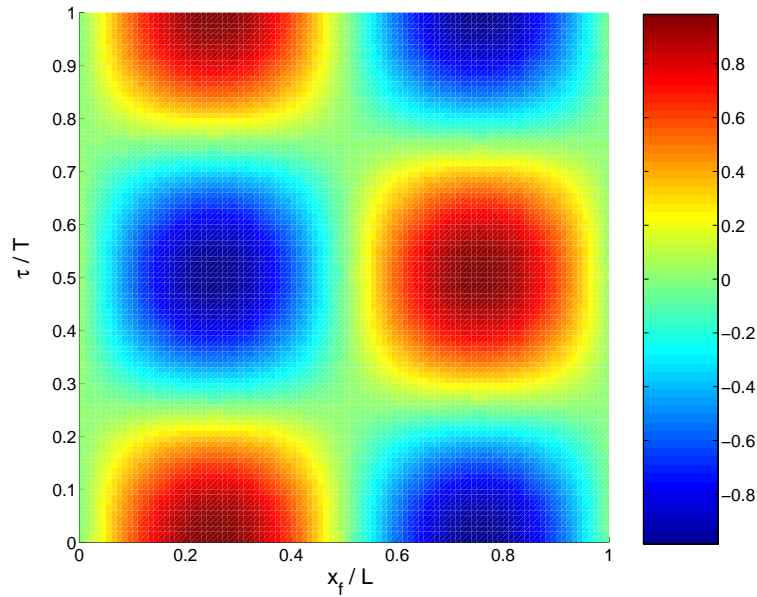


Figure 1.2: Graphical representation of Rayleigh Index and the regions of potential instability ($RI > 0$)

The amplitude of the third order nonlinearity is introduced with the ϵ coefficient. If this representation is incorporated in Eq 1.1, the following simplified form is obtained,

$$RI = \frac{\hat{P}\hat{Q}}{4} \cos(\omega\tau) \sin\left(2\frac{\pi}{L}x_f\right) \left(1 + \frac{3\epsilon}{4}\hat{Q}^2 \cos^2\left(\frac{\pi}{L}\right)\right). \quad (1.8)$$

This equation, when compared to Eq. 1.4, introduces an additional term with ϵ coefficient. If $\epsilon > 0$, then the nonlinear contribution of the term is positive, and if $\epsilon < 0$, the nonlinear contribution of the term is negative. This shows in an exemplary manner that the nonlinearity has a stabilizing or destabilizing effect on thermo-acoustic oscillations. In literature, the expression “saturation of thermo-acoustic instability” is frequently used. This expression means that nonlinear effects tend to stabilize (limit) the unstable growth of thermo-acoustic oscillations. In this simple example, only one mode of the oscillation is taken into account. If the acoustic pressure and velocity are expressed as superposition of the modes, then the nonlinearity (in this case we consider only

the nonlinearity in the combustion response to velocity perturbation) causes the coupling terms of the modes to appear. Eventually, thermo-acoustic oscillations lead to nonlinear steady state periodic oscillations which are called “limit cycle”. Damping and the losses of the acoustic energy will be equal to the energy gained from the heat source when the limit cycle is reached.

1.2 Nonlinear Effects in Thermo-Acoustic Systems

Nonlinearities in thermo-acoustic systems can be of several types.

Heat source nonlinearity: For most velocity sensitive thermo-acoustic systems (heat release is a function of the acoustic velocity perturbation in the immediate vicinity), the dominant source of the nonlinearity is the relationship between the flow in the vicinity of the heat source and heat release oscillations. With increasing amplitudes of the velocities with respect to the mean, nonlinear effects become important.

The nonlinear effects in a simple resonator tube (“Rijke tube”) configuration have been numerically and experimentally analyzed by Heckl [59]. It has been shown that nonlinearity in the heat source with increasing amplitudes determines the saturation of the instability in the Rijke tube. As the heat source mode, a correlation that is widely used in hot wire anemometry based on “King’s Law” has been used. It has a square root type nonlinearity with one time lag.

Hantschk and Vortmeyer [57] have performed numerical simulation of the Rijke tube using computational fluid dynamics (CFD). Heating bands kept at constant temperature have been used as the heating element. The two dimensional compressible Navier-Stokes and energy equation for a Rijke tube with open-open and open-closed boundary conditions have been solved. It has been shown that flow reversal in the vicinity of the heat source (for velocity fluctuation amplitude at 30% of the mean where the nonlinearity in the heat source kicks in) is responsible for the system to reach limit cycle.

Matveev [87] has derived a nonlinear transfer function model of the heat

source using convective heat transfer equation in unsteady flow. A quasi-steady approach has been utilized, and the amplitude dependent nonlinearity in the phase of the transfer function has not been taken into account. The heat source model in this study is very similar to the one that has been used by Heckl [59]. It has been shown that the flow reversal at the heat source is critical for the nonlinear addition of the heat transfer.

The above mentioned studies have been performed for a simple configuration of a thermo-acoustic device (Rijke tube). The nonlinearity in the heat source is the determining factor for these systems to achieve limit cycle oscillations.

It is sometimes useful to check the heat source response (nonlinear dynamic response of the heat source) to harmonic acoustic perturbations of high amplitude. This type of analysis gives valuable information about the nonlinear heat source behavior on the overall stability of thermo-acoustic system.

Nonlinearity in the heat release response to harmonic velocity forcing for the heat source, in isolation from the thermo-acoustic system, has been investigated for a laminar premixed flame by Lieuwen [81]. It has been shown that the phase has negligible dependence on the forcing amplitude in contrast to gain of the transfer function. The nonlinearity has been found to increase with frequency and, at comparable amplitudes, the response of the V-flame is more nonlinear than that of a conical flame.

The response of the diffusion flame model (infinite chemistry) to uniform velocity disturbances has been studied both analytically and numerically by Balasubramanian and Sujith [9]. It has been shown that in contrast to laminar flame model, the gain exhibits no dependence on the forcing amplitude, and the phase shows some weak deviations from the linear behavior at high frequencies. Even though an exponential type nonlinearity was observed in the flame heat release response, the FFT diagrams showed almost linear behavior for the considered ranges of amplitudes and frequencies.

Gas dynamics nonlinearity: Gas dynamics nonlinearity is valid in the entire flow domain, as compared to the local nonlinear effects, and is primarily induced by the instability in rockets, where fluctuating amplitude of the pressure reaches 20-50% of the mean.

Culick and co-workers [102, 142] have considered second and third order non-linearity for gas dynamics in combustion chambers. Approximate solutions based on modal approach and spatial averaging using conservation equations have been reported. Existence and the stability of the limit cycle have been analyzed.

Nonlinear instability of oscillations in gas-filled tubes has been studied by Karpov and Prosperetti [68]. Asymptotic analysis has been used, with expansion up to fourth order in the perturbation parameter. Limit cycle amplitude dependence upon the temperature difference in the stack, and stack plate spacing have been obtained.

Yuan et al. [143] have analyzed the thermo-acoustic prime movers with heat transfer and drag effects in the nonlinear regime. A numerical scheme has been developed that can handle steep wave forms.

These studies show that nonlinear gas dynamics is important for some thermo-acoustic systems to saturate the instability into limit cycle oscillations. But in many premixed combustors at low Mach numbers, at the onset of the nonlinearity, the magnitude of the pressure fluctuations is quite small. The reported pressure amplitudes are of the order of 1-5% of the mean [80]. In this case linear acoustic treatment is adequate.

Nonlinearity of the losses: Nonlinearities of acoustic losses could be due to the reflection of the waves from the boundaries, losses in the acoustic boundary layer, and convection losses of the sound due to the mean flow [59, 88].

Atig et al. [3] investigated numerically, the effect of nonlinear losses localized at the open end of the tube for a clarinet-like instrument. The nonlinear losses have been found to have significant influence on the playing range of the clarinet.

Heckl [59] has showed that with increasing amplitudes, the nonlinearity at the reflections from the tube ends may also contribute to the saturation of the instability.

Nonlinearities limit the growth of the unstable modes of the oscillations and determine the final amplitude. If it is not possible to avoid thermo-acoustic

instabilities altogether, then it becomes important to predict the amplitude of the nonlinear oscillations. This is required since the detrimental effects of instabilities on the combustor lifetime and noise emissions depend on the limit cycle amplitude. Therefore, it is necessary to find the amplitude dependence of the limit cycle oscillation and its stability to system parameters for design objective of thermo-acoustic systems.

To suppress the thermo-acoustic instabilities, active and passive control strategies have been developed [2, 60, 113]. In passive control, modifications in the system hardware, either for the chamber dynamics or combustion dynamics (modification of the burners, addition of the resonators, baffles), have been proposed [33]. In active feedback control of thermo-acoustics, a controller is designed, which prevents the favorable coupling between heat release and acoustics such that oscillations would decay [37]. On the other hand, a nonlinear controller may be necessary for the following reasons [127]:

- To improve the performance of the controlled system (to operate in a wide range of conditions; a linear controller may have poor performance or even become unstable).
- To deal with some special types of nonlinearities like hysteresis or saturation, whose linear approximations do not exist (see Appendix B for the hysteresis and saturation type nonlinearity).
- To deal with model uncertainties (linear controllers generally require that the model parameters should be known, as the uncertainties in the model parameters may cause poor performance or unstable operation. Nonlinear controllers can be designed to incorporate nonlinearity in the controller to tolerate the uncertainties.)

1.3 Non-Normality of Thermo-Acoustic Systems

A system is said to be non-normal if its operator or system matrix does not commute with its adjoint. Thermo-acoustic systems have non-normal operators, which are caused by the heat source [8, 10]. Non-normal systems have

non-orthogonal eigenvectors (Eigenvectors are obtained from the system matrices. In vibrational analysis, eigenvectors represent the shape of the vibrational mode, and the eigenvalues show the frequencies of these modes). A decay of the individual eigenvectors does not necessarily indicate a decay of the response [8, 123, 136]. In the short time-scales involved, there may be energy exchange between the modes, and this may cause an amplification of the initial energy. If this short time growth of initial energy achieves high enough amplitudes, then the nonlinearity present in the system will be excited (nonlinear driving). Therefore, a classical stability analysis based on the normal-modes may give unreliable predictions.

In the context of combustion instabilities, Balasubramanian and Sujith [8] have studied the non-normal nature of the flame/acoustic interactions in a ducted diffusion flame. An infinite chemistry diffusion flame model with one dimensional acoustics has been used. Both the combustion response and the system acoustics have been represented in terms of the basis functions (modal representation). It has been shown that for the coupled system, for certain initial conditions, the oscillations decay, whereas for certain other initial conditions the oscillations grow (for the same set of parameters).

Balasubramanian and Sujith [10] have shown the non-normality in a Rijke tube with a heat source model based on King's law. The full thermo-acoustic system has been simulated in time domain with the Galerkin method. The delay time in this heat source model is short and a Taylor series approximation has been made to eliminate the delay term. If the system has large delays which are caused by the heat source, i.e. when flame is used as heat source, one has to deal with the delay term.

Subramanian and Sujith have studied the non-normal behavior for a ducted premixed flame [129]. In this approach, system acoustics has been coupled with the flame front displacement equation (G-equation).

In these approaches, introducing additional degrees of freedom from the combustion response to the system matrices may introduce non-normality. It is hard to judge if the non-normality introduced in this way is a numerical or physical effect.

1.4 Modeling Approaches of Thermo-Acoustic Systems

Thermo-acoustic systems can be simulated either in time or frequency domain. A variety of approaches exist with differences in complexity, accuracy and flexibility. Low order modeling of thermo-acoustic systems has become important since a reduction in the computational demand (time and resources) is achieved. System stability and performance dependency upon the system parameters can be quickly checked (i.e. limit cycle amplitude dependence upon the damping, heat source location). A schematic representation of the system modeling approaches of thermo-acoustic systems along with their capabilities is shown in Fig. 1.3.

Finite Volume Finite Element	Method	Domain	Limit Cycle Prediction	Non-Modal Stability	Solution Type
	CFD Navier - Stokes	Time	Yes	Yes	Nonlinear Partial Differential Equations
Computational Acoustics	Time	Yes	Yes	Linearized Partial Differential Equations	
Modal Based	Galerkin	Time	Yes	Yes	Delay Differential Equations
	Network Models	Frequency	No	No	Algebraic Equations
	Sinusoidal Describing Function	Frequency	Yes	No	Algebraic Equations
	Coupled Modes	Frequency	Yes	No	Algebraic Equations

Figure 1.3: A schematic of the modeling approaches for thermo-acoustic systems

1.4.1 Time Domain System Models

In CFD based modeling of the thermo-acoustic systems, compressible Navier-Stokes equation along with the energy equation are solved using finite dif-

ference/element/volume techniques. CFD models of the full thermo-acoustic systems could predict the limit cycle. Entezam et al. [44] have observed the limit cycle oscillations in the Rijke tube by numerical simulation with CFD. Chattereajie et al. [25] have obtained the amplitude and the frequency of the nonlinear oscillations for a reacting flow inside a Rijke tube combustor using CFD. Even though the finite element/volume solvers can deal with thermo-acoustic systems in complex geometric configurations, different length and time scales involved in the combustion/acoustic interactions make it hard to achieve converged results. Even in the case of a simple duct (one dimensional acoustics), expensive computational resources and time are required.

Linearizing the Navier-Stokes equation yields the inhomogeneous wave equation for pressure fluctuations, with a source term which represents the heat release rate from combustion [100, 101]. Pankewitz [99–101] has solved the inhomogeneous wave equation for complex geometries using finite element method. In this approach, heat source is modeled by a flame transfer function obtained either from experiments or numerical simulations.

Approximate solution of the partial differential equation for the inhomogeneous wave equation can be obtained using Galerkin method [31, 32, 145]. Powell and Zinn [112] applied a Galerkin expansion technique to investigate the longitudinal and transversal instability in liquid rocket motors. The technique has also been used by Culick in several studies [1, 31, 32]. In the Galerkin method, acoustic velocity and pressure are expressed in terms of basis functions which satisfy the boundary conditions and constitute a complete set of basis. The computation is cheaper compared to the former approach. In the inhomogeneous wave equation and Galerkin method, a closure term for the combustion response (heat release/transfer rate) is required. When the heat source has many constant delays, a delay differential equation has to be solved in the Galerkin method, which creates a difference in the computational time.

1.4.2 Frequency Domain System Models

Low order models of thermo-acoustic system in the frequency domain, called “network models”, have been developed and used to study the stability of

thermo-acoustic systems [35, 38, 45, 70, 74, 111]. The flame jump conditions along with the network elements, which are described by their flame transfer functions/matrices yield a set of equations to be solved to determine the frequency and the growth rate of the oscillation. An analytical investigation of the thermo-acoustic stability with network elements has been performed by Merk [90]. In this approach, individual elements of thermo-acoustic networks are represented by their transfer functions/matrices. Transfer functions/matrices can be obtained analytically for simple acoustic elements, such as area change and pressure loss, or can be determined from experimental measurements [103, 104, 106]. System identification has been offered as a tool to determine the transfer function/matrices of complicated elements like a turbulent flame [53, 54]. This frequency domain approach works only in the linear regime and is incapable of predicting the limit cycle amplitude.

To find the amplitude of the nonlinear oscillations of thermo-acoustic systems in the frequency domain, sinusoidal describing function technique has been used in which the nonlinearity in the heat source is taken into account [36, 39, 96]. Describing function is simply an amplitude dependent frequency response of the nonlinear element [36, 52, 96]. The method can be considered as an extension of the linear network models to the nonlinear regime with the nonlinear elements described by their describing functions [36, 96]. Dowling [36] has used a saturation type nonlinearity for the flame model to use in the describing function method to predict the frequency and amplitude of the limit cycle. Dowling and Stow [128] have used a nonlinear flame transfer function model in a network approach to obtain the limit cycle amplitude and frequency for a lean premixed prevaporised combustor. In these studies, the amplitude dependent frequency response of the flame (only for the gain) has been used to predict the approximate limit cycle amplitude. Noiray et al. [96] have used the nonlinearity in the combustion response for a laminar flame using single harmonic forcing. In this study, both the gain and the phase of the nonlinearity for the flame frequency response have been taken into account. In the sinusoidal describing function method, the effect of modal coupling has been ignored. This approach approximates the nonlinear oscillations when the system acoustics filter the higher harmonic components that are produced by the nonlinear heat source.

1.5 Thesis Overview and Contributions

The aim of this research is to develop methods for limit cycle amplitude prediction. We start with a model for the heat source with many degrees of freedom, and proceed to derive a “low-order” dynamic model that can be used as part of some system model to predict system stability. Firstly, a nonlinear dynamic model of the heat source is obtained using system identification procedures or a proper orthogonal decomposition technique. This model of the heat source is then directly coupled to a time domain system model of the full thermo-acoustic system, i.e. Galerkin time domain. Higher order transfer functions as the extension of the linear transfer functions to the nonlinear regime is developed and used in the frequency domain to investigate the nonlinear heat source/acoustic interaction. Then, a frequency domain system model with coupled modes of the full thermo-acoustic system is developed. This system model goes beyond the existing sinusoidal describing function approach and does take into account the interactions of various modes. Rayleigh index in the nonlinear regime is investigated.

As model problems for the heat source, three different configurations have been used: a heated wire mesh in pulsating flow, a heated plate in pulsating flow and a laminar premixed flame. The basic physics of these model problems is well understood and they have been found to have adequate nonlinearity even at the relatively small pressure fluctuations. This would ease the analysis of the system for implementation and validation of the various nonlinear identification strategies and modeling approaches.

The major goals of the research reported in this thesis are:

1. System identification for the nonlinear heat source

To obtain a low-order/efficient dynamic model of the heat source that is valid for a range of operating conditions (different amplitudes and frequencies), nonlinear system identification methods are used. A variety of nonlinear system identification methods developed for applications such as signal processing and control, appear suitable. The input-output data set generated either from the CFD (for the wire in pulsating flow) or from

the flame governing equations (laminar premixed flame, G-equation) are used in the nonlinear identification procedures. In this way, a time domain model of the heat source with the nonlinear input-output relation (input is the acoustic velocity at the vicinity of the heat source and the output is the heat transfer from the wire or heat release from the flame) is obtained.

2. **Physics based nonlinear modeling with Proper Orthogonal Decomposition (POD)**

To obtain a nonlinear dynamic model of the heat source with system identification is a challenging task, and generally requires trial and error approaches. Modeling approaches using governing equations of the system could be advantageous. A physics based nonlinear modeling approach with POD is developed to obtain a low order model of the nonlinear heat source. A heated plate in pulsating flow is used instead of the wire for the sake of simplicity in the numerical processing with POD. The input-output relation is included in the low order model equation (coupled system of ordinary differential equations (ODEs) describing the evolution of the POD modes). POD modes, obtained from a multivariate approach (collects unsteady CFD computations of the heat source for different amplitudes and frequencies of the forcing (input)) are used in the low order model to define the heat source over the desired range of operating conditions.

3. **Nonlinear system model in frequency domain with coupled modes**

With increasing amplitude, energy is transferred to the higher order modes due to nonlinear effects. It is commonly argued that, at the higher frequencies, dissipative mechanisms are stronger and the energy that is driven to the higher harmonic is easily dissipated. However, an energy balance between the modes has not been analyzed yet in detail since the current modeling approach of the nonlinear thermo-acoustic system in the frequency domain is a one mode approximation (sinusoidal describing function method). A coupled modes frequency domain system modeling approach that could take the interactions of various modes into account, is developed. Higher order transfer functions which describe

the heat source nonlinearity are used in this system modeling approach. When the acoustic velocity and pressure are expressed as superposition of the modes, then these modes are coupled through the higher order transfer functions to give energy contribution at the different harmonics (contribution of the higher order modes to the fundamental mode and the energy transfer of the fundamental mode to the higher order modes due to nonlinearity). Rayleigh index in the nonlinear regime is investigated and an energy balance between the modes, analyzed.

4. **Non-modal stability**

A systematic approach is presented to study the non-normal behavior of thermo-acoustic systems when the heat source is obtained from system identification. System identification method gives more flexibility for the modeling of the heat source (complex configurations of the heat source, and no restriction on the delay time). This approach can handle large delay times resulting from the heat source.

In Chapter 2, CFD models of the wire mesh and plate in pulsating flow are presented. Heat transfer basics in pulsating flow is reviewed, and the laminar premixed flame configuration is discussed in this work.

In Chapter 3, linear system identification basics are reviewed and the equations for the correlation based identification method are developed. A widely used heat source model based on King's law and the heat source model based on CFD (wire gauze) is identified. Then the premixed laminar axisymmetric V-flame is identified and the linear transfer functions of the different heat source models are calculated. Advantages of the dynamic modeling with system identification is discussed for different wire heat sources (heat source model based on King's law, heat source model obtained using unsteady boundary layer equations, and heat source obtained from system identification using input-output data set from CFD computations).

In Chapter 4, different nonlinear identification procedures are used to obtain the nonlinear dynamic model of the heat source. First, calculation of the nonlinear transfer function from FFT is considered. Then a polynomial based equation error type (one step ahead prediction) identification is derived. This

identification procedure is extended into frequency domain with two different approaches: a harmonic balance approach (in which the nonlinear transfer functions are derived from a set of nonlinear system of equations) and a harmonic probing approach (in which the higher order transfer functions are derived using recursive relations). The nonlinear transfer functions of the heat source are obtained from these frequency domain models. Then a neural network nonlinear identification strategy is used in time domain and converted into frequency domain using the expansion of the sigmoid activation function into a polynomial approximation. CFD model heat source is identified and nonlinear transfer functions with different nonlinear identification strategies have been derived. The laminar premixed flame is also identified using neural network based system identification. Finally a fuzzy based identification procedure is introduced and CFD model heat source is identified by this identification method. In the conclusion section of this chapter, advantages of the nonlinear system identification and the reason for using a wide range of identification procedures are discussed.

In Chapter 5, a low order model of the heat source (heated plate in pulsating flow) is developed based on the proper orthogonal decomposition technique. Equations are derived for the low order model after the projection of the governing equations onto the modes. A multivariate approach, which collects data from different databases of the unsteady CFD, is utilized to describe the heat source over a range of amplitudes and frequencies.

In Chapter 6, various system modeling approaches are discussed and equations are derived for a simple duct. Then the frequency domain coupled modes system modeling approach based on the higher order transfer functions is introduced. Rayleigh index and energy balancing between the modes in the nonlinear regime have been analyzed, and the effect of the modal coupling in determining the limit cycle amplitude is discussed.

In Chapter 7, an approach is presented to study the non-normal behavior of the thermo-acoustic systems when the full thermo-acoustic system is simulated in time domain using the Galerkin method, and the heat source is obtained from linear system identification. The method has the flexibility to deal with the complex configuration of the heat source using system identification.

Moreover, it can handle large delay times resulting from the heat source.

2 Transient Simulation of the Heat Source

Three different configurations of heat source are chosen as model problems; a heated wire mesh, a heated plate and a laminar premixed flame. The basic physics of these model problems are well understood and they have adequate nonlinearity even at relatively small pressure fluctuations. This eases the analysis of the system for implementation and validation of the various nonlinear identification strategies and modeling approaches. The first and second heat source models (wire and plate in pulsating flow) are simulated in time domain with finite volume and finite element techniques. The laminar premixed flame is simulated using a finite difference scheme for the one-dimensional partial differential equations derived from simplified assumptions (G-equation). The time series for input-output (heat transfer/release response to velocity forcing) is generated and used in linear / various nonlinear system identification procedures for the wire in pulsating flow and for the laminar flame. For the sake of numerical simplicity, a flat plate is used instead of a wire to obtain a low order model of the heat source with POD approach.

In this chapter, the numerical configurations for the wire and plate in pulsating flow are first introduced. Then, the governing equations for the plate are presented, as these are used later in the POD modeling approach. Heat transfer basics in pulsating flow are reviewed and the mechanism of the nonlinearity in heat transfer is discussed. Lastly, the flame configuration is introduced along with the governing equation.

2.1 CFD Model of Heat Transfer of the Wire in Pulsating Flow

The heat source is a wire gauze in the Rijke tube in the presence of the mean flow. A schematic of the Rijke tube with the heating element is shown in

Fig. 2.1. The basic physics of this simple model problem is well understood. The analytical result for the transfer function (heat transfer response to velocity forcing) is derived using unsteady boundary layer equations by Lighthill [83]. Moreover, various identification procedures using input-output data set generated from unsteady CFD are implemented and validated.

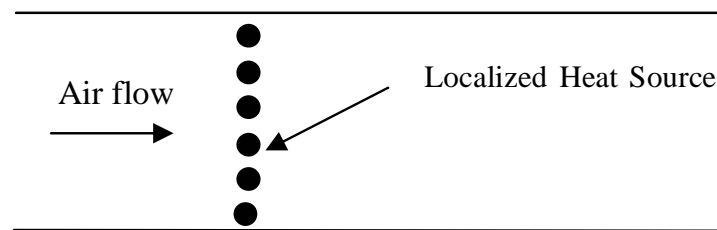


Figure 2.1: Schematic of the Rijke tube with a concentrated heat source

Numerical Setup

The model of the heat source in CFD is the flow over a cylinder, representing the vicinity of one half of a wire of a Rijke tube. The body-fitted mesh is composed of 16540 quadrilateral elements and is refined close to the cylinder surface. Mesh independence of the solutions have been confirmed.

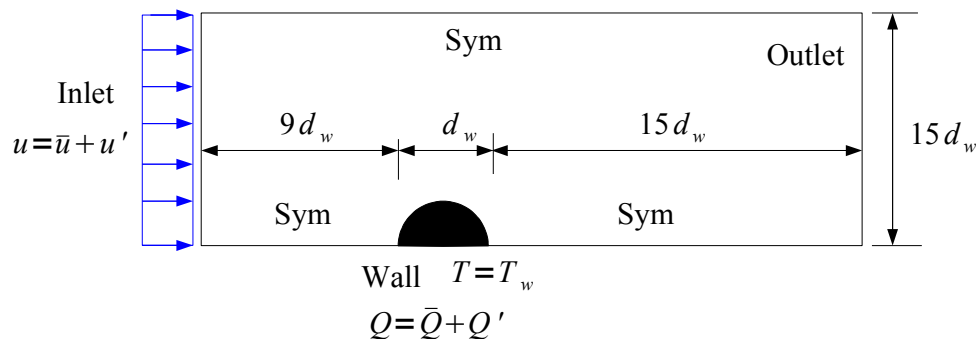


Figure 2.2: Geometry and boundary conditions for CFD modeling of a single wire

The computational domain along with the boundary conditions is shown in Fig. 2.2. The unsteady incompressible Navier-Stokes equation along with the energy equation is solved with FLUENT 6.1 segregated solver (a general purpose finite volume solver) [49]. A second order implicit formulation in time, with a time step of 10^{-4} s and a second order accurate spatial discretization, is used. Second order upwind schemes are used for the momentum and the energy equations. The global convergence for the continuity, momentum and energy residuals are set to 10^{-4} , 10^{-5} and 10^{-5} . The fluid model is incompressible, and the fluid properties are chosen to be temperature independent. Karman vortex streets are observed downstream of a cylinder at Reynolds number $Re > 40$. The Reynolds number based on the characteristic length (wire diameter, d_w) is given by,

$$Re = \frac{\rho \bar{u} d_w}{\mu}, \quad (2.1)$$

where \bar{u} , ρ and μ represent the mean velocity, density and dynamic viscosity of the flow, respectively.

In the present case, $Re = 13$, such that Karman vortices are absent. The use of symmetry boundary conditions at the top and bottom of the domain to reduce the size of the computational domain is thus justified. The diameter of the cylinder d_w is much smaller than the acoustic wavelength of the highest frequency of interest, i.e. the wire is “acoustically compact”, and an incompressible fluid model is adequate. The harmonic perturbation at the inlet is transmitted immediately to the outer flow near the cylinder because of the incompressibility assumption.

2.2 Numerical Simulation of Pulsating Flow with Wall Heat Transfer for a Heated Plate

For the sake of simplicity in numerical processing with POD, a flat plate instead of a cylinder in pulsating flow is considered. The CFD model is restricted to the vicinity of the local heat source for the flow over a heated (kept at con-

stant temperature) wall section, as shown in Fig. 2.3. The fluid model is incompressible, and the material properties are assumed to be temperature independent as in the case of the cylinder in cross-flow. The Reynolds number, based on the length L of the heated section, is 13. An unstructured mesh, with 44150 quadrilateral elements and coarsened away from the heated section, is used. Mesh independence of the solution is assured.

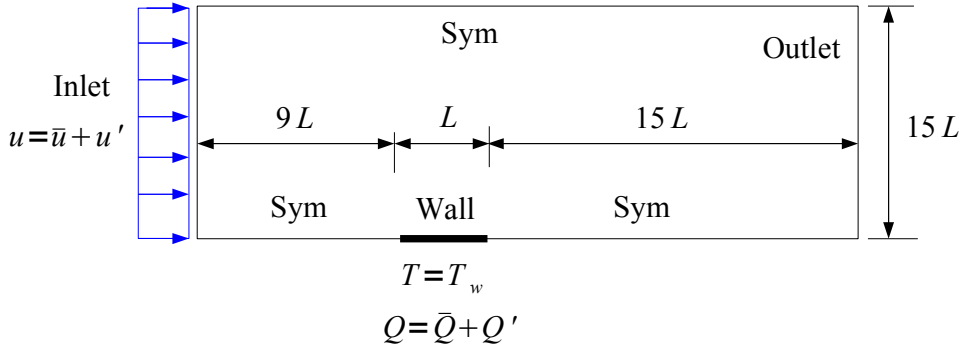


Figure 2.3: Computational domain and boundary conditions with the fluctuating part of the velocity u' and the fluctuating part of the heat transfer rate Q'

Governing Equations

In the case of the wire in pulsating flow and the flame heat sources, only the input-output data set generated from the numerical simulation is used in identification procedures to create dynamical models. On the other hand, the governing equations of the system are used in the POD approach to obtain a low order dynamic model of the heat source.

The non-dimensionalization and governing equations are as follows:

$$u = 1 + \frac{u'}{\bar{u}}, \quad T = \frac{T'}{T_w - \bar{T}}, \quad x = \frac{\tilde{x}}{L}, \quad y = \frac{\tilde{y}}{L}, \quad t = \frac{\bar{u}}{L} \tilde{t}.$$

The superscripts $(\bar{\quad})$, (\prime) , $(\tilde{\quad})$, and T_w denote the mean values, fluctuating parts, dimensional values (for coordinates x, y and for time t) and wall temperature, respectively. Then, the dimensionless form of the incompressible Navier-

Stokes and energy equations becomes,

$$\frac{Du}{Dt} = -\nabla p + \frac{1}{\text{Re}} \Delta^2 u, \quad (2.2)$$

$$\frac{DT}{Dt} = \frac{1}{\text{PrRe}} \Delta^2 T. \quad (2.3)$$

Reynolds and Prandtl numbers are defined as,

$$\text{Re} = \frac{\rho \bar{u} L}{\mu}, \quad (2.4)$$

$$\text{Pr} = \frac{c_p \mu}{\lambda}. \quad (2.5)$$

The symbols c_p and λ denote the specific heat capacity at constant pressure and the thermal conductivity, respectively. Equations (2.2) and (2.3) are solved using Comsol Multi-physics 6.1 solver (a general purpose finite element solver) [28] with a time step of 1/50 th of the period of the harmonic excitation at the inlet. Harmonic excitations at different amplitudes and frequencies are applied at the inlet. At the heated section, the unsteady heat transfer rate per unit area (thermal flux, units W/m²) is extracted as an area-averaged value over the heated flat plate. In the CFD model, a perturbation of small or large amplitude is imposed on the steady state solution, which is used as the initial condition for the unsteady calculations.

2.3 Heat Transfer in Oscillatory Flow

In the case of forced convection, the non-dimensional heat transfer rate, Nusselt number (Nu), is a function of Reynolds (Re) and Prandtl (Pr) numbers [7, 122], such that,

$$\text{Nu} = f(\text{Re}, \text{Pr}). \quad (2.6)$$

Simple empirical correlations are available for the heat transfer from the wire and plate for different Reynolds ranges. Hilpert [61] gave such a relation for the range between 1 and 240000 using different wire diameters.

King's Law

A correlation by King [71] now known as King's law, is widely used in hot wire anemometry:

$$Q(t) = L_w(T_w - T) \left(\lambda_a + 2\sqrt{\pi\lambda_a c_v \bar{\rho} \frac{d_w}{2} |u(t-\tau)|} \right). \quad (2.7)$$

Material properties of the fluid are denoted by $\bar{\rho}$ for the mean density, c_v for the specific heat at constant volume, and λ_a for the heat conductivity of fluid. L_w and d_w represent the length and the diameter of the wire, respectively. T_w is the temperature of the wire, and τ is the time lag.

Heat transfer rate from the wire, for small imposed fluctuation at the inlet, has a linear dependence upon the amplitude of the fluctuating part of the incoming velocity at a fixed frequency. This dependence for the high and low frequency limits has also been shown by Lighthill [83]. This linear relation can also be seen from King's law, where the square root nonlinearity becomes a linear relation between the unsteady part of the heat transfer rate and the unsteady velocity for a constant time lag. The relation in Eq. (2.7) is written as,

$$Q'(t) + \bar{Q} = K_1 + K_2 \sqrt{\left| 1 + \frac{u'(t-\tau)}{\bar{u}} \right|}, \quad (2.8)$$

where K_1 and K_2 are constants that are defined as,

$$K_1 = L_w(T_w - T)\lambda_a, \quad K_2 = 2L_w(T_w - T)\sqrt{\pi\lambda_a c_v \bar{\rho} \frac{d_w}{2\bar{u}}}.$$

For flow velocities much less than the mean velocity, a Taylor series approximation for the square-root nonlinearity is written as,

$$\sqrt{\left| 1 + \frac{u'(t-\tau)}{\bar{u}} \right|} = 1 + \frac{1}{2} \frac{u'(t-\tau)}{\bar{u}} - \frac{1}{8} \left(\frac{u'(t-\tau)}{\bar{u}} \right)^2 + \dots, \quad \text{for } \frac{u'(t-\tau)}{\bar{u}} < 1. \quad (2.9)$$

Neglecting the square term and other higher order terms of the above equation, a linearized form for the fluctuating parts becomes,

$$Q'(t) = \frac{K_2}{2} \frac{u'(t - \tau)}{\bar{u}}. \quad (2.10)$$

This is the widely used heat source formulation, the so-called “ $n - \tau$ ” formulation for combustion systems.

Wall Heat Transfer in Laminar Flow

In order to obtain the heat transfer from the unsteady boundary layer equations, similarity solutions or integral equations are used, in which assumed profiles (generally polynomials of various orders) for the velocity and temperature boundary layers are introduced [7, 122]. If the outer flow imposes a low amplitude harmonic time dependent perturbation on the base flow, then the solution of the unsteady boundary layer can be obtained when the frequency of the imposed oscillation is very low or very high (expanding around frequency). When the perturbation amplitudes are comparable to that of the mean, nonlinear contributions in the boundary layer cannot be neglected thereafter. Higher harmonics as well as the nonlinear streaming part appear in the thermal and hydrodynamic boundary layer responses [133]. These nonlinear contributions have an influence on the heat transfer. A linear relation is no more valid for higher amplitudes of the fluctuation.

Heat transfer at the wall for a laminar flow is computed by the Fourier’s Law as,

$$Q_w = -\lambda \left. \frac{\partial T}{\partial y} \right|_w = h(T_w - T_\infty), \quad (2.11)$$

where λ , h , T_∞ and y denote the thermal conductivity of the fluid, heat transfer coefficient, free stream temperature and wall normal coordinate, respectively. In the numerical simulation, the wall heat transfer is computed by the approximation of the temperature gradient at the wall based on the nearest element to the wall.

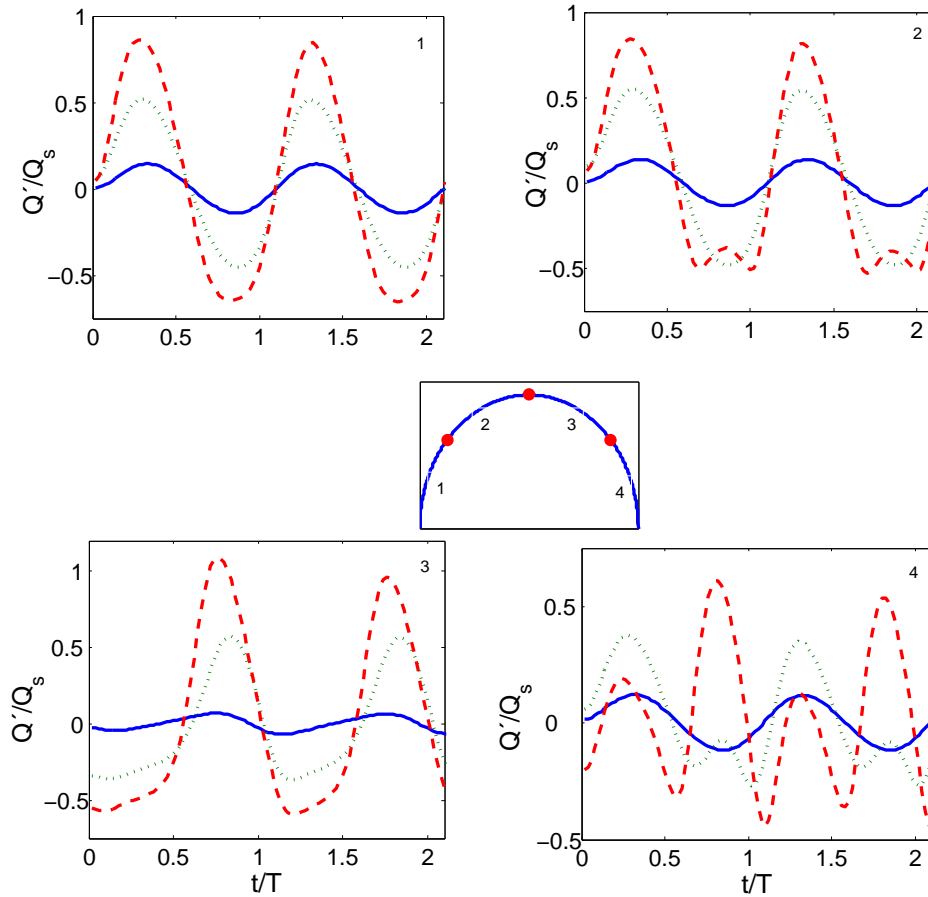


Figure 2.4: Normalized heat transfer rate of the sections 1,2,3 and 4 on the wire's surface for different velocity amplitude fluctuations (dashed lines-2, dotted lines-1 continuous lines-0.3)

The flow passed over the heated wire, reverses back in the second half of the period and reduces the effective heat transfer rate from the cylinder when the fluctuating part of the flow velocity has a value comparable to the mean. Heat transfer rate is monitored at four different sections on the wire as indicated in Fig. 2.4. The normalized fluctuating heat transfer rates (Q') with respect to steady state values (Q_s) are shown for three different fluctuating amplitudes. Time axis is normalized with respect to the period of the excitation (T). Non-dimensional amplitude and the frequency of the forcing, velocity amplitude ratio (A), and Strouhal Number, (Str) are defined as,

$$A = \frac{u'}{\bar{u}}, \quad (2.12)$$

$$\text{Str} = \omega \frac{d_w}{\bar{u}}, \quad (2.13)$$

for fluctuating velocity u' , forcing radial frequency ω , wire diameter d_w and the mean velocity \bar{u} . Most of the heat transfer takes place in the first quadrant, and the heat transfer rates for $A = 0.3$ show almost linear behavior at every section (pure sinusoid). The first nonlinear contribution is seen for $A = 2$ in the second quadrant. In the last two quadrants, nonlinear contributions for $A = 1$ and $A = 2$ become significant.

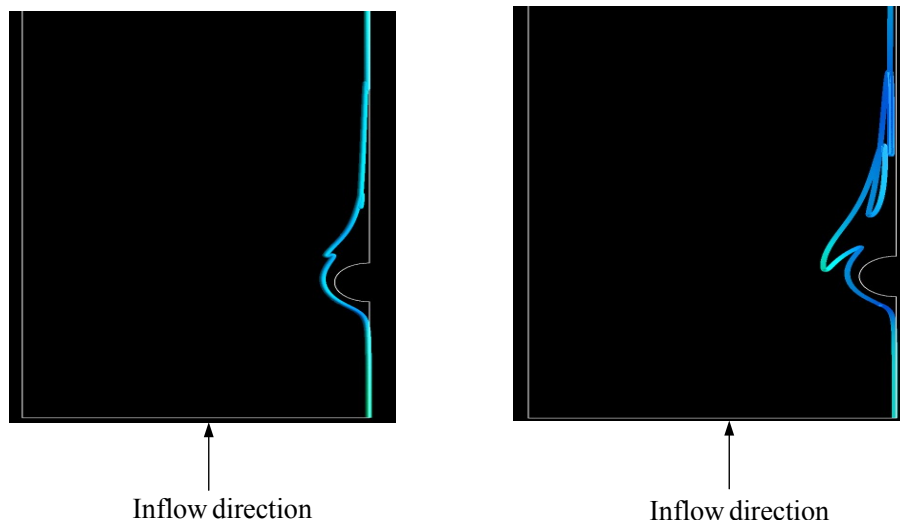


Figure 2.5: Path of massless particles released at inlet for $\text{Str} = 0.721$ and $A = 1$ (left), $A = 2$ (right)

In order to visualize the flow reversal at the wire with increasing velocity amplitudes, massless particles are introduced at the inlet and tracked over time. The Lagrangian trajectories of a massless particle released at the inlet position, for two different velocity amplitude ratios at $\text{Str} = 0.721$, are shown in Fig. 2.5.

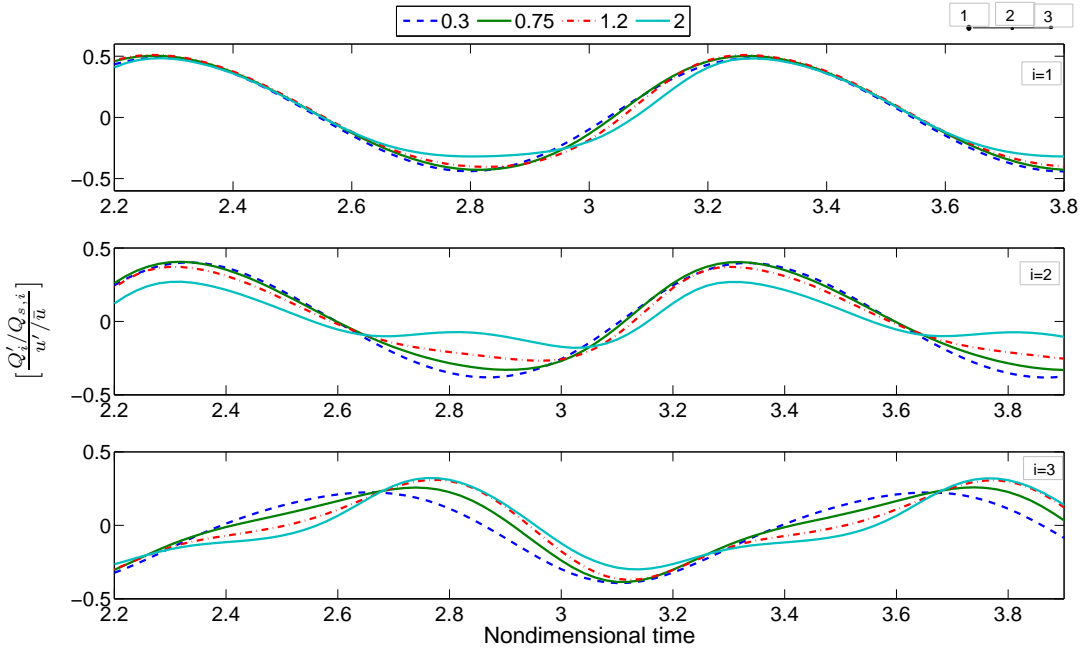


Figure 2.6: Non-dimensionalized heat flux (with respect to the steady state values at the local positions and amplitude of the forcing at the inlet) at three points of the heated flat part

In Fig. 2.6, the non-dimensionalised (with respect to steady state value) fluctuating heat transfer rate per unit area at three points of the heated flat part are shown for $A = 0.3, 0.75, 1.2$ and 2 , at $\text{Str} = 10$ (based on the length of the plate L),

$$\text{Str} = \frac{\tilde{\omega}L}{\bar{u}}, \quad (2.14)$$

where $\tilde{\omega}$ is the dimensional angular frequency.

The nonlinearity in the portion of the signal is clearly seen from the distortion of a pure harmonic with the addition of a higher harmonic for high amplitude of fluctuation for the second and third points.

The complex interactions between the hydrodynamic and the thermal boundary layer with the nonlinear contributions prevent the correlation of the heat transfer rate at the wire and the fluctuating part of the incoming velocity using unsteady boundary layer equations [122, 133]. In the following sections,

nonlinear dynamic models for the input-output relation (input is the velocity forcing and output is the fluctuating part of the heat transfer rate either from the wire or plate) are obtained using nonlinear system identification procedures and proper orthogonal decomposition technique.

2.4 Laminar Premixed Flame Configuration

As a third example of the heat source, a laminar premixed flame is considered. The flame is an axi-symmetric V- flame attached at one point, and is shown in Fig. 2.7. The laminar flame dynamics is described by front tracking equations, called the G-equations, and at the flame front, the following equation holds [40, 48, 81, 129] good,

$$\frac{DG}{Dt} = S_L |\nabla G|, \quad (2.15)$$

where G is a field property. The other assumptions are the spatially uniform velocity field (purely axial) and a constant laminar flame speed. With these simplifications, the following flame front tracking equation is obtained when the incoming velocity is assumed to be $\vec{u} = (0, v)$ for a coordinate system aligned with the flow.

$$\frac{\partial \xi'}{\partial t} + (\bar{v} + v') \cos(\alpha) \frac{\partial \xi'}{\partial X} - (\bar{v} + v') \sin(\alpha) = -S_L \sqrt{1 + \left(\frac{\partial \xi'}{\partial X}\right)^2}, \quad (2.16)$$

where the velocity components along and perpendicular to the flame are given as $v \cos(\alpha)$, $v \sin(\alpha)$, respectively, and α is the inclination of the flame to incoming flow. Further analysis of the resulting partial differential equation (linearization) and a numerical scheme to solve it are described in [129].

The heat release, Q , for a laminar premixed flame is written as,

$$Q = \rho S_L \Delta q_r A, \quad (2.17)$$

where ρ is the density of the incoming mixture, Δq_r is the heat release per unit mass of the mixture [J/kg], and A is the flame surface area.

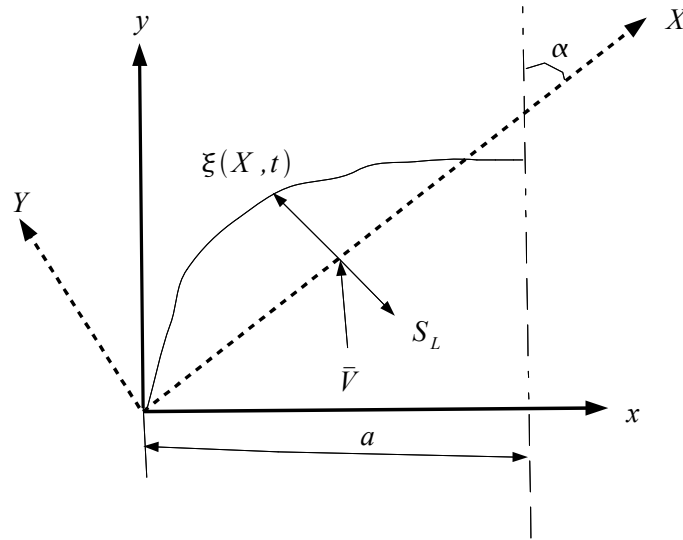


Figure 2.7: Schematic of the axi-symmetric V-flame attached at one point

In the absence of the equivalence ratio fluctuations from the above equation, the response is related to the area fluctuation as,

$$\frac{Q'}{\bar{Q}} = \frac{A'}{\bar{A}}. \quad (2.18)$$

The flame area A is calculated from the flame front position by the following relation [81, 129],

$$A(t) = 2\pi \int_0^{a/\sin(\alpha)} (X \sin(\alpha) - \xi \cos(\alpha)) \sqrt{1 + \left(\frac{\partial \xi}{\partial X}\right)^2} dX. \quad (2.19)$$

We have used the code developed at IIT Madras (Prof. Sujith's group) [129] for the laminar flame to get the input (acoustic forcing) and output (heat release rate of the flame) data set, which is used in the system identification methods.

3 Linear System Identification

System identification can be used to construct dynamic models from the input-output data sets that may be obtained from an experimental test rig or numerical simulation [84, 124]. For the CFD model of the wire heat source, obtaining a linear transfer function (heat transfer response of the wire to small acoustic perturbations for a frequency range) may be challenging due to the complex interactions in the hydrodynamic and thermal boundary layer. Lighthill has derived an analytical transfer function using unsteady boundary layer equations in the low- and high-frequency regimes, respectively [83]. Linear transfer function of the CFD model of the wire heat source is computed from an FFT of the response with single sinusoid excitations for different frequencies. On the other hand, with the linear identification method based on correlation, one can obtain the same transfer function using a broadband excitation signal with less computational effort. More complex configurations of the heat source, such as a turbulent flame, are identified in the linear regime (linear transfer function is obtained) using the input-output data set from unsteady CFD computations or experimental setup [54, 132]. It is advantageous to know some of the physical parameters of the system a priori, e.g. the order of the maximum lag, when constructing dynamic models from identification. This information can also be obtained from the identification as in a black-box approach [144]. In this chapter, the common procedures and model structures used in linear system identification are presented. Then, equations for a correlation based linear identification in time domain is derived. Three different heat source models, which include CFD model of the wire heat source, heat source model based on King's law and a simple model for the laminar premixed flame, are identified using this correlation based linear identification. Transfer functions are derived. Moreover, the transfer functions for the heat source based on King's law, CFD model of the wire heat source and Lighthill's derivation are compared.

3.1 Procedures and Model Structures used in Linear System Identification

Identification methods can generally be classified as parametric and non-parametric. In the parametric approaches, the system is described with differential/difference equations, and the aim is to find the parameters of this mathematical description. Well known non-parametric representations are the *Impulse Response* (in the time domain) and the *Frequency Response* (in the frequency domain).

The input-output representation of an LTI (Linear Time Invariant, see Appendix A for the definition of an LTI system) system in polynomial form is expressed as [84] :

$$A(z)Q(t) = \frac{B(z)}{F(z)}u(t) + \frac{C(z)}{D(z)}v(t), \quad (3.1)$$

where A, B, C, D, F are polynomials in terms of z , u and Q are the input and output of the system, and v is the error term. z is a shift operator namely,

$$zQ(t) = Q(t+1). \quad (3.2)$$

Here, $Q(t+1)$ is a shorthand notation for $Q(t+\Delta t)$, for the time step Δt . This operator simply shifts one step ahead value of the input or output to the current time. The past inputs ($u(t-1), \dots, u(t-N_u)$) and outputs ($Q(t-1), \dots, Q(t-N_Q)$) are called the *regressors*. Depending on the polynomials used, different model structures appear [84].

FIR (Finite Impulse Response):

$$A = C = D = F = 1$$

This is the simplest model structure to be considered. The past inputs are used as regressors. The structure results in a linear least square problem for minimizing the cost function (e.g. Euclidean norm of the residual between the actual and the estimated output). It requires many regressors and the convergence rate is slow.

ARX (Auto Regressive with eXogenous input):

$$C = D = F = 1$$

This model structure uses the past inputs and past outputs as regressors. This again results in linear least square description where the cost function needs to be minimized.

ARMAX (Auto Regressive Moving Average with eXogenous input): $D = F = 1$

OE (Output Error): $A = C = D = 1$

In the identification, a model structure is selected and the number of past inputs and outputs are specified. Another classification that is important (for an application in “divide and conquer”) is based on whether the simulated or measured past outputs are used as regressors in the model structure. In an output error type modeling approach, the simulated past outputs obtained from the model structure are used, whereas, in an equation error type modeling approach, the measured past outputs are used as regressors. A criterion to minimize the difference between the actual output and output from identification are specified in order to get the parameters of the model structures. In an equation error/output error type modeling approach, this criterion results in a linear/nonlinear least square fit.

Identification methods have the following procedures in common [84, 124, 126]:

- **An appropriate choice of the input signal:** The system is excited with a proper signal for the excitation of all relevant modes of interest. Generally, broadband forcing, chirp signals or pseudo random binary sequences, which have white noise characteristics, are used to excite the system for a wide range of frequencies.
- **Model structure selection:** Equation error or output error model structures are used.
- **Selection of the number of past inputs and outputs used in the model structure (the system “memory”):** A priori information about the maximum time lag of the system is helpful. Depending on the maximum frequencies of interest and the time lag of the system under consideration,

the number of regressors is specified.

- **An algorithm to minimize the cost function:** The difference between responses of the time series data generated from numerical simulation or experiment and identification is minimized. Marquardt-Levenberg algorithm, Gauss-Newton methods or other nonlinear optimization (genetic algorithms, particle swarm optimization) methods are used.
- **Model Validation:** The identified model is tested against signals which have not been used in the estimation. In a broadband forcing, half of the data is used for the fit (minimization of the cost function) while the other half is used for validation.

3.2 Time Domain Identification using Correlation Analysis

For an LTI system, the output in discrete form is expressed by the following equation [84],

$$Q(t) = \sum_{l=-\infty}^{\infty} h(l)u(t-l) + v(t), \quad t = 1, 2, \dots \quad (3.3)$$

where Q , u , h and v denote the output, input, unit impulse and additive noise, respectively.

For a causal Finite Impulse Response (FIR) model with maximum length of L , (the impulse coefficients will be zero after L terms) this relation is written as [84, 137],

$$Q(t) = h(0)u(t) + h(1)u(t-1) + \dots + h(L)u(t-L). \quad (3.4)$$

If the input u is a stationary process with zero mean and uncorrelated with the additive noise v , then

$$R_{uv}(r) = \langle u(t)v(r-t) \rangle = 0, \quad \forall r, \quad (3.5)$$

$$R_{Qu}(r) = \langle Q(t)u(r-t) \rangle = \sum_{l=0}^L h(l)R_{uu}(l-r), \quad \forall r, \quad (3.6)$$

where $\langle \dots \rangle$ denotes the ensemble average over the data record.

If the unit impulse response coefficients $h(l)$ of a system are not known a priori, they can be computed (“estimated”) from the auto-correlation matrix of the signal R_{uu} and the cross-correlation vector between the signal and the response R_{Qu} by the following relation:

$$h = R_{uu}^{-1}R_{Qu}. \quad (3.7)$$

This equation, sometimes called the inversion of the Wiener-Hopf equation [107, 110], is written in expanded form as [84, 137],

$$\begin{bmatrix} h(0) \\ h(1) \\ \vdots \\ h(L) \end{bmatrix} = \begin{bmatrix} R_{uu}(0) & R_{uu}(1) & \dots & R_{uu}(L) \\ R_{uu}(-1) & R_{uu}(0) & \dots & R_{uu}(L-1) \\ \vdots & \vdots & \dots & \vdots \\ R_{uu}(-L) & R_{uu}(-L+1) & \dots & R_{uu}(0) \end{bmatrix}^{-1} \begin{bmatrix} R_{Qu}(0) \\ R_{Qu}(1) \\ \vdots \\ R_{Qu}(L) \end{bmatrix}. \quad (3.8)$$

For the finite time series data $\{u(t), Q(t)\}$ of length M , the individual elements of the auto-correlation matrix and the cross correlation vector are,

$$R_{uu}(l-r) = \frac{1}{M-L+1} \sum_{t=L}^M u(t-l)u(t-r), \quad l, r = 0, \dots, L, \quad (3.9)$$

$$R_{Qu}(r) = \frac{1}{M-L+1} \sum_{t=L}^M Q(t)u(t-r), \quad r = 0, \dots, L. \quad (3.10)$$

Three different heat source models are identified using this correlation based identification. First, a simple model of the heat source based on King’s law is identified. Next, the time series of heat transfer rate fluctuations in response to broadband forcing of velocity is generated from the CFD model described in the previous chapter. The response is obtained in terms of the unit impulse response h and the frequency response $F(\omega)$, valid for a range of frequencies. Transfer function of the CFD model of the wire heat source is compared with an analytical transfer function derived by Lighthill [83] and also with the heat source model based on King’s law [71]. Finally, a laminar premixed axisymmetric V- flame is identified. Linear transfer function of the flame derived

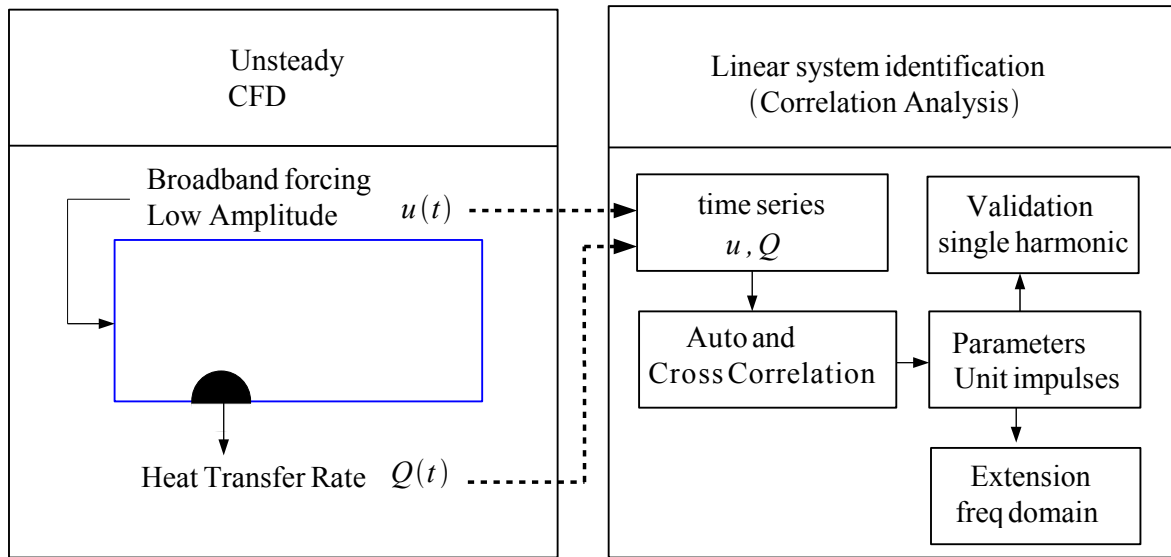


Figure 3.1: Schematic of the correlation based linear system identification with unsteady CFD

analytically is compared with the transfer function obtained from identification.

A schematic of the identification scheme for CFD model of the wire heat source is given in Fig. 3.1.

3.3 Identification of a Simple Model (“King’s law”) for the Heat Source

As described in the previous chapter, King’s law relates the heat transfer rate $Q(t)$ to the input $u(t - \tau)$ at an earlier time $t - \tau$, where τ is a characteristic time delay. A modified version of King’s law is used, that has been proposed by Heckl [59] for the study of nonlinear effects in a Rijke tube:

$$Q'(t) = k \left(\sqrt{\left| \frac{1}{3} + u'_f(t - \tau) \right|} - \sqrt{\frac{1}{3}} \right), \quad (3.11)$$

with

$$k \equiv \frac{2L_w(T_w - T_0)}{S\sqrt{3}} \sqrt{\pi \lambda c_v \bar{\rho} \frac{d_w}{2} \bar{u}}. \quad (3.12)$$

An estimation for the delay time τ is given by Lighthill [83] for frequencies $f \ll 20\bar{u}/d_w$ as,

$$\tau = 0.2 \frac{d_w}{\bar{u}}. \quad (3.13)$$

In the case with a wire diameter $d_w = 10^{-3}$ m and a mean flow velocity $\bar{u} = 0.2772$ m/s, the delay term is $\tau = 7.215 \times 10^{-4}$ s. In the non-dimensional form (see Galerkin time domain model in the system modeling chapter for the reference values of the non-dimensionalization), this corresponds to $\tau c_0/L_d = 0.261$. Here, c_0 and L_d denote the speed of the sound and duct length, respectively.

In the identification, low amplitude forcing is used for the fluctuating part of the velocity. The linearized form of Eq. (3.11) is as follows,

$$Q'(t) = \frac{k\sqrt{3}}{2} u'_f(t - \tau). \quad (3.14)$$

This simple linear form is identified using the procedure outlined above. As the input, a broadband forcing of amplitude 15% of the mean value ($A = 0.15$) is used with a non-dimensional time step $\Delta t = 0.0181$. The length of the input signal is 10000 time steps, and with these conditions the maximum resolved non-dimensional frequency is $f_{\text{Nyquist}} = 22$, with a non-dimensional frequency spacing of $\Delta f = 0.0055$ [107, 144].

The coefficients of the unit impulse response are shown in Fig. 3.2, and as expected only one non-zero element appears at the 15th position, which corresponds to the approximate time lag of $\tau_{\text{approx}} = 0.253$. The time lag of the model $\tau = 0.261$ is not an integer multiple of the time step Δt , but the time lag is obtained with less than 3% error. Decreasing the time step will increase the accuracy in the estimation of the time lag. Once the unit impulses are found, they are used to check the response against single sinusoidal excitations from the analytical model. A schematic of the validation approach is given in Fig. 3.3.

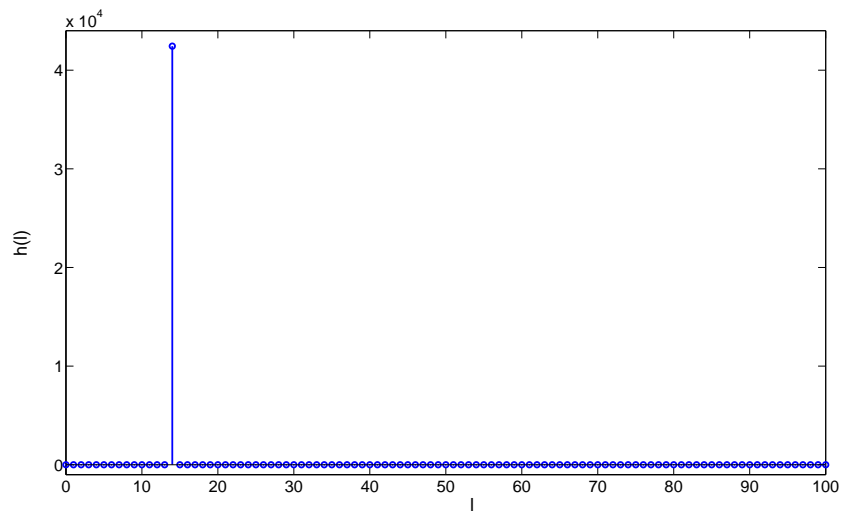


Figure 3.2: Coefficients $h(l), l = 0, 1, \dots, 100$ of the unit impulse response identified from King's law (Only one non-zero element at position $l = 15$.)

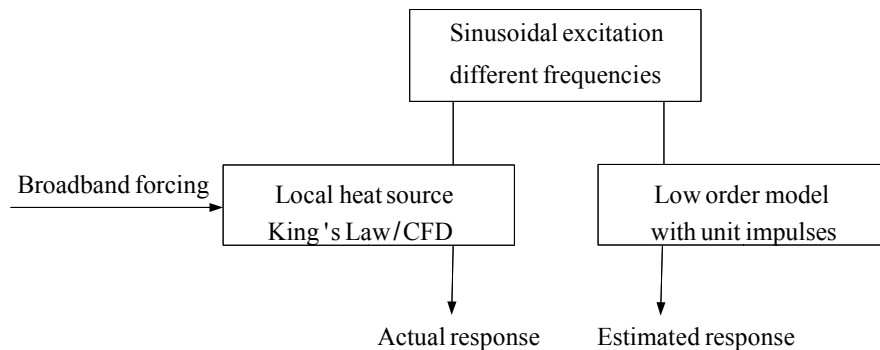


Figure 3.3: Schematic of the validation for sinusoidal excitation at different frequencies

3.4 Identification of the CFD Model Heat Source

A broadband excitation signal is imposed on the steady state velocity at the inlet position for unsteady calculations. The form of the excitation signal is:

$$u(t) = \bar{u} + 0.15\bar{u}(2 \times \text{rand}(M, 1) - 1), \quad (3.15)$$

where rand function generates the pseudo-random numbers between 0-1 with uniform distribution [86]. The amplitude of the perturbation is 15% of the mean value ($A = 0.15$). Time series data (input-output) generated from CFD model is used for the identification. CFD calculation is performed with $M = 20000$ time steps and a step size of $\Delta t = 5 \times 10^{-5}$ s.

Half of the data is used for identification and the other half is used for validation. The maximum resolved frequency is 4000 Hz at a frequency spacing of 1 Hz (if all the data set is used for the identification) [144]. The number of unit impulses is chosen as $L = 200$. Further increment of this number does not improve the accuracy of identification.

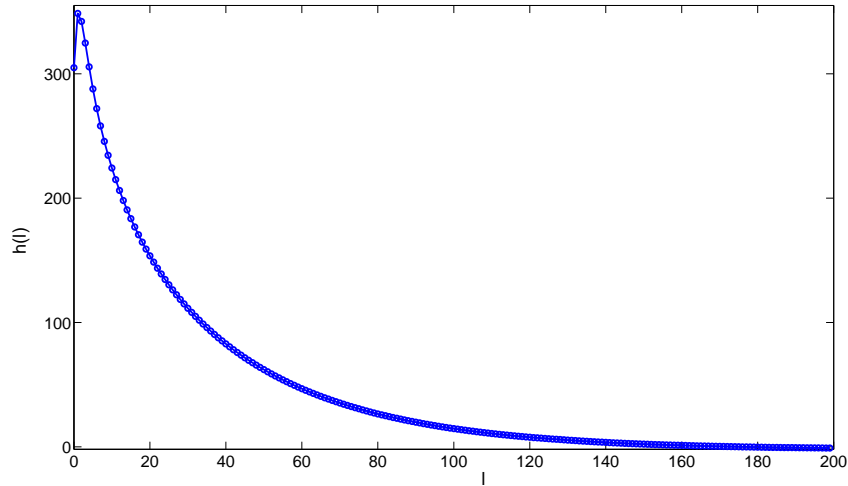


Figure 3.4: Coefficients $h(l)$, $l = 0, 1, \dots, 200$ of the unit impulse response identified from the CFD simulation (For $l > 200$, there is no significant contribution to the response.)

A measure of the quality of identification is the match between the output Q_{pred} predicted by the dynamic model and the actual output Q_{CFD} computed with CFD:

$$\text{Fit} = \left[1 - \sqrt{\frac{\sum_{k=1}^N (Q(k)_{\text{CFD}} - Q(k)_{\text{pred}})^2}{\sum_{k=1}^N Q(k)_{\text{CFD}}^2}} \right] \times 100. \quad (3.16)$$

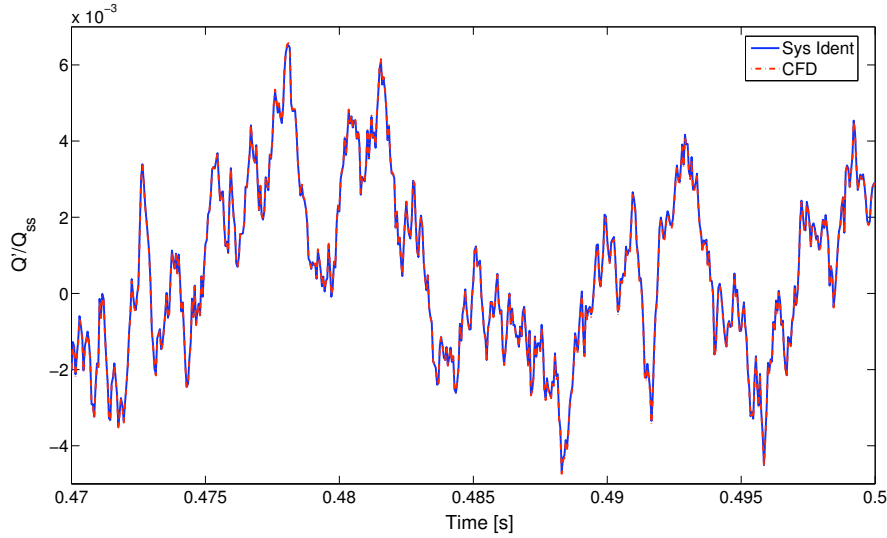


Figure 3.5: Normalized (with respect to steady state values) heat transfer rates obtained from CFD and linear system identification using second half of the data set

The validated model fit for the second half part of the data is 98.7.

Transfer function of the CFD model of the wire heat source is calculated by z-transform of the unit impulses which are obtained after a broadband forcing as,

$$F(\omega) = \sum_{l=1}^L h_l e^{-i\omega l \Delta t}. \quad (3.17)$$

Transfer functions obtained from Lighthill’s analytical approximation, from heat source model based on King’s law and from CFD model heat source are shown in Fig. 3.6. The low frequency limits of the transfer functions, $F(\omega)_{\omega \rightarrow 0}$, are used for the normalization factor. As can be seen in the plot, King’s law approximates Lighthill’s result only at low frequencies. At higher frequency, the gain of the transfer function decreases, while the phase deviates from the linear decay and eventually asymptotes a constant value. However, the phase approaches -90 deg in Lighthill’s transfer function and -70 deg for the identified CFD heat source model transfer function [50, 83, 122].

For further validation, sinusoidal excitation responses (non-dimensionalised

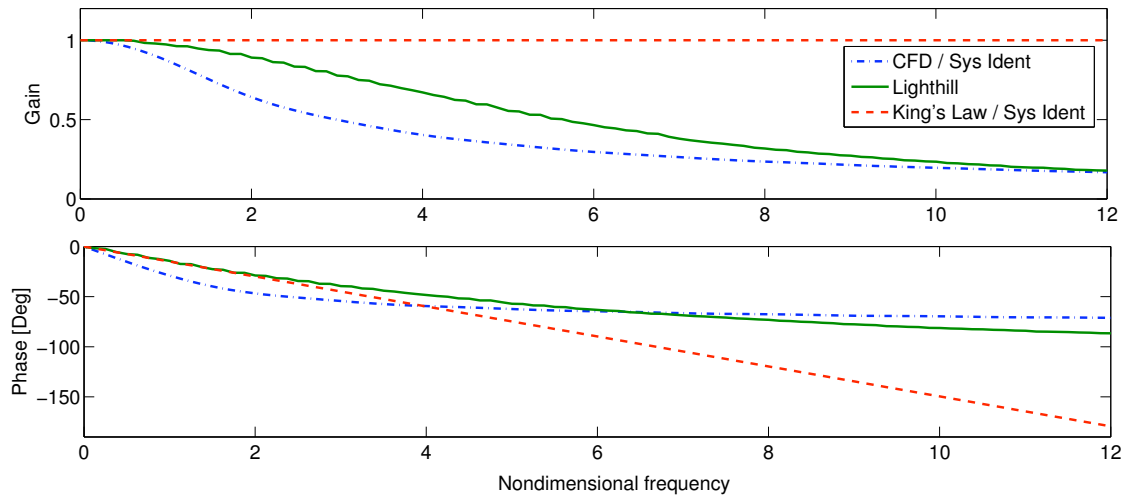


Figure 3.6: Gain and phase of the transfer function obtained from inverse z-transform of the unit impulses for the identified King’s law and CFD model along with the Lighthill’s analytical approximation of the transfer function

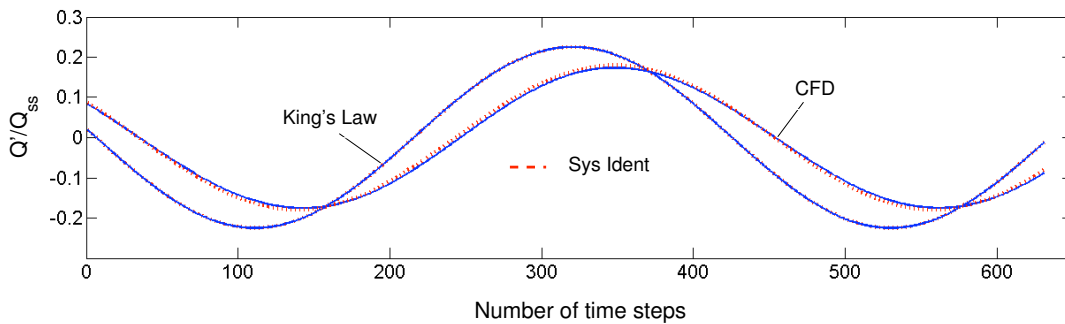


Figure 3.7: Non-dimensionalised (with respect to steady state values) heat transfer fluctuations for King’s law and CFD along with the results from linear system identification (dashed lines), for sinusoidal excitation at non-dimensional frequency of 1.658

with respect to the steady state values) from the identified model and the CFD model are compared for non-dimensional excitation frequency of 1.658 and amplitude of 10% of the steady state value ($A = 0.1$) as shown in Fig. 3.7. In the plot, the response of the identified King’s law is also added at the same non-dimensional frequency. The fit of the models from identification is 98 for CFD

model of the wire heat source and 99 for the heat source based on King's law.

3.5 Identification of a Laminar Premixed Flame Model

A chirp signal with linearly varying frequency component over time is used as the input signal for the identification. The form of the signal is,

$$u(t) = \bar{u} + 0.01 \bar{u} \sin \left(\left(\omega_{\max} - \left(\frac{\omega_{\max} - \omega_{\min}}{M} k \right) \right) k \Delta t \right), \quad k = 1, 2, \dots, M, \quad (3.18)$$

with maximum and minimum frequencies of $\omega_{\min} = 150$ and $\omega_{\max} = 1000$ in rad/s, and amplitude $0.01 \bar{u}$, (1% of the mean value, $A = 0.1$). The values $M = 15000$ and $\Delta t = 1.2566 \times 10^{-4}$ s denote the number of total samples used and time step, respectively. A frequency domain representation of the input signal and the heat release response from the flame is shown in Fig. 3.8

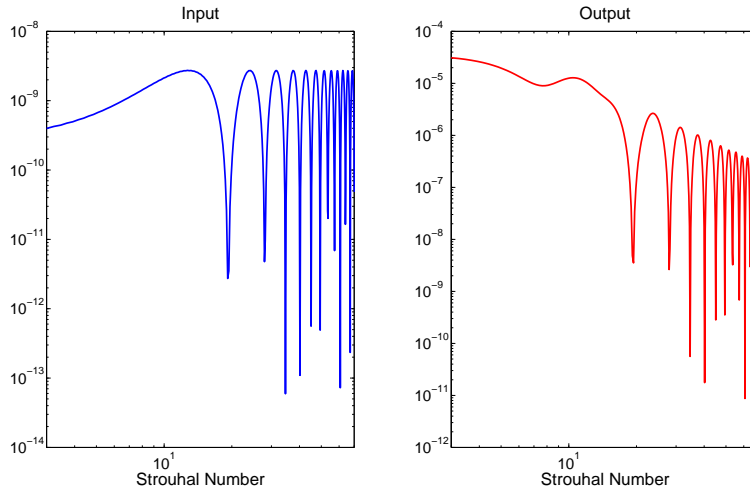


Figure 3.8: Input and output (heat release fluctuation response) in frequency domain

An estimate of the time lag for the flame is given as [48, 129],

$$\tau_f = \frac{b}{S_L \cos(\alpha)}. \quad (3.19)$$

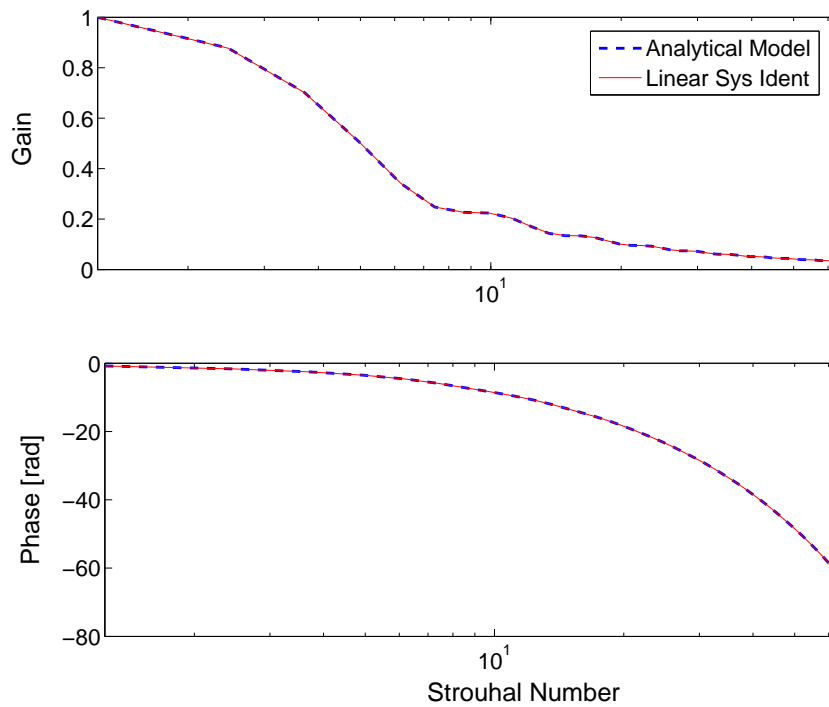


Figure 3.9: Transfer function calculated analytically and obtained from linear system identification

For flame radius $b = 0.0075$ m, laminar flame speed $S_L = 0.1231$ m/s and the inclination angle of $\alpha = 10$ deg, the time lag becomes $\tau_f = 0.061$ s.

For a Finite Impulse Response model structure, with the given time step Δt , the filter length (memory) or the number of regressors that should be retained in the model structure is at least

$$N_u = \frac{\tau_f}{\Delta t} = 492. \quad (3.20)$$

In the identification, a filter length of $L = 600$ is chosen. The transfer function or the frequency response of the laminar flame (heat release response to acoustic perturbations) is calculated by z -transform of the unit impulses.

A comparison of the transfer functions derived analytically [40] and calculated from identification is shown in Fig. 3.9.

3.6 Discussions and Conclusions

System identification methods are used as a tool to construct linear dynamic models using time series (input-output data set) generated from an unsteady CFD computation or experimental test rig. Fast Fourier Transformation is used to produce the frequency response of complicated elements with excitation at discrete forcing frequencies. On the other hand, linear system identification delivers the frequency response in a fast and efficient manner using one simulation and appropriate choice of the excitation signal.

Comparison of the transfer functions of three different heat sources; heat source model based on King's law, Lighthill's analytical derivation and the CFD model of the wire heat source, give different results. The phase approaches -90 deg in Lighthill's transfer function and -70 deg for the identified CFD heat source model transfer function. In Lighthill's derivation, there is no explicit dependence on the Re number [83]. The Re number should be greater than 10 to fulfill the boundary layer assumption. The results are derived in both the low- and high-frequency regimes. The results for the intermediate frequencies are obtained with interpolation. Heat source model based on King's law has one time lag and approximates Lighthill's result only at low frequencies. On the other hand, transfer function calculation using unsteady CFD computation and system identification is more effective. Firstly, there is no restriction on the time delay as in heat source model based on King's law. Secondly, it is possible to determine the effect of the Re number on the heat transfer behavior. The transfer function is obtained at $Re = 13$. Even though the heat source in CFD is modeled as a cylinder that is kept at constant temperature and the flow with temperate independent material properties, it is possible to include a constant heat input to the cylinder as the boundary condition [50] and temperature dependent material properties of the flow as well.

The results for the laminar premixed flame show that the approximate time lag is captured with system identification as the memory length of the filter. Moreover, the results from the analytically derived transfer function matches very well with those obtained from linear system identification.

4 Nonlinear System Identification

Nonlinear system identification can be used to obtain nonlinear dynamic models using the the input-output data set of a nonlinear system/process [18, 93, 126]. To correlate the heat transfer response of the wire to pulsating flow velocity (amplitude and frequency), unsteady boundary layer equations are utilized. In this case, due to the complex interactions between the hydrodynamic and thermal boundary layer with the nonlinear contribution and streaming parts, it is not possible to derive an analytical closed form solution for the input-output relation. Some parts of the problem (simplified unsteady boundary layer equations) have to be solved numerically [133]. Fast Fourier Transformation (FFT) is utilized to obtain the nonlinear transfer function (“describing function”). In this case, CFD model of the heat source is excited with single sinusoids for different amplitudes-frequencies, and the heat transfer at the wire is then calculated at the forcing frequency. This approach has some drawbacks. Firstly, in order to cover the relevant range of dynamics, it may require many expensive CFD calculations. Secondly, nonlinear transfer function can only be used in a sinusoidal describing function model of the full thermo-acoustics, in which the effect of the higher order modes is neglected (refer to “Prediction and Analysis of Thermo-Acoustic Limit Cycles” chapter for a detailed explanation). As an alternative, nonlinear system identification methods promise to provide an effective and fast way of obtaining the input-output relation from the observation of the input-output data set. A nonlinear dynamic model of the heat source is obtained that works in the desired range of frequencies and amplitudes. This modeling approach is used for more advanced configurations of the heat source (even for a flame of technical interest).

Another important aspect is a proper system model of the thermo-acoustics along with the nonlinear dynamic model of the heat source. If the full thermo-

acoustic system is simulated in time domain, then a nonlinear model of the heat source in time domain is required. In this case, neural network or fuzzy based identification methods is utilized, which are the universal functional approximators. If a frequency domain simulation of the thermo-acoustic system (sinusoidal describing function is the only method available until now) is required with the nonlinear heat source, then the computation of the amplitude and frequency dependent nonlinear transfer function of the heat source is necessary. A system model is developed in the frequency domain that goes beyond the “sinusoidal describing function”. In this approach, input-output relation is expressed in polynomial form with memory. Extension of this polynomial model into frequency domain gives the higher order transfer functions. Heat source nonlinearity is expressed in terms of higher order transfer functions. This then makes it possible to include the coupling of the modes for a thermo-acoustic system simulated in the frequency domain. One drawback of the method is the resulting large number of parameters when the delay time is large and the polynomial order of the approximation is high, which are the challenges both for the identification and post-processing of the said parameters.

In this chapter, the calculation of the amplitude dependent nonlinear transfer function for the CFD model of the wire heat source from FFT is considered.

Next, nonlinear system identification problem and the procedures are discussed.

The equations for a second order polynomial identification using an equation error type model structure are then derived. The identification method is extended into the frequency domain using two different approaches, namely, a harmonic balance approach and a harmonic probing approach. Computational Fluid Dynamics (CFD) model of the wire heat source is identified and nonlinear transfer functions are calculated.

A nonlinear identification method based on neural networks and its extension into the frequency domain are presented. Higher order transfer functions developed from this approach for the CFD model of the wire heat source is used in the coupled modes frequency domain system model (refer to the chapter

“Prediction and Analysis of Thermo-Acoustic Limit Cycles”). The weakly nonlinear laminar premixed flame is also identified, and the difficulties encountered in the nonlinear identification for this model heat source are discussed.

Finally, the CFD model of the wire heat source is identified using a fuzzy based identification procedure.

4.1 Nonlinear Transfer Function from Fast Fourier Transformation (FFT)

To capture the nonlinearity in the heat transfer, FFT of the responses to harmonic excitations are computed and amplitude dependent nonlinear behavior is obtained [1, 20, 32]. The computations are performed for discrete amplitudes and frequencies, and the values in between are obtained with interpolation.

$$F(\omega)_{A_0, \omega_0} = \frac{\text{FFT}(Q'/Q_s)}{\text{FFT}(u'/u_s)} \Big|_{A_0, \omega_0}, \quad (4.1)$$

gives the nonlinear transfer function at the forcing frequency ω_0 and amplitude A_0 . This heat source, which is nonlinear through its explicit amplitude dependence, is then used in a frequency domain thermo-acoustic system model, i.e. in a sinusoidal describing function method.

The responses (heat transfer rates) of the cylinder to harmonic forcing at the inlet for a range of Str (0.361, 1.08, 1.80, 3.61) and for a range of A (0.3, 0.75, 1, 1.5 and 2) are obtained. Fast Fourier Transformations of the response and the excitation signals are then performed. At the forcing frequency, the amplitude and the phase relation between the unsteady heat transfer rate and the unsteady velocity is calculated. In Fig. 4.1, it is seen that the peaks at the multiple integer of the fundamental harmonic forcing increase with high fluctuation amplitudes. For $A = 2$, the second harmonic reaches nearly 80% of the fundamental harmonic at the lowest frequency.

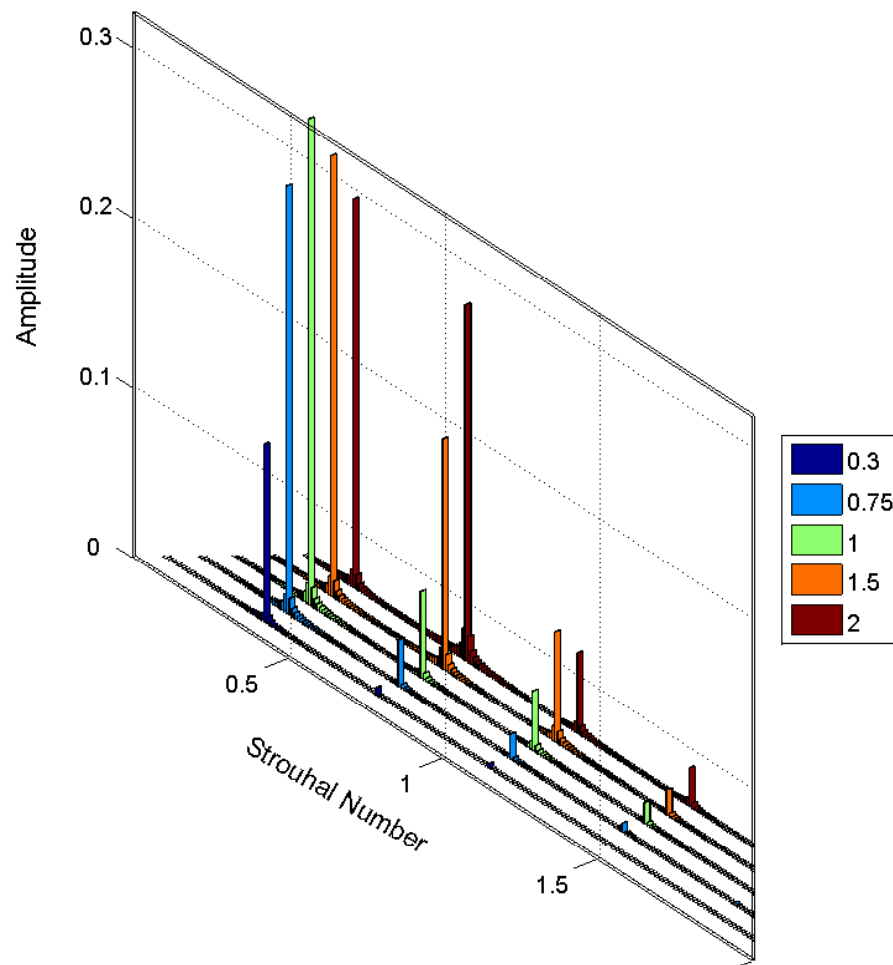


Figure 4.1: FFTs of the heat transfer rates for different velocity amplitude ratios and at $\text{Str} = 0.361$

In Fig. 4.2, the comparison of the transfer function for different velocity amplitude ratios is shown along with a linear transfer function computed by Föllner et al. [8]. At $A = 0.3$, the behavior is linear. The deviation from the linear transfer function is more pronounced at low Strouhal numbers and high velocity amplitude ratios. At higher frequencies, the response approaches linear transfer behavior, a decrease in the gain and an asymptotic value of -70 deg in the phase. Gain is more sensitive than the phase, and the amplitude dependence of the phase can be neglected up to $A = 1.5$. Another observation is the non-monotonic behavior for $A = 2$ in the gain, where a decrease in the gain is followed by an increase and then a decrease. Many CFD computations are re-

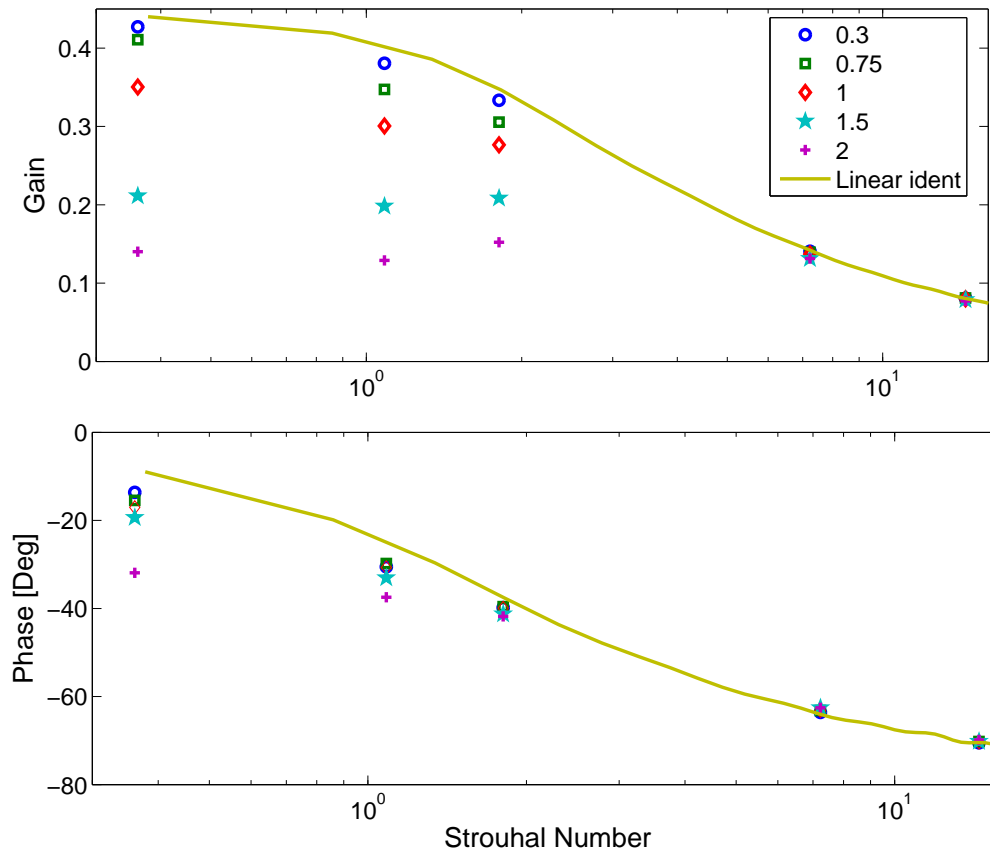


Figure 4.2: Gain and phase of the transfer function for forcing with single sinusoids at different velocity amplitude ratios and Strouhal numbers along with a linear transfer function obtained from linear identification on a semi-logarithmic plot

quired to cover the relevant range of dynamics. Some nonlinear dynamic behavior (non-monotonic behavior) cannot be captured, unless the interesting range of frequencies and amplitudes are not considered. Another disadvantage of the method is that the response is obtained at the forcing frequency only. But in the nonlinear modeling of system behavior it is also important to consider the higher harmonics. Drawbacks of the FFT approach can be circumvented with nonlinear system identification methods which will be discussed in the following sections. These discrete points (at specific A and Str) then serve as a reference to check the validity of our nonlinear identification

methods.

4.2 Nonlinear Identification Problem

Input-output modeling of the nonlinear systems are generally categorized as nonparametric -functional series expansion (Volterra, Wiener series expansion)- and parametric (differential/difference equation models, neural network models, polynomial models) [18, 97]. Volterra series is the extension of the impulse response of the linear system to the nonlinear case [19, 119]. These are the Taylor series expansion applied to functionals. Orthogonalization of the Volterra series has been proposed to express the input-output modeling of the nonlinear system with less number of parameters and to obtain the parameters of the nonlinearity using broadband type excitation signals [72, 77]. In Hammerstein and Wiener identification methods, a linear dynamic block is connected to a static nonlinear input and/or output block structure [18, 73]. Neural network is a black-box identification method which uses expansion functions through the units (layers) to model the nonlinear input-output relation [92, 98, 105, 126]. There also exist local linear models which use fuzzy based algorithms that could be utilized as nonlinear identification tools [5, 6, 130].

The procedures and requirements used in the nonlinear system identification are comparable to those of the linear system identification. The input signal covers the relevant range of frequencies, as well as amplitudes. In the identification, it is common to add past outputs in the regressor set in order to achieve better convergence rates and to use small number of regressors. The actual outputs, or computed outputs, is then used in the set of regressors. In the former case, analytical closed form solution to derive the parameters is obtained for some choice of the function like polynomials. It is then easily extended into the frequency domain. In the latter case, the computed outputs from the model (output from the identified model, Q_m) are used in the set of regressors as the past outputs. Even though it seems attractive and is the method of choice in the time domain thermo-acoustic system model (e.g. Galerkin time domain simulation), obtaining a model with this identification may have

stability and nonlinear optimization problems (optimum initial guess, trapping into local minimum). A schematic representation of the equation error and output error type model structures is shown in Fig. 4.3. In the figure, z represents the shift operator which simply shifts the one step ahead value of the input or output to the current time (refer to “Linear System Identification” chapter).

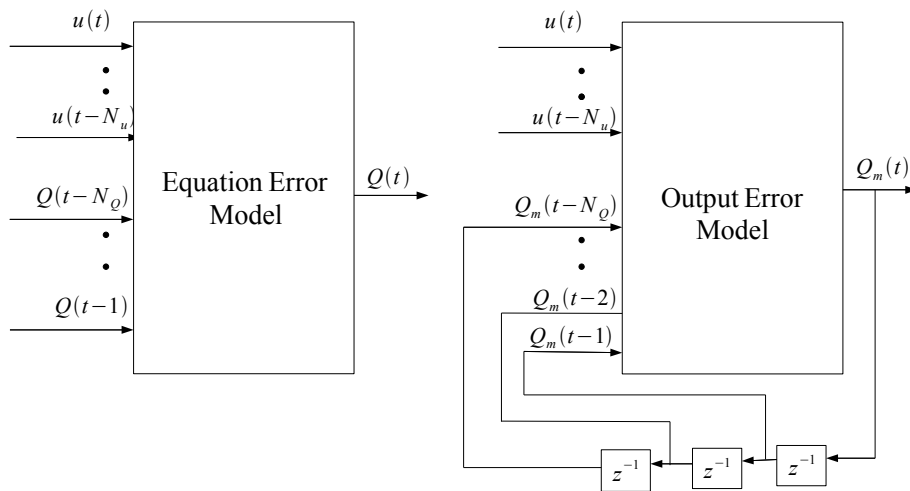


Figure 4.3: Schematic of the equation error and output error model structures

The nonlinear dynamic fit is generally expressed as,

$$Q(t) = F(Q(t-1), \dots, Q(t-N_Q), u(t), \dots, u(t-N_u)). \quad (4.2)$$

The function F is linear with respect to its arguments (regressors, $Q(t-i)$, $u(t-j)$) for a linear system. In linear identification, it is not so difficult to obtain a dynamic model using one of the existing model structures and appropriate choice of the excitation signal. For a nonlinear system, the form of the function F is not known a priori. This function is approximated using expansion functions and polynomials. One can encounter the problem of the “curse of dimensionality” (a significant amount of increase in the parameters by adding extra dimensions corresponding to the degree of nonlinearity and the number of regressors) depending on the maximum time lag of the system, relevant maximum and minimum frequencies and the degree of the nonlin-

earity. Nonlinear extensions of the linear model structures are named as NFIR, NARX and NARMAX, and NOE [26].

4.3 Polynomial Identification

4.3.1 Derivation

The first identification method discussed is the second order polynomial identification which is of type NARX. It utilizes only past inputs and outputs (actual output) consisting of nonlinear terms up to second order in the regressor set; the bilinear products of uu and uQ ,

$$Q(t) = Q_{\text{approx}}(t) + v(t). \quad (4.3)$$

The output is approximated by Q_{approx} which is a second order polynomial,

$$\begin{aligned} Q_{\text{approx}}(t) &= \sum_{k=1}^{N_u} h_u(k)u(t-k+1) + \sum_{l=1}^{N_Q} h_Q(l)Q_{\text{CFD}}(t-l) \\ &+ \sum_{k=1}^{N_u} \sum_{l=1}^{N_Q} h_{uQ}(k,l)u(t-k+1)Q_{\text{CFD}}(t-l) \\ &+ \sum_{k=1}^{N_u} \sum_{m=1}^{N_u} h_{uu}(k,m)u(t-k+1)u(t-m+1). \end{aligned} \quad (4.4)$$

Here, Q_{CFD} and Q represent the actual output obtained from CFD computation and model output, respectively. The matrix of inputs U , vector of unknown parameters P and regressor set Z are defined as,

$$U = [u(t-k+1), Q_{\text{CFD}}(t-l), u(t-k+1)u(t-m+1), u(t-k+1)Q_{\text{CFD}}(t-l)], \quad (4.5)$$

$$P = [h_u(k), h_Q(l), h_{uu}(k,m), h_{uQ}(k,l)], \quad (4.6)$$

$$Z^M = [u(t-k+1), Q_{\text{CFD}}(t-l)], \quad (4.7)$$

$$k, m = 1, \dots, N_u, \quad l = 1, \dots, N_Q.$$

The difference (error) between the approximated and actual outputs is minimized in a least square sense;

$$V(Z^M; P) = \frac{1}{M} \sum_{i=1}^M (Q_{\text{CFD}} - PU)^2, \quad (4.8)$$

where i is a time index. The vector of the unknown parameters is derived from,

$$\frac{\partial V}{\partial P} = 0, \quad \text{as} \quad (4.9)$$

$$P = \frac{1}{M} \sum_{i=1}^M (Q_{\text{CFD}} U^T) \frac{1}{M} \sum_{i=1}^M (U U^T)^{-1}. \quad (4.10)$$

Since the actual outputs are used in the regressor set (label “CFD” is attached), an analytical closed form solution for the unknown parameters P is obtained. This simply represents the product of the cross correlation between the input matrix U and output vector Q , and the inverse of autocorrelation of the input matrix U .

4.3.2 Identification of the Heat Transfer of Wire in Pulsating Flow from Unsteady CFD

The CFD model for the heat transfer of the wire in pulsating flow that has been described in the previous chapters is excited with a broadband forcing at the inlet position. In order to excite the nonlinearity in the heat transfer rate of the wire, $A = 2$ is chosen as the perturbation amplitude. The unsteady CFD is calculated for $M = 10000$ time steps with a time step of $\Delta t = 10^{-4}$ s. Half of the data is used for estimation and the other half is used for validation. Validation is also performed against single frequencies and different amplitudes.

The information about the time lag is got from system identification methods. For accurate identification in the linear regime, maximum filter length is chosen to exceed all time delays of the system [109]. The estimation of the order of the time lag in the linear regime, which has been given by Lighthill [83] is rewritten as,

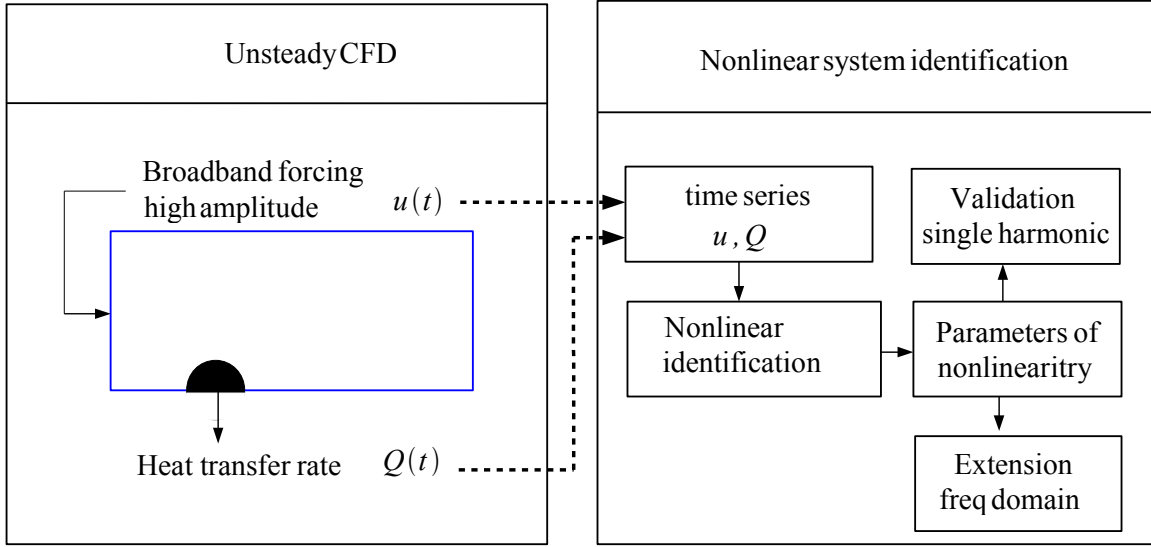


Figure 4.4: Schematic of the nonlinear identification from input-output data set of unsteady CFD computation in order to obtain a dynamic model of a heat source

$$\tau = 0.2 \frac{d_w}{\bar{u}}, \quad f \ll 20 \frac{\bar{u}}{d_w}. \quad (4.11)$$

In our case, this corresponds to a time lag of $\tau = 7.2 \times 10^{-4}$ s for frequencies $f \ll 5544$ Hz (with the characteristic length -wire diameter $d_w = 10^{-3}$ m, and mean velocity $\bar{u} = 0.2772$ m/s). This time lag for the linear system is used as an initial option while choosing the filter lengths (number of past inputs and outputs in the regressor set) for nonlinear system identification.

The parameters that are chosen in the second order polynomial identification are N_u and N_Q , which correspond to the maximum time lag in the input and output data, respectively. Also the time lag between the input and the output is selected to be different from zero. If only inputs (NFIR model structure) are used in the identification, then at least 10 is used as the memory filter, according to the time lag of the linear system and the time step of the unsteady CFD computations. On the other hand on using past outputs in the model structure, the memory length becomes less. The parameters are chosen as $N_u = 4$, $N_Q = 3$.

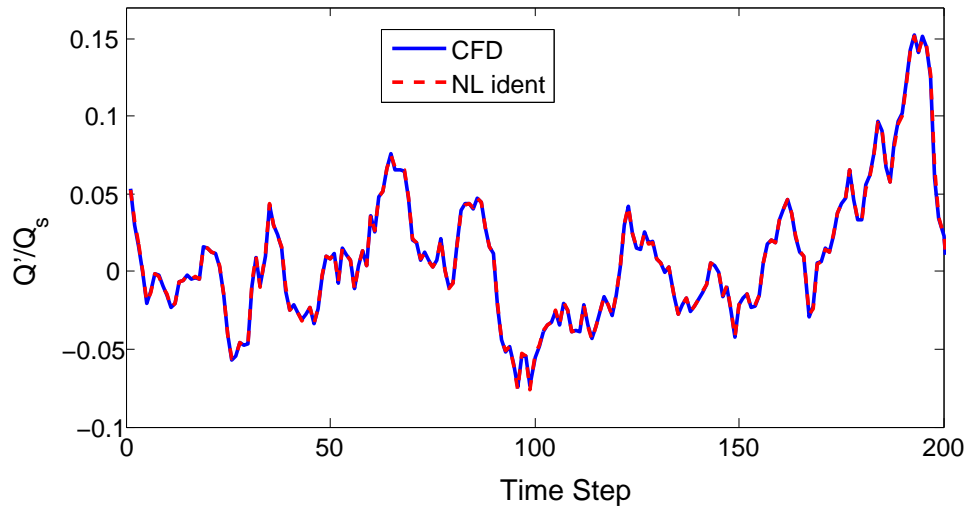


Figure 4.5: The degree of the fit between the CFD data (validation data set) and nonlinear system identification, $N_u = 4$, $N_Q = 3$

The degree of the fit which has been defined earlier in the “Linear System Identification” chapter for the validation data is 98.15.

Validation for Single Harmonics

The parameters obtained from the polynomial identification with broadband forcing describe the CFD model of the wire heat source for a range of amplitudes and frequencies. To check this, validation is performed for a single harmonic at different amplitudes. A schematic representation of the validation for a single harmonic is shown in Fig. 4.6. The actual output which is labeled with CFD is used in the regressor set.

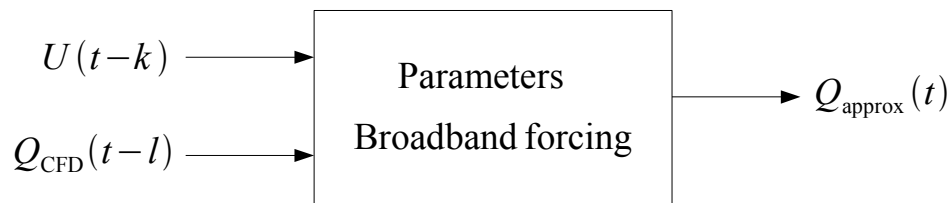


Figure 4.6: Schematic of the validation procedure for single harmonic forcing

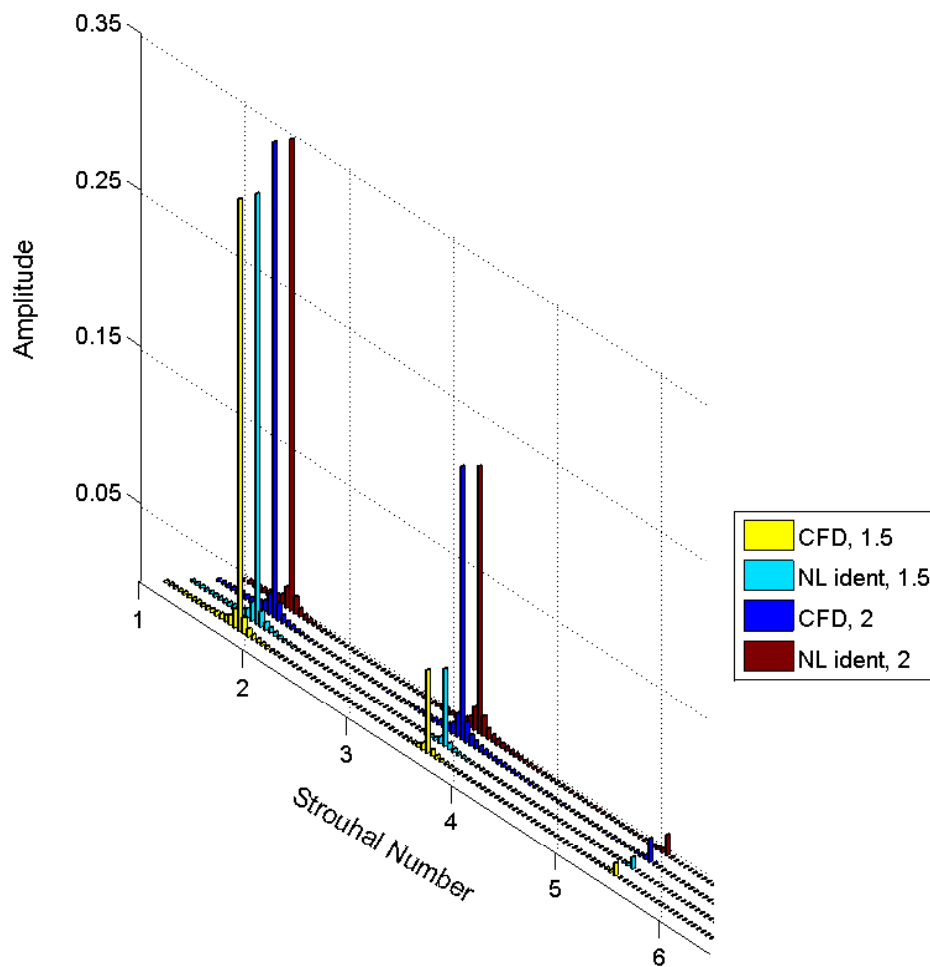


Figure 4.7: FFT with CFD and nonlinear identification for $A = 1.5$ and $A = 2$ at $\text{Str} = 0.361$

Fast Fourier Transformations of the heat transfer rates from the CFD and from the identified model are shown for $\text{Str} = 0.361$ in Fig. 4.7 on a single plot for $A = 1.5$ and $A = 2$. The percentage of the error in the amplitude of fundamental peak never exceeds 1%, but for second harmonic it is in the level of up to 5% for $\text{Str} = 0.361$ and $\text{Str} = 1.807$. At $\text{Str} = 7.229$, it exceeds 10%. This is caused by the time step that is used in CFD. In the single harmonic forcing corresponding to $\text{Str} = 7.229$, $1/50$ of the period is used as time step, which is less than the time step for the identification with broadband forcing. The results are interpolated from a fine time interval grid to a coarse one. This explains there is a slight difference at high Str where nonlinearity is less. Distortions from the

ellipses in the phase portraits are interpreted as indication of the nonlinearity in the heat transfer rate. As seen in Fig. 4.8, there is a slight difference at $A = 2$ for $\text{Str} = 0.361$ in the phase portraits.

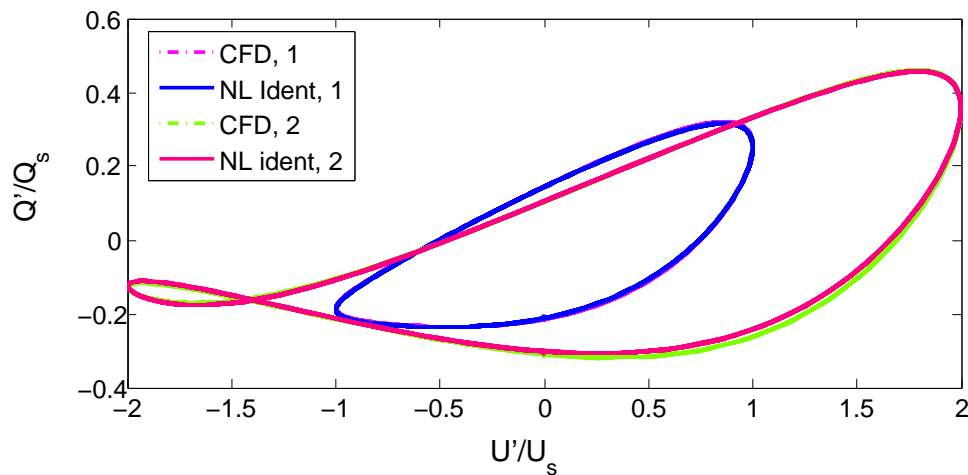


Figure 4.8: Phase portraits with CFD and with nonlinear identification at $\text{Str} = 0.361$, $A = 1$ and $A = 2$

Although the accuracy with this identification method (equation error type) is high, the set of regressors require past outputs from CFD model of the wire heat source. This nonlinear heat source model cannot be coupled with acoustics in a time domain simulation of a thermo-acoustic system. In this case, the only method of choice is to use the identification procedures which require only input (NFIR model structure) or the model outputs from the identified heat source (NOE). Nevertheless, the advantage of accuracy and ease of the equation error type identification scheme is used in extending it into frequency domain with two different approaches, namely, a harmonic balance method and a harmonic probing method which is considered next.

4.3.3 Nonlinear Transfer Function

4.3.3.1 Harmonic Balance

Let us assume we have a sinusoidal input,

$$u(t) = \frac{U_0}{2i} (e^{i\omega t} - e^{-i\omega t}), \quad (4.12)$$

and as the output we consider harmonics up to second order;

$$Q(t) = Q_0 + \frac{Q_1}{2} e^{i\omega t} + \frac{Q_{-1}}{2} e^{-i\omega t} + \frac{Q_2}{2} e^{2i\omega t} + \frac{Q_{-2}}{2} e^{-2i\omega t}, \quad (4.13)$$

where Q_1 , Q_{-1} , and Q_2 , Q_{-2} are complex conjugate coefficients.

The input and output will be replaced in the second order polynomial structure (see Eq. (4.4)). Equating the exponentials with the same harmonic (exponentials with terms 0, $i\omega t$, $2i\omega t$) on both sides of the equation, a system of nonlinear equations for the unknown coefficients (Q_1 , Q_{-1} , Q_2 , Q_{-2}) is set. The resulting equations for the unknown coefficients are:

Zeroth harmonic: $e^{0i\omega t} (\dots) = 0$,

$$\begin{aligned} Q_0 - Q_0 \sum_{l=1}^{N_Q} h_Q(l) - \frac{U_0^2}{4} \sum_{k=1}^{N_u} \sum_{m=1}^{N_u} h_{uu}(k, m) (e^{-i\omega(k-m)\Delta t} + e^{-i\omega(m-k)\Delta t}) \\ - \sum_{k=1}^{N_u} \sum_{l=1}^{N_Q} h_{uQ}(k, l) \left(\frac{U_0 Q_{-1}}{4i} e^{-i\omega(k-1-l)\Delta t} - \frac{U_0 Q_1}{4i} e^{-i\omega(l-k+1)\Delta t} \right) = 0. \end{aligned} \quad (4.14)$$

First harmonic: $e^{i\omega t} (\dots) = 0$,

$$\begin{aligned} Q_1 - \frac{U_0}{2i} \sum_{k=1}^{N_u} h_u(k) e^{-i\omega(k-1)\Delta t} - \frac{Q_1}{2} \sum_{l=1}^{N_Q} h_Q(l) e^{-i\omega l \Delta t} \\ - \sum_{k=1}^{N_u} \sum_{l=1}^{N_Q} h_{uQ}(k, l) \left(\frac{U_0 Q_0}{2i} e^{-i\omega(k-1)\Delta t} - \frac{U_0 Q_2}{4i} e^{-i\omega(-k+1+2l)\Delta t} \right) = 0. \end{aligned} \quad (4.15)$$

Second harmonic: $e^{2i\omega t} (\dots) = 0$,

$$\begin{aligned} \frac{Q_2}{2} - \frac{Q_2}{2} \sum_{l=1}^{N_Q} h_Q(l) e^{-2i\omega l \Delta t} + \frac{U_0^2}{4} \sum_{k=1}^{N_u} \sum_{m=1}^{N_u} h_{uu}(k, m) e^{-i\omega(k+m-2)\Delta t} \\ - \frac{U_1 Q_1}{4i} \sum_{k=1}^{N_u} \sum_{l=1}^{N_Q} h_{uQ}(k, l) e^{-i\omega(k+l-1)\Delta t} = 0. \end{aligned} \quad (4.16)$$

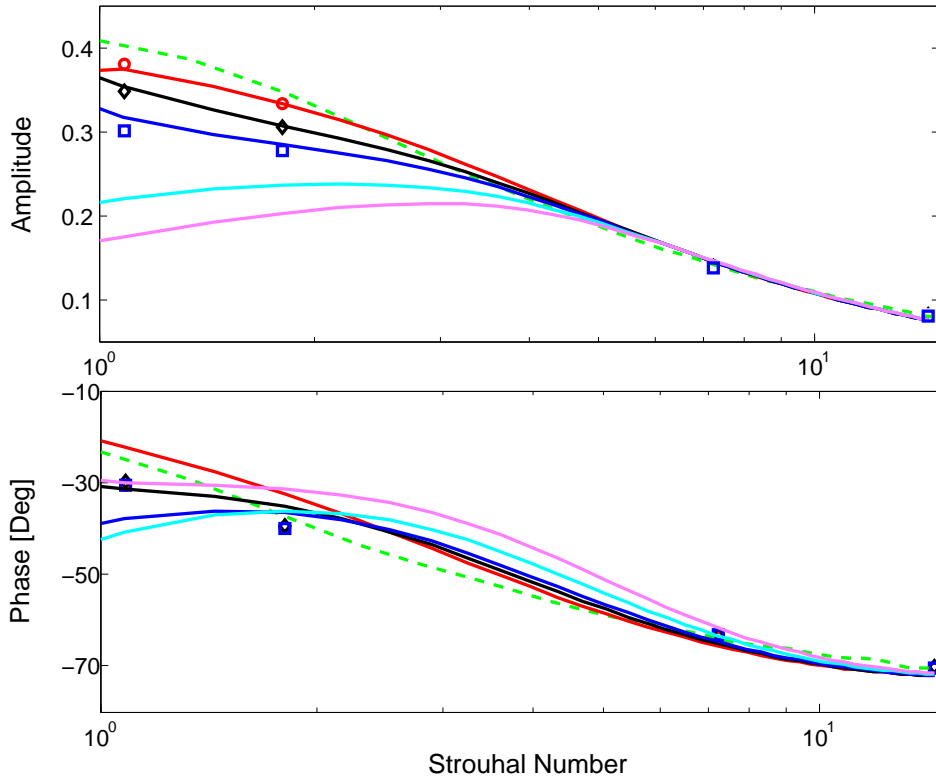


Figure 4.9: Gain and the phase of the transfer function obtained with single harmonic forcing, second order identification and linear identification on a semi-logarithmic plot. NL Ident (red - 0.30, black - 0.75, blue - 1, cyan - 1.5, pink - 2), green - Linear Identification, Single Harmonic Forcing (Markers, same color)

The system of equations is included for the complex conjugate parts. Although this step is not necessary, it is useful to check if the resulting coefficients indeed are complex conjugate. Inclusion of third and fourth harmonics has neg-

ligible influence on the solution, whereas addition of five or more harmonics results in numerical problems for the nonlinear system of equations. In Fig. 4.9, the results for the amplitude and phase of the transfer function at the forcing frequency are shown.

The comparison of the nonlinear transfer function from single harmonic forcing and harmonic balancing of the second order identification shows good agreement for the gain up to $A = 1$, where the nonlinear effect is already captured by a decrease in the gain of the transfer function. The agreement in the gain deteriorates at low Str for $A = 1.5$ and $A = 2$. The deviation for the phase is even stronger than that of the gain. But the phase has a negligible amplitude dependence nonlinearity up to $A = 1.5$, which has been shown earlier when deriving the nonlinear transfer function from FFT.

4.3.3.2 Harmonic Probing

A wide class of nonlinear systems is expressed as Volterra series representation [20, 79]. This is the extension of the impulse response of a linear system into the higher dimensions. The transfer function of a linear system is calculated by transforming the unit impulses into frequency domain (z-transform for a discrete case). The same analogy is used to define the higher order transfer functions of the nonlinear system by extension of the higher order impulses (Volterra kernels) into frequency domain. In the following sections, the higher order transfer functions are computed using second order polynomial identification derived earlier, and harmonic probing approach introduced by Bedrosian et al. [13].

The response of a nonlinear system is represented by Volterra series approximation as;

$$Q(t) = \underbrace{\int_{-\infty}^{\infty} h_1(\tau_1) u(t - \tau_1) d\tau_1}_{\text{Impulse response}} + \int_{-\infty}^{\infty} \dots \int_{-\infty}^{\infty} \underbrace{h_n(\tau_1, \dots, \tau_n)}_{n^{\text{th}} \text{ order kernel}} u(t - \tau_1) \dots u(t - \tau_n) d\tau_1 \dots d\tau_n + \dots \quad (4.17)$$

The extension of the higher order Volterra kernels in the frequency domain gives the higher order transfer functions [13]. The first order or linear transfer function is defined as,

$$H_1(\omega) = \int_{-\infty}^{\infty} h_1(\tau_1) e^{-i\omega\tau_1} d\tau_1, \quad (4.18)$$

and similar definitions apply for the other kernels. The n th order transfer function is defined as,

$$H_n(\underbrace{\omega_1, \dots, \omega_n}_{\omega_1 + \dots + \omega_n = \omega}) = \int_{-\infty}^{\infty} \dots \int_{-\infty}^{\infty} h_n(\tau_1, \dots, \tau_n) e^{-i\omega_1\tau_1 - \dots - i\omega_n\tau_n} d\tau_1 \dots d\tau_n. \quad (4.19)$$

The input spectra at a specific frequency could produce terms which can be multiple integer frequencies, and inter modulations which are specific to non-linear systems. The higher order transfer functions take these effects into account [76, 141]. The computation of higher order transfer functions is performed by harmonic probing method as by Bedrosian et al. [13]. A schematic representation of the approach to find the higher order transfer functions is shown in Fig. 4.10 .

To find the first order transfer function, the system is excited with single harmonic forcing,

$$u(t) = e^{i\omega t}, \quad (4.20)$$

and the corresponding response calculated from Volterra series representation is given as,

$$Q(t) = H_1(\omega) e^{i\omega t} + H_2(\omega, \omega) e^{2i\omega t} + H_3(\omega, \omega, \omega) e^{3i\omega t}. \quad (4.21)$$

The input (Eq. (4.20)) and output (Eq. (4.21)) are then used in the second order polynomial identification (Eq. (4.4)). Taking only the linear terms in the re-

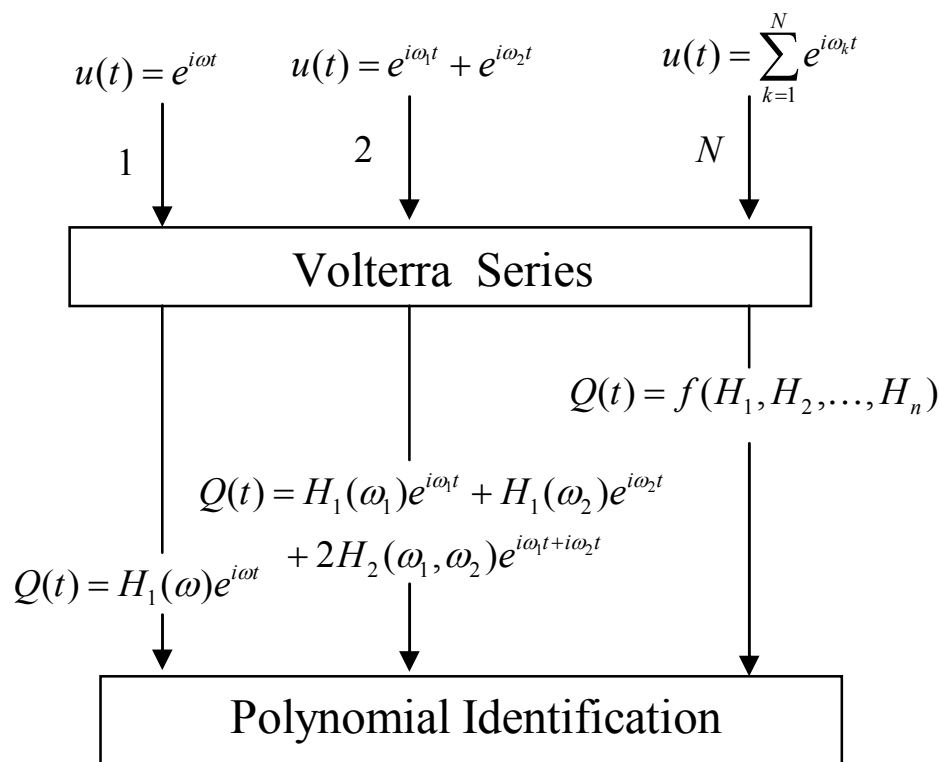


Figure 4.10: Schematic of the harmonic probing method to find the higher order transfer functions

sponse and equating the terms of the first order exponentials, the linear transfer function is obtained as,

$$H_1(\omega) = \frac{\sum_{k=1}^{N_u} h_u(k) e^{-i(k-1)\omega\Delta t}}{1 - \sum_{l=1}^{N_Q} h_Q(n) e^{-il\omega\Delta t}}. \quad (4.22)$$

The computation of the second order transfer function requires harmonic forcing at two different frequencies [13, 24],

$$u(t) = e^{i\omega_1 t} + e^{i\omega_2 t}. \quad (4.23)$$

The corresponding nonlinear response is obtained from Volterra series representation as,

$$Q(t) = H_1(\omega_1)e^{i\omega_1 t} + H_1(\omega_2)e^{i\omega_2 t} + 2H_2(\omega_1, \omega_2)e^{i\omega_1 t + i\omega_2 t}. \quad (4.24)$$

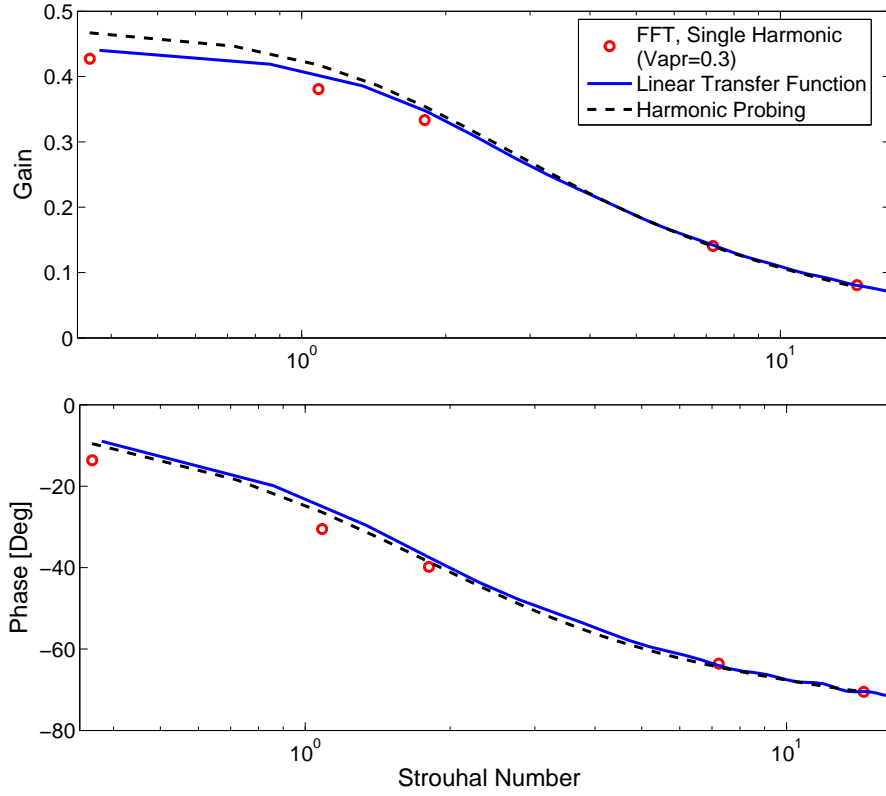


Figure 4.11: Gain and the phase of the first order transfer function calculated from single sinusoid forcing at $A = 0.3$, linear system identification and harmonic probing on a semi-logarithmic plot

Again, this response is used in the polynomial identification structure in Eq. (4.4), and the terms of exponentials which correspond to the sum of the frequencies are equated to find the second order transfer function as,

$$H_2(\omega_1, \omega_2) = \frac{\left(\begin{aligned} &\sum_{k=1}^{N_u} \sum_{m=1}^{N_u} h_{uu}(k, m)(e^{-i(k-1)\omega_1 \Delta t} + e^{-i(m-1)\omega_1 \Delta t}) \\ &+ \sum_{k=1}^{N_u} \sum_{l=1}^{N_Q} h_{uQ}(k, l) H_1(\omega_1) e^{-i(k-1)\omega_2 \Delta t - i l \omega_1 \Delta t} \\ &+ \sum_{k=1}^{N_u} \sum_{l=1}^{N_Q} h_{uQ}(k, l) H_1(\omega_2) e^{-i(k-1)\omega_1 \Delta t - i l \omega_2 \Delta t} \end{aligned} \right)}{2 - 2 \sum_{l=1}^{N_Q} h_Q(l) e^{-i l \omega \Delta t}}. \quad (4.25)$$

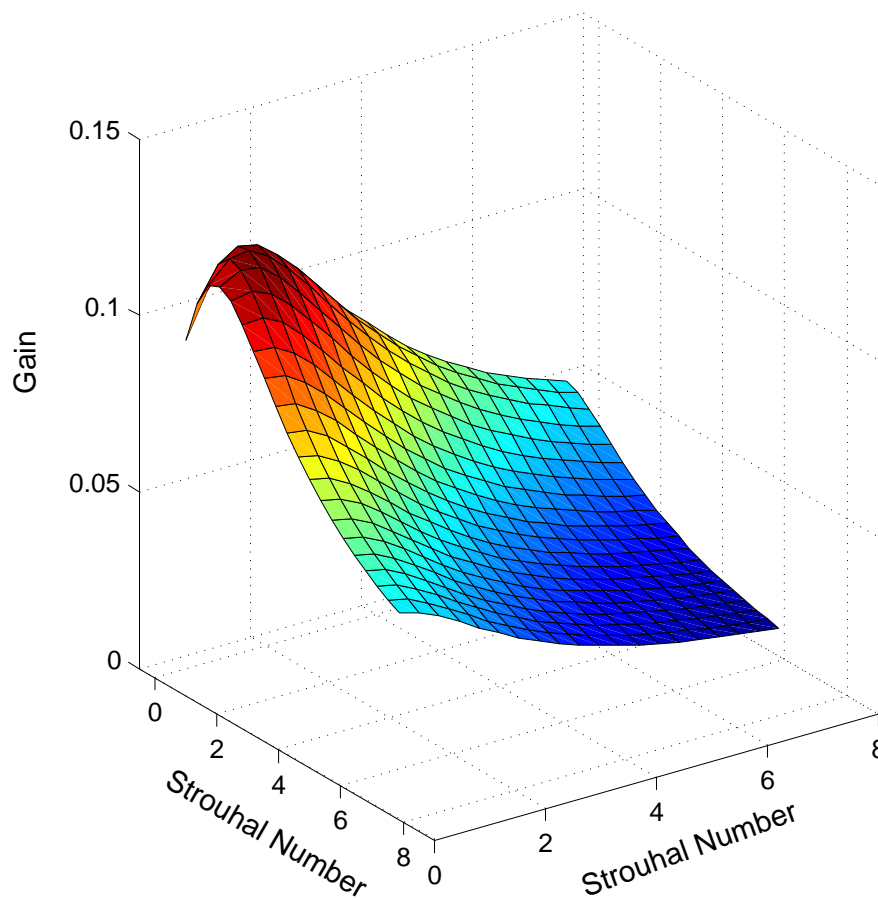


Figure 4.12: Gain of the second order transfer function computed from the recursive relation of the harmonic probing approach

The computation of the third order transfer function requires excitation at three different frequencies. The computation of higher order transfer functions is straightforward using this method, once the coefficients of the polynomial identification are obtained with unsteady CFD and broadband forcing. The higher order transfer functions are then computed as the functions of frequency and the coefficients. The relation is recursive as also seen from Eq. (4.25). Although the procedure to compute the higher order transfer functions with this approach is time consuming, generally a small number of higher order transfer functions are sufficient to achieve convergence in the response.

In Fig. 4.11, the responses from the single harmonic forcing, at $A = 0.3$, and linear identification are compared with the first order transfer function computed from harmonic probing. The overall agreement between the different methods is good for both phase and gain. In Fig. 4.12, the gain of the second order transfer function is shown. It is a surface plotted over two Strouhal values, and highest values are achieved on the main diagonal. It is hard to represent and interpret the higher order transfer functions of third and higher order degrees. In Fig. 4.13, the gain of the first three transfer functions is shown. The amplitude of the third order transfer function on the main diagonal is much less than the first order transfer function.

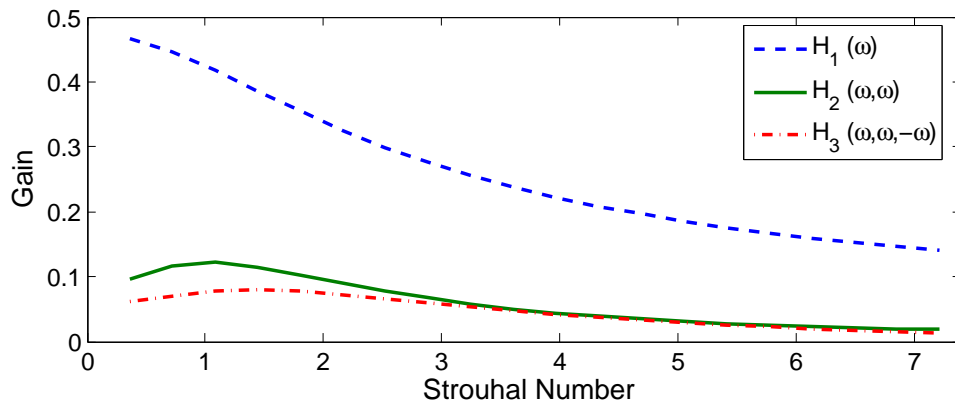


Figure 4.13: Gain of the first three transfer functions on the main diagonal computed from the recursive relation of the harmonic probing approach

4.4 Neural Network Identification

Neural network identification methods belong to parametric nonlinear black box identification procedures [92, 98, 105, 126]. They appear promising in the identification of any nonlinearity up to a specified degree of accuracy (universal function approximators). For highly nonlinear systems, black box identification can be used if little or no priori information about the complex physics is available. As mentioned in the previous chapters, in the case of a wire in pulsating cross flow, nonlinear complex interactions take place in the bound-

ary layer when the pulsating flow velocity achieve higher values. It is possible to obtain a dynamic model (input-output relation) that is valid for a range of amplitudes and frequencies with nonlinear black box identification based on only the measured input and output data set. Nonlinear dynamic models of more advanced configurations of the heat source can also be obtained with this approach (in the case of a turbulent combustion). A detailed discussion about the nonlinear black-box identification methods is found in [67, 126]. Figure 4.14 shows the neural network identification scheme for the nonlinear heat source.

Based on the measured input-output data set, a dynamical model is constructed. The procedure consists of 3 steps:

1. The number of past inputs and outputs, which are called the regressors, is selected. The model structures that are used are the nonlinear extension of linear model structures like NARX, NFIR, NOE [26].
2. A nonlinear map is created from the space of regressors to the nonlinear response, using functional expansion with the hyperbolic tangent activation function within a unit.
3. The criterion to minimize the difference between the actual output and output from identification results in a nonlinear least square fit. Optimization techniques like Gauss-Newton or Levenberg-Marquardt are used to find the parameters of nonlinearity.

Network structures are classified as feed-forward or recurrent [92, 105]. In a recurrent network structure, computed outputs from the network are fed as the input to the layers. In this study a feed-forward network structure is used, and only past inputs are considered as the input to the neural network (NFIR-model). The network has only 1 hidden layer and a tangent hyperbolic as the activation function. A schematic of the neural network topology along with the regressors that are used as the input is shown in Fig. 4.15.

Let φ be the set of regressors with memory length L , input u , and output y

$$\phi = [1 \ u(t-1) \ \dots \ u(t-L)], \quad (4.26)$$

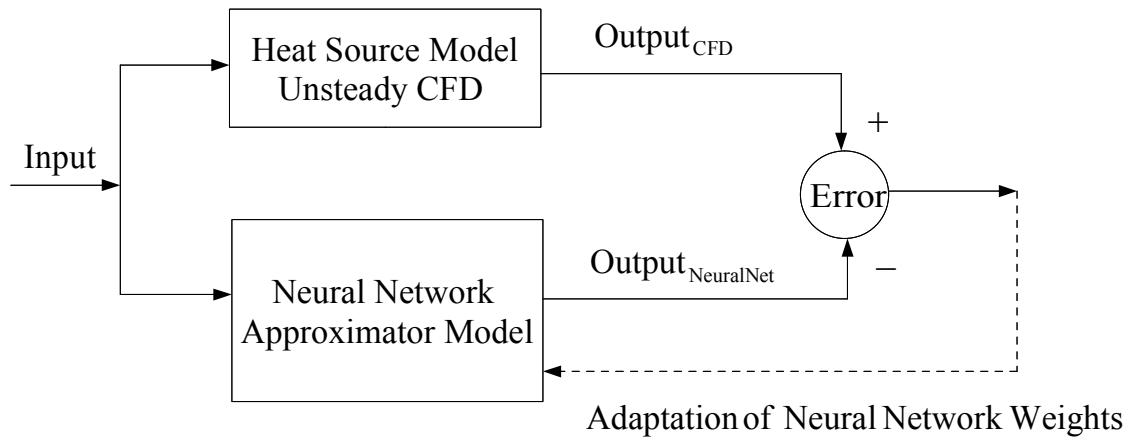


Figure 4.14: Nonlinear identification using unsteady CFD and Neural Network approximation

and Z^N is the set of the input-output data (training set) up to time N .

The identification problem is then formulated as the minimization of the error between the CFD model output and the output from neural network, which is

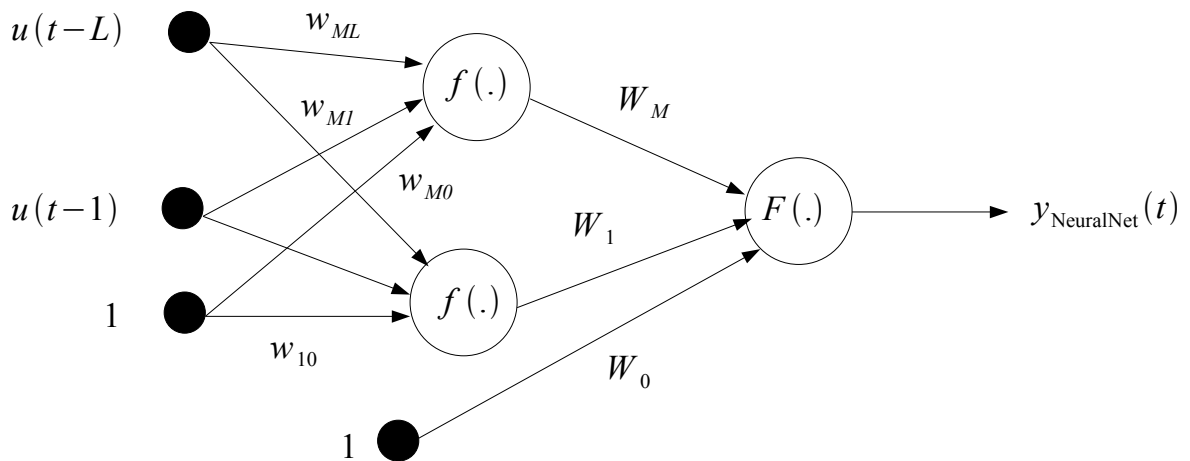


Figure 4.15: 1 hidden layer feed-forward neural network structure along with regressors with tangent hyperbolic activation function f and the linear function F at the output layer, M is the number of units and L is the memory length of the regressors

represented as,

$$V_N(\theta) = \frac{1}{N} \sum_{t=1}^N [y_{\text{CFD}}(t) - y_{\text{NeuralNet}}(t)]^2. \quad (4.27)$$

This function is minimized by some nonlinear iterative search algorithms. Moreover, Levenberg-Marquardt technique is used to find the minimum of the function and hence the weights of neural networks which are denoted by θ .

The output from the neural network is written in terms of the weights of the network as,

$$y_{\text{NeuralNet}}(t) = \sum_{j=1}^M W_j f\left(\sum_{l=1}^L w_{jl} \phi_l + w_{j0}\right) + W_0, \quad (4.28)$$

where w and W 's are the weights of the neural network for the input and output to the hidden layer, and f is the tangent hyperbolic activation function.

4.4.1 Extraction of Volterra Kernels in terms of Neural Network Weights

As mentioned earlier, a wide class of nonlinear systems can be represented in Volterra series form for the input-output relation [18, 19]. This is the extension of the Taylor series approximation applied for the functionals. For an input-output data set $(u(t), y(t))$ with memory length L , this relation is written for a third order nonlinearity in discrete form as,

$$\begin{aligned} y(t) = & h_0 + \sum_{\tau=1}^L h_1(\tau) u(t-\tau) + \sum_{\tau_1=1}^L \sum_{\tau_2=1}^L h_2(\tau_1, \tau_2) u(t-\tau_1) u(t-\tau_2) \\ & + \sum_{\tau_1=1}^L \sum_{\tau_2=1}^L \sum_{\tau_3=1}^L h_3(\tau_1, \tau_2, \tau_3) u(t-\tau_1) u(t-\tau_2) u(t-\tau_3). \end{aligned} \quad (4.29)$$

Different approaches exist in literature to extract the kernels. A correlation based analysis with broadband forcing has been developed by Schetzen et al. [120]. This method requires lengthy signals and the number of parameters (h coefficients) is huge. A orthogonalization of the above expression using a

Gram-Schmidt algorithm has been purposed by Korenberg et al. [72]. This has the advantage of not requiring a specific type (like broadband) of signal for the excitation of the system. Wray et al. [139] have developed a strategy to get improved accuracy of the nonlinear approximation in comparison to Toeplitz matrix inversion proposed by Korenberg et al. [72]. In this study the approach proposed by Wray et al. [139] is used.

The idea is to expand the neural network approximation output as in Eq. (4.28) for the tangent hyperbolic function around the bias term. Taylor series approximation of the tangent hyperbolic function around zero is written as, [139],

$$\tanh(x) = \sum_{n=1}^{\infty} (-1)^{n+1} \frac{B_n(2^{4n} - 2^{2n})x^{2n-1}}{(2n)!}, \quad (4.30)$$

where B_n is the n th order Bernolli number and is defined as,

$$B_n = \frac{2(2n)!}{(2\pi)^{2n}} \sum_{s=1}^{\infty} \frac{1}{s^{2n}}. \quad (4.31)$$

Expanding the activation function in Eq. (4.28), the neural network output is expressed as,

$$y_{\text{NeuralNet}}(t) = \sum_{j=1}^M W_j \left[\frac{\sum_{k=1}^{\infty} (-1)^{k+1} B_k (2^{4k} - 2^{2k}) \left(\sum_{l=1}^L w_{jl} \phi_l + w_{j0} \right)^{2k-1}}{(2k)!} \right] + W_0. \quad (4.32)$$

Combining this representation with Volterra series of third order in the form as in Eq. (4.29), the kernels are expressed in terms of the weights of the neural network.

The zeroth order kernel:

$$h_0 = \sum_{j=1}^M W_j \left[\frac{\sum_{k=1}^{\infty} (-1)^{k+1} B_k (2^{4k} - 2^{2k}) C(2k-1, 0) w_{j0}^{2k-1}}{(2k)!} \right] + W_0. \quad (4.33)$$

The first order kernels:

$$h_1(a) = \sum_{j=1}^M W_j \left[\frac{\sum_{k=1}^{\infty} (-1)^{k+1} B_k (2^{4k} - 2^{2k}) C(2k-1, 1) w_{ja} w_{j0}^{2k-2}}{(2k)!} \right], \quad (4.34)$$

$a = 1 \dots L.$

The second order kernels:

$$h_2(a, b) = \sum_{j=1}^M W_j \left[\frac{\sum_{k=1}^{\infty} (-1)^{k+1} B_k (2^{4k} - 2^{2k}) C(2k-1, 2) w_{ja} w_{jb} w_{j0}^{2k-3}}{(2k)!} \right], \quad (4.35)$$

$a, b = 1 \dots L.$

The definition of the n th order kernel is hence given as,

$$h_n(a_1, \dots, a_n) = \sum_{j=1}^M W_j \left[\frac{\sum_{k=1}^{\infty} (-1)^{k+1} B_k (2^{4k} - 2^{2k}) C(2k-1, n) w_{ja_1} \dots w_{ja_n} w_{j0}^{2k-n-1}}{(2k)!} \right], \quad (4.36)$$

$a_1, \dots, a_n = 1 \dots L.$

where C is defined as,

$$C(m, n) = \begin{cases} \frac{m!}{n!(m-n)!} & \text{for } m \geq n \\ 0, & \text{otherwise.} \end{cases} \quad (4.37)$$

4.4.2 Higher Order Transfer Functions

Once the kernels of various orders are calculated, these are then extended into frequency domain to obtain the higher order transfer functions. When the system experiences different frequencies, one can see how the nonlinearity of the system effects these frequencies in order to produce sum of the frequencies, and differences between the frequencies which are typical for a nonlinear system. For a thermo-acoustic system, these transfer functions allow us to see how different modes interact with each other and transfer energy to higher order modes.

The first order transfer function is computed from z-transform of the first order kernel as,

$$H_1(\omega) = \sum_{k=1}^L h_1(k) e^{-i\omega k \Delta t}. \quad (4.38)$$

The second order transfer function is obtained from z-transform of the second order kernel along the two frequency directions as,

$$H_2(\omega_1, \omega_2) = \sum_{k=1}^L \sum_{l=1}^L h_2(k, l) e^{-i\omega_k \Delta t} e^{-i\omega_l \Delta t}. \quad (4.39)$$

Finally, the third order transfer function is computed from z-transform along the three frequency directions of the third order kernel and is written as,

$$H_3(\omega_1, \omega_2, \omega_3) = \sum_{k=1}^L \sum_{l=1}^L \sum_{m=1}^L h_3(k, l, m) e^{-i\omega_k \Delta t} e^{-i\omega_l \Delta t} e^{-i\omega_m \Delta t}. \quad (4.40)$$

If suppose the system experiences a sinusoid input with amplitude U_0 and frequency ω ,

$$u(t) = U_0 \sin(\omega t) = U_0 \left(\frac{e^{i\omega t} - e^{-i\omega t}}{2i} \right), \quad (4.41)$$

then the corresponding output in the frequency domain in terms of the higher order transfer functions is computed as,

$$Y(\omega) = U_0 H_1(\omega) + \frac{3U_0^3}{4} H_3(\omega, \omega, -\omega). \quad (4.42)$$

In this expression, the contribution of the nonlinearity is seen in the third order transfer function. The advantage of this representation of the nonlinearity will be clearer when a frequency domain thermo-acoustic system model is developed.

4.4.3 Nonlinear Identification of the Wire in Pulsating Flow from CFD and Nonlinear Transfer Function

As the input to the heat source, a chirp signal of varying amplitudes is used with Str ranging from 0.72 to 2.88. The perturbation amplitudes are $A = 0.3, 1, 1.5$ and 2 . The memory length of the regressors is 15, and the neural network is a structure with one hidden layer and 12 neurons, composed of tangent hyperbolic functions and a linear output layer.

The corresponding nonlinear approximation with the neural network along with Volterra series approximation up to third order is shown in Fig. 4.16. The fit to the CFD output is 86% for both the approximations. Next the kernels of various orders are extracted with the procedure outlined in the previous section. Figure 4.17 shows the first and second order kernels. The value of the h_0 is -0.00186 .

For a sinusoidal input, the output from the heat source model is calculated using Eq. (4.42) in terms of higher order transfer functions and amplitude of

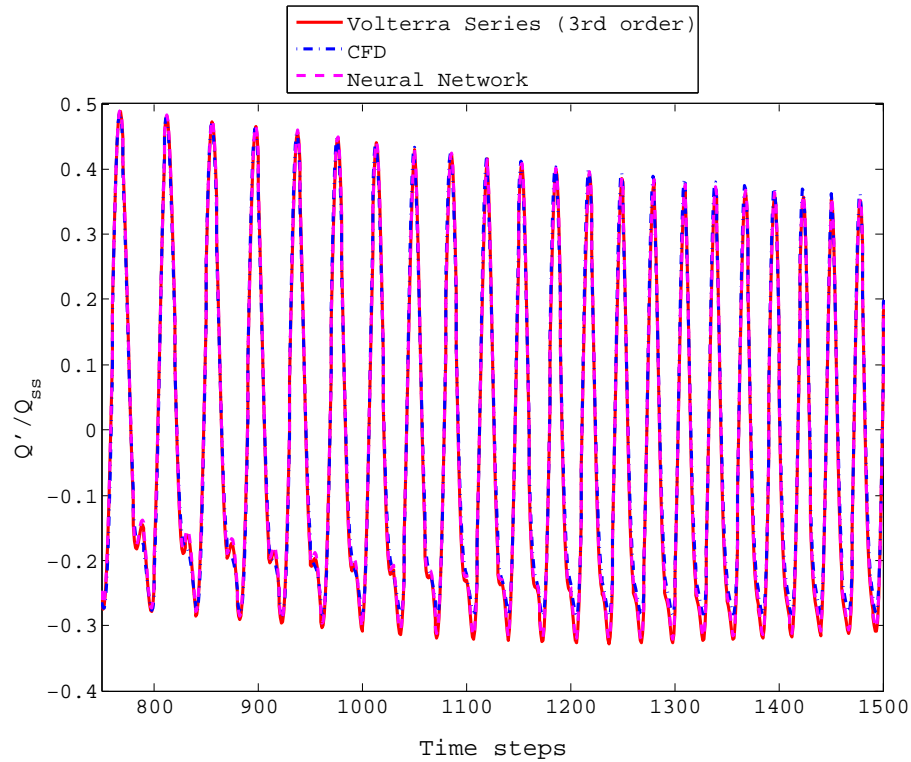


Figure 4.16: Approximation of the nonlinear heat transfer rate (non-dimensionalized with respect to the steady state value) from the heat source for a chirp signal of varying amplitude with Neural Network identification and Volterra series of third order approximation

the sinusoid. A comparison with the single sinusoidal response from CFD is shown in Fig. 4.19 for $A = 1.5, 2$ and for $Str = 1.08, 1.8, 2.16, 2.88$ along with a linear transfer function. The maximum deviation is observed at $A = 1.5$ and $Str = 1.08$, but this is less than 6%, and an overall agreement between the model output and CFD output is adequate for the considered range of amplitudes and frequencies.

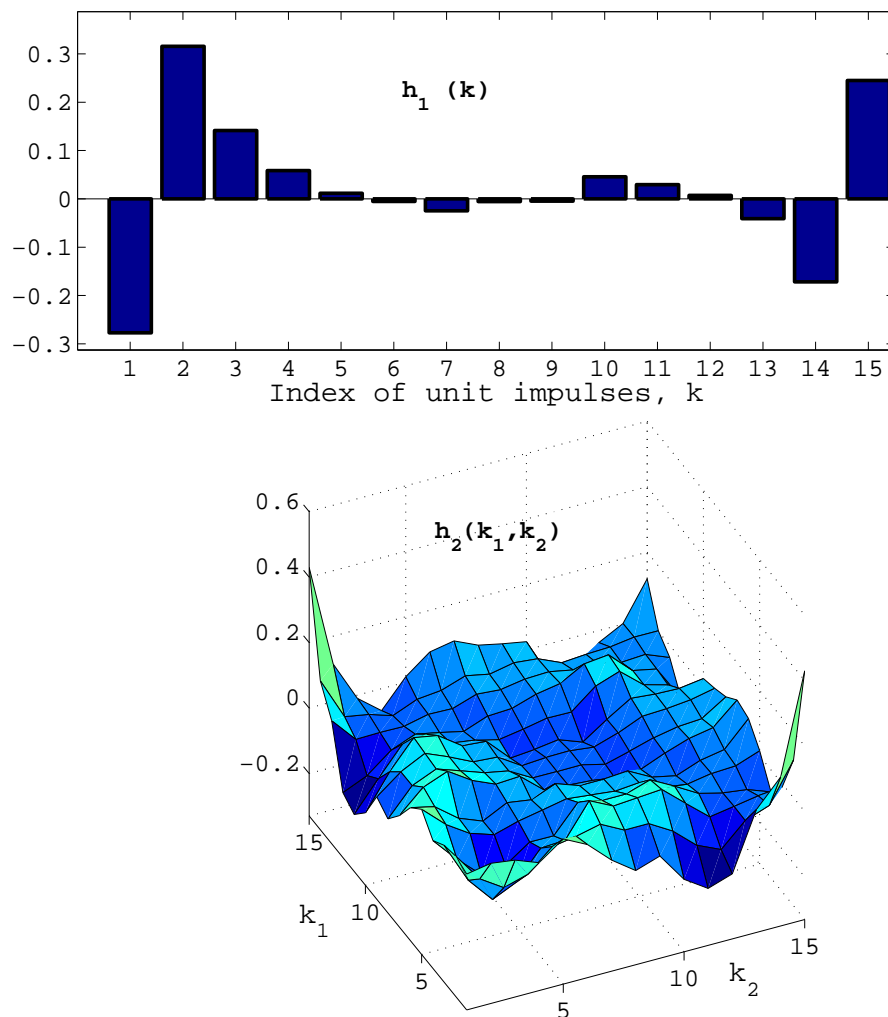


Figure 4.17: First (top) and second (bottom) order kernels (Number of the regressors is 15)

4.4.4 Nonlinear Identification of the Laminar Premixed Flame

The flame model considered in the previous chapters is excited with a chirp signal of varying amplitudes. The Str ranges from 6.2 to 49.5. Perturbation amplitudes are $A = 0.5, 0.4, 0.3$ and 0.1. The flame model is weakly nonlinear and nonlinearity increases with the increasing frequency. The second harmonic for a single sinusoid excitation at high amplitude and frequency for the forcing velocity (at $A = 0.5$ and $\text{Str} = 49.5$) gives a peak about 7% of the fundamental

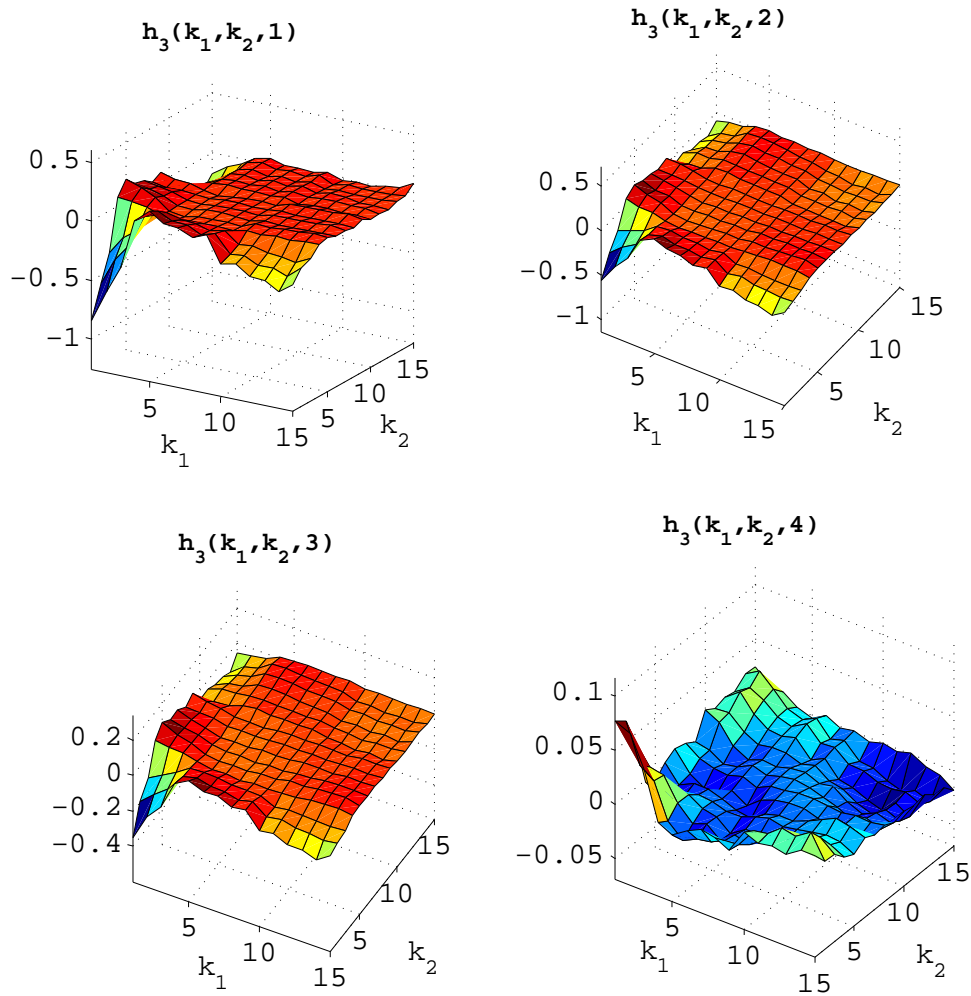


Figure 4.18: Third order kernels for the first four fixed third dimension

harmonic.

A first estimation for the number of regressors is involved in the model structure (NFIR), and is calculated from the time step of the simulation $\Delta t = 1.5708 \times 10^{-4}$ s and estimated time lag of the laminar flame $\tau_f = 0.0619$ s as $N_u = 394$. Increasing the range of frequency increases the number of regressors.

The number of regressors is taken as 420. In Fig. 4.20, at the top, the approximation of the flame response with neural network identification is shown. At the bottom of Fig. 4.20, a detail of the signal with the approximation for

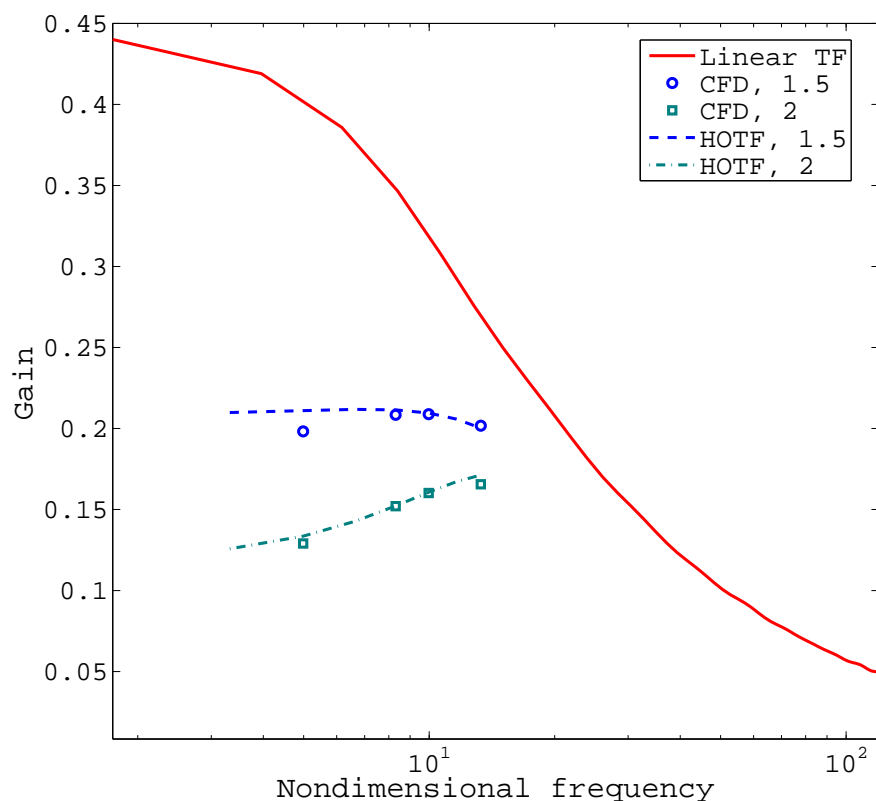


Figure 4.19: Gain of the transfer function calculated from CFD for single sinusoidal input ($A = 1.5, 2$, $\text{Str} = 1.08, 1.8, 2.16, 2.88$), and obtained from higher order transfer functions along with a linear transfer function on a semi-logarithmic plot

different orders of Volterra series is shown. A second order approximation is adequate in this case. Taking third order terms into account does not increase the accuracy in approximation. In comparison to the previous model (CFD of the wire in pulsating flow), the number of regressors is changed from 15 to 420. Premixed flames have larger time delays, and this has a significant effect on the nonlinear identification because of the “curse of dimensionality”. For the premixed flame model considered here (it allows a maximum $A = 0.5$, and flashback is not allowed in the code), a second order model is adequate, but a third order approximation has to deal with $420^3 = 74.08 \times 10^6$ terms. When a wide range of frequencies is taken into account, it may be computationally expensive for the identification algorithm and post-processing with a large

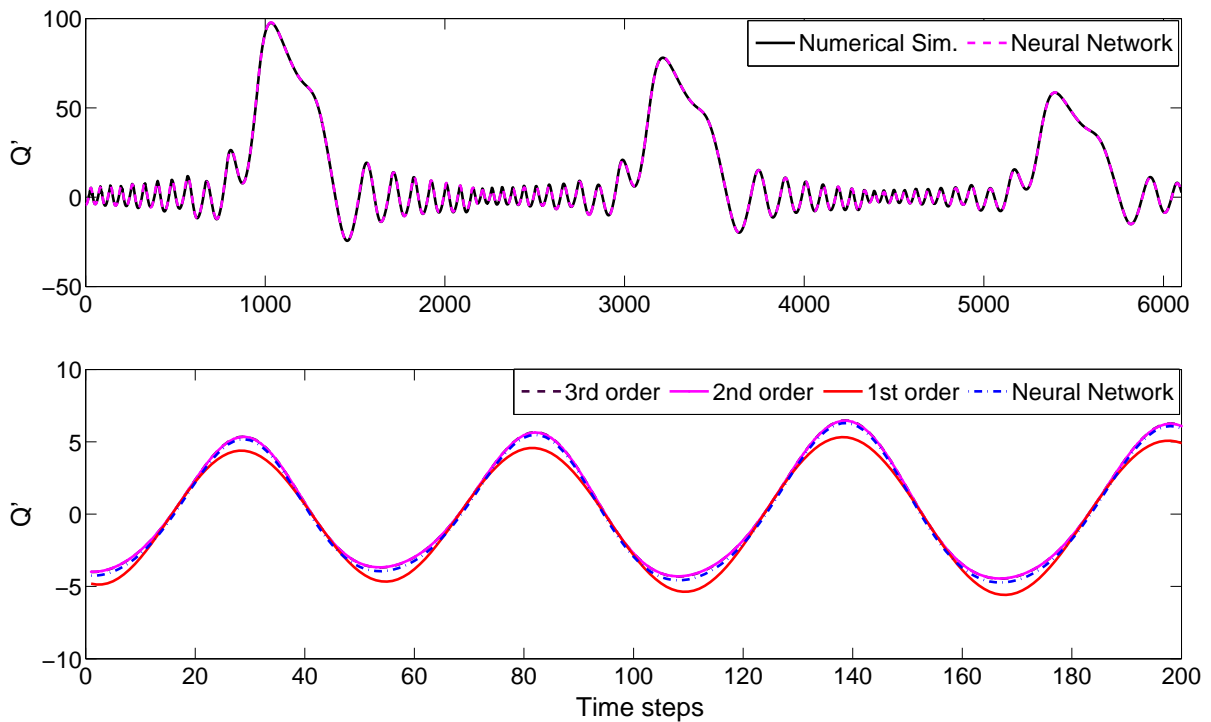


Figure 4.20: Top - Approximation of the heat release of the laminar flame using neural network identification. Bottom - Approximation with various kernel orders

number of parameters.

4.5 Other Nonlinear Identification Strategies

4.5.1 Block Oriented Structures

In this modeling approach, static nonlinearity in the input/output is followed before/after a linear dynamic part in Hammerstein/Wiener models. In Hammerstein-Wiener models, static nonlinearity in both the input and output is considered. A schematic representation of Hammerstein, Wiener and Hammerstein-Wiener cascade models are shown in Fig. 4.21. An approximation as the sum of Wiener systems (cascade model) is possible for a system that could be written as Volterra series representation [73].

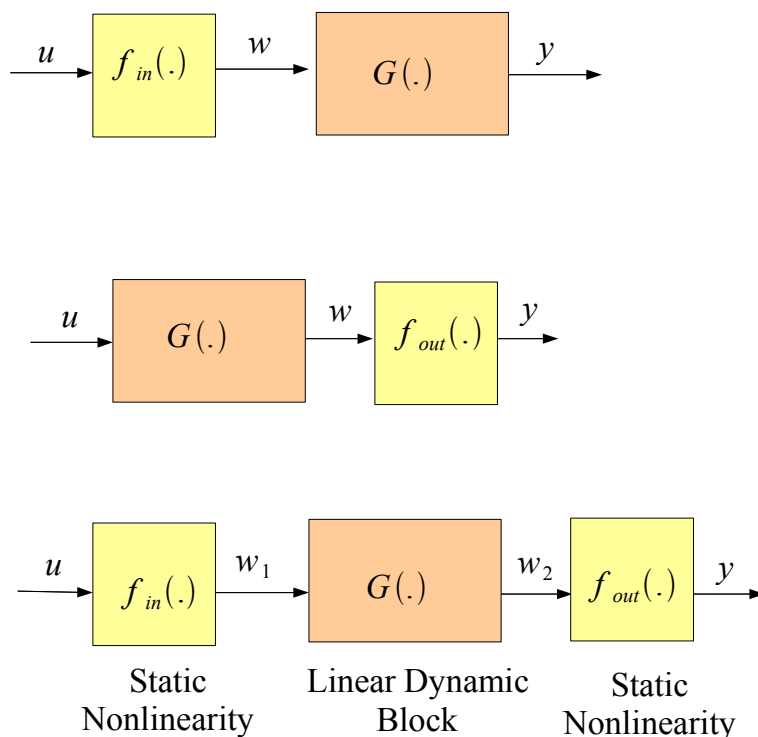


Figure 4.21: Cascade block models. Top - Hammerstein model, Middle - Wiener model, Bottom - Hammerstein -Wiener model

Let us consider a Hammerstein model. The static input nonlinearity is parametrized with polynomial up to degree p_o as,

$$f_{in}(u) = a_1 u + a_2 u^2 + \dots + a_{p_o} u^{p_o}. \quad (4.43)$$

In fact, a different basis other than polynomials and different nonlinear shapes, i.e. saturation type nonlinearity, are used. In the linear block, different linear model structures (FIR, ARX, OE) are assumed. Let us consider an FIR representation for the linear dynamic part which is denoted by G in Fig. 4.21.

$$G(z) = c_0 z^0 + c_1 z^{-1} + \dots + c_L z^{-L}, \quad (4.44)$$

where z is the shift operator. The corresponding output with these parametrizations for a maximum filter length L becomes,

$$y(t) = \sum_{k=1}^{p_o} \sum_{l=0}^L c_l a_k u^k(t-l). \quad (4.45)$$

In the identification using the above parameterizations, the aim is to find the parameters of this nonlinear representation by minimizing the difference between the experimental measurement/ CFD simulation output and the Hammerstein model output.

4.5.2 Identification based on Fuzzy Logic

Fuzzy Logic

Fuzzy logic and fuzzy sets are used as function approximation and also for input-output modeling of dynamical systems [5, 6, 130]. A system is defined by a collection of **if-then** rules with fuzzy relation.

If velocity is high **then** nonlinearity becomes greater.

In this example, 'velocity is high' - is an antecedent proposition and, 'nonlinearity becomes greater' - is a consequent proposition. This aptly applies to fuzzy sets. A membership function for a fuzzy set A is a mapping of the antecedent (x) , $\mu_A(x) : X \rightarrow [0, 1]$. The value of $\mu_A(x)$ is the membership value of $x \in X$. If $\mu_A(x) = 1$, x completely belongs to fuzzy set A . Fundamental operations of union and intersection is performed on fuzzy sets with the membership functions [131]. Intersection of the fuzzy sets A and B is defined as,

$$\mu_A(x) \wedge \mu_B(x) = \mathbf{min}(\mu_A(x), \mu_B(x)). \quad (4.46)$$

In Linguistic fuzzy model, the antecedent and consequent propositions are fuzzy propositions whereas, in Takagi-Sugeno (TS) fuzzy model, the antecedent is a fuzzy proposition, and the consequent is a crisp function [130, 131].

From the identification point of view, an NFIR structure which uses only past inputs, $y(t) = F(u(t), u(t-1), \dots, u(t-N_u+1))$, rule i (R_i), is expressed in linguistic fuzzy model using **if-then** structures as,

$$R_i : \mathbf{If} \ u(t) \text{ is } A_{i1} \ \mathbf{and... and} \ u(t - N_u + 1) \text{ is } A_{iN_u} \ \mathbf{then} \ y(t) \text{ is } B_{i1},$$

where A_i and B_i are the antecedent and consequent linguistic terms, respectively.

In order to obtain the output of the TS fuzzy model, a fuzzy inference method is used without performing defuzzification. For a TS fuzzy model defined as,

R_i : **If** x_1 is A_{i1} **and..and** x_n is A_{in} **then** $y_i = c_{i0} + c_{i1}x_1 + \dots + c_{in}x_n$, for $i = 1, \dots, K$

the corresponding output will be [130, 131]

$$y = \frac{\sum_{i=1}^K \beta_i y_i}{\sum_{i=1}^K \beta_i}, \quad (4.47)$$

and degree of the fulfillment β_i is defined as [131],

$$\beta_i = \mu_{A_{i1}}(x_1) \wedge \mu_{A_{i2}}(x_2) \dots \mu_{A_{in}}(x_n). \quad (4.48)$$

$\mu_{A_{ik}}(x_k)$ denotes the membership value of the fuzzy set A_{ik} .

The above equation can be viewed as local linearization for the approximation of a nonlinear function [5, 6].

Fuzzy Clustering

Data clustering is used to divide the element of the data into clusters so that the elements in the same clusters are as similar as possible whereas elements of the different classes are as dissimilar as possible [6]. The degree of similarity is defined in terms of suitable distance measure. In fuzzy clustering, elements can belong to more than one cluster, and an associated degree of the memberships of the elements to the clusters are defined.

In one of the popular fuzzy clustering algorithms, Fuzzy c-Means [17], a data set $S = [z_1, z_2, \dots, z_k]$ is partitioned into r clusters with cluster centers $C = [c_1, \dots, c_r]$ for a given objective function. The partition matrix $PM = [\mu_{ij}]$ obtained from the algorithm denotes the degree of the membership of the element i to cluster j . In the objective function, a parameter that controls the fuzziness of the clusters m is included. A higher value represents greater overlapping of the clusters, and a typical value for m is 2 [17].

The shape of the clusters is determined by the distance measure that is also included in the objective function. Fuzzy c-Means algorithm searches for the spherical clusters, whereas Gustafson-Kessel clustering algorithm finds the ellipsoidal clusters [56]. Clusters obtained with Gustafson-Kessel method can be represented by a number of TS rules [6]. A specific procedure, where the fuzzy sets or so-called membership functions are obtained by projecting the clusters onto the antecedent variables (which are the regressors in the nonlinear identification problem), is utilized to find these rules. Details about the procedure is found in [6] .

Identification of CFD Model of the Wire Heat Source

A multilevel (7 level) excitation signal is chosen as the input to the heat source [11, 12]. The input-output signals (normalized with respect to the steady state values) are shown in Fig. 4.22. Time step of the CFD computation is $\Delta t = 3 \times 10^{-4}$ s , and the length of the signal is $M = 1468$. The input-output data set (time series generated from unsteady CFD) is used in Fuzzy-Identification Toolbox [4]. The number of regressors $N_u = 10$, number of clusters $r = 13$, and the fuzziness exponent $m = 2$ are chosen as the parameters for the identification algorithm. Membership functions are obtained from the projection of the clusters onto the regressors. The membership degree of the regressors to each of the clusters is shown in Fig. 4.23 with the membership functions. The first plot represents the degree of membership of the first regressor ($u(t)$) to each of the clusters with the shown functions.

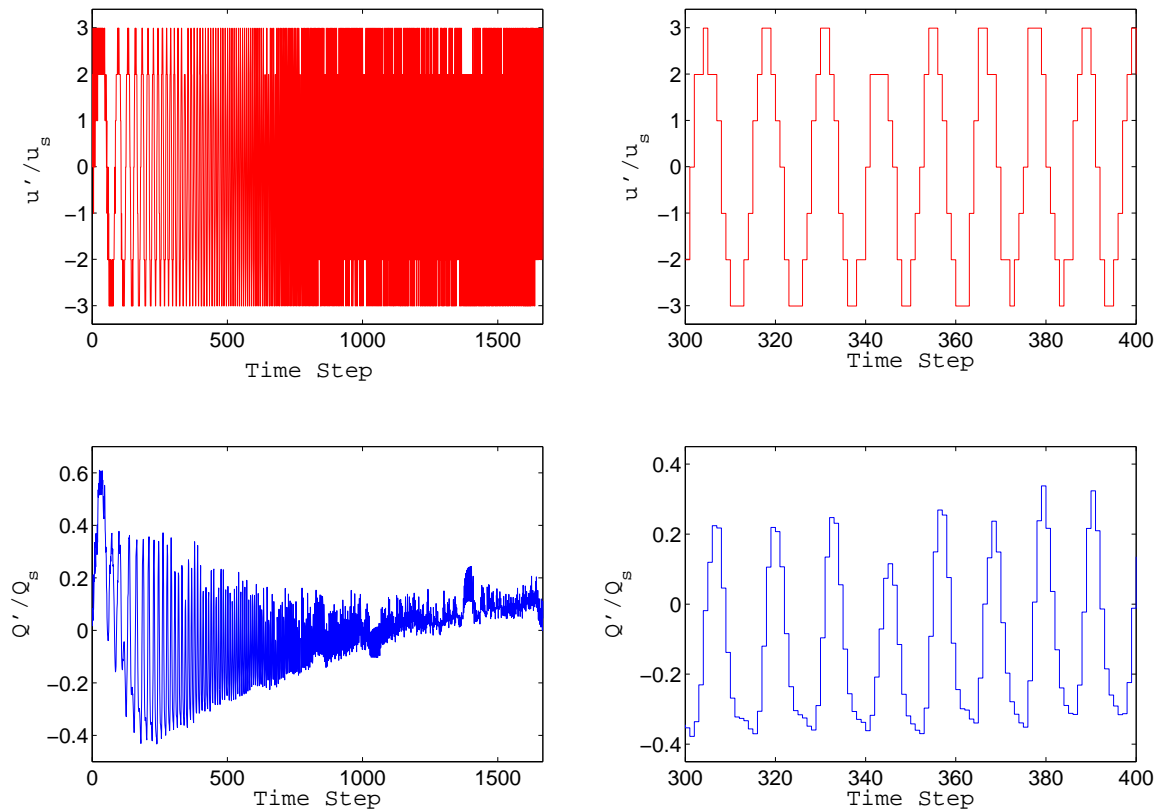


Figure 4.22: Above - a multi level excitation signal and a detail of the signal,
 Below - heat transfer rate of the wire and a detail of the response

Validation is performed against single sinusoids. Figure 4.24 shows CFD output and output from fuzzy model for $A = 1, 1.5, 2, 2.65$, and $Str = 1.08, 1.80, 1.80$ and 2.67 . The degree of the fits between the fuzzy model outputs and CFD model outputs are 98%, 98%, 95% and 92%, respectively.

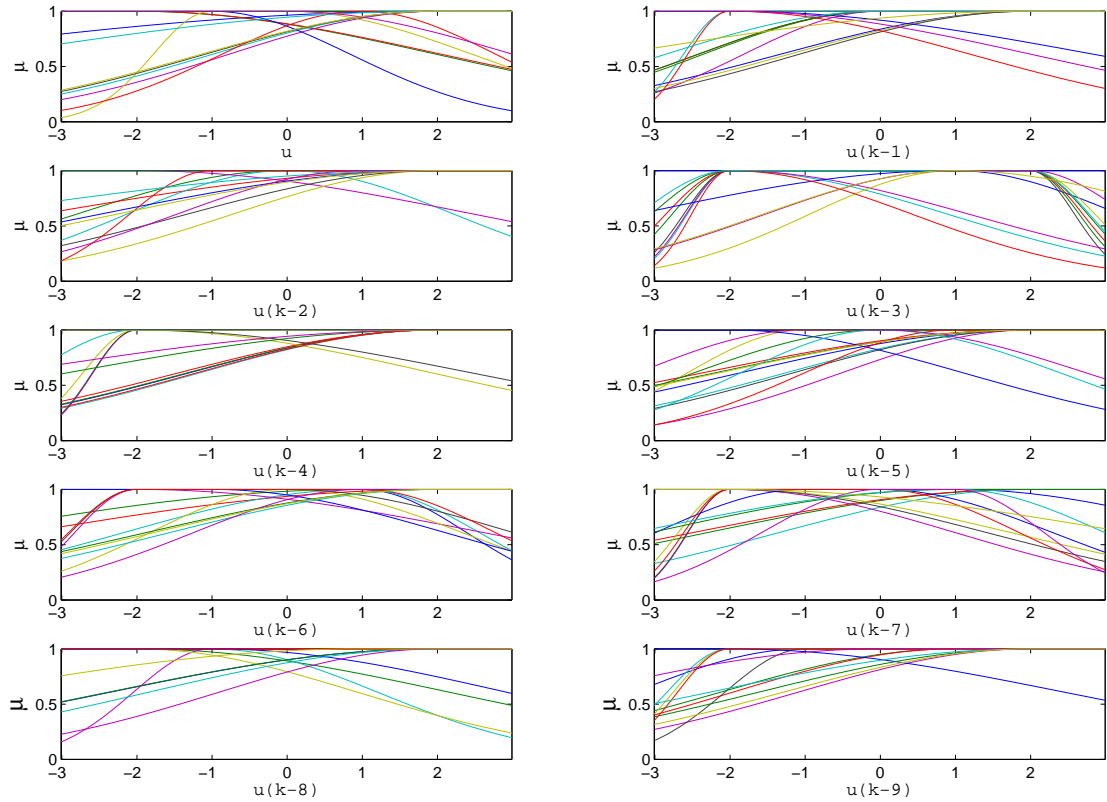


Figure 4.23: Membership functions, where first plot shows the membership degree of the regressor $u(k)$ to each of the clusters

Table 4.1 and Table 4.2 show the consequent parameters and cluster centers obtained from identification algorithm. The first two rules from the table are read as,

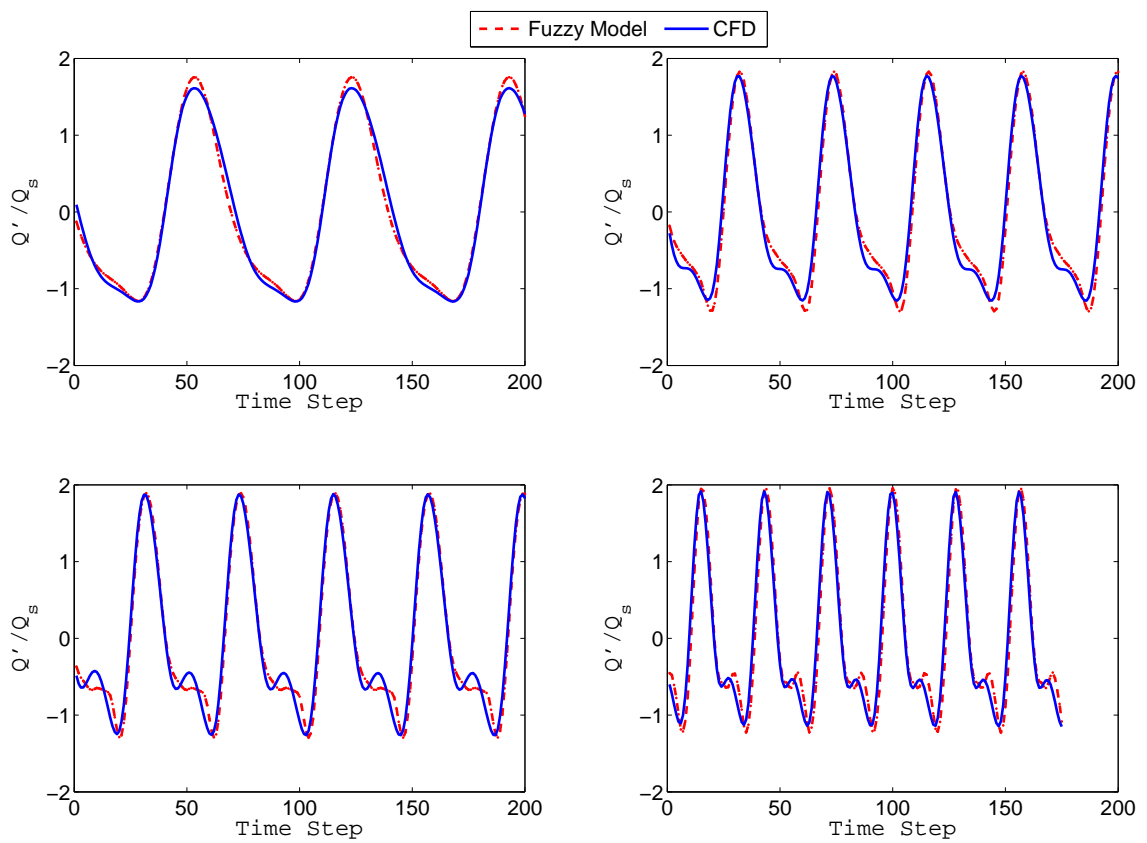


Figure 4.24: Validation for single sinusoids Top - $A = 1, 1.5$ and $Str = 1.08, 1.80$
 Bottom - $A = 2, 2.65$ and $Str = 1.8, 2.67$

1. **If** u is A_{11} **and** $u(k-1)$ is A_{12} **and** $u(k-2)$ is A_{13} **and** $u(k-3)$ is A_{14} **and**
 $u(k-4)$ is A_{15} **and** $u(k-5)$ is A_{16} **and** $u(k-6)$ is A_{17} **and** $u(k-7)$ is A_{18}
and $u(k-8)$ is A_{19} **and** $u(k-9)$ is A_{110} **then**

$$y(k) = 6.2 \cdot 10^{e-2} u + 4.5 \cdot 10^{e-2} u(k-1) + 4.2 \cdot 10^{e-2} u(k-2) + 6.4 \cdot 10^{e-2} u(k-3) \\ + 2.6 \cdot 10^{e-3} u(k-4) + 5.5 \cdot 10^{e-2} u(k-5) - 6.2 \cdot 10^{e-2} u(k-6) + 6.1 \cdot 10^{e-2} u(k-7) \\ - 5.2 \cdot 10^{e-2} u(k-8) - 1.1 \cdot 10^{e-2} u(k-9) + 9.7 \cdot 10^{e-2}$$

2. **If** u is A_{21} **and** $u(k-1)$ is A_{22} **and** $u(k-2)$ is A_{23} **and** $u(k-3)$ is A_{24} **and**
 $u(k-4)$ is A_{25} **and** $u(k-5)$ is A_{26} **and** $u(k-6)$ is A_{27} **and** $u(k-7)$ is A_{28}
and $u(k-8)$ is A_{29} **and** $u(k-9)$ is A_{210} **then**

$$y(k) = -1.0 \cdot 10^{e-1} u + 7.5 \cdot 10^{e-2} u(k-1) - 3.3 \cdot 10^{e-1} u(k-2) + 1.2 \cdot 10^{e-1} u(k-3) \\ - 1.7 \cdot 10^{e-1} u(k-4) + 1.5 \cdot 10^{e-1} u(k-5) - 2.1 \cdot 10^{e-1} u(k-6) + 4.2 \cdot 10^{e-1} u(k-7) \\ - 5.7 \cdot 10^{e-2} u(k-8) + 1.7 \cdot 10^{e-1} u(k-9) - 7.8 \cdot 10^{e-1}$$

Table 4.1: Consequent parameters.

rule	u	$u(k-1)$	$u(k-2)$	$u(k-3)$	$u(k-4)$	$u(k-5)$	$u(k-6)$	$u(k-7)$	$u(k-8)$	$u(k-9)$	offset
1	$6.2 \cdot 10^{-2}$	$4.5 \cdot 10^{-2}$	$4.2 \cdot 10^{-2}$	$6.4 \cdot 10^{-2}$	$2.6 \cdot 10^{-3}$	$5.5 \cdot 10^{-2}$	$-6.2 \cdot 10^{-2}$	$6.1 \cdot 10^{-2}$	$-5.2 \cdot 10^{-2}$	$-1.1 \cdot 10^{-2}$	$9.7 \cdot 10^{-2}$
2	$-1.0 \cdot 10^{-1}$	$7.5 \cdot 10^{-2}$	$-3.3 \cdot 10^{-1}$	$1.2 \cdot 10^{-1}$	$-1.7 \cdot 10^{-1}$	$1.5 \cdot 10^{-1}$	$-2.1 \cdot 10^{-1}$	$4.2 \cdot 10^{-1}$	$-5.7 \cdot 10^{-2}$	$1.7 \cdot 10^{-1}$	$-7.8 \cdot 10^{-1}$
3	$2.5 \cdot 10^{-1}$	$3.1 \cdot 10^{-2}$	$3.8 \cdot 10^{-1}$	$-2.2 \cdot 10^{-1}$	$1.3 \cdot 10^{-1}$	$-3.4 \cdot 10^{-1}$	$8.4 \cdot 10^{-2}$	$-4.4 \cdot 10^{-1}$	$-5.7 \cdot 10^{-3}$	$-1.5 \cdot 10^{-1}$	$8.0 \cdot 10^{-1}$
4	$1.1 \cdot 10^{-1}$	$1.9 \cdot 10^{-1}$	$-3.4 \cdot 10^{-1}$	$1.3 \cdot 10^{-1}$	$-2.4 \cdot 10^{-1}$	$2.7 \cdot 10^{-1}$	$1.5 \cdot 10^{-1}$	$3.2 \cdot 10^{-1}$	$-2.2 \cdot 10^{-3}$	$3.6 \cdot 10^{-1}$	$-8.6 \cdot 10^{-1}$
5	$-3.6 \cdot 10^{-1}$	$1.4 \cdot 10^{-1}$	$2.5 \cdot 10^{-2}$	$8.0 \cdot 10^{-2}$	$5.9 \cdot 10^{-2}$	$-1.8 \cdot 10^{-1}$	$7.6 \cdot 10^{-3}$	$-3.9 \cdot 10^{-1}$	$1.3 \cdot 10^{-1}$	$1.3 \cdot 10^{-2}$	$5.5 \cdot 10^{-1}$
6	$-3.1 \cdot 10^{-1}$	$-6.1 \cdot 10^{-2}$	$5.5 \cdot 10^{-1}$	$2.2 \cdot 10^{-1}$	$4.3 \cdot 10^{-1}$	$-4.8 \cdot 10^{-1}$	$-6.3 \cdot 10^{-2}$	$9.7 \cdot 10^{-2}$	$-2.1 \cdot 10^{-1}$	$1.6 \cdot 10^{-1}$	$-6.3 \cdot 10^{-1}$
7	$2.3 \cdot 10^{-1}$	$1.0 \cdot 10^{-1}$	$-9.2 \cdot 10^{-2}$	$4.5 \cdot 10^{-2}$	$-3.4 \cdot 10^{-1}$	$4.0 \cdot 10^{-1}$	$-1.1 \cdot 10^{-1}$	$2.4 \cdot 10^{-1}$	$-1.4 \cdot 10^{-1}$	$2.3 \cdot 10^{-1}$	$-8.2 \cdot 10^{-1}$
8	$-1.7 \cdot 10^{-1}$	$-8.7 \cdot 10^{-2}$	$-5.1 \cdot 10^{-2}$	$-4.2 \cdot 10^{-3}$	$3.6 \cdot 10^{-3}$	$2.9 \cdot 10^{-3}$	$8.1 \cdot 10^{-3}$	$1.4 \cdot 10^{-2}$	$-2.0 \cdot 10^{-2}$	$-8.7 \cdot 10^{-2}$	$-7.8 \cdot 10^{-1}$
9	$1.2 \cdot 10^{-2}$	$-8.4 \cdot 10^{-2}$	$6.4 \cdot 10^{-2}$	$9.5 \cdot 10^{-3}$	$2.0 \cdot 10^{-1}$	$-2.7 \cdot 10^{-2}$	$2.3 \cdot 10^{-1}$	$-5.2 \cdot 10^{-2}$	$1.0 \cdot 10^{-1}$	$1.3 \cdot 10^{-2}$	$-9.8 \cdot 10^{-3}$
10	$-5.0 \cdot 10^{-1}$	$-2.5 \cdot 10^{-1}$	$1.9 \cdot 10^{-1}$	$5.2 \cdot 10^{-2}$	$1.5 \cdot 10^{-1}$	$-1.2 \cdot 10^{-1}$	$-1.9 \cdot 10^{-1}$	$-4.0 \cdot 10^{-2}$	$-2.5 \cdot 10^{-1}$	$-5.1 \cdot 10^{-1}$	$2.4 \cdot 10^{-1}$
11	$-5.7 \cdot 10^{-2}$	$1.6 \cdot 10^{-1}$	$5.6 \cdot 10^{-2}$	$6.1 \cdot 10^{-2}$	$-1.7 \cdot 10^{-1}$	$1.5 \cdot 10^{-1}$	$-1.7 \cdot 10^{-1}$	$3.8 \cdot 10^{-2}$	$-4.9 \cdot 10^{-2}$	$-2.1 \cdot 10^{-2}$	$9.7 \cdot 10^{-2}$
12	$8.4 \cdot 10^{-2}$	$1.0 \cdot 10^{-2}$	$-5.1 \cdot 10^{-2}$	$3.7 \cdot 10^{-2}$	$-2.3 \cdot 10^{-2}$	$1.3 \cdot 10^{-2}$	$-1.5 \cdot 10^{-1}$	$-1.9 \cdot 10^{-2}$	$-1.0 \cdot 10^{-1}$	$7.4 \cdot 10^{-2}$	$4.0 \cdot 10^{-1}$
13	$-1.0 \cdot 10^{-2}$	$3.4 \cdot 10^{-2}$	$2.5 \cdot 10^{-2}$	$8.9 \cdot 10^{-2}$	$-1.1 \cdot 10^{-2}$	$-1.6 \cdot 10^{-2}$	$1.6 \cdot 10^{-2}$	$2.9 \cdot 10^{-2}$	$1.6 \cdot 10^{-2}$	$-6.5 \cdot 10^{-3}$	$8.1 \cdot 10^{-2}$

Table 4.2: Cluster centers.

rule	u	$u(k-1)$	$u(k-2)$	$u(k-3)$	$u(k-4)$	$u(k-5)$	$u(k-6)$	$u(k-7)$	$u(k-8)$	$u(k-9)$
1	$-5.6 \cdot 10^{-1}$	$1.5 \cdot 10^{-1}$	$3.6 \cdot 10^{-1}$	$-5.5 \cdot 10^{-1}$	$1.2 \cdot 10^{-1}$	$3.9 \cdot 10^{-1}$	$-5.4 \cdot 10^{-1}$	$8.6 \cdot 10^{-2}$	$4.2 \cdot 10^{-1}$	$-5.3 \cdot 10^{-1}$
2	$-2.1 \cdot 10^{-1}$	$-1.8 \cdot 10^{-1}$	$-8.5 \cdot 10^{-2}$	$3.7 \cdot 10^{-2}$	$1.1 \cdot 10^{-1}$	$1.2 \cdot 10^{-1}$	$5.1 \cdot 10^{-2}$	$-4.1 \cdot 10^{-2}$	$-1.0 \cdot 10^{-1}$	$-1.1 \cdot 10^{-1}$
3	$-1.2 \cdot 10^{-1}$	$-1.2 \cdot 10^{-1}$	$-8.1 \cdot 10^{-2}$	$-1.3 \cdot 10^{-2}$	$4.9 \cdot 10^{-2}$	$8.9 \cdot 10^{-2}$	$8.9 \cdot 10^{-2}$	$5.9 \cdot 10^{-2}$	$2.3 \cdot 10^{-2}$	$-1.9 \cdot 10^{-2}$
4	$-7.9 \cdot 10^{-2}$	$-8.4 \cdot 10^{-2}$	$-8.9 \cdot 10^{-2}$	$-9.3 \cdot 10^{-2}$	$-4.0 \cdot 10^{-2}$	$-1.5 \cdot 10^{-3}$	$-1.7 \cdot 10^{-2}$	$-6.8 \cdot 10^{-2}$	$-1.3 \cdot 10^{-1}$	$-1.4 \cdot 10^{-1}$
5	$-6.3 \cdot 10^{-2}$	$-6.2 \cdot 10^{-2}$	$1.3 \cdot 10^{-2}$	$4.7 \cdot 10^{-2}$	$-4.7 \cdot 10^{-2}$	$-1.0 \cdot 10^{-1}$	$-1.1 \cdot 10^{-2}$	$7.0 \cdot 10^{-2}$	$-1.3 \cdot 10^{-2}$	$-1.0 \cdot 10^{-1}$
6	$-4.6 \cdot 10^{-2}$	$-1.0 \cdot 10^{-1}$	$-5.2 \cdot 10^{-2}$	$-2.5 \cdot 10^{-2}$	$-1.2 \cdot 10^{-1}$	$-8.5 \cdot 10^{-2}$	$2.4 \cdot 10^{-2}$	$-1.0 \cdot 10^{-1}$	$-1.4 \cdot 10^{-1}$	$1.8 \cdot 10^{-2}$
7	$-3.5 \cdot 10^{-2}$	$-1.0 \cdot 10^{-1}$	$6.0 \cdot 10^{-3}$	$9.3 \cdot 10^{-3}$	$-4.7 \cdot 10^{-2}$	$-1.4 \cdot 10^{-1}$	$5.1 \cdot 10^{-3}$	$9.6 \cdot 10^{-2}$	$-5.2 \cdot 10^{-2}$	$-1.3 \cdot 10^{-1}$
8	$-2.4 \cdot 10^{-2}$	$5.8 \cdot 10^{-2}$	$-6.2 \cdot 10^{-2}$	$3.3 \cdot 10^{-3}$	$3.6 \cdot 10^{-2}$	$-4.1 \cdot 10^{-2}$	$3.4 \cdot 10^{-2}$	$-1.3 \cdot 10^{-2}$	$-3.1 \cdot 10^{-2}$	$1.5 \cdot 10^{-2}$
9	$2.7 \cdot 10^{-2}$	$-3.4 \cdot 10^{-2}$	$-9.3 \cdot 10^{-2}$	$-1.2 \cdot 10^{-1}$	$-1.2 \cdot 10^{-1}$	$-7.9 \cdot 10^{-2}$	$-1.3 \cdot 10^{-2}$	$4.4 \cdot 10^{-2}$	$8.4 \cdot 10^{-2}$	$9.1 \cdot 10^{-2}$
10	$2.7 \cdot 10^{-2}$	$-5.6 \cdot 10^{-2}$	$-1.3 \cdot 10^{-1}$	$-5.2 \cdot 10^{-2}$	$5.3 \cdot 10^{-2}$	$9.4 \cdot 10^{-3}$	$-1.3 \cdot 10^{-1}$	$-1.5 \cdot 10^{-1}$	$1.5 \cdot 10^{-2}$	$9.9 \cdot 10^{-2}$
11	$6.1 \cdot 10^{-2}$	$-6.2 \cdot 10^{-2}$	$-1.9 \cdot 10^{-1}$	$-3.0 \cdot 10^{-1}$	$-3.6 \cdot 10^{-1}$	$-3.9 \cdot 10^{-1}$	$-3.5 \cdot 10^{-1}$	$-2.9 \cdot 10^{-1}$	$-2.0 \cdot 10^{-1}$	$-1.0 \cdot 10^{-1}$
12	$1.8 \cdot 10^{-1}$	$1.8 \cdot 10^{-1}$	$2.1 \cdot 10^{-1}$	$1.7 \cdot 10^{-1}$	$2.2 \cdot 10^{-1}$	$2.2 \cdot 10^{-1}$	$2.2 \cdot 10^{-1}$	$2.9 \cdot 10^{-1}$	$2.7 \cdot 10^{-1}$	$3.3 \cdot 10^{-1}$
13	$4.3 \cdot 10^{-1}$	$6.3 \cdot 10^{-2}$	$-3.5 \cdot 10^{-1}$	$4.4 \cdot 10^{-1}$	$3.8 \cdot 10^{-2}$	$-3.5 \cdot 10^{-1}$	$4.4 \cdot 10^{-1}$	$3.2 \cdot 10^{-2}$	$-3.5 \cdot 10^{-1}$	$4.6 \cdot 10^{-1}$

4.6 Discussions and Conclusions

In this chapter different approaches of nonlinear system identification have been explored with the aim of obtaining a dynamic model of nonlinear heat source. In this modeling approach, a dynamic model is constructed using only the input-output data set that may be generated from an unsteady CFD computation or obtained from experiment. This affords flexibility for the formulation of the heat source model (refer to “Discussions and Conclusions” section of the “Linear System Identification” chapter).

Nonlinear system identification problem is interpreted as a general nonlinear functional (function of the past inputs and past outputs) approximation. In the first step of the identification, a suitable excitation signal is chosen in order to excite all relevant modes as well as amplitudes of interest. A broadband signal with high amplitude, a chirp signal with varying amplitudes and a multi-level signal are used for the excitation signal. A priori knowledge of the approximate time lag of the system is useful, but this information could be obtained as a black-box approach as well. The number of past inputs and outputs that should be retained in the model is then selected according to the time step of the simulation and time lag of the system. Laminar premixed flame has large delay time compared to wire in pulsating flow. This makes the nonlinear identification of the premixed flame challenging when large ranges of operating conditions (frequencies and amplitudes) are considered as it has been shown in section 4.4 of this chapter.

Another issue is whether the full thermo-acoustic system is simulated in time domain or frequency domain. In the former case, equation error type model structures are useless since they require actual outputs for the set of regressor. Output error models, which make use of outputs from the model, may lead to instability and typical problems of the nonlinear optimization as discussed in section 4.2. First, an equation error type model (one step ahead prediction) for a parametrization of the input-output modeling with the polynomials up to second order is considered. The approach is extended into the frequency domain with two different approaches; with a harmonic balance approach and a harmonic probing approach, which provides the nonlinear transfer function

and higher order transfer function of the heat source. In the former case, a system of equations for the coefficients of the harmonic ansatz, and in the latter case, a recursive relation to compute the higher order transfer functions is obtained. The latter approach is computationally inefficient when the computation of the transfer functions with order more than four is considered. But generally, a few higher order transfer functions are sufficient to get convergence in the response. These nonlinear transfer functions are used for the full thermo-acoustic system modeling in frequency domain, i.e. in a sinusoidal describing function approach.

On the other hand, universal approximation capabilities of the neural networks can be used to capture the nonlinearity in the response of the heat source. Neural networks can approximate any nonlinearity up to a desired degree of accuracy with layered structures using activation functions like sigmoid. A polynomial type representation is obtained with the help of neural networks either by using polynomials as activation functions or approximating the sigmoid with polynomials around the bias term. This type of representation (polynomial type input-output) of the nonlinearity in the heat source response has greater advantages when it is considered to be extended into frequency domain. The identified heat source with neural network is also used in the time domain simulation of thermo-acoustic system.

Fuzzy based identification has shown to be used for general functional approximation and can also be used to obtain nonlinear dynamic models from the observation of the input-output data set. They give a transparent representation of the nonlinearity, and the input-output is stated with linguistic interpretation in terms of rules.

In this chapter, various nonlinear identification methods have been considered. Most of the procedures have similar steps (input signal design, minimization of the cost function, and validation) and they differ only in approximating the functional representation with regressors. Nonlinearities are diverse, and obtaining a dynamic model using only the input-output data set is generally a challenging task. It requires much trial (optimum excitation signals, selection of the memory lengths and common problems of nonlinear optimization) and error efforts. In time domain, one can start with general

function approximations like fuzzy models and neural networks. To get the nonlinear transfer function of the heat source from the identification, extension of the polynomial type equation error models into frequency domain is considered. This has the advantage of requiring a smaller number of regressors and fast convergence rates for the nonlinear optimization problem (refer to section 4.3 for the harmonic probing and harmonic balance approach). Higher order transfer functions, which are the extension of the linear transfer functions to the nonlinear regime, may be computed economically by extending the neural network into frequency domain (refer to section 4.4). This then serves as a basis for the system modeling strategy with coupled modes in the frequency domain. In the previous studies for modeling approaches of the full thermo-acoustic systems, sinusoidal describing function was the only method considered in the frequency domain, since an adequate representation of the nonlinear heat source in the frequency domain was not available. Using the concept of higher order transfer functions, system modeling that also allows to consider the modal coupling is possible (refer to the section “Frequency Domain System Model with Coupled Modes” of the chapter “Prediction and Analysis of Thermo-Acoustic Limit Cycles”).

5 Low Order Model of the Heat Source with POD

Obtaining a nonlinear dynamic model from system identification (refer to “Nonlinear System Identification” chapter) is a challenging task since the functional form of the approximation, the number of regressors that should be retained in the model structure, optimum initial conditions and local minimum problems of nonlinear optimization are unknown. Creation of dynamic models from nonlinear system identification generally requires considerable trial and error. On the other hand, using governing equations of the system to obtain a nonlinear low order model of the system could be an alternative to nonlinear system identification. In this approach, system variables (velocities, temperature) are expressed as superposition of basis functions which constitute a complete set of basis. Basis functions satisfy the orthogonality condition, and different basis, such as Lagrange and Fourier, can be used. Proper Orthogonal Decomposition (POD) technique provides basis functions (POD modes) that are optimal in the sense that the energy is captured with the least number of modes. Low order models of the system can be obtained by projecting the governing system equations onto the POD basis.

POD is widely used in capturing the coherent structures in turbulent flow [15,125]. It has statistical basis and is equivalent to principal component analysis and the Karhunen-Loeve method used in statistics. The equivalence of singular value decomposition, principal component analysis and Karhunen-Loeve decomposition has been discussed by Wu et al. [140]. Reduced order models for the flow past bluff bodies have been obtained by POD. The interesting features of these flow types have been successfully captured by POD [34,51,85].

The application of POD to heat transfer problems has been rarely studied.

Hasan and Sanghi [58] performed POD analysis of 2D flow in a thermally driven rotating cylinder and obtained a reduced order model. A hybrid approach was utilized to estimate the flow field for an intermediate Reynolds number using the hybrid POD modes. Huang and Baumann [63] have obtained a low order model of the laminar premixed flame heat source and coupled this model with system acoustics to get the amplitude of the limit cycle oscillation.

Our aim in this chapter is to obtain a nonlinear dynamic model of the heat source with POD. The incompressible Navier-Stokes equation along with the energy equation are used as the governing system equations. The aim is to obtain a heat source model valid for a range of operating conditions, which include amplitudes and frequencies of the flow pulsating velocity. A multivariate approach, which collects data from different databases, is utilized to describe the dynamics within the desired range of amplitudes and frequencies. The forcing at the inlet (fluctuating part of the velocity) is introduced explicitly in the ordinary differential equations (ODE) of the low order model. The non-vanishing pressure term resulting from the incompressible Navier-Stokes equation is included using a calibration technique [51]. This nonlinear heat source model can be used to predict the limit cycle oscillations for the full coupled thermo-acoustic system in time domain. Nonlinear transfer function can also be calculated from this low order model. A flow chart of the proposed approach is shown in Fig. 5.1.

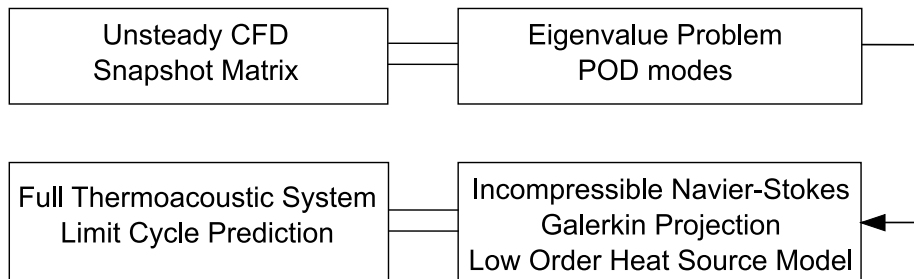


Figure 5.1: Flow chart of the approach to obtain a low order model of the heat source

5.1 Low Order Model with Proper Orthogonal Decomposition

5.1.1 Computing POD Modes

An ensemble of data, either from numerical simulations or experiments, can be expressed in terms of a reduced order basis. The data set is projected onto the new basis, and the difference between the original data and the projected data is minimized in a least square sense.

A data set obtained from unsteady CFD calculations is denoted by q . It is then expanded in terms of basis functions as,

$$q_j = \sum a_{ji} \Phi_i, \quad j = 1, 2, \dots, M, \quad i = 1, 2, \dots, N, \quad (5.1)$$

where j is the time index and i is the index for the mode number truncated at N . The modes are then calculated by minimizing the distance between the original data and approximated (projected) data [78],

$$\|q - \text{Proj}(q)\| \rightarrow \min. \quad (5.2)$$

This is equivalent to maximizing the inner product of ensemble average, normalized by the inner product of the basis vectors [78],

$$\langle q, \Phi \rangle / \langle \Phi, \Phi \rangle \rightarrow \max. \quad (5.3)$$

For two vector field variables \vec{a} and \vec{b} , the inner product is defined as the integration of the scalar product of the variables over the domain Ω ,

$$\langle \vec{a}, \vec{b} \rangle = \int_{\Omega} \left(\sum_{i=1}^3 a_i b_i \right) d\Omega. \quad (5.4)$$

The expression in Eq.(5.3) is then reformulated as an integral eigenvalue problem. The integral is Fredholm integral of 1st type,

$$\int_{\Omega} \langle q(x) \otimes q(x') \rangle \Phi(x') dx' = \lambda \Phi(x). \quad (5.5)$$

The first integrand is the autocorrelation tensor. This integral can either be solved numerically or by using singular value decomposition. The first mode

captures the greatest fraction of the energy, and the second mode gets the second greatest portion of energy. This energy is associated with the norm that is defined, and is not necessarily the energy of the system under investigation.

The POD expansion is generally used for the fluctuating part of the variables, but when the total values (sum of the fluctuating and the mean values) are expressed as expansion of POD modes, the first mode shows the mean of the field variables. POD can be used as scalar or vectorial mode. In the scalar mode, the number of ordinary differential equations after projection increases by a factor of the number of field variables used in the POD expansion. However, vectorial POD modes show good long term behavior compared to the scalar POD modes [118].

5.1.2 Galerkin Projection

Velocities and temperature are expressed in terms of vectorial modes as,

$$[u(\vec{x}, t), v(\vec{x}, t), T(\vec{x}, t)] = \sum_{k=1}^N a_k(t) [\phi_k^u(\vec{x}), \phi_k^v(\vec{x}), \phi_k^T(\vec{x})]. \quad (5.6)$$

(The velocities and the temperature are nondimensionalised, refer to the governing equations of the heated plate in “Transient Simulation of the Heat Source” chapter.) Substitution in the incompressible Navier-Stokes and energy equations yields,

$$\begin{aligned} & \sum_{k=1}^N \frac{da_k}{dt} [\phi_k^u, \phi_k^v, \phi_k^T] = \\ & \sum_{k=1}^N a_k \left[\frac{\partial^2 \phi_k^u}{\partial x^2} + \frac{\partial^2 \phi_k^u}{\partial y^2}, \frac{\partial^2 \phi_k^v}{\partial x^2} + \frac{\partial^2 \phi_k^v}{\partial y^2}, \frac{1}{\text{Pr}} \left(\frac{\partial^2 \phi_k^T}{\partial x^2} + \frac{\partial^2 \phi_k^T}{\partial y^2} \right) \right] \\ & + \sum_{k=1}^N \sum_{l=1}^N a_k a_l \left[-\phi_k^u \frac{\partial \phi_l^u}{\partial x} - \phi_k^v \frac{\partial \phi_l^u}{\partial y}, -\phi_k^u \frac{\partial \phi_l^v}{\partial x} - \phi_k^v \frac{\partial \phi_l^v}{\partial y}, -\phi_k^u \frac{\partial \phi_l^T}{\partial x} - \phi_k^v \frac{\partial \phi_l^T}{\partial y} \right] \\ & + \left[\frac{-\partial p(\vec{x}, t)}{\partial x}, -\frac{\partial p(\vec{x}, t)}{\partial y}, 0 \right], \end{aligned} \quad (5.7)$$

where the coefficients $a(t)$ depend only on time t , while the modal functions $\phi(\vec{x})$ depend only on spatial coordinates \vec{x} .

Using the orthogonality of the POD modes, namely

$$\int_{\Omega} \phi_k \phi_l d\Omega = \delta_{kl}, \quad (5.8)$$

where δ_{kl} represents the Kronecker delta function, the reduced order model is obtained as

$$\begin{aligned} \dot{a}_m(t) = & \sum_{k=1}^N \frac{a_k(t)}{\text{Re}} \langle M_k^{(2)}(\vec{x}), R_m(\vec{x}) \rangle \\ & + \sum_{k=1}^N \sum_{l=1}^N a_k(t) a_l(t) \langle M_{kl}^{(1)}(\vec{x}), R_m(\vec{x}) \rangle + \langle -\nabla p(\vec{x}, t), S_m(\vec{x}) \rangle, \end{aligned} \quad (5.9)$$

where functions $R(\vec{x})$, $S(\vec{x})$ and $M^{(i)}(\vec{x})$ are defined as,

$$\begin{aligned} R_m &= [\phi_m^u, \phi_m^v, \phi_m^T], \\ S_m &= [\phi_m^u, \phi_m^v], \\ M_{kl}^{(1)} &= \left[-\phi_k^u \frac{\partial \phi_l^u}{\partial x} - \phi_k^v \frac{\partial \phi_l^u}{\partial y}, -\phi_k^u \frac{\partial \phi_l^v}{\partial x} - \phi_k^v \frac{\partial \phi_l^v}{\partial y}, -\phi_k^u \frac{\partial \phi_l^T}{\partial x} - \phi_k^v \frac{\partial \phi_l^T}{\partial y} \right], \\ M_k^{(2)} &= \left[\frac{\partial^2 \phi_k^u}{\partial x^2} + \frac{\partial^2 \phi_k^u}{\partial y^2}, \frac{\partial^2 \phi_k^v}{\partial x^2} + \frac{\partial^2 \phi_k^v}{\partial y^2}, \frac{1}{\text{Pr}} \left(\frac{\partial^2 \phi_k^T}{\partial x^2} + \frac{\partial^2 \phi_k^T}{\partial y^2} \right) \right]. \end{aligned}$$

For clarity of notation, \vec{x} -dependencies are not shown explicitly in the above equations.

5.1.3 Incorporating the term related to the pressure

The formulation for the low order model in Eq. (5.9) has an inner product related to the pressure,

$$\begin{aligned} \langle \nabla p(\vec{x}, t), S_m(\vec{x}) \rangle &= \int_{\Omega} (\nabla p(\vec{x}, t)) \cdot S_m(\vec{x}) d\Omega = \\ &= \int_{\Omega} \nabla \cdot (p(\vec{x}) S_m(\vec{x})) d\Omega - \int_{\Omega} p(\vec{x}) \nabla \cdot S_m(\vec{x}) d\Omega = \int_{\Gamma} p(\vec{x}, t) S_m(\vec{x}) \vec{n} d\Omega, \end{aligned} \quad (5.10)$$

where \vec{n} is outward normal vector. The above relation is obtained from Green's theorem and divergence free properties of the POD modes. The only contribution is from the boundaries. At the inlet and side boundaries there is contribution from pressure, and this inner product does not vanish. Different approaches are available to include this non-vanishing term. Noack et al. [95] utilized the pressure-Poisson equation, in which the inner product results in additional quadratic terms in the Galerkin low order model. An analytical procedure to compute the resulting contribution was presented. In an alternative approach, Noack et al. [95] utilized an empirical pressure model which uses the following linear form,

$$\langle -\nabla p(\vec{x}, t), S_m(\vec{x}) \rangle = \sum_{k=1}^N a_k(t) C_{km}. \quad (5.11)$$

Based on the information for the evolution coefficients, which is obtained from the projection of the data onto the modes and the time dependent values of the pressure on the chosen grid points, a system of equation will be set to compute the C coefficients. The above equation for pressure snapshots results in an overdetermined system of equations for the C coefficients since the number of modes retained in the model is much less than the number of snapshots. In another approach proposed by Galletti et al. [51], the same linear relation in Eq. (5.11) is assumed for the inner product. However, to find the coefficients, an optimization problem is proposed. We use the approach of Galletti et al. in this study. The reference values of the evolution coefficients are obtained by projecting the snapshot data onto the POD modes.

$$\tilde{a}_k(t_i) = \langle \text{Snapshot}(\vec{x}, t_i), \phi_k(\vec{x}) \rangle, \quad (5.12)$$

where k is an index related to the mode number and i is the time index. The optimization problem is constructed by finding the minimum of

$$V = \sum_{m=1}^M \sum_{k=1}^N (\dot{\tilde{a}}_k(t_m) - \dot{a}_k(t_m))^2 \rightarrow \min. \quad (5.13)$$



Figure 5.2: Domain decomposition into the inlet boundary domain and the inner domain for the integral computation resulting from the inner products for a discrete case

5.1.4 Incorporating the Inlet Boundary Condition

On incorporating the inner product related to the pressure gradient, the reduced order model becomes,

$$\dot{a}_m(t) = \sum_{k=1}^N \frac{a_k(t)}{\text{Re}} \langle M_k^{(2)}(\vec{x}), R_m(\vec{x}) \rangle + \sum_{k=1}^N \sum_{l=1}^N a_k(t) a_l(t) \langle M_{kl}^{(1)}(\vec{x}), R_m(\vec{x}) \rangle + a_k(t) C_{km}. \quad (5.14)$$

Based on Fig. 5.1, the main aim is to obtain the input-output relation, where the input corresponds to different amplitudes and frequencies, and the output is the evolution coefficient of the temperature modes. The structure of the Eq. (5.14) does not provide any useful information, since this relation is included implicitly. The structure can be rearranged to obtain the effect of input in the reduced order model with an approach proposed by Efe [41], and Efe and Özbay [42].

For a discrete case, the decomposition of the domain is shown in Fig. 5.2 with the inlet boundary and inner domain. The total domain D can be written as a sum of the sections Γ_1 , Γ_2 , and Γ_h . The inlet is composed of the grid points which are located at the midpoint of section Γ_1 along the vertical axis.

$$D \rightarrow \text{Domain}, \quad N \rightarrow \text{Inner Domain}, \quad \Gamma_1 \rightarrow \text{Inlet}, \quad D/\Gamma_1 = N, \Gamma_1 \cup \Gamma_2 \dots \cup \Gamma_h = D.$$

The inner product over the domain can be written as a sum of inner products

over the inlet boundary and inner domain.

$$\langle a, b \rangle_D = \int_D ab dD = \sum_{i=1}^h \int_{\Gamma_i} ab d\Gamma_i = \int_{\Gamma_1} ab d\Gamma_1 + \sum_{i=2}^h \int_{\Gamma_i} ab d\Gamma_i = \langle a, b \rangle_{\Gamma_1} + \langle a, b \rangle_N. \quad (5.15)$$

The forcing condition at the inlet is expressed as,

$$f(t) = \sum_{k=1}^N a_k(t) R_k(\vec{x})_{\Gamma_1}. \quad (5.16)$$

This then can be written as,

$$a_m(t) R(m)_B = f(t) - \sum_{k \neq m}^N a_k(t) R_k(\vec{x})_{\Gamma_1}. \quad (5.17)$$

Expressing the low order model as a sum of the inlet boundary and the inner domain yields,

$$\dot{a}_m(t) = \frac{1}{\text{Re}} \sum_{k=1}^N a_k(t) \langle M_k^{(2)}(\vec{x}), R_m(\vec{x}) \rangle_{\Gamma_1} + \sum_{k=1}^N \sum_{l=1}^N a_k(t) a_l(t) \langle M_{kl}^{(1)}(\vec{x}), R_m(\vec{x}) \rangle_{\Gamma_1}. \quad (5.18)$$

This further can be written as,

$$\begin{aligned} \dot{a}_m(t) &= \frac{a_m(t)}{\text{Re}} \langle M_m^{(2)}(\vec{x}), R_m(\vec{x}) \rangle_{\Gamma_1} + \sum_{k \neq m}^N \frac{a_k(t)}{\text{Re}} \langle M_k^{(2)}(\vec{x}), R_m(\vec{x}) \rangle_N \\ &\quad + \sum_{k=1}^N \sum_{l=1}^N a_k(t) a_l(t) \langle M_{kl}^{(1)}(\vec{x}), R_m(\vec{x}) \rangle_{\Gamma_1} + \frac{1}{\text{Re}} \sum_{k=1}^N a_k(t) \langle M_k^{(2)}(\vec{x}), R_m(\vec{x}) \rangle_N \\ &\quad + \sum_{k=1}^N \sum_{l=1}^N a_k(t) a_l(t) \langle M_{kl}^{(1)}(\vec{x}), R_m(\vec{x}) \rangle_N + \sum_{k=1}^N a_k(t) C_{km}. \end{aligned} \quad (5.19)$$

The first inner product over the inlet boundary in Eq. (5.19) can be written as,

$$\frac{a_m(t)}{\text{Re}} \langle M_m^{(2)}(\vec{x}), R_m(\vec{x}) \rangle_{\Gamma_1} = \left\langle \frac{M_m^{(2)}(\vec{x})}{\text{Re}}, f(t) \right\rangle_{\Gamma_1} - \sum_{k=m}^N \frac{a_k(t)}{\text{Re}} \langle M_m^{(2)}(\vec{x}), R_k(\vec{x}) \rangle_{\Gamma_1}. \quad (5.20)$$

Substituting Eq. (5.20) in Eq. (5.19) yields,

$$\dot{a}_m(t) = \left\langle \frac{M_m^{(2)}(\vec{x})}{\text{Re}}, f(t) \right\rangle_{\Gamma_1} + \sum_{k=1}^N \frac{a_k(t)}{\text{Re}} (\langle M_k^{(2)}(\vec{x}), R_m(\vec{x}) \rangle_D - \langle M_m^{(2)}(\vec{x}), R_k(\vec{x}) \rangle_{\Gamma_1}). \quad (5.21)$$

The second inner product over the inlet boundary in Eq. (5.18) can be expressed as,

$$\begin{aligned} \sum_{k=1}^N \sum_{l=1}^N a_k(t) a_l(t) \langle M_{kl}^{(1)}(\vec{x}), R_m(\vec{x}) \rangle_{\Gamma_1} &= \sum_{k=1}^N \sum_{l=1}^N a_k(t) a_l(t) \langle -\phi_k^u(\vec{x}) \frac{\partial \phi_l^u(\vec{x})}{\partial x}, \phi_m^u(\vec{x}) \rangle_{\Gamma_1} \\ &= f(t) \sum_{l=1}^N a_l(t) \langle \frac{\partial \phi_l^u(\vec{x})}{\partial x}, \phi_m^u(\vec{x}) \rangle_{\Gamma_1}. \end{aligned} \quad (5.22)$$

The final form of the reduced order model with the dynamic boundary condition incorporated at the inlet is,

$$\begin{aligned} \dot{a}_m(t) = \frac{f(t)}{\text{Re}} \langle M_m^{(2)}(\vec{x}), 1 \rangle_{\Gamma_1} &+ \frac{1}{\text{Re}} \sum_{k=1}^N a_k(t) (\langle M_k^{(2)}(\vec{x}), R_m(\vec{x}) \rangle_D - \langle M_m^{(2)}(\vec{x}), R_k(\vec{x}) \rangle_{\Gamma_1}) \\ &+ f(t) \sum_{l=1}^N a_l(t) \langle \frac{\partial \phi_l^u(\vec{x})}{\partial x}, \phi_m^u(\vec{x}) \rangle_{\Gamma_1} + \sum_{k=1}^N a_k(t) C_{km} \\ &+ \sum_{k=1}^N \sum_{l=1}^N a_k(t) a_l(t) \langle M_{kl}^{(1)}(\vec{x}), R_m(\vec{x}) \rangle_N. \end{aligned} \quad (5.23)$$

5.1.5 Multivariate Approach

To construct a low order model for the heat source that can be used over a range of amplitudes and frequencies, the snapshots from the different databases are taken and the multivariate modes are calculated from this data set. In the multivariate model, the aim is to predict the response of the system using POD modes, such that a system limit cycle can be computed with frequencies and amplitudes that are not known a priori. The intermediate values for the calibration matrices C are obtained by applying a Lagrange interpolation. In the first case three different A (0.3, 1 and 2) at a fixed $\text{Str} = 10$ is considered. The validation case is for $A = 1.2$ at $\text{Str} = 10$. In the next case three different Str (10, 17.5 and 25) at a fixed $A = 2$ is considered. The validation case is chosen at $A = 2$ and at $\text{Str} = 15$. The number of modes considered for these two cases is 10. As the next case, three different A (0.3, 1 and 2) and three different Str (15, 17.5, and 25) are considered. For the calibration matrices C , a two dimensional Lagrange interpolation is used. The test case is chosen as

$A = 1.2$ and $Str = 20$. In this test case, the first 15 POD modes are taken into account. Finally a low order model with 15 POD modes is constructed between A in the range of 0.3-3.5, and Str in the range of 45-75 (which covers the fundamental frequency of the limit cycle for a tube of 1 m length with open-open boundary conditions) taking into account 18 unsteady CFD calculations. The case $A = 0.3$ is chosen as the limit of the linear regime for the forcing, since the amplitude of the second harmonic peak in an FFT diagram reaches less than 5% of the fundamental harmonic.

5.2 Results

5.2.1 POD modes and eigenspectra at single harmonic excitation

First, a sinusoidal excitation at $Str = 10$ and $A = 2$ is considered. The POD modes are computed with the singular value decomposition of the snapshot matrix, which is obtained from the computational field for the two velocity components and temperature. The grid size for the data extraction is 100 points along the y -axis, and 200 points along the x -axis (parallel to the heated section).

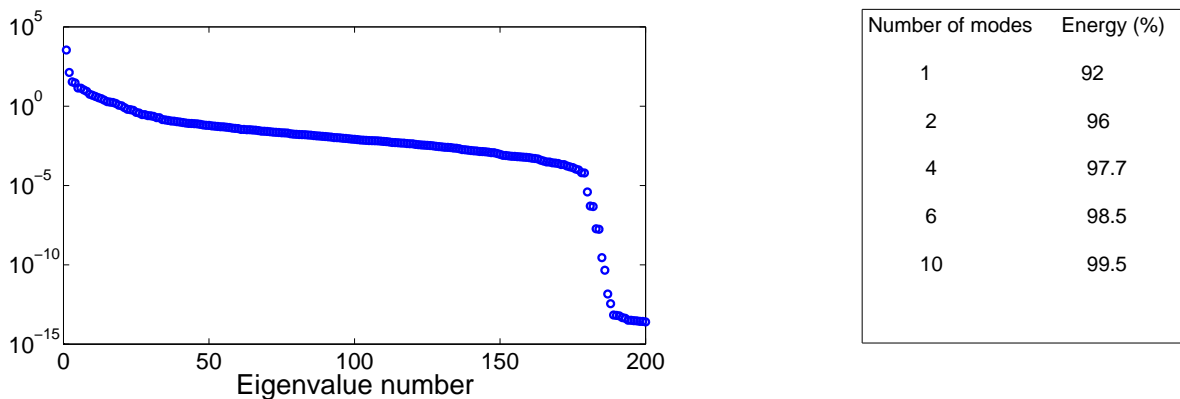


Figure 5.3: Eigenspectra on a semi-logarithmic scale for $Str = 10$ and $A = 2$

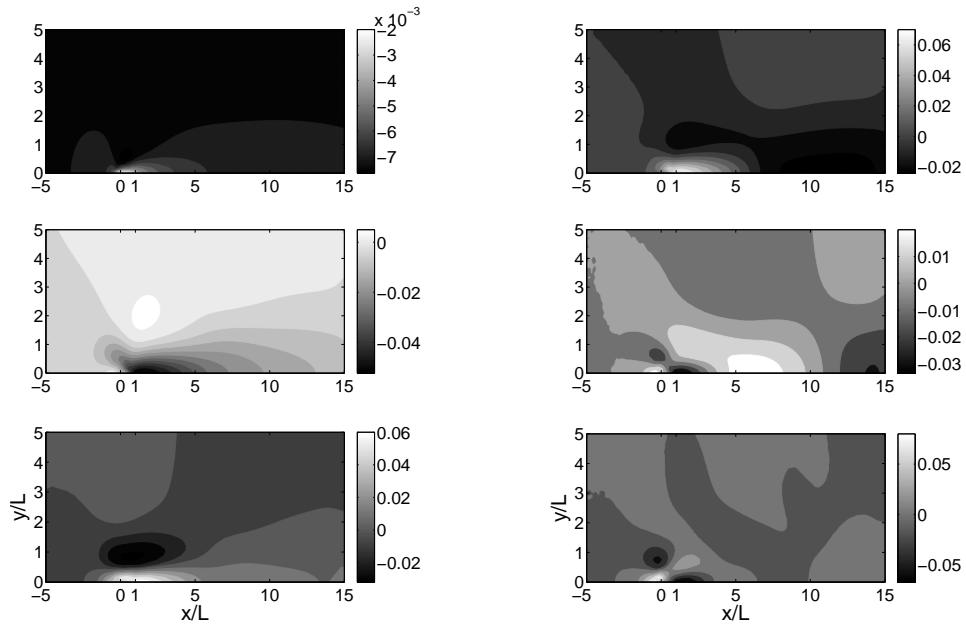
Fig. 5.3 shows the eigenvalues, which represent the energy level captured by each of the POD modes on a semi-logarithmic scale. The energy levels for each of the modes are represented in a hierarchical way. The first ten modes capture 99.5% of the energy associated with the selected inner product.

Figure 5.4(a) and Figure 5.4(b) show the first six POD modes for the u velocity component and temperature along with the heated flat section (between coordinates 0 and 1 along the horizontal direction), respectively. The first mode gives the mean value, as the mean values have not been subtracted from the ensemble a priori. The higher modes develop into smaller scales with less energy. In our case, the smaller scales represent the nonlinear effects, while the linear effects are captured by the first few modes. Evolution coefficients for the POD modes, which are obtained by the projection of the data on the POD modes for $Str = 10$, at $A = 0.3$ and $A = 2$, are shown in Fig. 5.2.1. These coefficients will be used as the reference values when constructing the low order model after the projection of the governing system equations onto the POD basis which has been discussed in the previous sections. The sixth and seventh coefficients for $A = 2$ have higher frequencies compared to $A = 0.3$, which is an indication of the nonlinearity.

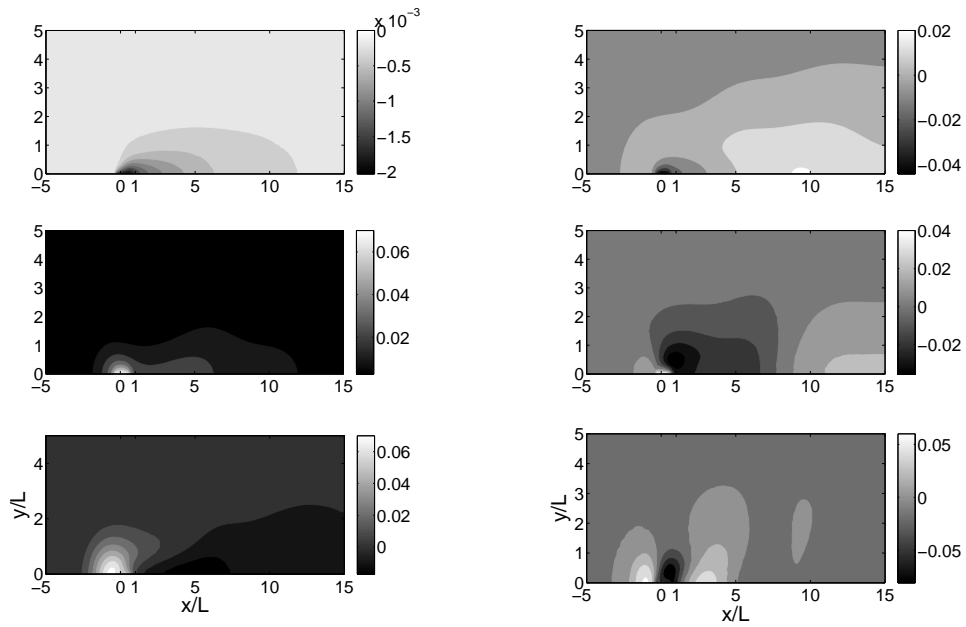
5.2.2 Mono-variate model: constant amplitude or constant frequency

In the mono-variate approach, only one parameter, i.e. either amplitude or frequency of the forcing at the inlet, of the low order model is changed in Eq. (5.23). The POD modes are computed from the singular value decomposition of the snapshot matrix that is taken either for a range of frequencies or amplitudes from the unsteady CFD computations. For any frequency or amplitude within the range considered, the field variables can be represented as a superposition of these POD modes.

First, for the snapshot matrix, while $A = 2$, three different Str (10, 17.5 and 25) are considered. Figure 5.6(a) shows the evolution coefficients for the six POD modes obtained with POD based low order model (POD/LOM) and from the unsteady CFD calculations for $Str = 15$. Next, for the snapshot matrix, Str is kept constant at 10, and three different A (0.3, 1 and 2) are considered. As the



(a) U-Velocity Modes



(b) Temperature Modes

Figure 5.4: First six POD modes for U-Velocity and Temperature (left 1-3-5, right 2-4-6). The heat source is located between the coordinates 0 and 1 along the horizontal direction

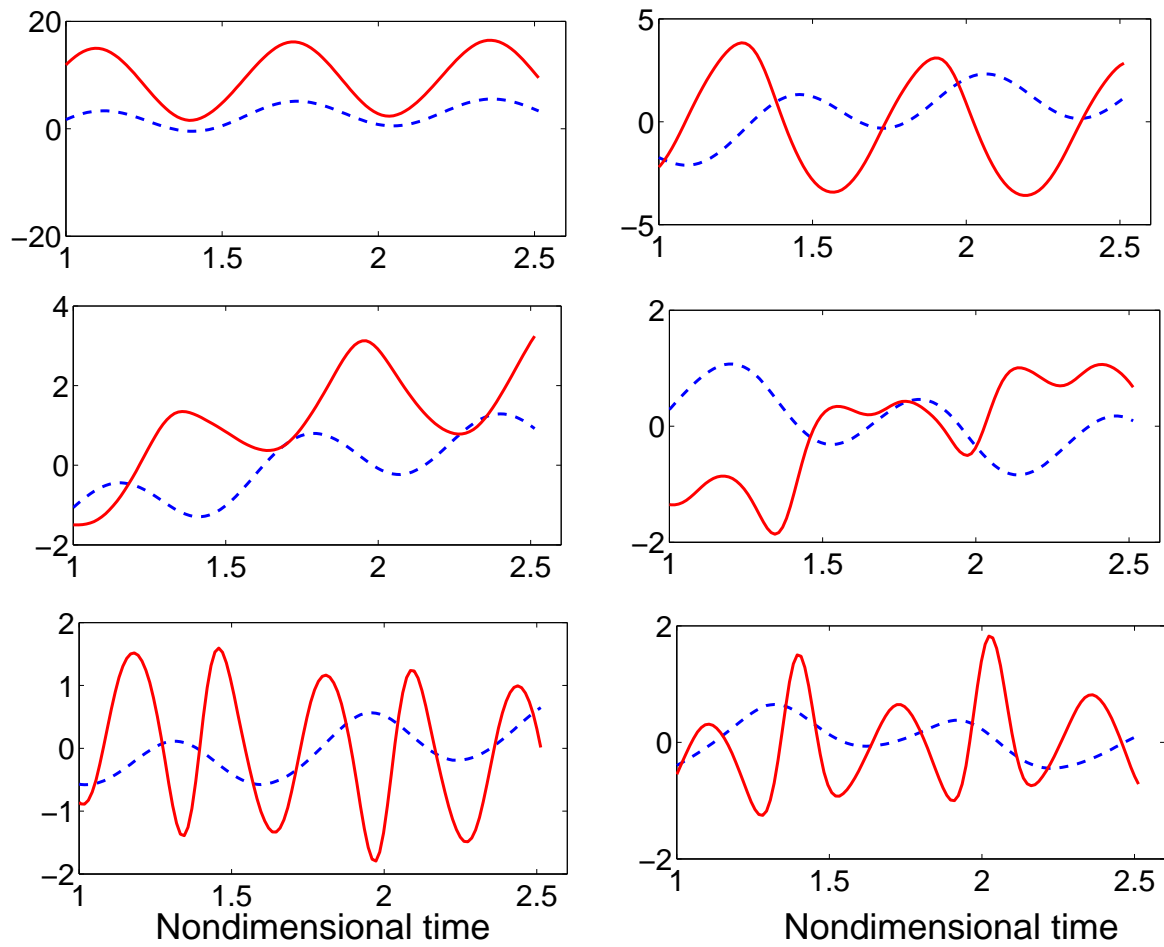
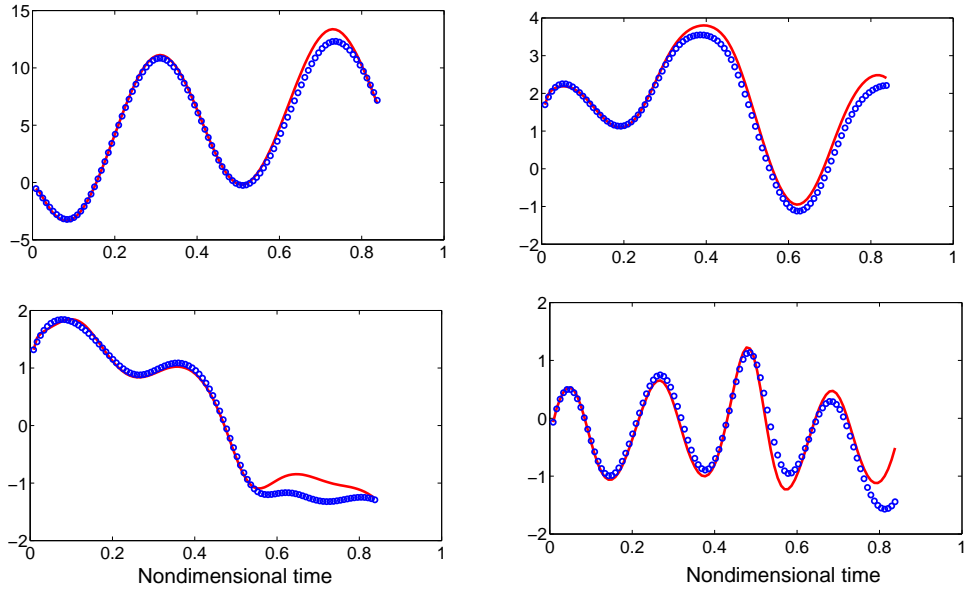
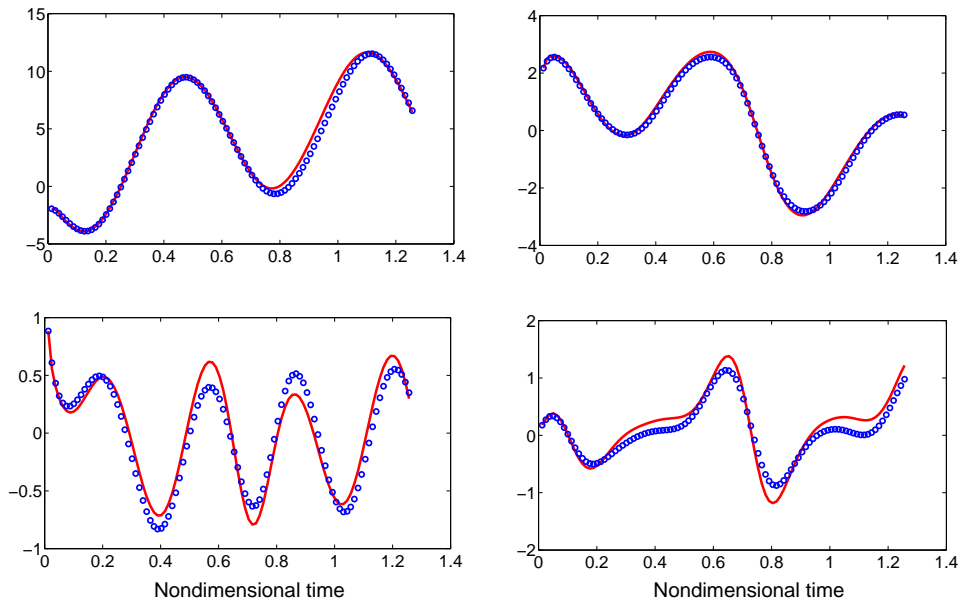


Figure 5.5: Evolution coefficients at Strouhal number 10 and for $A = 0.3$ (dashed lines) and $A = 2$ (continuous lines). On the left for 2-4-6th POD modes, and on the right for 3-5-7th POD modes



(a) Mono-variate model at constant A , $Str = 15$



(b) Mono-variate model at constant Str , $A = 1.2$

Figure 5.6: Evolution coefficients (left: 2, 5 right: 3, 7) with CFD (continuous line) and with POD/LOM (circles)

validation case, for $A = 1.2$, the evolution coefficients of the six POD modes are compared in Fig. 5.6(b) from the CFD (projected data onto POD basis) and the POD based low order model (model described in Eq. (5.23)). In both these cases (constant amplitude or constant frequency), the number of modes considered in the low order model is 10. Considering 15 modes leads to instability in the ODEs describing the evolution coefficients.

5.2.3 Bivariate model for a range of amplitudes and frequencies

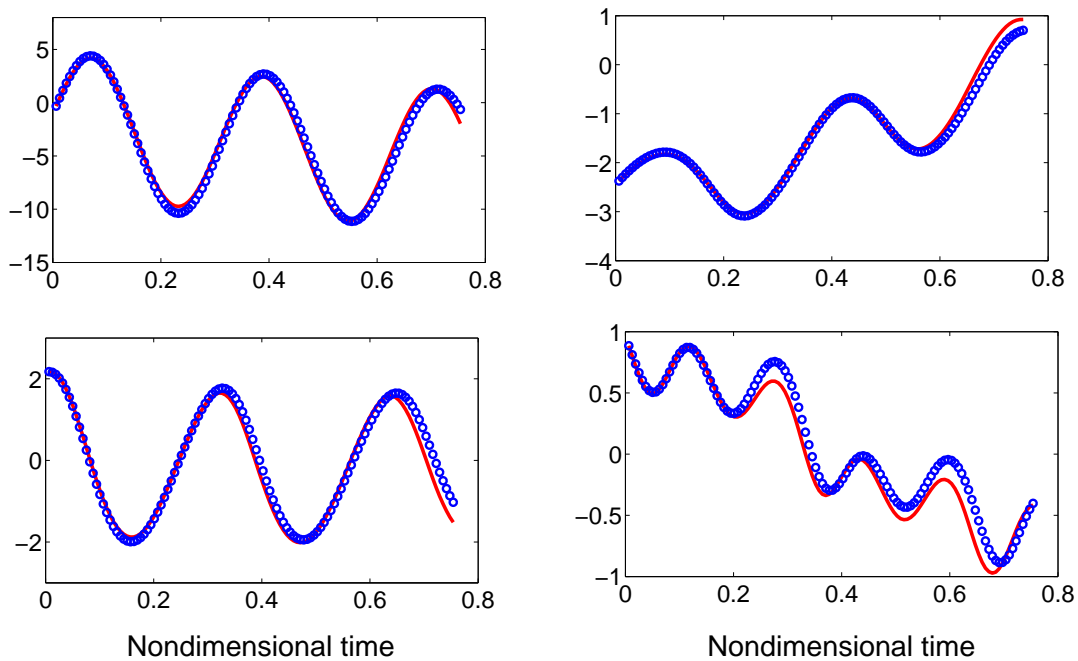


Figure 5.7: Evolution coefficients (left: 2, 4 right: 3, 6) at $A = 1.2$, and $Str = 20$ with CFD (continuous line) and with POD/LOM (circles)

In the bivariate model, both the amplitudes and frequencies of the forcing function at the inlet boundary are changed. In this way a low order model of the heat source that should be valid for a range of frequencies and amplitudes is constructed. The amplitude and the frequency of the forcing considered in the snapshot matrix are chosen as $A = 0.3, 1$, and 2 , and $Str = 10, 17.5$, and 25 . In total, nine different unsteady CFD computations are collected in the data set. Using the POD modes calculated from this snapshot matrix, it should be

possible to express any operating point within this range as the superposition of these modes. The first 15 POD modes are considered for the low order model. It was observed that with an increasing number of modes, the ODEs for the evolution coefficients become unstable especially for higher Strouhal number (above 20). On the other hand, when only the first 10 POD modes are considered, the accuracy in the approximation decreases, especially for high velocity amplitude ratios. The evolution coefficients for a test case at $A = 1.2$ and $\text{Str} = 20$ is shown in Fig. 5.7.

The time domain evolution of any field variable at any location of the computational domain can be written in terms of the expansion with the POD modes after the evolution coefficients are obtained from the low order model. For the temperature, the expansion can be written as,

$$T(x, y, t) = \sum_{k=1}^{15} a_k(t) \Phi_k^T(x, y). \quad (5.24)$$

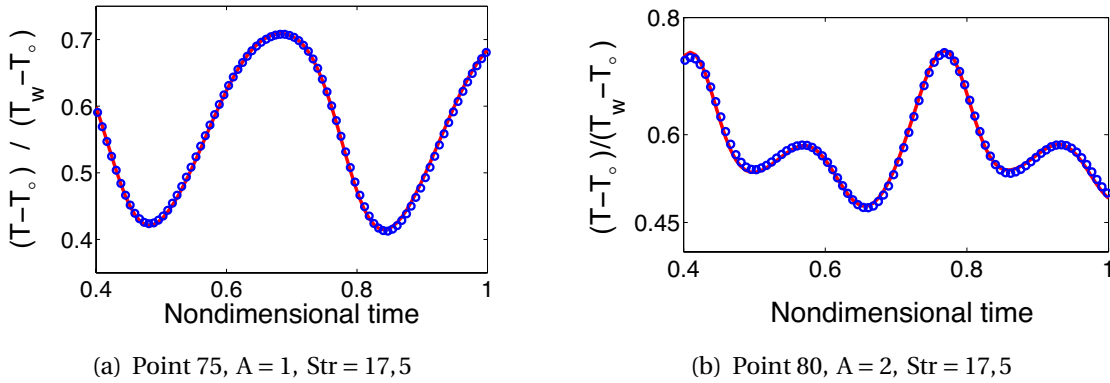


Figure 5.8: Evolution of temperature at two points (located one element length above the heated plate) with CFD (continuous line) and with POD/LOM (circles)

The heat transfer at the wall for a laminar flow is computed by the Fourier's Law,

$$Q_w = -\lambda_f \left. \frac{\partial T}{\partial y} \right|_w = h(T_w - T_\infty), \quad (5.25)$$

where thermal conductivity of the fluid is λ_f , heat transfer coefficient is h and wall normal coordinate is y . In the numerical simulation, the wall heat transfer

is computed with the approximation of the temperature gradient at the wall based on the nearest element to the wall. For small perturbations (amplitude of the unsteady velocity at the inlet), boundary layer equations could also be used to obtain simplified expressions for the unsteady heat transfer rate at the wall [122]. When the perturbation levels are comparable to that of the mean, nonlinear contributions in the boundary layer cannot be neglected further (e.g. nonlinear streaming part) [133]. In this case, a semi-analytical solution is obtained and a part of the problem is solved numerically. In Fig. 5.8(a) and Fig. 5.8(b), the evolution of the temperature is shown for two points along the heated section, just one element length above it. 200 equidistant grid points are considered in the x -direction (parallel to the heated section) for the snapshot matrix, where the heated part corresponds to the points between the 73rd and 83rd grid points.

5.2.4 Nonlinear transfer function of the heat source from low order model

Next, Str in the range of 45 to 75, and A 0.3 to 3.5 are considered. Three Str (45, 60 and 75) values and six A (0.3, 1, 2, 2.5, 3 and 3.5) values are considered. In this case, the limit of the linear regime is taken as $A = 0.3$ since for Str ranges considered, a sinusoid forcing at $A = 0.3$ gives a second harmonic peak which is less than 5% of the fundamental. In total, 18 CFD calculations are collected for the snapshot matrix. All data within this range is expressed as expansion of the POD modes calculated from this data set. The range of the frequency will cover the limit cycle fundamental frequency of an open-open duct of 1 m length. 15 POD modes are considered in the low order model. Figure 5.9 shows the normalized averaged heat transfer rate at the heated section with respect to the steady state value for $A = 2.5$, $A = 3.5$ and $Str = 60$ (left) / $Str = 75$ (right). The nonlinearity in the heat transfer rate, which appears as distortions from a pure sinusoid, is captured with the low order model based on POD with 15 modes. The approximations with 13 and 10 POD modes are also shown in the plots.

Figure 5.10 shows the gain and the phase of the transfer function at $Str = 60$ for the amplitude range considered from the low order model and the CFD.

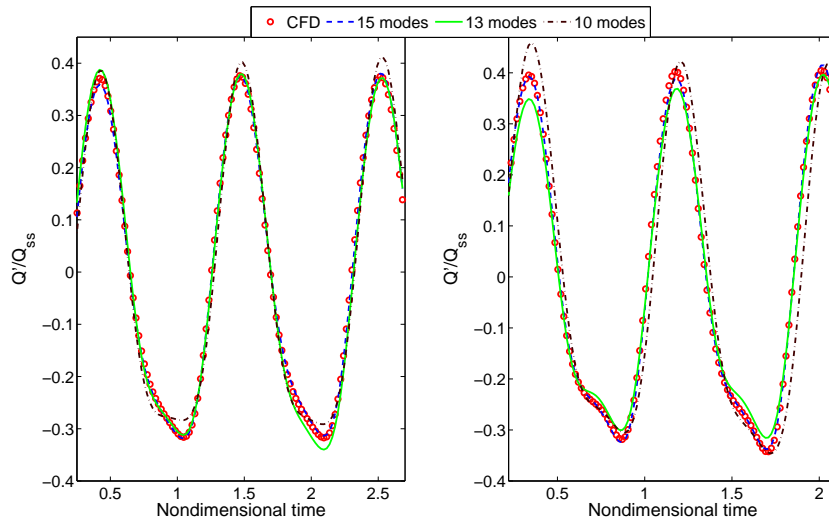


Figure 5.9: Non-dimensionalized (with respect to steady state value) averaged heat transfer rate at the heated section – CFD vs. POD/LOM results. Left: $A = 2.5$, $Str = 60$, Right: $A = 3.5$, $Str = 5$

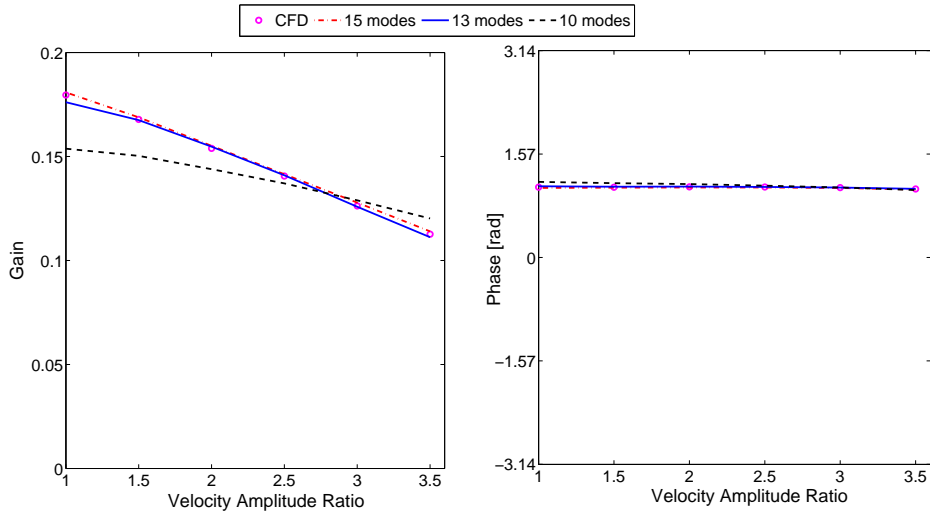


Figure 5.10: Gain and phase of the transfer function for different A at $Str = 60$ with CFD and with POD/LOM of different number of modes

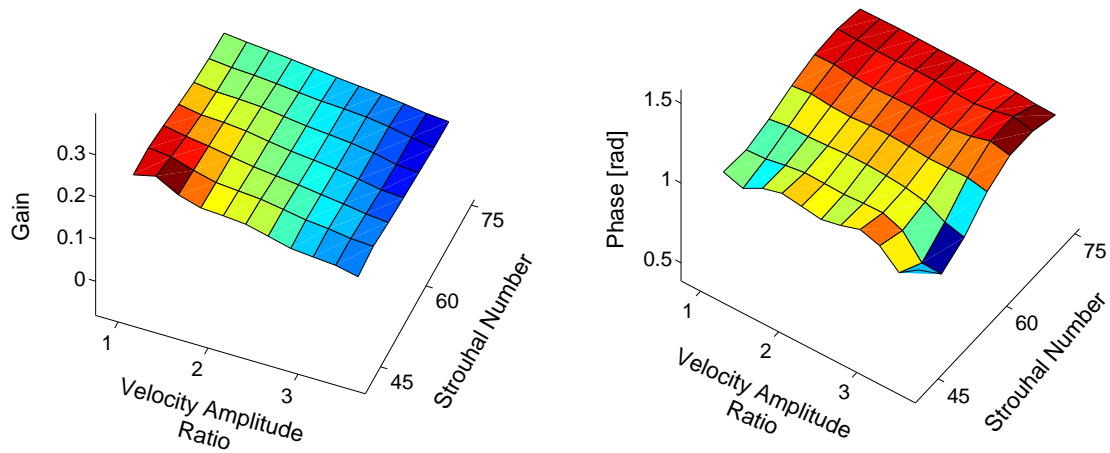


Figure 5.11: Shape of the nonlinearity for gain and phase of the transfer function obtained from POD based low order model

The approximation of the transfer function from the low order models with different number of POD modes is also shown. The accuracy in the gain with the model with 13 modes is comparable to that with 15 modes, whereas it deviates in the phase especially for low amplitudes. A change in length of the heated plate will change the Reynolds number and this may have an effect on the transfer function. Figure 5.11 shows the nonlinear map for the transfer function as a function of Str and A considered within the range obtained from the low order model. This simplified representation of nonlinearity of the heat source could be used in the “sinusoidal describing function” model for a full thermo-acoustic system to predict limit cycle amplitudes [96].

5.3 Discussion and Conclusion

A nonlinear low order model for the heat transfer dynamics of a heated plate in pulsating flow has been obtained with POD technique. POD modes have been used as the basis for the representation of the system variables (velocities and temperature) in the low dimensional space. The snapshot matrix has been constructed from unsteady CFD computations that have been performed for

a range of amplitudes and frequencies. POD modes have been calculated by singular value decomposition of this matrix. Nonlinear dynamic model of the heat source has been obtained by projecting the governing equations of the system (unsteady Navier-Stokes and energy) onto the POD basis. The effect of the pressure term resulting from incompressibility has been included with a calibration method. The desired input (forcing velocity at the inlet) and output (temperature) have been written explicitly in the low order model equations.

It has been observed that ODEs describing the evolution of POD modes may lead to unstable results depending on the number of modes taken (generally for a large number of modes). On the other hand, nonlinearity could not be represented adequately when small number of modes were taken. One may also get unstable results for the long term behavior of the ODEs.

Low order model obtained from POD describes the heat source for the desired range of pulsating amplitudes and frequencies. It could be coupled with the time domain simulation of the full thermo-acoustic system. Alternatively, nonlinear transfer function can be obtained from this low order model.

In this study, data was collected for single sinusoid forcing at different amplitudes and frequencies. The system could be excited with a broadband forcing at high amplitudes, a chirp signal with varying amplitudes or with a multilevel excitation signal to cover the desired range of amplitudes and frequencies. After such an excitation, POD modes were seen to describe the system for the spatial description of the operating range. ODEs of the modal coefficient describe the time dependent part. This then provides a powerful alternative for the nonlinear system identification to get a nonlinear dynamic model of the heat source (refer to “Conclusion and Outlook” section of the “Nonlinear System Identification” chapter).

A very simple geometry was also considered for the sake of simplicity in the numerical processing with POD. More complex geometrical configurations, such as cylinder in pulsating flow, can also be considered. It requires only accurate numerical integration and differentiation resulting from the inner products (as functions of POD modes) on the computational domain. The explicit Re dependence of the equations can be used to include the effect of tur-

bulence. The computations for several Re numbers from a direct numerical simulation can be collected in the snapshot matrices to construct the POD modes. Flow field for an intermediate Re number can be predicted using the low order model equations.

6 Prediction and Analysis of Thermo-Acoustic Limit Cycles

Nonlinear effects of the thermo-acoustic system limit the growth of unstable mode of oscillation and lead to steady state periodic nonlinear oscillations which are called “limit cycle”. If it is not possible to avoid thermo-acoustic instabilities altogether, then it becomes important to predict the amplitude of the nonlinear oscillations. This is required since the detrimental effects of instabilities on the combustor lifetime and noise emissions depend on the limit cycle amplitude.

As discussed in the previous chapters, accurate predictions of the stability limits and limit cycle amplitudes require an adequate heat source model valid in the nonlinear regime, and also a suitable system model. CFD computations of the full thermo-acoustic system could model limit cycle. These computations generally demand huge computational resources and time since thermo-acoustic instabilities involve various physical phenomena covering a wide range of length and time scales [108, 138]. Moreover, the simulations are performed for one set of parameters in one simulation [33]. In the design stage, the limit cycle amplitude dependency on various system parameters has to be checked, which makes the full CFD modeling approach of thermo-acoustic instability unfeasible.

Linearized Navier-Stokes equation yields the inhomogeneous wave equation for pressure fluctuations with a source term, which represents the heat release rate from combustion [100, 101]. Approximate solution of the partial differential equation for the inhomogeneous wave equation can be obtained by the Galerkin method [31, 32, 145]. In the Galerkin method, acoustic velocity and pressure are expressed in terms of basis functions which satisfy the boundary conditions and constitute a complete set of basis. The computations will be

economical compared to the former approach. A nonlinear dynamic model of the heat source has been obtained with neural network based system identification as discussed in detail in the chapter “Nonlinear System Identification”. This heat source model results in a representation with many constant delays. A delay differential equation with many delay terms is obtained when this heat source model is used in the Galerkin time domain equations. Numerical integration of this delay differential system is also computationally expensive (time consuming). The inhomogeneous wave equation and the Galerkin method can predict limit cycle amplitudes.

On the other hand, frequency domain system models are attractive since they require solving a set of algebraic equations instead of partial differential equations. Linear network models of thermo-acoustic system have been developed [35, 38, 45, 70, 74, 111]. In this approach, individual elements of thermo-acoustic network are described by their transfer functions/matrices which could be derived analytically, measured from the experiments or computed from the numerical simulations. Polifke and co-workers have used linear system identification method as an effective tool to construct transfer functions/matrices using input-output data set generated from unsteady CFD computations [64, 65, 110, 132]. Network models of the thermo-acoustic systems can predict the frequency and the growth rate of the oscillations, but are incapable of predicting the limit cycle amplitudes.

An extension of the linear network models to the nonlinear regime has been achieved with describing function method [36, 96]. Sinusoidal describing function is an amplitude dependent frequency response of the nonlinear element to sinusoidal input [36, 52, 96]. The input to the heat source (the only nonlinear element in our case) is assumed to be sinusoidal and the nonlinear element produces higher harmonics, which are at multiple integers of the fundamental harmonic. When the system acoustic filters these higher harmonics, an approximation for the limit cycle amplitude is possible. Describing function method neglects the effect of coupling between modes since it is a one-mode (sinusoid) approximation.

Our aim in this chapter is to develop a coupled modes system model in the frequency domain. In this approach, acoustic velocity and pressure are ex-

pressed as superposition of the modes. Equations have been derived from the Galerkin time domain system model. Network models can also be extended to the nonlinear regime (see Appendix C for a derivation). This approach goes beyond the “sinusoidal describing function method”, as coupling of the modes is involved. The nonlinearity in the heat source is expressed in terms of the higher order transfer functions through which the modes are coupled. Higher order transfer functions have been developed from the extension of the neural network identification method to the frequency domain (see details for the derivation of the higher order transfer functions in the “Nonlinear System Identification” chapter). The energy exchange between the modes (from fundamental to the higher order modes and from the higher harmonics to the fundamental mode through coupling) can be analyzed. The contribution of the coupling terms of different modes to the Rayleigh index in the nonlinear regime can be obtained. Moreover, the method is computationally efficient in comparison to a time domain simulation and it can capture the shape and amplitude of the limit cycle.

In this chapter, the Galerkin time domain method for one dimensional acoustics is first introduced, since the limit cycle can be predicted with this method. Moreover, the system model equations for the frequency domain with the coupled modes have been derived from this method. Nonlinear dynamical system analysis from the Galerkin model equations has been considered. Time domain simulation of the thermo-acoustic instability in the Rijke tube, with the heat source obtained from nonlinear system identification, has been performed.

Then, the sinusoidal describing function method is introduced and the describing functions for some simple nonlinearities are derived (see Appendix B for the describing function table for some common nonlinearities). Amplitude prediction of the limit cycle with describing function has been considered, and equations have been derived from the Galerkin method. Next, the model obtained from POD approach is considered (a heated plate in pulsating flow, refer to the chapter “Low Order Model of the Heat Source with POD”) as a nonlinear heat source. Nonlinear transfer function of this model heat source is used in the equations for the prediction of the limit cycle amplitude and

frequency.

Finally, the frequency domain system model with coupled modes is considered. Equations are derived from the Galerkin method. When the input to the heat source is expressed as a superposition of the modes, these will be coupled through the higher order transfer functions (when the heat source nonlinearity is expressed in terms of higher order transfer functions). Simulation results have been shown for the Galerkin time domain method, describing function method and the coupled modes system model. The Rayleigh index in the nonlinear regime is considered, and the contribution of the individual terms is determined.

A schematic representation of the limit cycle prediction in time domain with the Galerkin method and in the frequency domain with coupled modes approach, when the heat source is obtained from the nonlinear system identification, is shown in Fig. 6.1.

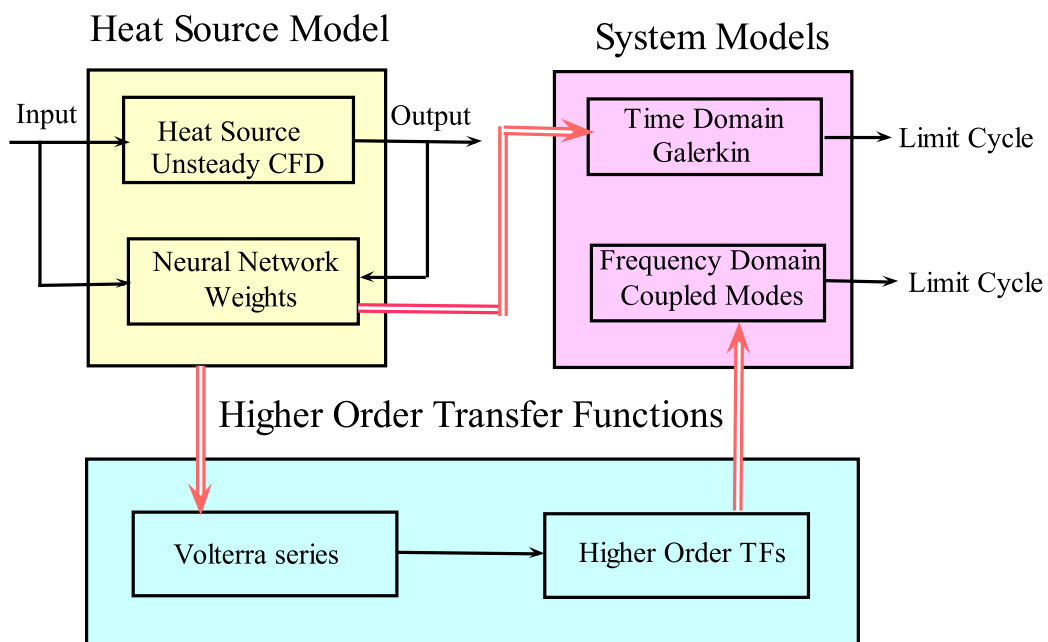


Figure 6.1: Schematic of the proposed approach from the nonlinear identification of the heat source to the simulation in time and frequency domain for the full thermo-acoustic system

6.1 Galerkin Time Domain

6.1.1 Derivation

In this modeling approach, acoustic velocity and pressure are expressed in terms of a set of basis functions, which constitute a complete basis and satisfy the boundary conditions [10, 31, 32]. Using the orthogonality of the basis functions, partial differential equations are projected onto the basis functions and one has to solve a set of ordinary differential equations instead of partial differential equations. Even though the method used here is for a simple geometry (Rijke tube), it can also be applied to complex geometries of practical interest. In this case (complex geometry case, also including more general boundary conditions), the basis functions (mode shapes) could be obtained from a three dimensional finite element simulation of the acoustics of the system [16]. Acoustic variables (pressure and velocity) are then written as the superposition of these mode shapes with the time dependent coefficients.

The governing equations for one dimensional acoustic field with the heat source term can be written as [10, 38]

Acoustic Momentum:

$$\bar{\rho} \frac{\partial \tilde{u}'}{\partial \tilde{t}} + \frac{\partial \tilde{p}'}{\partial \tilde{x}} = 0. \quad (6.1)$$

Acoustic Energy:

$$\frac{\partial \tilde{p}'}{\partial \tilde{t}} + \gamma \bar{p} \frac{\partial \tilde{u}'}{\partial \tilde{x}} = (\gamma - 1) Q'. \quad (6.2)$$

If the equations are non-dimensionalized using the duct parameters and mean values,

$$t = \frac{\tilde{t}}{\frac{L}{c_0}}, \quad x = \frac{\tilde{x}}{L}, \quad u' = \frac{\tilde{u}'}{\bar{u}}, \quad p' = \frac{\tilde{p}'}{\bar{p}}, \quad \rho = \frac{\tilde{\rho}}{\bar{\rho}}, \quad \text{Ma} = \frac{\bar{u}}{c_0}, \quad (6.3)$$

then the non-dimensional form of the equations can be written as,

$$\gamma\text{Ma} \frac{\partial u'}{\partial t} + \frac{\partial p'}{\partial x} = 0, \quad (6.4)$$

$$\frac{\partial p'}{\partial t} + \gamma\text{Ma} \frac{\partial u'}{\partial x} = \frac{(\gamma-1)}{c_0 \bar{p}} Q' \delta(x - x_f). \quad (6.5)$$

In the Galerkin method, acoustic velocity and pressure are written in terms of the natural modes of the duct [31, 32],

$$u'(x, t) = \sum_{m=1}^N \eta_m(t) \cos(m\pi x), \quad p'(x, t) = - \sum_{m=1}^N \frac{\gamma\text{Ma}}{m\pi} \dot{\eta}_m(t) \sin(m\pi x). \quad (6.6)$$

Using the above expansions for the acoustic velocity and pressure in the non-dimensional acoustic energy equation (Eq. (6.5)), and integrating over the domain $[0, 1]$ we obtain,

$$\begin{aligned} & -\gamma\text{Ma} \sum_{m=1}^N \frac{\ddot{\eta}_m(t)}{m\pi} \int_0^1 \sin(m\pi x) \sin(j\pi x) dx \\ & -\gamma\text{Ma} \sum_{m=1}^N m\pi \eta_m(t) \int_0^1 \sin(m\pi x) \sin(j\pi x) dx \\ & = \frac{\gamma-1}{c_0 p_0} Q' \sin(j\pi x_f) \end{aligned} \quad (6.7)$$

Using the orthogonality of the modes, namely

$$\int_0^1 \sin(m\pi x) \sin(j\pi x) dx = \begin{cases} \frac{1}{2} & \text{for } m = j \\ 0 & \text{for } m \neq j \end{cases} \quad (6.8)$$

results in a set of ordinary differential equations for the time dependent coefficients of the expansion, which are,

$$\frac{d^2\eta_j}{dt^2} + 2\xi_j\omega_j\frac{d\eta_j}{dt} + \omega_j^2\eta_j = \frac{2(1-\gamma)}{\text{Ma}c_0p_0\gamma}j\pi\sin(j\pi x_f)Q', \quad (6.9)$$

with $\omega_j = j\pi$. The linear damping mechanism included in the above equation takes into account the acoustic boundary layer at the tube walls, sound radiation from open ends of the tube and sound convected away due to the mean flow. The damping coefficients have been experimentally determined by Matveev and expressed using the following relation [88],

$$\xi_j = \frac{1}{2\pi} \left(c_1 \frac{\omega_j}{\omega_1} + c_2 \sqrt{\frac{\omega_1}{\omega_j}} \right). \quad (6.10)$$

In the equations above, the heat source is written explicitly, and in the case of a heat source model from linear/nonlinear system identification, one has to solve a delay differential equation with multiple fixed delays. If the number of the fixed delays is large, the computations may be time consuming.

6.1.2 Stability Analysis of Nonlinear Dynamical System

Two mode approximation is assumed and the King's law heat source model is used in the Galerkin formulation. The equations can be written as,

$$\dot{x}_1 = x_2, \quad (6.11)$$

$$\dot{x}_2 = -2\xi_1\omega_1x_2 - \omega_1^2x_1 + D\sin(\pi x_f) \left(\sqrt{\left| \frac{1}{3} + x_1\cos(\pi x_f) + x_2\cos(2\pi x_f) \right|} - \sqrt{\frac{1}{3}} \right), \quad (6.12)$$

$$\dot{x}_3 = x_4, \quad (6.13)$$

$$\dot{x}_4 = -2\xi_2\omega_2x_4 - \omega_2^2x_3 + 2D \sin(2\pi x_f) \left(\sqrt{\left| \frac{1}{3} + x_1 \cos(\pi x_f) + x_2 \cos(2\pi x_f) \right|} - \sqrt{\frac{1}{3}} \right). \quad (6.14)$$

For the sake of simplicity, the delay term τ is assumed to be 0 and for the ease of notation, $x_1 \rightarrow \eta_1$, $x_3 \rightarrow \eta_2$ convention is used.

In the compact form, the above equations can be written as,

$$\dot{x} = f(x), \quad (6.15)$$

where f is a nonlinear function of the state vectors. For dynamical systems, **Hartman-Grobman** theorem states that near the hyperbolic fixed point, the nonlinear system has qualitatively the same structure as that of the linearized system [134].

$(0, 0, 0, 0)$ is a steady state solution of the above equations, where $\dot{x}_i = 0$, for $i = 1, 2, 3, 4$.

Linearization of the Eq. (6.15) around the steady state points can be written as,

$$\dot{x} = \left. \frac{\partial f}{\partial x} \right|_{x_0} x, \quad (6.16)$$

where the Jacobian matrix can be computed at the steady state points from the following relation as

$$J(x) = \frac{\partial f}{\partial x} = \begin{bmatrix} \frac{\partial f_1}{\partial x_1} & \dots & \dots & \frac{\partial f_1}{\partial x_4} \\ \dots & \dots & \dots & \dots \\ \dots & \dots & \dots & \dots \\ \frac{\partial f_4}{\partial x_1} & \dots & \dots & \frac{\partial f_4}{\partial x_4} \end{bmatrix}. \quad (6.17)$$

The individual elements of the Jacobian matrix are,

$$\begin{aligned}
 J(1, 1) &= J(1, 3) = J(1, 4) = 0, \quad J(1, 2) = 1, \\
 J(2, 1) &= -\omega_1^2 + D \sin(\pi x_f) \cos(\pi x_f) \sqrt{\frac{3}{4}}, \\
 J(2, 2) &= -2\omega_1 \xi_1 + D \sin(\pi x_f) \cos(\pi x_f) \sqrt{\frac{3}{4}}, \\
 J(2, 3) &= J(2, 4) = 0, \\
 J(3, 1) &= J(3, 2) = J(3, 3) = 0, \quad J(3, 4) = 1, \\
 J(4, 1) &= 2D \sin(\pi x_f) \cos(\pi x_f) \sqrt{\frac{3}{4}}, \\
 J(4, 2) &= 2D \sin(2\pi x_f) \cos(2\pi x_f) \sqrt{\frac{3}{4}}, \\
 J(4, 3) &= -\omega_2^2, \quad J(4, 4) = -2\xi_2 \omega_2.
 \end{aligned} \tag{6.18}$$

System stability analysis can be studied using the eigenvalues of the Jacobian matrix. If all the eigenvalues have negative real parts, then the system is stable near the steady state (fixed) points. If none of the eigenvalues of the Jacobian has a zero real part, then the system is hyperbolic at this fixed point. If the system is hyperbolic and at least one of the eigenvalues has a positive real part, then the system is unstable.

For the first case, the damping coefficients, and coefficient of the heat source are chosen to be $c_1 = 0.01$, $c_2 = 0.001$, and $D = 8$, respectively. In Fig. 6.2, the real parts of the eigenvalues are shown when the heat source location is changed. All eigenvalues have non-zero real parts, so that the system is hyperbolic at the fixed point. The critical positions of the heat source for the stability of the system are between 0-0.25 and 0.75-1, where the real part of the third and fourth eigenvalues exceed 0. For the second configuration, with the damping coefficients and heat source location chosen as $c_1 = 0.01$, $c_2 = 0.001$, and $x_f = 0.35$, respectively, the coefficient of the heat source is varied between 0 and 100. The critical value of this coefficient is found to be 25 from the lower part of the Fig. 6.3.

As stated by Culick [33], CFD computations provide information about one set of parameters of the thermo-acoustic systems. For example, a single CFD computation cannot provide information about the system behavior for dif-

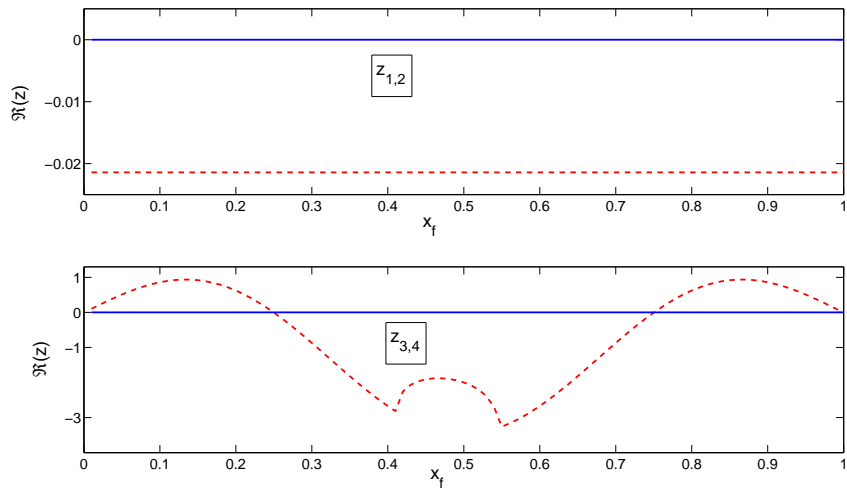


Figure 6.2: Real part of the eigenvalues vs heat source location for $c_1 = 0.01$, $c_2 = 0.001$, $D = 8$. Top(1st and 2nd eigenvalues), Bottom(3rd and 4th eigenvalues)

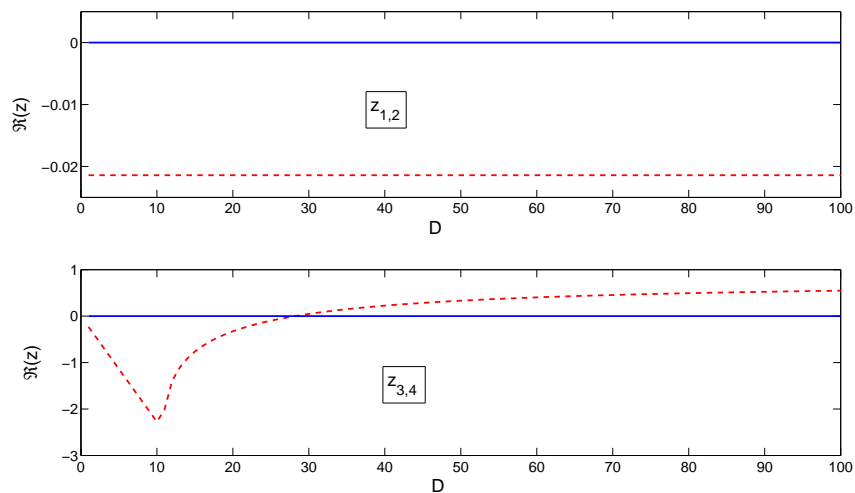


Figure 6.3: Real part of the eigenvalues vs coefficient of the heat source for $c_1 = 0.01$, $c_2 = 0.001$, $x_f = 0.35$. Top(1st and 2nd eigenvalues), Bottom(3rd and 4th eigenvalues)

ferent heat source locations. This type of analysis is quite useful for thermoacoustic systems to create the stability maps dependent on the system parameters. Furthermore, the time delay, which is an important parameter for the

stability of the thermo-acoustic systems, can also be included and the same type of analysis can be performed. Bethke et al. have performed a stability analysis of a gas turbine combustion chamber using the Galerkin model equations [16].

The local stability analysis with the linearization works only in the neighborhood of the steady state or fixed points. This analysis cannot provide information about the stability when the real part of one of the eigenvalues is zero and for locations far way from the fixed points.

6.1.3 Simulation with the CFD/SI Model of the Wire Heat Source

The dynamic model of the heat source (wire in pulsating flow) obtained from a neural network identification procedure has been used in time domain Galerkin simulation. Matlab DDE solver is used to solve the delay differential equations with the delays resulting from the identification part. For the first configuration, the heat source is located at $0.15L$ downstream of the tube inlet with the tube length, L . Total time of the simulation is set to 1000 (non-dimensional time), and a five mode approximation is utilized. In the second configuration, the heat source location is set to $0.25L$ downstream of the tube inlet, and the simulation time is 1500 (non-dimensional time).

Figures 6.4 and 6.5 show the evolution of the acoustic velocity (non-dimensionalized with respect to the mean value) at the heat source location.

Figure 6.6 at the top, shows the normalized heat transfer rate (with respect to the steady state value) and acoustic velocity when the limit cycle is reached for a heat source located at $0.15L$. This plot also shows how the heat source acts as a nonlinear element. At the bottom, the phase portrait of the non-dimensional acoustic pressure and non-dimensional heat transfer rate is shown. In Fig. 6.6, the same plots as before are shown for a heat source location at $0.25L$. The computational time for these simulations varies between 10-13 hours on a 64-Bit processor with 2.8 GHz.

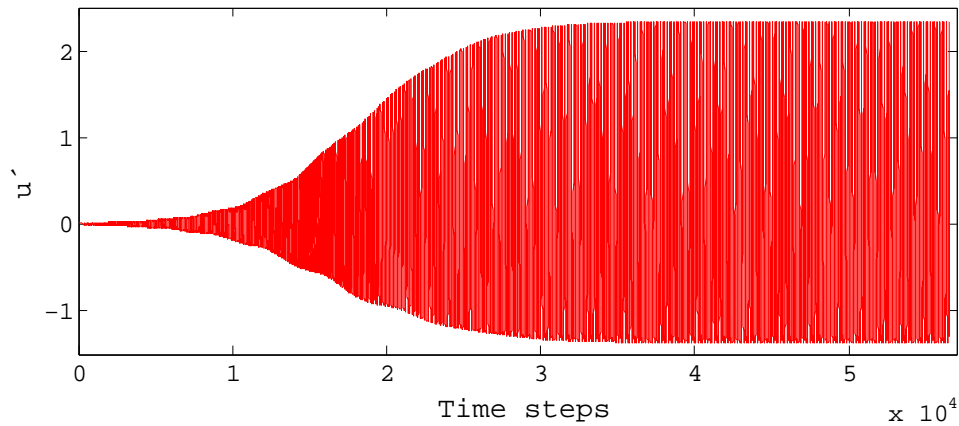


Figure 6.4: Evolution of the acoustic velocity at the heat source for the initial condition $\eta_1(0)=0.02$, duct length $L=5.65$, heat source location $x_f=0.15L$, and damping coefficients $c_1=0.0135$, $c_2=0.0015$

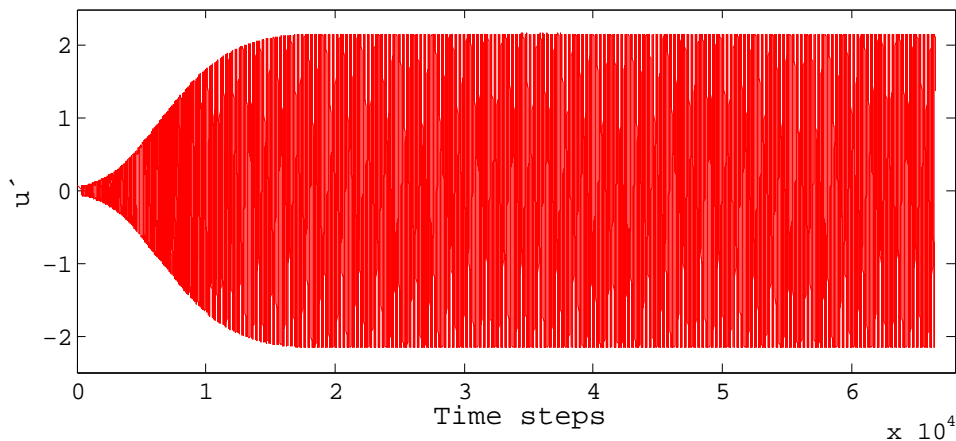


Figure 6.5: Evolution of the acoustic velocity at the heat source for the initial condition $\eta_1(0)=0.04$, duct length $L=5.65$, heat source location $x_f=0.25L$, and damping coefficients $c_1=0.0135$, $c_2=0.0015$

6.2 Describing Function

To predict the limit cycle amplitudes in the frequency domain, linear network models have been extended into frequency domain with describing function method [36, 96]. In the linear network models of thermo-acoustics, individual

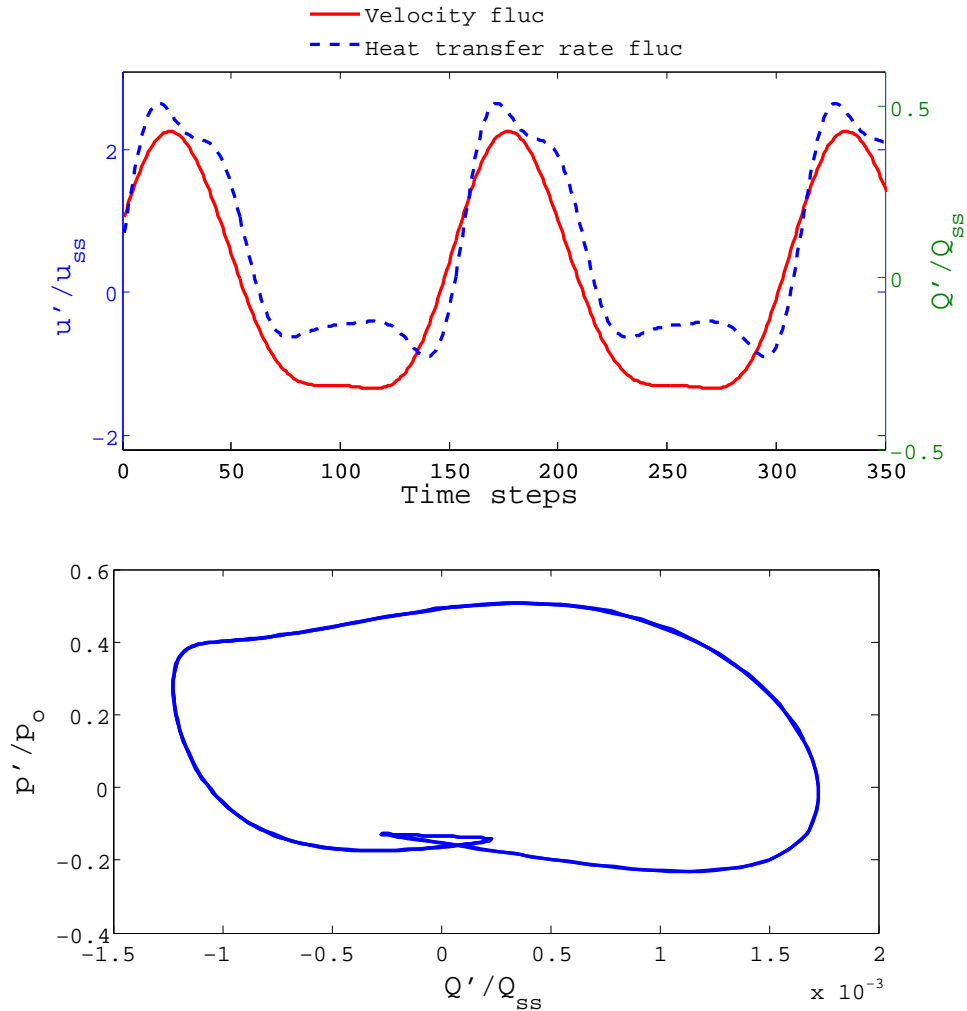


Figure 6.6: Top - Non-dimensional acoustic velocity and heat transfer rate when the limit cycle is reached (shows how the heat source acts as a nonlinear element), Bottom – Phase portrait of the non-dimensional acoustic pressure versus non-dimensional heat transfer rate for the initial condition $\eta_1(0)=0.02$, duct length $L=5.65$, heat source location $x_f=0.15L$, and damping coefficients $c_1=0.0135$, $c_2=0.0015$

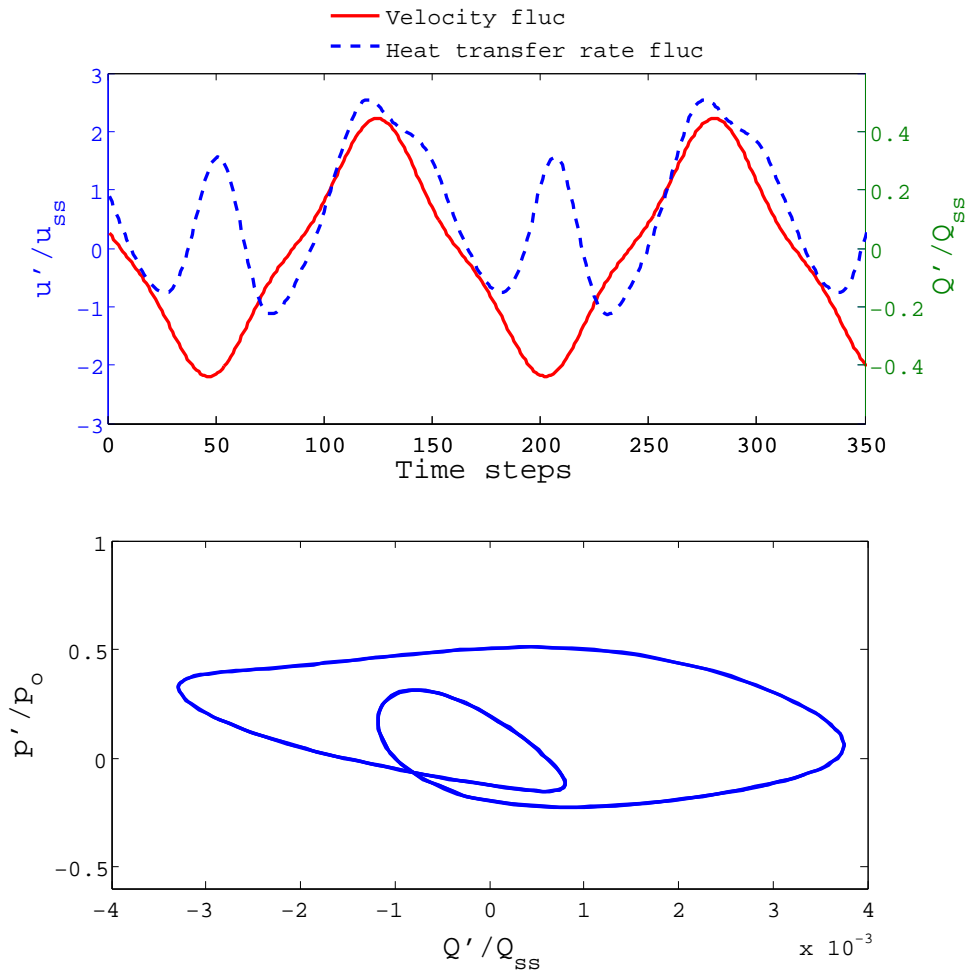


Figure 6.7: Top - Non-dimensional acoustic velocity and heat transfer rate when the limit cycle is reached (shows how the heat source acts as a nonlinear element), Bottom – Phase portrait of the non-dimensional acoustic pressure versus non-dimensional heat transfer rate for the initial condition $\eta_1(0)=0.04$, duct length $L=5.65$, heat source location $x_f=0.25L$, and damping coefficients $c_1=0.0135$, $c_2=0.0015$

elements are described by their transfer functions/matrices. A sinusoidal describing function is simply the amplitude-dependent frequency response of a nonlinear element to sinusoidal input [52].

A sinusoidal input to the heat source is assumed as,

$$u(t) = A \sin(\omega t). \quad (6.19)$$

The nonlinear heat source produces higher harmonics other than the fundamental. The periodic output can be expanded into a Fourier series expansion as,

$$Q(t) = \frac{A_0}{2} + \sum_{n=1}^{\infty} [A_n \cos(n\omega t) + B_n \sin(n\omega t)], \quad (6.20)$$

where the Fourier coefficients can be calculated as,

$$A_0 = \frac{1}{\pi} \int_{-\pi}^{\pi} Q(t) d(\omega t), \quad (6.21)$$

$$A_n = \frac{1}{\pi} \int_{-\pi}^{\pi} Q(t) \cos(n\omega t) d(\omega t), \quad (6.22)$$

$$B_n = \frac{1}{\pi} \int_{-\pi}^{\pi} Q(t) \sin(n\omega t) d(\omega t). \quad (6.23)$$

Let us assume $A_0 = 0$ (odd nonlinearity) and at the output consider only the fundamental component,

$$Q(t) = A_1 \cos(\omega t) + B_1 \sin(\omega t). \quad (6.24)$$

The describing function $N(A, \omega)$ of the nonlinear element is defined as,

$$N(A, \omega) = \frac{B_1}{A} + j \frac{A_1}{A}. \quad (6.25)$$

Describing function is a function of amplitude and frequency for general non-linear elements [127]. Simplified analytical closed form expressions for the describing functions can be obtained for some nonlinear types (see Appendix B for a table of sinusoidal describing functions for some common nonlinearities).

6.2.1 Describing Function of Cubic and Saturation Type Nonlinearity

Cubic Nonlinearity : The input-output relation is given by

$$Q = u^3 = A^3 \sin^3(\omega t). \quad (6.26)$$

The Fourier coefficient $A_1 = 0$ and

$$B_1 = \frac{1}{\pi} \int_{-\pi}^{\pi} A^3 \sin^3(\omega t) \sin(\omega t) d(\omega t) = \frac{3A^3}{4}. \quad (6.27)$$

Therefore, the fundamental harmonic at the output is,

$$Q_1(t) = B_1 \sin(\omega t), \quad (6.28)$$

and the corresponding describing function is calculated as,

$$N(A) = \frac{B_1}{A} = \frac{3A^2}{4}. \quad (6.29)$$

Saturation Type Nonlinearity : For a sinusoid input $u = A \sin(\omega t)$, the input-output relation is in the linear regime for $A \leq r$. The output is $nA \sin(\omega t)$ and the corresponding describing function is n (slope of the input-output curve

in linear region). A graphical representation of the input-output relation and saturated output is shown in Fig. 6.8.

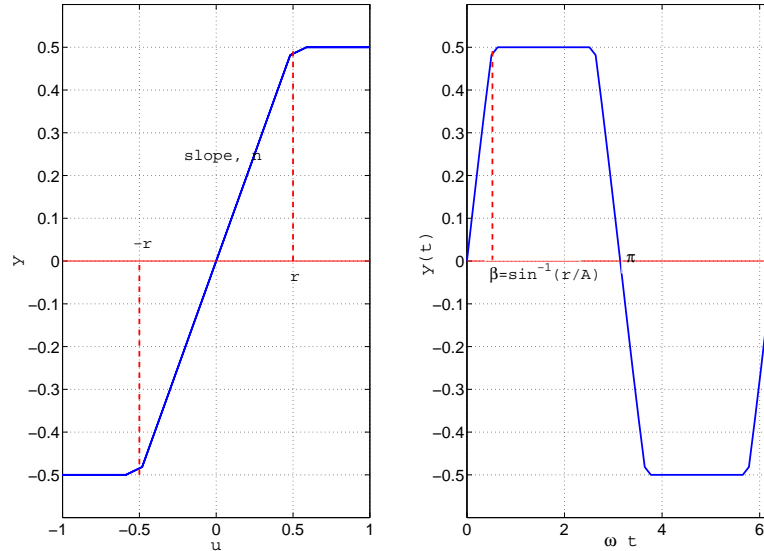


Figure 6.8: Input-output for a saturation type nonlinearity (left) and saturated output (right)

Due to the symmetry of the nonlinearity, the Fourier coefficient is calculated over a quarter of the period for $A \geq r$ as,

$$B_1 = \frac{4}{\pi} \int_0^{\pi/2} nA \sin(\omega t) \sin(\omega t) d(\omega t) + \frac{4}{\pi} \int_{\beta}^{\pi/2} nA \sin(\omega t) d(\omega t) = \frac{An}{\pi} (2\beta + \sin(2\beta)), \quad (6.30)$$

and the corresponding describing function is

$$N(A) = \frac{B_1}{A} = \frac{n}{\pi} (2\beta + \sin(2\beta)), \quad (6.31)$$

with $\beta = \sin^{-1}(r/A)$.

In the above nonlinearities, describing functions are found to be independent of the frequency. Generally, the describing function of the heat source

is a function of both amplitude and frequency.

6.2.2 Limit Cycle Calculation with Describing Function

After obtaining the describing function of the nonlinear element, the existence and the oscillation amplitude of the limit cycles are checked. A schematic representation of the self excited thermo-acoustic system is shown in Fig. 6.9.

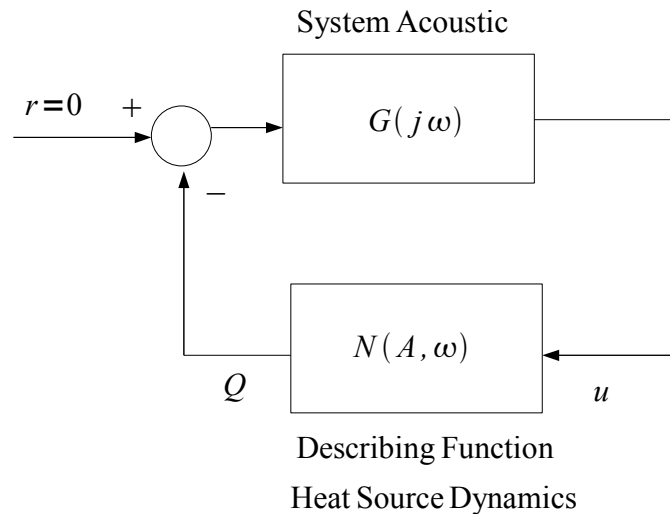


Figure 6.9: Closed loop thermo-acoustic system with describing function and linear acoustic element

The following equations are satisfied for the closed loop system [52, 127];

$$Q = N(A, \omega) u, \quad (6.32)$$

$$u = -G(j\omega)Q, \quad (6.33)$$

and therefore the limit cycle equation can be obtained as,

$$1 + G(j\omega)N(A, \omega) = 0. \quad (6.34)$$

Two equations are obtained for the real and imaginary parts of the expression in Eq. (6.34) for the amplitude A and frequency ω of the limit cycle.

Generally, the equation is written as,

$$G(j\omega) = \frac{-1}{N(A, \omega)} = \frac{-1}{K(A, \omega)e^{j\phi(A, \omega)}}, \quad (6.35)$$

and a graphical search is done by plotting the left and right hand side of the equations, and at the intersection point, the amplitude and frequency of the limit cycle are obtained [52]. In the above equation, the dependency of the gain (K) and phase (ϕ) of the transfer function upon amplitude and frequency is written explicitly.

Now, the equation for limit cycle calculation from Galerkin time domain equations is derived. The Laplace transform of Eq. (6.9) with the transformed variables can be written as,

$$\eta_m(t) \xrightarrow{\mathcal{L}} N_m(s), \quad \omega = \frac{s}{j},$$

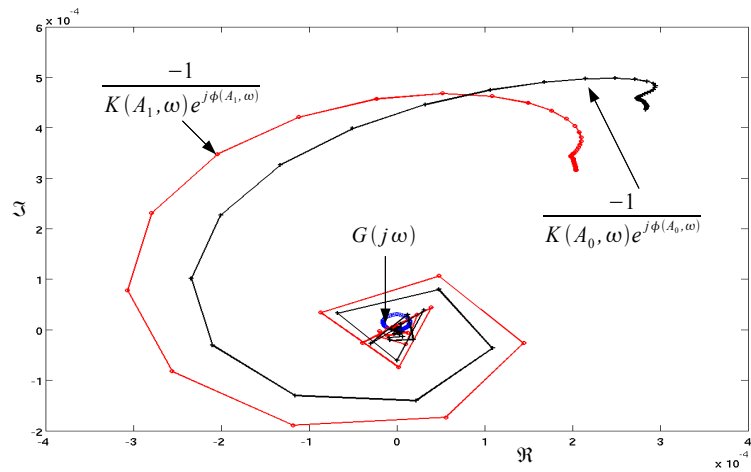
$$N_m(s) (s^2 + 2\xi_j \omega_m s + \omega_m^2) = \frac{2(1-\gamma)}{\text{Mac}_0 p_0} m\pi \sin(m\pi x_f) Q(s). \quad (6.36)$$

Converting the input to the heat source in s -domain yields,

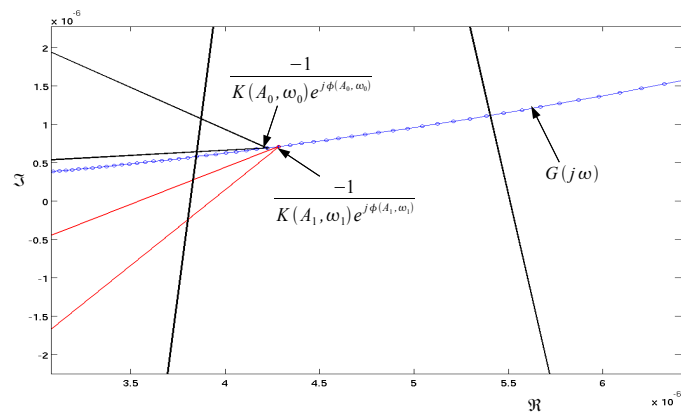
$$u(s) = \sum_{m=1}^N N_m(s) \cos(j\pi x_f). \quad (6.37)$$

Transfer function of the linear acoustic part will be obtained as,

$$G(s) = \frac{u(s)}{Q(s)} = \frac{(1-\gamma)\pi}{\text{Mac}_0 p_0} \sum_{m=1}^N \left(\frac{m \sin(2m\pi x_f)}{s^2 + 2\xi_m \omega_m s + \omega_m^2} \right). \quad (6.38)$$



(a) Graphical search for limit cycle amplitude and frequency



(b) Detail of the above plot for the intersection

Figure 6.10: Graphical search for limit cycle with describing function

The model obtained from the POD modeling approach is considered as the heat source model. The amplitude and frequency dependent nonlinear transfer function for the gain and phase is parametrized using two dimensional Lagrange polynomials.

A graphical representation for the intersection of the linear acoustic part and inverse of describing function is shown in Fig. 6.10(a), and in detail in Fig. 6.10(b) for two different amplitudes. Two different limit cycles with the amplitudes and frequencies, $(A_0, \omega_0) = (1.45, 3.62)$ and $(A_1, \omega_1) = (2.92, 3.63)$, are found. Nonlinear heat source model obtained from POD is valid for the predicted limit cycle amplitudes and frequencies. The frequency (non-dimensional) of fundamental mode of oscillation for a 1m length tube at open-open boundary conditions without heat source, is 3.141.

6.3 Frequency Domain System Model with Coupled Modes

In this system modeling approach, it is assumed that the main source of the nonlinearity is due to the heat source for a thermo-acoustic system. A model of the heat source has been obtained from neural network based nonlinear identification using input-output data set generated from the unsteady CFD computations. A polynomial representation of the input-output is obtained after an approximation of the expansion function (tangent hyperbolic) used in the units of the neural network with polynomials. Extensions of the linear transfer function to higher dimensions, the so-called higher order transfer functions, are obtained in the frequency domain. Details of the procedure to compute the higher order transfer functions have been described earlier in the “Nonlinear System Identification” chapter. This type of representation of the nonlinearity has great advantages when used in a modal basis representation of the thermo-acoustic system. It allows the input to the heat source to be the sum of the modes, and accounts for the interaction of the modes. An analysis of the energy balance (harmonic balance) of the modes (transfer of energy from the fundamental mode to the higher order modes and contribution of the higher order modes to the fundamental mode) is possible with this approach. Rayleigh index in the nonlinear regime can be studied, and the con-

tribution of the higher order modes to this index can be found out. In the current version, Galerkin time domain equations are used, in which the system variables (acoustic velocity and pressure) are expressed as sum of the modes. However, linear network modeling approach can also be used for an extension into the nonlinear regime with this nonlinear representation of the heat source (see Appendix C for a derivation of Nonlinear Network Model).

6.3.1 Derivation

The evolution coefficient in front of the m th mode in the frequency domain can be written as,

$$\eta_m(t) = A_m \sin(\omega_m t) + B_m \cos(\omega_m t) = \left(\frac{B_m}{2} + \frac{A_m}{2i} \right) e^{i\omega_m t} + \left(\frac{B_m}{2} - \frac{A_m}{2i} \right) e^{-i\omega_m t}. \quad (6.39)$$

Let us denote the following,

$$C_m = \frac{B_m}{2} + \frac{A_m}{2i}, \quad D_m = \frac{B_m}{2} - \frac{A_m}{2i}. \quad (6.40)$$

The time derivatives then become,

$$\frac{d\eta_m(t)}{dt} = i\omega_m C_m e^{i\omega_m t} - i\omega_m D_m e^{-i\omega_m t}, \quad (6.41)$$

$$\frac{d^2\eta_m(t)}{dt^2} = -(\omega_m)^2 C_m e^{i\omega_m t} - (\omega_m)^2 D_m e^{-i\omega_m t}. \quad (6.42)$$

Next, the heat source model is obtained in terms of coupled modes. The input to the heat source (acoustic velocity in the immediate vicinity) is assumed to be sum of the modes,

$$u'(t) = \sum_{m=1}^N \eta_m(t) \cos(m\pi x) = \sum_{m=1}^N (C_m e^{i\omega_m t} + D_m e^{-i\omega_m t}) \cos(m\pi x_f). \quad (6.43)$$

On substituting this in place of the input in the polynomial input-output representation and using the definitions of the higher order transfer functions, the corresponding output is obtained in terms of the coupled modes as,

$$\begin{aligned}
 Q'(t) = & \sum_{d_1=1}^N (C_{d_1} H_1(\omega d_1) e^{i\omega d_1 t} + D_{d_1} H_1(-\omega d_1) e^{-i\omega d_1 t}) \cos(\pi d_1 x_f) \\
 & + \sum_{d_1=1}^N \sum_{d_2=1}^N \left(\begin{array}{l} C_{d_1} C_{d_2} H_2(\omega d_1, \omega d_2) e^{i\omega(d_1+d_2)t} \\ + C_{d_1} D_{d_2} H_2(\omega d_1, -\omega d_2) e^{i\omega(d_1-d_2)t} \\ + D_{d_1} C_{d_2} H_2(-\omega d_1, \omega d_2) e^{i\omega(-d_1+d_2)t} \\ + D_{d_1} D_{d_2} H_2(-\omega d_1, -\omega d_2) e^{i\omega(-d_1-d_2)t} \end{array} \right) \cos(\pi d_1 x_f) \cos(\pi d_2 x_f) \\
 & + \sum_{d_1=1}^N \sum_{d_2=1}^N \sum_{d_3=1}^N \left(\begin{array}{l} C_{d_1} C_{d_2} C_{d_3} H_3(\omega d_1, \omega d_2, \omega d_3) e^{i\omega(d_1+d_2+d_3)t} \\ + C_{d_1} C_{d_2} D_{d_3} H_3(\omega d_1, \omega d_2, -\omega d_3) e^{i\omega(d_1+d_2-d_3)t} \\ + D_{d_1} C_{d_2} D_{d_3} H_3(-\omega d_1, \omega d_2, -\omega d_3) e^{i\omega(-d_1+d_2-d_3)t} \\ + D_{d_1} D_{d_2} C_{d_3} H_3(-\omega d_1, -\omega d_2, \omega d_3) e^{i\omega(-d_1-d_2+d_3)t} \\ + C_{d_1} D_{d_2} C_{d_3} H_3(\omega d_1, -\omega d_2, \omega d_3) e^{i\omega(d_1-d_2+d_3)t} \\ + D_{d_1} C_{d_2} C_{d_3} H_3(-\omega d_1, \omega d_2, \omega d_3) e^{i\omega(-d_1+d_2+d_3)t} \\ + C_{d_1} D_{d_2} D_{d_3} H_3(\omega d_1, -\omega d_2, -\omega d_3) e^{i\omega(d_1-d_2-d_3)t} \\ + D_{d_1} D_{d_2} D_{d_3} H_3(-\omega d_1, -\omega d_2, -\omega d_3) e^{i\omega(-d_1-d_2-d_3)t} \end{array} \right) \begin{pmatrix} \cos(\pi d_1 x_f) \\ \cdot \cos(\pi d_2 x_f) \\ \cdot \cos(\pi d_3 x_f) \end{pmatrix}. \quad (6.44)
 \end{aligned}$$

In this representation, the modes are coupled through the higher order transfer functions. On substituting the time derivatives and heat source in terms of the higher order transfer functions in Eq. (6.9) and harmonic balancing (equating the exponentials of the same order), the equation for mode number m becomes,

$$-\omega_m^2 C_m + 2i\xi_m m\pi\omega_m C_m + m^2 \pi^2 C_m = \frac{2(1-\gamma)}{\text{Mac}_0 p_0 \gamma} m\pi \sin(m\pi x_f) Q_m, \quad (6.45)$$

where Q_m denotes the m th exponential term for the heat source model.

Let us assume using one mode (as done in a sinusoidal describing function technique – one sinusoidal input to the heat source), then the equation for this mode will be,

$$-\omega^2 C + 2i\xi\pi\omega C + \pi^2 C = \frac{2(1-\gamma)}{\text{Mac}_0 p_0 \gamma} \pi \sin(\pi x_f) \left(\begin{array}{l} C H_1(\omega) \cos(\pi x_f) \\ + 3C^2 D H_3(\omega, \omega, -\omega) \cos^3(\pi x_f) \end{array} \right). \quad (6.46)$$

The symmetry of the kernels is used, and the nonlinearity in the heat source can be seen through the third order transfer function. It is known that C and D are complex conjugate numbers and are defined as,

$$C = \frac{B}{2} - \frac{A}{2}i, \quad D = \frac{B}{2} + \frac{A}{2}i, \quad (6.47)$$

with the modal coefficient

$$\eta(t) = A \sin(\omega t) + B \cos(\omega t), \quad (6.48)$$

where A and B are real numbers. The unknowns of the equation are A , B and ω . Two equations result by equating the imaginary and the real part of the above expression (Eq. 6.46) to zero. There is a need for an extra equation. This problem is handled by equating, for example, the real part of the coefficient of the mode to zero ($B = 0$). This means the phase of the mode is kept at a fixed value.

The set of equations for a two mode approximation is detailed.

The equation for the fundamental mode using Eq. 6.44 and Eq. 6.45 can be obtained as,

$$-\omega^2 C_1 + 2i\xi_1\pi\omega C_1 + \pi^2 C_1 = \frac{2(1-\gamma)\pi \sin(\pi x_f)}{\text{Mac}_0 p_0 \gamma} \left(\begin{array}{l} C_1 H_1(\omega) \cos(\pi x_f) \\ + 2C_2 D_1 H_2(2\omega, -\omega) \cos(2\pi x_f) \cos(\pi x_f) \\ + 3C_1^2 D_1 H_3(\omega, \omega, -\omega) \cos^3(\pi x_f) \\ + 6C_1 C_2 D_2 H_3(\omega, 2\omega, -2\omega) \cos(\pi x_f) \cos^2(2\pi x_f) \end{array} \right). \quad (6.49)$$

In the same manner, the equation for the second harmonic can be written as,

$$-4\omega^2 C_2 + 4i\xi_2 \pi \omega C_2 + 4\pi^2 C_2 = \frac{4(1-\gamma)\pi \sin(2\pi x_f)}{\text{Mac}_0 p_0 \gamma} \begin{pmatrix} C_2 H_1(2\omega) \cos(2\pi x_f) \\ + C_1^2 H_2(\omega, \omega) \cos^2(\pi x_f) \\ + 6C_1 D_1 C_2 H_3(\omega, -\omega, 2\omega) \cos^2(\pi x_f) \cos(2\pi x_f) \\ + 3C_2^2 D_2 H_3(2\omega, 2\omega, -2\omega) \cos^3(2\pi x_f) \end{pmatrix}. \quad (6.50)$$

The unknowns of the problem are the complex conjugate coefficients C_1/D_1 , C_2/D_2 and the frequency ω . There are five unknowns (two for each of the coefficients and one for the frequency). Four equations are obtained by equating the real and imaginary parts of Eq. 6.49 and Eq. 6.50 to zero. Once more, an additional equation for the frequency component can be obtained by equating one of the imaginary parts of the coefficients to zero, i.e. $\Im(C_1) = 0$.

6.3.2 Interpretation of Modal Coupling

Now, let us take a three mode approximation. In this case, we consider the harmonics -3ω , -2ω , $-\omega$, ω , 2ω , 3ω . Then the right hand side of the equation for the fundamental mode will have terms that are coupled through the higher order transfer functions. In this case, the sum of the arguments for the higher order transfer functions will be the fundamental harmonic. Such terms and their meanings are expressed in detail as;

$C_2 D_1 H_2(2\omega, -\omega) \cos(2\pi x_f) \cos(\pi x_f) \rightarrow$ Second mode couples with the fundamental through the second order transfer function

$C_3 D_2 H_2(3\omega, -2\omega) \cos(3\pi x_f) \cos(2\pi x_f) \rightarrow$ Third mode couples with the second mode through the second order transfer function

$C_3 D_1 D_1 H_3(3\omega, -\omega, -\omega) \cos(3\pi x_f) \cos^2(\pi x_f) \rightarrow$ Third mode couples with the fundamental through the third order transfer function

In general, the contribution of the terms that result in the coupling between the k modes through the n th order transfer function for the fundamental mode equation can be expressed as,

$$S_{d_1} \dots S_{d_r} H_n(\underbrace{\omega d_1, \dots, \omega d_r}_{d_1 + \dots + d_r = 1}) \cos(\pi d_1 x_f) \dots \cos(\pi d_r x_f) \quad \text{for } -k \leq d_i \leq k, \quad i = 1 \dots r, \quad (6.51)$$

where S is defined as,

$$S_{d_i} = \begin{cases} C_{d_i}, & \text{if } d_i > 0 \\ D_{-d_i}, & \text{if } d_i < 0 \end{cases} \quad (6.52)$$

The advantage of this type of representation of the heat source is that it allows us to find the contribution of the higher harmonics to the fundamental and it takes various interactions between different harmonics into account.

6.3.3 Comparison with Time Domain Simulation and Describing Function

Another advantage of the low order model in the frequency domain is that it requires solving a system of nonlinear algebraic equations instead of solving ordinary differential equations with delay terms, which makes a big difference in the computational time.

The computational time with the coupled mode frequency domain model is drastically reduced from 10-13 hours (with time domain) to 5-8 minutes. Figure 6.11 shows the acoustic velocity when the limit cycle is reached, which is obtained from time domain simulation, describing function method and coupled modes frequency domain system model, for the heat source located at $0.15L$ and $0.25L$ downstream of the tube inlet, respectively. In the above plot, the discrepancy between the describing function and time domain simulation is large. In the second plot, the second mode instability is suppressed

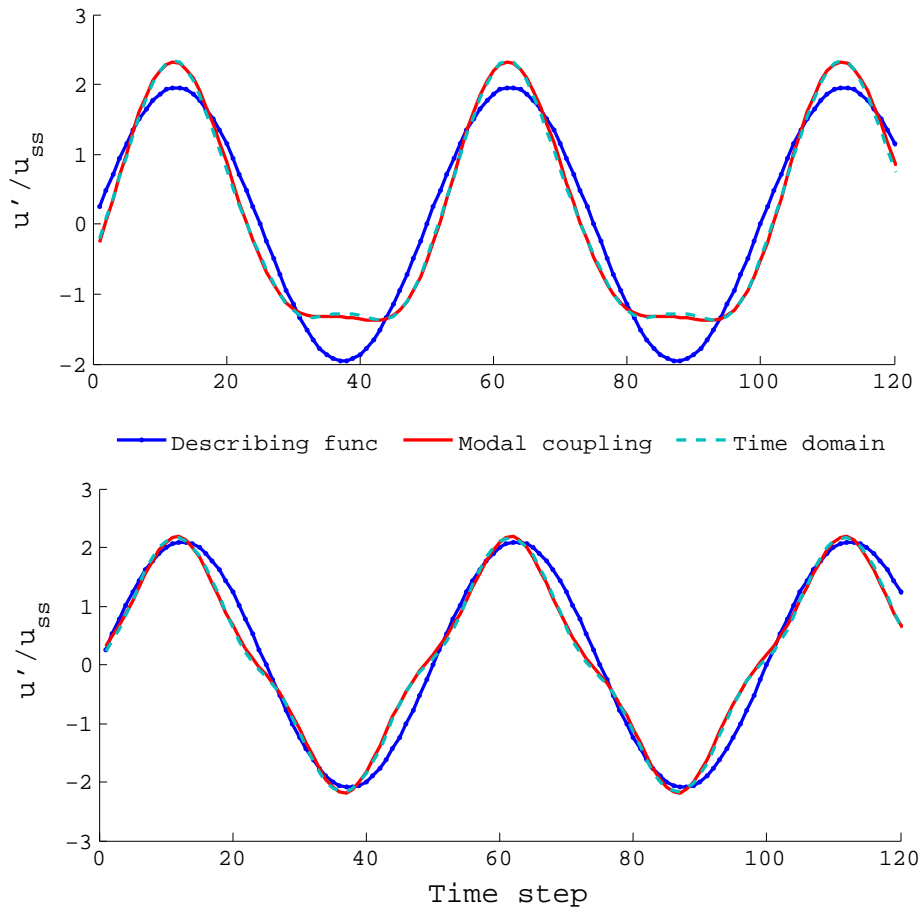


Figure 6.11: Top - Non-dimensional acoustic velocity at the limit cycle obtained from the time domain simulation (Galerkin), frequency domain coupled modes and describing function method for the initial condition $\eta_1(0) = 0.02$, duct length $L = 5.65$, heat source location $x_f = 0.15$, damping coefficients $c_1 = 0.0135$, $c_2 = 0.0015$
 Bottom - heat source location $x_f = 0.25$

(no contribution from the second mode) and describing function can approximate the amplitude of the limit cycle, but not the shape. In both cases, the coupled modes frequency domain system model captures the amplitude and the shape of the nonlinear oscillation.

6.3.4 Rayleigh Index and Energy Balance in the Nonlinear Regime

The energy gained from the heat source will be equal to energy dissipated by the modes when the limit cycle is reached. The energy gained from the local heat source can be directly related to the Rayleigh Index which is defined for one cycle of the oscillation as [46, 114],

$$\text{RI} = \frac{1}{T} \int_0^T p' Q' dt. \quad (6.53)$$

Next, the amount of gained energy distributed among the individual coupling terms is discussed. Let us assume a three mode approximation. Substitution of the modal representation of the pressure and the nonlinear heat source in the definition of the Rayleigh Index results in an expression with 21 terms. The first 7 terms represent the energy gained at the fundamental harmonic, the second 7 terms represent the energy gained at the second harmonic, and so on.

Energy gained at the fundamental harmonic:

$$\text{RI}_\omega = \Re \left(\frac{i\gamma \text{Ma}\omega}{\pi} \sin(\pi x_f) \begin{pmatrix} -D_1 C_1 H_1(\omega) \cos(\pi x_f) \\ -3C_1^2 D_1^2 H_3(\omega, \omega, -\omega) \cos^3(\pi x_f) \\ -2C_2 D_1^2 H_2(2\omega, -\omega) \cos(2\pi x_f) \cos(\pi x_f) \\ -2C_3 D_2 D_1 H_2(3\omega, -2\omega) \cos(3\pi x_f) \cos(2\pi x_f) \\ -6D_1 C_2^2 D_2 H_3(\omega, 2\omega, -\omega) \cos(\pi x_f) \cos^2(2\pi x_f) \\ -3D_1 C_2^2 D_3 H_3(2\omega, 2\omega, -3\omega) \cos^2(2\pi x_f) \cos(3\pi x_f) \\ -6C_1 D_1 C_3 D_3 H_3(\omega, 3\omega, -3\omega) \cos(\pi x_f) \cos^2(3\pi x_f) \end{pmatrix} \right). \quad (6.54)$$

Energy gained at the second harmonic:

$$\text{RI}_{2\omega} = \Re \left(\frac{2i\gamma\text{Ma}\omega}{\pi} \sin(2\pi x_f) \begin{pmatrix} -D_2 C_2 H_1(2\omega) \cos(2\pi x_f) \\ -2D_2 C_1^2 H_2(\omega, \omega) \cos^2(\pi x_f) \\ -2D_2 C_3 D_1 H_2(3\omega, -\omega) \cos(3\pi x_f) \cos(\pi x_f) \\ -6D_2 C_1 C_2 D_1 H_3(\omega, 2\omega, -\omega) \cos^2(\pi x_f) \cos(2\pi x_f) \\ -6D_2^2 C_1 C_3 H_3(\omega, 3\omega, -2\omega) \cos(\pi x_f) \cos(2\pi x_f) \cos(3\pi x_f) \\ -3D_2^2 C_2^2 H_3(2\omega, 2\omega, -2\omega) \cos^3(2\pi x_f) \\ -3D_2 C_2 C_3 D_3 H_3(2\omega, 3\omega, -3\omega) \cos(2\pi x_f) \cos^2(3\pi x_f) \end{pmatrix} \right). \quad (6.55)$$

Energy gained at the third harmonic:

$$\text{RI}_{3\omega} = \Re \left(\frac{3i\gamma\text{Ma}\omega}{\pi} \sin(3\pi x_f) \begin{pmatrix} -D_3 C_3 H_1(3\omega) \cos(3\pi x_f) \\ -2D_3 C_1 C_2 H_2(2\omega, \omega) \cos(\pi x_f) \cos(2\pi x_f) \\ -D_3 C_1^3 H_3(\omega, \omega, \omega) \cos^3(\pi x_f) \\ -6D_3 C_1 C_3 D_1 H_3(\omega, 3\omega, -\omega) \cos^2(\pi x_f) \cos(3\pi x_f) \\ -3D_3 C_2 C_2 D_1 H_3(2\omega, 2\omega, -\omega) \cos^2(2\pi x_f) \cos(\pi x_f) \\ -6D_3 C_2 C_3 D_2 H_3(2\omega, 3\omega, -2\omega) \cos^2(2\pi x_f) \cos(3\pi x_f) \\ -3D_3 C_3^2 D_3 H_3(3\omega, 3\omega, -3\omega) \cos^3(3\pi x_f) \end{pmatrix} \right). \quad (6.56)$$

The representation of the heat source in terms of the higher order transfer functions makes it possible to find the effect of the coupling terms. First component of the Rayleigh Index gives the energy that is gained by the heat source at the fundamental harmonic. Fourth and sixth components specify the contribution of the energy through the coupling of the second and third modes. This means, the higher harmonic components can also contribute to the fundamental mode. As can be seen for the second element of first component of Rayleigh Index, energy is driven to the higher harmonics with the nonlinearity (see also the second element in the second component of Rayleigh Index, and third element in the third component of the Rayleigh index).

If the system has low pass filter characteristics, the amplitude levels of the higher order harmonics will be small and the coupling terms can be neglected. This is the case where describing function method works. Heat source is generally a low pass filter, but the nonlinearity of the heat source at a specific frequency and amplitude is what is important. When only one sinusoid acts as an input to the heat source, it produces higher harmonics. If these components

are not suppressed by the system acoustics, the coupling terms appearing in Rayleigh Index cannot be neglected any longer.

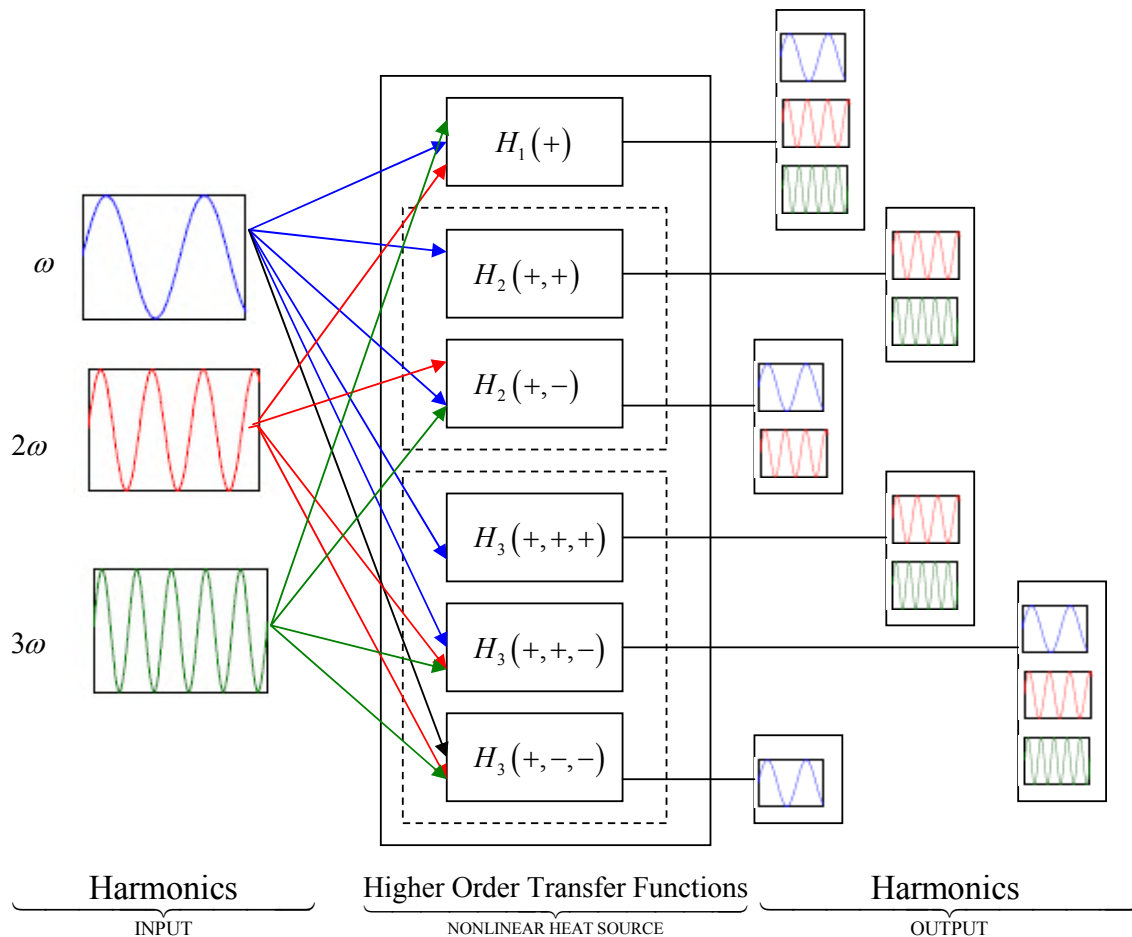


Figure 6.12: Schematic of the coupling relation between the harmonics through the higher order transfer functions of the nonlinear heat source for a three mode approximation (also shows the direction of the flow of the energy that is driven to higher harmonics from the fundamental mode, and from the higher harmonics to the fundamental mode)

Figure 6.12 shows the coupling relation between the harmonics through the higher order transfer functions of the nonlinear local heat source for a three mode approximation. This schematic representation also shows the direction of flow of the energy that is driven to higher harmonics from the fundamental mode, and from the higher harmonics to the fundamental mode.

The individual elements of the Rayleigh Index for the 21 terms as defined in Eq. (6.54), Eq. (6.55) and Eq. (6.56) are shown in Fig. 6.13 at the top and bottom for the heat source located at $0.15L$ and $0.25L$ downstream of the tube inlet, respectively, for a three mode approximation. In the plots, the contributions when only one sinusoid acts as the input to the heat source (sinusoidal describing function), are also shown.

At the top, the second and the fifth terms of the Rayleigh index (energy gained at the fundamental harmonic),

$$-3C_1^2 D_1^2 H_3(\omega, \omega, -\omega) \cos^3(\pi x_f), \quad -6D_1 C_2^2 D_2 H_3(\omega, 2\omega, -\omega) \cos(\pi x_f) \cos^2(2\pi x_f)$$

have negative contributions (stabilizing effect on the nonlinear oscillations). The eighth and ninth terms of the Rayleigh Index (energy gained at second harmonic),

$$-D_2 C_2 H_1(2\omega) \cos(2\pi x_f), \quad -2D_2 C_1^2 H_2(\omega, \omega) \cos^2(\pi x_f)$$

have positive contributions (destabilizing effect), while the eleventh term,

$$-6D_2 C_1 C_2 D_1 H_3(\omega, 2\omega, -\omega) \cos^2(\pi x_f) \cos(2\pi x_f)$$

has positive contribution.

At the bottom, since the second mode instability is suppressed, the fifth, ninth and eleventh terms of the Rayleigh Index have no contributions.

Figure 6.14 shows energy balance of the modes when the limit cycle is reached for a three mode approximation and describing function. Energy gained at fundamental, second and third harmonics with the coupling terms via higher order transfer functions that are included is equal to the energy dissipated by the first, second and third modes. The gained and damped energies are represented by RI and D, respectively. As it is shown in table 6.1, the net energy contributions at the second and third harmonics are positive, whereas for the first harmonic it is negative when the heat source is located at $x_f = 0.15L$. For the second configuration ($x_f = 0.25L$), the energy gained at the fundamental harmonic is positive.

For thermo-acoustic systems, it is generally assumed that the energy contribution of the higher order modes can be neglected since the damping factors are

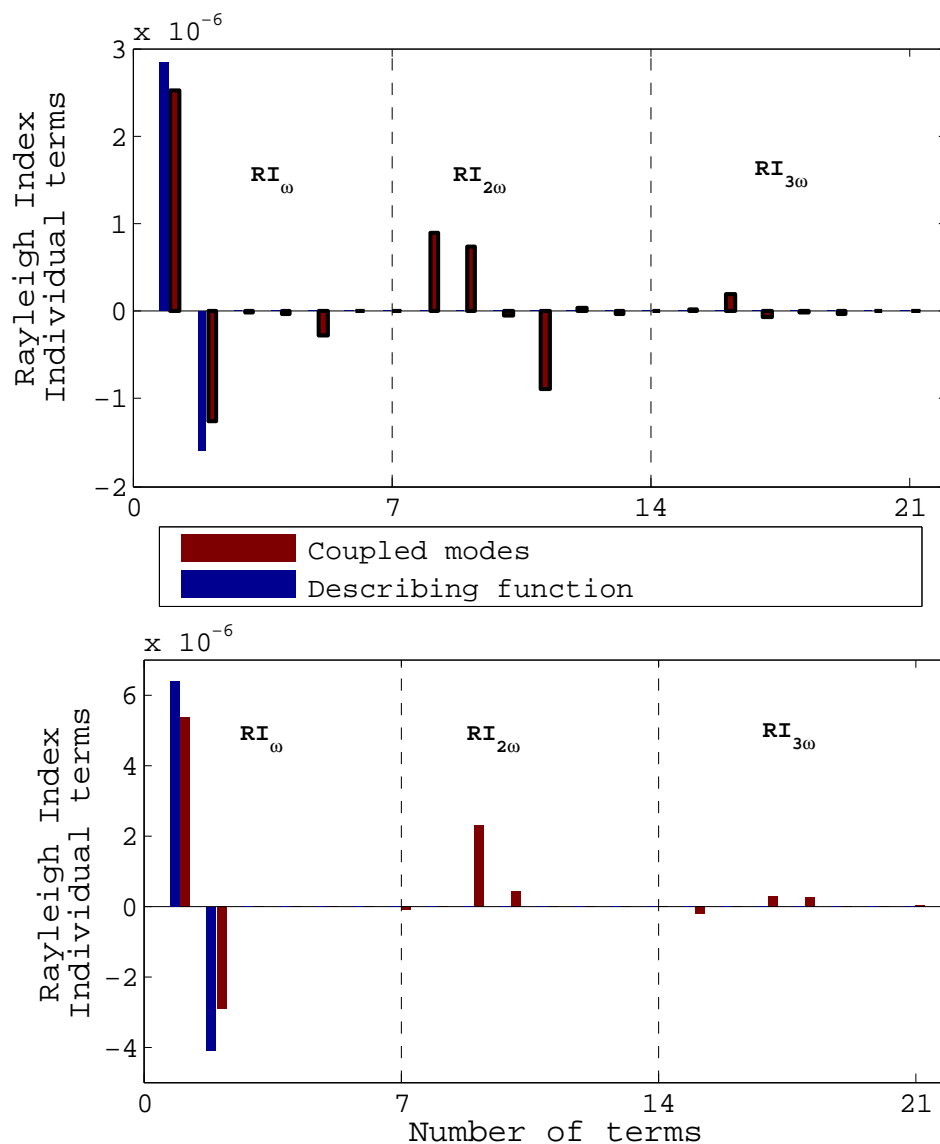


Figure 6.13: Top- Individual elements of the Rayleigh Index for a three mode approximation and describing function, for the duct length $L=5.65$, heat source location $x_f=0.15L$, and damping coefficients $c_1=0.0135$, $c_2=0.0015$, Bottom- heat source location $x_f=0.25L$

large at higher frequencies. It is observed that the coupling terms of the higher order modes have a stabilizing effect (a negative contribution to the energy gain) or destabilizing effect (a positive contribution to the energy gain). Consideration of these coupling terms along with the damping can then provide

an accurate analysis of the energy balance for the thermo-acoustic systems.

Table 6.1: Energy gained and damped at different harmonics

	$x_f = 0.15$			$x_f = 0.25$		
	ω	2ω	3ω	ω	2ω	3ω
RI	9.344×10^{-7}	6.959×10^{-7}	0.9341×10^{-7}	23.56×10^{-7}	26.7×10^{-7}	2.90×10^{-7}
D	10.05×10^{-7}	6.339×10^{-7}	0.850×10^{-7}	20.76×10^{-7}	29.21×10^{-7}	3.19×10^{-7}
Net Contribution	-0.706×10^{-7}	0.62×10^{-7}	0.0841×10^{-7}	2.8×10^{-7}	-2.51×10^{-7}	-0.29×10^{-7}

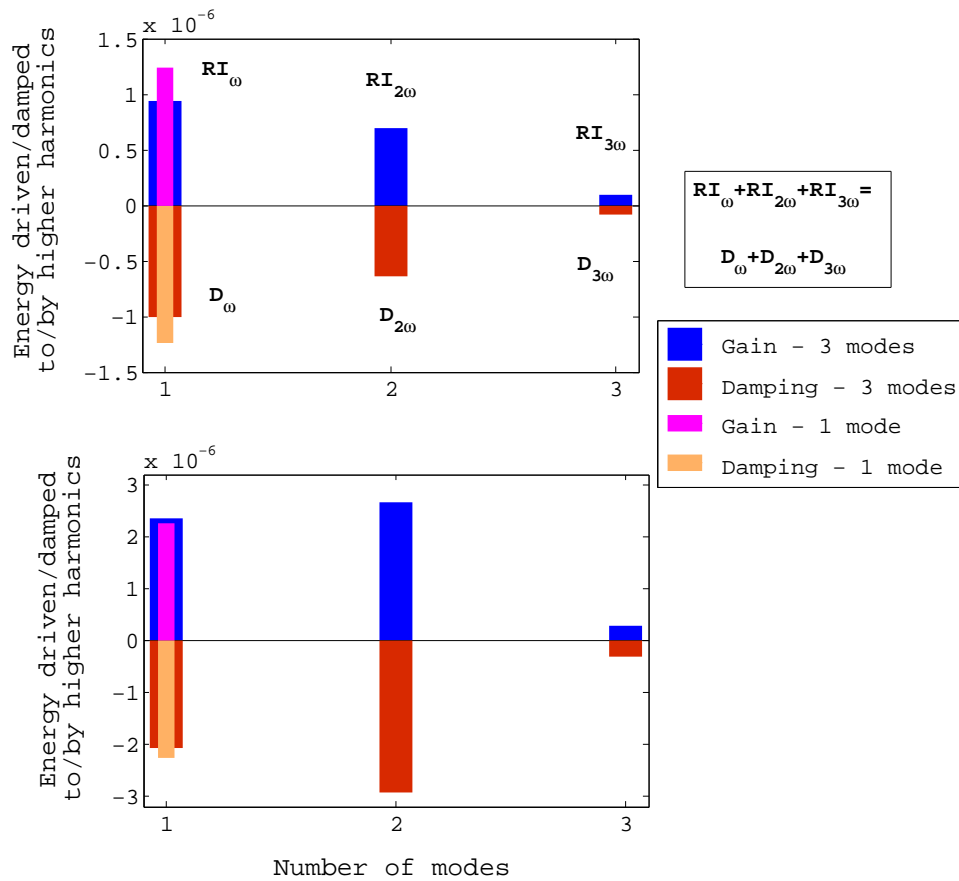


Figure 6.14: Top - Energy balance of the system when the limit cycle is reached for a three mode approximation and describing function for the duct length $L=5.65$, heat source location $x_f=0.15L$, and damping coefficients $c_1=0.0135$, $c_2=0.0015$, Bottom - heat source location $x_f=0.25L$

6.4 Conclusions and Outlook

In this chapter, a nonlinear, low order model for thermo-acoustic systems in the frequency domain has been considered. An approach has been developed that can take into account the coupling of the modes due to the nonlinearity. In this method, system variables (acoustic velocity and pressure) are expressed as a superposition of the modes. Nonlinearity in the heat source is expressed in terms of higher order transfer functions, which have been derived earlier in the “Nonlinear System Identification” chapter. The modes are then coupled through the higher order transfer functions. The equations have been derived using Galerkin method, but an extension of the network models to the nonlinear regime is also possible with this approach (see Appendix C for a derivation of the Nonlinear Network Models).

Simulation results have shown one case where the describing function approach fails to predict limit cycle, since the effect of the coupling terms of higher order modes due to the nonlinearity could not be neglected. In this case, the coupled modes system model gives the amplitude and the shape of the nonlinear oscillation correctly. Moreover, a reduction in the computational time is achieved from 10-13 hours to 5-8 minutes in comparison to the Galerkin time domain simulation. An energy balancing of the modes in the limit cycle showed that the coupling terms may give either positive or negative energy contributions. Therefore, an accurate analysis of the energy balance for the thermo-acoustic systems requires to consider the coupling terms along with the damping.

The approach has also some drawbacks since the higher order transfer functions are obtained using polynomial type representation of the nonlinearity. The challenges in this approach are described in the following cases:

- when the heat source introduces large delay terms,
- when a large range of frequencies are considered,
- when the approximation of the nonlinearity requires a higher order polynomial degree.

When the network models are extended to the nonlinear regime, then it is possible to add a jump condition in the area/temperature and investigate their effects on the limit cycle amplitudes. A possible coupling of the gas dynamics and the heat source nonlinearity can be investigated, since the system equations have been derived from the Galerkin method, and nonlinear gas dynamics have been derived using Galerkin for second and third order nonlinearities by Culick and co-workers [102, 142].

7 Non-Modal Analysis of Thermo-Acoustic Stability

Eigenvalues and eigenvectors play important roles in many applications of physics and engineering (stability, vibration analysis, and molecular orbitals in quantum mechanics). Systems with self adjoint operators/matrices have orthogonal eigenvectors. As a result, if small disturbances imposed on the normal directions decay with time, i.e. if the system is “linearly stable”, then the overall system response also decays with time [123, 136]. A system is said to be “non-normal” if its operator/matrices does not commute with its adjoint,

$$LL^T \neq L^T L, \quad (7.1)$$

where L is the system operator/matrices. Systems governed by non-normal operators/matrices have non-orthogonal eigenvectors. These systems show transient amplification of the initial disturbance because of the non-orthogonality [123, 136]. In Fig. 7.1, on the left is shown the eigenvectors of a normal system. The individual eigenvectors decay with time and hence, the overall response which is denoted by $\phi(t)$ decays. On the other hand, as it is illustrated on the right of the same Fig. 7.1, even though the individual eigenvectors decay with time, the overall response grows in amplitude. In a non-normal system, the short term behavior is important, and a small perturbation may exhibit transient growth of amplitude. The importance of the non-normality has been shown in many applications, such as hydrodynamic stability [116], magnetohydrodynamics [47], lasers [75], plasma physics [23], and control theory [117]. When considering the stability of the shear flows, the transition to instability at low Reynolds numbers is associated with the non-normality [123]. In the context of the combustion instabilities, Sujith and co-workers [8, 10, 69] have studied the non-normal nature of the thermo-acoustic systems. Non-orthogonality of the eigenvectors for a thermo-acoustic system,

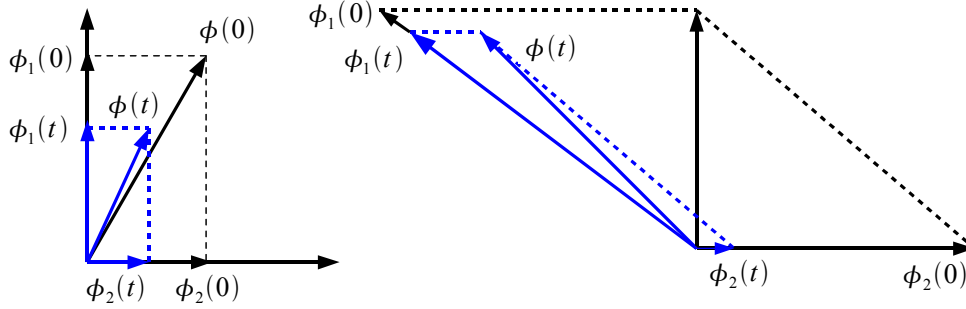


Figure 7.1: Schematic of transient a) decay in normal eigenvectors, b) growth in non-normal eigenvectors. (A decay of the non-normal eigenvectors in time does not necessarily indicate a decay of the response in time)

due to the heat source or general complex impedance boundary conditions, has been shown by Nicoud et al. [94].

Let us assume the heat release response is a linear function of the acoustic velocity perturbation as,

$$Q(t) = \hat{Q}u(t - \tau). \quad (7.2)$$

Non-dimensional momentum and energy equations for one-dimensional acoustics with $\tau = 0$ can be written as (see Galerkin time domain equations in the previous chapter),

$$\frac{\partial}{\partial t} \begin{pmatrix} u' \\ \frac{p'}{\gamma \text{Ma}} \end{pmatrix} = \underbrace{\begin{pmatrix} 0 & -\frac{\partial}{\partial x} \\ -\frac{\partial}{\partial x} + \hat{Q} & 0 \end{pmatrix}}_L \begin{pmatrix} u' \\ \frac{p'}{\gamma \text{Ma}} \end{pmatrix}. \quad (7.3)$$

Without heat release, i.e. $\hat{Q} = 0$, the system operator will be normal ($LL^T = L^T L$). Increasing the interaction index from the heat source (\hat{Q}) increases the non-normality. In the derivation above, for the sake of simplicity, the delay term is assumed to be zero. However, the combined effect of interaction index and delay has to be taken into account.

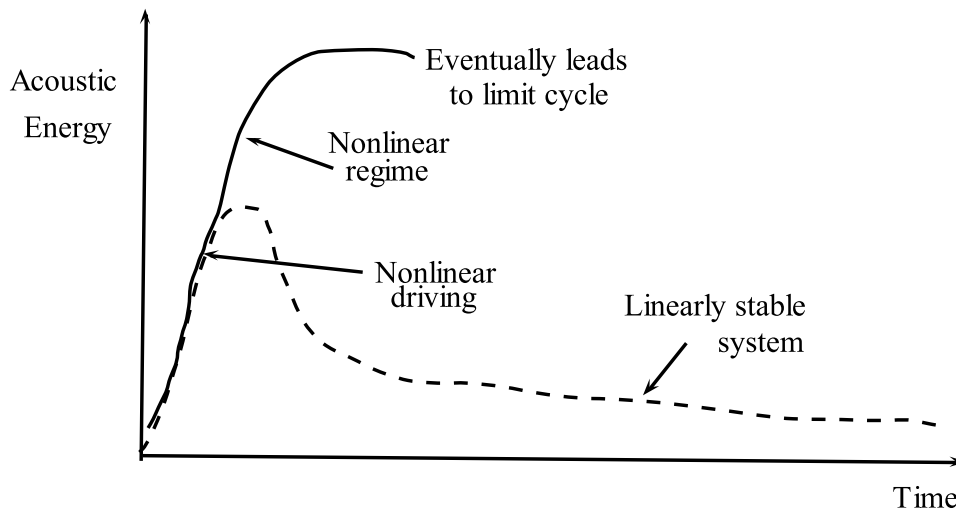


Figure 7.2: Schematic representation of transient growth and nonlinear driving mechanism

The combined effect of non-normality and nonlinearity is important for thermo-acoustic applications. If the system under investigation has nonlinearities, then the disturbance can reach high amplitude levels (because of transient growth due to the non-orthogonality of the eigenvectors), where nonlinearities are significant, and cause “nonlinear driving”. In that case classical analysis with normal operators is not adequate for linear stability. A schematic representation of the nonlinear driving is illustrated in Fig. 7.2. In the figure, the threshold value where the nonlinearity kicks in is lower than the maximum value of transient amplification.

In this chapter, we develop a systematic approach to investigate the non-modal stability of thermo-acoustic systems. The thermo-acoustic system is simulated in time domain using the Galerkin method to obtain a compact representation of the governing equations of the system in state space form. Sujith and co-workers have pioneered this type of system representation in time domain in several non-normal studies of thermo-acoustics [8, 10, 129]. A novelty in our approach is that the heat source is obtained using linear system identification and unsteady CFD computations (CFD/SI approach). This provides increased flexibility for the modeling of the heat source, i.e., no restriction on the time delay (refer to “Discussions and Conclusions” section of

the “Linear System Identification” chapter). The heat source obtained from CFD/SI approach has many constant discrete delays. The full system of coupled thermo-acoustics is a delay differential equation (DDE) with many constant delays. Another novelty of the proposed approach is that it can handle large delay times. Eigenvalues of the system have been obtained from the solution operator discretization. Pseudo-spectra diagrams have been used to study the behavior of the eigenvalues under perturbations. Lower bounds on the maximum growth factor (maximum amplification of perturbation energy over all initial conditions and over all time instances) have been extracted from the pseudo-spectra diagrams.

The approach is illustrated for the Rijke tube for two different heat sources; a heat source model based on “King’s law” and the wire in pulsating flow, which have been discussed in the previous chapters. The linear identification scheme used for the wire in pulsating flow is the correlation analysis which has been derived in “Linear System Identification” chapter.

In this chapter, first the compact form representation of the thermo-acoustic system as delay differential equations (DDE) is considered. Eigenvalues of the DDE is obtained using a solution operator discretization method. Then, pseudo-spectra computation and extraction of information for the maximum growth factor from pseudo-spectra diagrams are considered.

Results are shown for the Rijke tube with two different heat source models.

7.1 Thermo-Acoustics as Delay Differential System

Frequency domain system modeling approaches, such as the network modeling approach, neglect the transient effects and cannot be used for non-modal stability analysis of thermo-acoustic systems. The Galerkin method is used for the time domain simulation of thermo-acoustic system, which gives a compact representation of the system’s equation.

The equation for the evolution coefficient of the j th mode with the heat source included explicitly with Galerkin approach, is rewritten as,

$$\frac{d^2\eta_j}{dt^2} + 2\xi_j\omega_j\frac{d\eta_j}{dt} + \omega_j^2\eta_j = \frac{2(1-\gamma)}{\text{Ma}c_0p_0\gamma}j\pi\sin(j\pi x_f)Q', \quad (7.4)$$

where $\eta_j(t)$ represents the evolution coefficient of the j th mode.

In the following equations, the simple model of the heat source based on King's law and the heat source model obtained from unsteady CFD and linear system identification (CFD/SI) are used.

The equations for the system model with the heat source based on King's law (with one delay term) is written in compact form as,

$$\frac{d\chi(t)}{dt} = A_0\chi(t) + A_1\chi(t - \tau), \text{ where} \quad (7.5)$$

$$\chi(t) \equiv \left[\eta_1(t), \frac{\dot{\eta}_1(t)}{\pi}, \dots, \eta_N(t), \frac{\dot{\eta}_N(t)}{N\pi} \right], \quad (7.6)$$

with A 's defined as,

$$A_0 = \begin{bmatrix} 0 & 1 & 0 & 0 & \dots & 0 & 0 \\ -\omega_1 & -2\xi_1 & 0 & 0 & \dots & 0 & 0 \\ 0 & 0 & 0 & 1 & \dots & 0 & 0 \\ 0 & 0 & -\omega_2 & -2\xi_2 & \dots & 0 & 0 \\ \vdots & \vdots & \vdots & \vdots & \vdots & \vdots & \vdots \\ 0 & 0 & 0 & 0 & \dots & 0 & 1 \\ 0 & 0 & 0 & 0 & \dots & -\omega_N & -2\xi_N \end{bmatrix}, \quad (7.7)$$

$$A_1 = \begin{bmatrix} 0 & 0 & 0 & 0 & \dots & 0 & 0 \\ s_1 \cos(\pi x_f) & 0 & s_1 \cos(2\pi x_f) & 0 & \dots & s_1 \cos(N\pi x_f) & 0 \\ 0 & 0 & 0 & 0 & \dots & 0 & 0 \\ s_2 \cos(\pi x_f) & 0 & s_2 \cos(2\pi x_f) & 0 & \dots & s_2 \cos(N\pi x_f) & 0 \\ \vdots & \vdots & \vdots & \vdots & \vdots & \vdots & \vdots \\ 0 & 0 & 0 & 0 & \dots & 0 & 0 \\ s_N \cos(\pi x_f) & 0 & s_N \cos(2\pi x_f) & 0 & \dots & s_N \cos(N\pi x_f) & 0 \end{bmatrix}, \quad (7.8)$$

$$s_j = \frac{k\sqrt{3}(1-\gamma)}{\text{Ma } c_0 \rho_0 \gamma} j\pi \sin(j\pi x_f), \quad \text{for } j = 1 \dots N. \quad (7.9)$$

The equation for the system that models the heat source using CFD/SI approach is written in the compact form as,

$$\frac{d\chi(t)}{dt} = B_0\chi(t) + \sum_{l=1}^L B_l\chi(t - l\Delta t), \quad (7.10)$$

with coefficients B defined as,

$$B_0 = A_0, \quad (7.11)$$

$$B_l = \begin{bmatrix} 0 & 0 & 0 & 0 & \dots & 0 & 0 \\ \beta_{l1} \cos(\pi x_f) & 0 & \beta_{l1} \cos(2\pi x_f) & 0 & \dots & \beta_{l1} \cos(N\pi x_f) & 0 \\ 0 & 0 & 0 & 0 & \dots & 0 & 0 \\ \beta_{l2} \cos(\pi x_f) & 0 & \beta_{l2} \cos(2\pi x_f) & 0 & \dots & \beta_{l2} \cos(N\pi x_f) & 0 \\ \vdots & \vdots & \vdots & \vdots & \vdots & \vdots & \vdots \\ 0 & 0 & 0 & 0 & \dots & 0 & 0 \\ \beta_{lN} \cos(\pi x_f) & 0 & \beta_{lN} \cos(2\pi x_f) & 0 & \dots & \beta_{lN} \cos(N\pi x_f) & 0 \end{bmatrix}, \quad (7.12)$$

$$\beta_{ij} = \frac{2(1-\gamma)h_i}{\text{Ma } c_0 \rho_0 \gamma} j\pi \sin(j\pi x_f); \quad j = 1, \dots, N; \quad i = 1, \dots, M. \quad (7.13)$$

The heat source model formulated in terms of the unit impulse response h involves dealing with many fixed discrete delay terms $l\Delta t$, $l = 0, \dots, L$. If all delay terms are small, $L\Delta t \ll 1$, a Taylor series expansion to first order in the delay times $l\Delta t$ can be used to convert the system to one without delay [10].

However, this approach is not general, as there is no a priori restriction on the magnitude of the delay term. In thermo-acoustic applications involving, e.g., a flame as heat source, the delay terms may become quite large.

7.2 Elements of the Non-Modal Stability Analysis

7.2.1 Eigenvalues

Eigenvalues of the system described by Eq. (7.10) are found to be the roots of characteristic equation,

$$\det(\Delta z) = 0, \text{ where} \quad (7.14)$$

$$\Delta(z) = zI - B_0 - \sum_{l=1}^L B_l e^{-zl\Delta t}. \quad (7.15)$$

A system is asymptotically stable if all the roots (z) lie on the left half plane $Re(z) < 0$. This transcendental equation has infinite roots, but the number of eigenvalues to the right of any vertical line with $Re(z) = r$, where r is a real number, is finite. Stability of the system can then be studied by a finite number of roots [43, 66]. This nonlinear eigenvalue problem is solved iteratively, or converted into a polynomial eigenvalue problem by approximating the exponential term with a rational polynomial. If the system matrices are large and their condition numbers are high, then the accuracy of these methods deteriorates.

As an alternative method, the delay differential equation is converted into a partial differential equation. This is illustrated by taking a delay system with one fixed delay and writing it as a partial differential equation. The delay differential equation with one fixed delay term is,

$$\dot{w}(t) = A_0 w(t) + A_1 w(t - \tau), \quad t \geq 0, \quad (7.16)$$

$$w(t) = \phi(t), \quad t \in [-\tau, 0], \quad (7.17)$$

where w is a state vector of dimension n , and A 's are matrices of dimension $n \times n$. Considering the delay term as an extra dimension along with the time dimension, the above equations are expressed as initial boundary value problem [66] with

$$\frac{\partial v}{\partial x} = \frac{\partial v}{\partial t}, \quad t \geq 0, \quad x \in [-\tau, 0], \quad (7.18)$$

as the partial differential equation and with the boundary value,

$$\frac{\partial v}{\partial x}(t, 0) = A_1 v(t, -\tau) + A_0 v(t, 0), \quad t \geq 0, \quad (7.19)$$

and the initial value,

$$v(0, x) = \phi(x), \quad x \in [-\tau, 0]. \quad (7.20)$$

Theorem 1 *If $w(t)$ is the solution of the delay differential equation (Eq. (7.16), Eq. (7.17)) and $v(t, x)$ is the solution of the partial differential equation (Eqs. (7.18), Eq. (7.19), Eq. (7.20)), then the following relation holds [66];*

$$v(t, x) = w(t + x), \quad x \in [-\tau, 0], \quad t \geq 0. \quad (7.21)$$

Proof of Theorem 1: First it is shown that if $w(t)$ is the solution of the delay equation and satisfies the relation in Eq. (7.21), then it satisfies the partial differential equation. Eq. (7.18) is satisfied automatically because of symmetry of w with respect to x and t .

$$v(t, 0) = w(t), \quad x = 0. \quad (7.22)$$

This relation is applied in equation (37),

$$\dot{w}(t) = \frac{\partial v}{\partial x}(t, 0), \quad (7.23)$$

$$A_0 w(t) + A_1 w(t - \tau) = A_0 v(t, 0) + A_1 v(t, -\tau), \quad (7.24)$$

which gives the boundary value equation in Eq. (7.19).

$$v(0, x) = w(x), \quad t = 0. \quad (7.25)$$

Using this relation in Eq. (7.17), the initial value equation (Eq. (7.20)) is obtained.

Now, if $v(t, x)$ is the solution of the initial boundary value problem and satisfies Eq. (7.21), then it will satisfy the delay differential equation. This is shown as,

$$v(t, 0) = w(t), \quad x = 0 \quad (7.26)$$

Considering this relation in the boundary value equation in Eq. (7.19) we obtain,

$$\frac{\partial v}{\partial x}(t, 0) = \dot{w}(t), \quad (7.27)$$

$$A_1 v(t, -\tau) + A_0 v(t, 0) = A_1 w(t - \tau) + A_0 w(t), \quad t \geq 0, \quad (7.28)$$

which gives the delay equation in Eq. (7.16).

$$v(0, x) = w(x), \quad t = 0. \quad (7.29)$$

Using the above relation in the initial value equation in Eq. (7.22) for the partial differential equation,

$$v(0, x) = \phi(x), \quad x \in [-\tau, 0], \quad (7.30)$$

the initial value equation in Eq. (7.17) is obtained for the delay system and this completes the proof.

For a given delay differential system it is thus possible to formulate an equivalent partial differential equation. Next, we consider how the corresponding solution operator can be discretized to compute the eigenvalues of the delay system. The partitioning of the delay dimension into $N + 1$ equidistant points as,

$$\Omega_N = \{mh \mid m = -N, \dots, -1, 0\}, \quad h = \frac{\tau}{N}, \quad (7.31)$$

and a first order finite difference approximation along the delay dimension, are considered.

The solution operator that satisfies the partial differential equation and the boundary condition will be

$$L = \begin{bmatrix} B \otimes I_m \\ A_1 \ 0 \dots 0 \ A_0 \end{bmatrix}, \quad (7.32)$$

which has the dimension of $n(N + 1) \times n(N + 1)$. The matrix B , which has dimension of $N \times (N + 1)$, is given as

$$B = \frac{1}{h} \begin{bmatrix} -1 & 1 & \dots & \dots & \dots \\ \dots & -1 & 1 & \dots & \dots \\ \vdots & \vdots & \vdots & \vdots & \vdots \\ \dots & \dots & \dots & -1 & 1 \end{bmatrix}. \quad (7.33)$$

I_m is the identity matrix of dimension $m \times m$ and \otimes is the tensor product.

The extension to a case with many discrete fixed delays and an approximation of the differential other than first order is discussed in [21]. In this study, the Matlab toolbox TRACE-DDE [22] is used to compute the eigenvalues of the resulting operator. The delay differential equations can also be written as an abstract Cauchy problem, and the corresponding solution operator is called the infinitesimal generator of the delay equation. An approximate discretization of the operator is performed to get the eigenvalues of the delay system [14,21].

7.2.2 Pseudo-spectra of the delay system

For a linear matrix (operator), the pseudo-spectra exhibit the behavior of its eigenvalues under perturbations. Systems governed by normal operators exhibit resonance when the forcing frequency is close to the spectrum. However, for non-normal systems, resonance may occur at frequencies far away from the spectrum [135, 136]. Pseudo-spectra also provide the bounds on the evolution operator [135, 136].

The characteristic equation for the system with many discrete fixed delays is given by Eq. (7.15).

Using a perturbation matrix

$$\tilde{\Delta}(z) = \delta B_0 + \sum_{l=1}^L \delta B_l e^{-zl\Delta t}, \quad (7.34)$$

the ε -pseudospectra are defined as [123, 136]

$$\Lambda_\varepsilon = \{z \in \mathbb{C} \mid \det(\Delta(z) + \tilde{\Delta}(z)) = 0 \text{ with } \|\delta B_i\| \leq \varepsilon\}. \quad (7.35)$$

In the above equation, $\|\cdot\|$ and ϵ represent the norm of the matrix and the perturbation level, respectively. An equivalent representation of the above definition using the 2-norm of the matrices can be written [55] as,

$$\Lambda_\epsilon = \left\{ z \in \mathbb{C} \mid \frac{\sigma_{\min}(\Delta(z))}{1 + \sum_{l=1}^L e^{-zl\Delta t}} \leq \epsilon \right\}, \quad (7.36)$$

with $\sigma_{\min}(\Delta(z))$ being the minimum singular value of the matrix $\Delta(z)$. The simplest approach to compute the pseudo-spectra is to find the minimum of the singular value and plot the contours of the above equation on a complex plane (two dimensional grid) [135].

7.2.3 Maximum growth factor and Kreiss' theorem

The maximum growth factor $G_{\max}(t)$ is an important parameter indicating the maximum amplification of perturbation energy over all initial conditions and over all time instances within a time interval $[0, t]$.

The solution of the linear system

$$\frac{d\chi(t)}{dt} = A\chi(t), \quad (7.37)$$

in compact notation without a delay term can be expressed as,

$$\chi(t) = e^{At}\chi(0). \quad (7.38)$$

Within a time interval $[0, t]$, the maximum growth factor is defined as [123],

$$G_{\max} = \max_t \left(\max_{\chi(0)} \frac{\|\chi(t)\|^2}{\|\chi(0)\|^2} \right) = \max_t \left(\|e^{At}\|^2 \right). \quad (7.39)$$

From the definition of the 2-norm, the square of the norm can be represented as [123],

$$\|\chi(t)\|^2 = \sum_{i=1}^N \left(\eta_i^2 + \frac{\dot{\eta}_i^2}{i^2\pi^2} \right). \quad (7.40)$$

The non-dimensional perturbation energy at any time t is given by, [91]

$$E(t) = \left(\frac{\gamma \text{Ma}}{2} \right)^2 \|\chi(t)\|^2 \quad (7.41)$$

On substituting the above definitions for G_{max} in Eq. (7.39), the maximum growth factor is stated as,

$$G_{max} = \max_t \left(\max_{E(0)} \frac{\text{Acoustic energy at time } t}{\text{Initial acoustic energy}} \right) \quad (7.42)$$

When the maximum growth G_{max} factor reaches infinity, the system becomes unstable. If it is less than one, the system is linearly stable (classical linear stability). When performing a parameter variation in the system, the interesting ranges of the parameter set will be the linearly stable regions with $1 < G_{max} < \infty$ (regions of potential instability) [91]. However in a delay system, the compact representation in Eq. (7.37) cannot be obtained and the computation of the maximum growth factor can be achieved using Kreiss' Theorem [62, 123]. This theorem relates the maximum growth factor and the pseudo-spectra by the relation and gives a lower bound on this quantity;

$$G_{max} \geq \sup_{\varepsilon > 0} \left(\varepsilon^{-1} \sup_{z \in \Lambda_\varepsilon} \Re(z) \right). \quad (7.43)$$

The right hand side of the above equation gives the maximum distance to the real axis divided by the perturbation, for all perturbations greater than zero, and is used as a lower bound on the approximation of the maximum growth factor. Since the pseudo-spectra of the delay systems can be calculated, the maximum growth factor for the Rijke tube with the heat source models from identification and simple correlation (King's law) can be compared for a range of parameters.

7.3 Results

The eigenvalues of the system with the heat source model, obtained from identification, have been calculated using the discretization of the solution

operator of the equivalent partial differential equation for the delay differential system. The toolbox TRACE-DDE, which uses a Chebyshev collocation scheme [22], has been utilized.

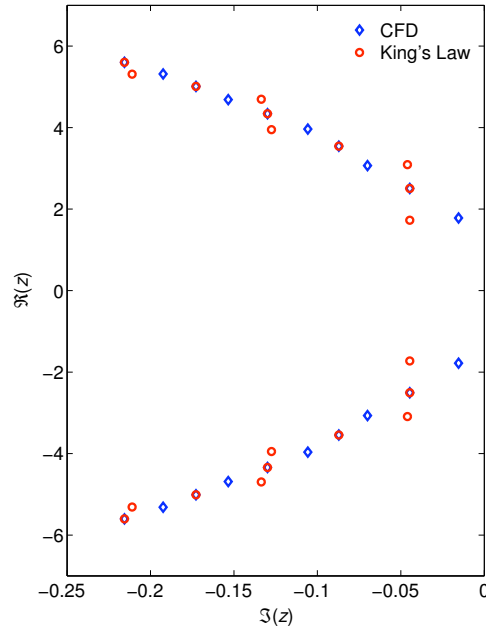


Figure 7.3: Comparison of the eigenvalues of the system resulting from King's law heat source (circles) and from identified CFD heat source (squares) with the duct parameters $x_f=0.25$, $c_1=0.135$, $c_2=0.05$, $L_d=1$

All the eigenvalues of the systems are on the left half plane indicating stability of the systems. When the eigenvalues are compared with the system (models of the heat transfer using King's law) eigenvalues as in Fig. 7.3, the first eigenvalue pairs are found to be closer to the zero of the real axis while the second eigenvalue pairs are at the same position. The first eigenvalue pairs near the zero axis are $-0.0154 \pm 1.781i$ for the CFD model, while for King's law model, the first two eigenvalue pairs are $-0.0446 \pm 1.7275i$, $-0.0447 \pm 2.506i$.

In Fig. 7.4, the pseudo-spectra is shown for the duct parameters and the various perturbation levels. The pseudo-spectra show symmetric behavior with respect to zero of the imaginary axis, and in Fig. 7.5, a detail of the pseudo-spectra is shown for the first two eigenvalue pairs that have negative imagi-

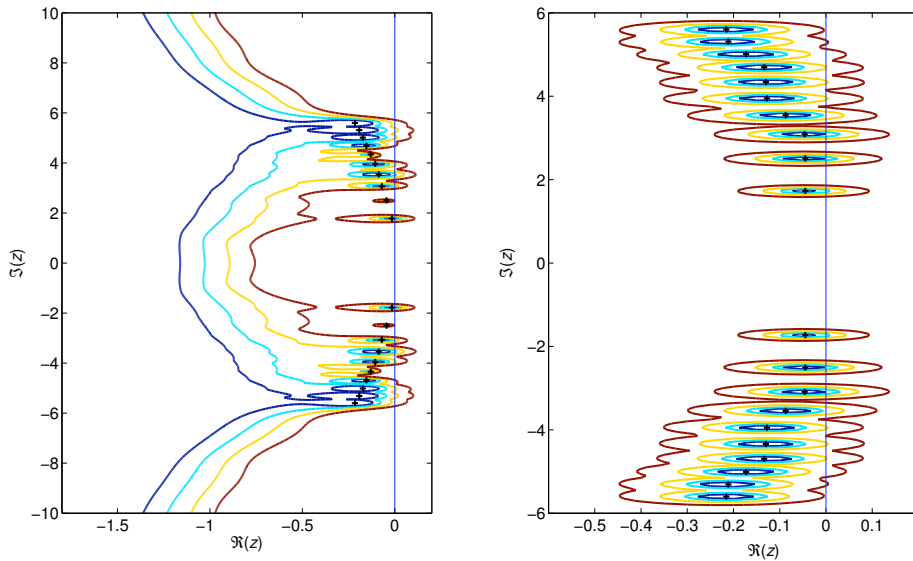


Figure 7.4: Comparison of the pseudo-spectra of the systems resulting from King's law heat source (right) and from identified CFD heat source (left) for perturbations of $\epsilon=10^{-1.8}$, $10^{-1.6}$, $10^{-1.4}$, $10^{-1.2}$ with the tube parameters $x_f=0.25$, $c_1=0.135$, $c_2=0.05$, $L_d=1$

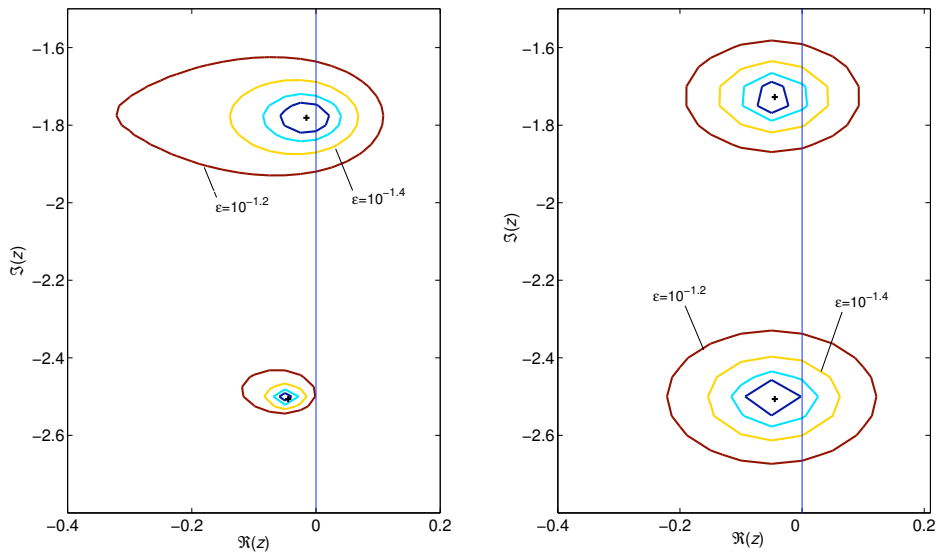


Figure 7.5: A detail of the above pseudo-spectra for the first two eigenvalues with negative imaginary parts near the zero of the real axis

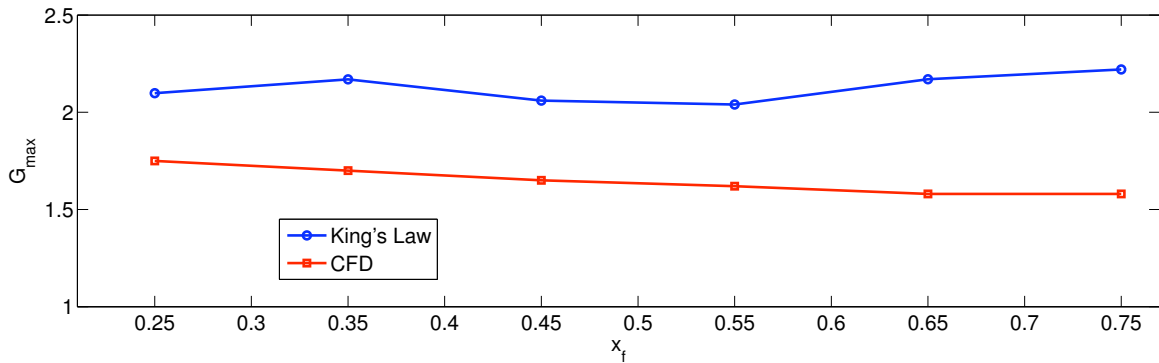


Figure 7.6: Maximum growth factor (lower bound calculated from pseudo-spectra) versus location of the heat source

nary parts. For the perturbation level of $\epsilon=10^{-1.4}$ (yellow colored contour), the first eigenvalue pairs of both the systems and the second eigenvalue pair of the system with King's law model reach the right half plane. On incrementing the perturbation level (brown colored contours), the distance of the contour from the zero of the real axis increases and the lower bound on the maximum growth factor is calculated from this distance. For perturbation $\epsilon=10^{-1.2}$, this distance for the CFD model is 0.11 and for King's law is 0.132, providing the maximum growth factors from the Kreiss' theorem as $0.11/10^{-1.2} = 1.75$ and $0.132/10^{-1.2} = 2.1$, respectively. These values are the lower bounds and greater than one, and therefore transient growth does occur in these systems.

Next, the heat source location is changed and the maximum growth factor is estimated from the pseudo-spectra for each of the heat source locations for both systems. In Fig. 7.6, the maximum growth factor for changing the heat source location is shown. The sensitivity of King's law heat source model is higher than that of the CFD heat source model.

7.4 Discussions and Conclusions

Thermo-acoustic systems have non-normal operators/matrices. These possess non-orthogonal eigenvectors. As a result of this, a transient amplifica-

tion of the initial disturbance may grow to high amplitude levels, where the nonlinearities are significant and cause “nonlinear driving”. Therefore, classical linear stability analysis based on orthogonal eigenvalues (growth rate of eigenmodes) may give wrong predictions.

In this chapter, an approach to study the non-normal behavior of thermo-acoustic systems is developed. The heat source is obtained from unsteady CFD computations and linear system identification (CFD/SI) approach. As discussed in the “Linear System Identification” chapter, this approach provides a lot of flexibility for modeling the heat source, i.e., no restriction on the time delay. Moreover, linear models for more complex configurations of the heat source can be obtained with this approach. Also, large delays resulting from the heat source can be handled. The complete thermo-acoustic system is simulated in time domain with the Galerkin method. This modeling of the full system has the advantage that the system’s equations can be represented in state space form.

Eigenvalues of the resulting delay differential system are obtained by the solution operator discretization method, where the delay system is converted into an equivalent partial differential equation using delay as an extra dimension along with time. Maximum growth factors, which represent the maximum amplification of perturbation energy over all initial conditions and over all time instances, are estimated from pseudo-spectra. Pseudo-spectra diagrams show the behavior of eigenvalues under perturbation, and the lower bounds for the maximum growth factor can be drawn from these diagrams.

To illustrate the procedure, a Rijke tube is modeled with two different heat sources, which include the heat source model based on King’s law and the wire in pulsating flow. The latter is obtained from CFD/SI approach (refer to “Linear Identification” chapter for details) and results in a representation with many constant delay terms. A comparison of the pseudo-spectra for a set of duct parameters as in Fig. 7.4 and Fig. 7.5 reveals that for some perturbation levels, the first and second eigenvalue pairs of both the systems reach the right half plane. Using Kreiss’ theorem the lower bounds estimated for the maximum growth factor are 1.75 and 2.1 for the systems with heat sources from CFD/SI approach and based on King’s law, respectively. These values indicate

transient growth in both systems. Next, the heat source location is changed and maximum growth factor is calculated from pseudo-spectra for each of the heat source locations. The sensitivity of heat source based on King's law is higher and has a maximum value when the heat source is located near the downstream end of the tube. These results highlight some interesting features of the non-normality in the Rijke tube.

8 Summary and Conclusions

In this concluding chapter, a series of questions are raised and discussed to highlight the salient aspects of the reported research and to clarify the ideas that have been generated.

What is the aim of your thesis?

A nonlinear dynamic model of the heat source (a part of the complete thermo-acoustic system) using system identification methods or physics based modeling approach with POD has been developed. A low order thermo-acoustic system model in the frequency model involving the coupling of the modes has also been developed.

Why do you obtain nonlinear dynamic models for the heat source from system identification and a nonlinear thermo-acoustic system model?

In linear network models of thermo-acoustic systems, each component of the system is represented by its transfer function/matrices. System identification can be utilized as an effective tool to obtain transfer functions/matrices of thermo-acoustic elements. In this approach, transfer functions of the complicated elements, like turbulent flame, is obtained using only the input-output data set. Stability analysis of full thermo-acoustic system is then studied by constructing the system matrices and analyzing its eigenvalues. It is a good idea to extend the identification procedure and system model to the nonlinear regime to predict limit cycle amplitudes.

Which nonlinear heat source models have you used?

Three different heat source models have been used. The first is a wire mesh as found in a Rijke tube. This heat source is modeled as flow over cylinder that

is kept at constant temperature for the CFD computations. Most of the nonlinear identification schemes have used the input-output data set generated from this model. For the sake of numerical simplicity in processing with POD, a heated flat plate in pulsating flow is used as the heat source model. As the third heat source, a laminar premixed flame is used. The physics of the nonlinear mechanism for these model problems is well understood and they show nonlinear behavior even at very low pressure perturbations.

Which nonlinear identification procedures have you used?

Nonlinear identification procedure is considered a functional approximation problem. In time domain, universal functional approximators (neural network and fuzzy logic) have been used. Nonlinear dynamic models obtained from these identification methods describe the heat source for a range of frequencies and amplitudes. The system is excited with a signal that covers a range of frequencies as well as amplitudes (chirp with varying amplitudes, broadband forcing with high amplitudes, and multi-level signals). This nonlinear dynamic model for the heat source is coupled to a time domain system model of thermo-acoustics, such as the Galerkin time domain.

Frequency domain models of the heat source have also been considered. Nonlinear transfer function is obtained from nonlinear system identification. Harmonic balance and harmonic probing are used to extend the equation error identification (one-step ahead prediction model structure, ARX model structure) into frequency domain. In the harmonic balance approach, a system of equations for the coefficients of the harmonic ansatz is obtained. In the harmonic probing approach, nonlinearity is expressed in terms of higher order transfer functions, which have been derived using recursive relations.

Higher order transfer functions are derived by converting the neural network based identification procedure into frequency domain. First, an equivalent representation is obtained in a polynomial type input-output nonlinearity by expanding tanh in the layer of the neural network. Then, this polynomial representation is converted into frequency domain to define the higher order transfer functions.

How do you describe the heat source with POD for a range of amplitudes

and frequencies?

Data set is collected for single sinusoidal excitations at different amplitudes and frequencies. Snapshot of the data matrices is constructed. Singular value decomposition of the snapshot matrices gives the POD modes. The governing equations are projected onto POD basis to obtain a set of coupled ordinary differential equations for the modal coefficients (describing the evolution of POD modes). The POD modes describe the spatial dependence of the problem (low order model) for the considered range of amplitudes and frequencies. The desired input (acoustic forcing) and output (temperature, heat transfer response) are included explicitly in the low order model. The pressure term resulting from the incompressibility is included using a calibration technique. This low order model of the heat source can be coupled with a time domain simulation of full thermo-acoustic system.

Explain your system modeling approach in the nonlinear regime?

Heat source nonlinearity is represented in terms of the higher order transfer functions. System variables (acoustic velocity and pressure) are expressed as superposition of the modes. A set of algebraic equations results if system variables are used in the Galerkin time domain equations or thermo-acoustic network equations (see Appendix C for a derivation). The modes are then coupled through the higher order transfer functions.

What are the advantages of your system model?

It is a frequency domain method that requires solving only a set of algebraic equations. It is much faster compared to a time domain simulation. It also allows modal coupling. The widely used approach in the frequency domain “sinusoidal describing function” is a one mode approximation which cannot model the coupling between the modes. An energy balance between the modes is performed when the limit cycle is reached. The Rayleigh index in the nonlinear regime is analyzed. Moreover, jump conditions in the area and temperature can be included.

What are the drawbacks of your system model?

Optimal initial conditions for the set of system of nonlinear equations are re-

quired (general problem of nonlinear optimization). When the delay time is large and polynomial order of the approximation is high, computation of the higher order transfer functions requires post-processing of a large number of parameters.

How do you contribute to non-normality in thermo-acoustic systems?

An approach has been developed to study non-normality in thermo-acoustic systems that allows more flexibility in heat source modeling and enables handling of large delay times of the heat source. The heat source model is obtained with unsteady CFD computations and linear system identification (CFD/SI approach). The complete thermo-acoustic system is simulated in time domain using the Galerkin method (a compact representation of the system equations in state space form). Eigenvalues are found from the solution operator discretization technique. Lower bounds of the maximum growth factor is estimated from pseudo-spectra diagrams.

Bibliography

- [1] N. Ananthkrishnan, S. Deo, and F. E. C. Culick. Reduced-order modeling and dynamics of nonlinear acoustic waves in a combustion chamber. *Comb. Sci. and Tech.*, 177:221–248, 2005.
- [2] A. M. Annaswamy and A. F. Ghoniem. Active control of combustion instability: theory and practice. *Control Systems Magazine*, 22 (6):37–54, 2002.
- [3] M. Atig, J. P. Dalmont, and J. Gilbert. Saturation mechanism in clarinet-like instruments, the effect of the localised non-linear losses. *Applied Acoustics*, 65:1133–1154, 2004.
- [4] R. Babuska. Fuzzy modeling and identification toolbox, 1998.
- [5] R. Babuska. *Fuzzy Modeling for Control*. Kluwer Academic Publishers, Boston, 1998.
- [6] R. Babuska and H.B. Verbruggen. *Multiple Model Approaches to Nonlinear Modeling and Control*. Taylor and Francis, London, UK, 1997.
- [7] H. D. Baehr and K. Stephan. *Heat and Mass Transfer*. Springer, 1998.
- [8] K. Balasubramanian and R. I. Sujith. Non-normality and nonlinearity in combustion-acoustic interaction in diffusion flames. *Journal of Fluid Mechanics*, 594:29–57, 2008.
- [9] K. Balasubramanian and R. I. Sujith. Nonlinear response of diffusion flames to uniform velocity disturbances. *Combust. Sci. and Tech.*, 180:418–436, 2008.

- [10] K. Balasubramanian and R. I. Sujith. Thermoacoustic instability in a rijke tube: Non-normality and nonlinearity. *Physics of Fluids*, 20, 2008.
- [11] H. A. Barker. Primitive maximum-length sequences and pseudo-random signals. *Transactions of the Institute of Measurement and Control*, 26:339–348, 2004.
- [12] H. A. Barker, A. H. Tan, and K. R. Godfrey. Optimal levels of perturbation signals for nonlinear system identification. *IEEE Transactions on Automatic Control*, 49(8):1404–1407, 2004.
- [13] E. Bedrosian and S. O. Rice. The output properties of volterra systems driven by harmonic and gaussian inputs. In *Proceedings IEEE*, 1971.
- [14] A. Bellen and S. Maset. Numerical solution of constant coefficient linear delay differential equations as abstract cauchy problems. *Numer. Math.*, 84:351–374, 2000.
- [15] G. Berkooz, P. Holmes, and J. L. Lumley. The proper orthogonal decomposition in the analysis of turbulent flows. *Annual Review of Fluid Mechanics*, 25:539–575, 1993.
- [16] S. Bethke, U. Wever, and W. Krebs. Stability analysis of gas-turbine combustion chamber. In *11th AIAA/CEAS Aeroacoustics Conference*, Monterey, California, 2005.
- [17] J. C. Bezdek. *Pattern recognition with fuzzy objective function algorithms*. Plenum Press, New York, 1981.
- [18] S.A. Billings. Identification of nonlinear systems - a survey. In *Proceedings of IEEE*, 1980.
- [19] S. Boyd and L. O. Chua. Fading memory and the problem of approximating nonlinear operators with volterra series. *IEEE Transactions on Circuits and Systems*, 32:1150–1161, 1985.
- [20] S. P. Boyd. *Volterra Series: Engineering Fundamentals*. PhD thesis, University of California, Berkeley, 1985.

- [21] D. Breda, S. Maset, and R. Vermiglio. Computing the characteristic roots for delay differential equations. *IMA Journal of Numerical Analysis*, 24:1–19, 2004.
- [22] D. Breda, R. Vermiglio, and S. Maset. Trace-dde, tool for robust analysis characteristic equation of delay differential equations, 2006.
- [23] E. Camporeale, D. Burgess, and T. Passot. Transient growth in stable collisionless plasma. *Physics of Plasmas*, 16:030703, 2009.
- [24] J. E. Chance, K. Worden, and G.R. Tomlison. Frequency domain analysis of narx neural networks. *J. of Sound and Vibration*, 213(5):915–941, 1998.
- [25] P. Chatterjee, U. Vandsburger, W. R. Saunders, V. K. Khanna, and W. T. Baumann. On the spectral characteristics of a self-excited rijke tube combustor—numerical simulation and experimental measurements. *Journal of Sound and Vibration*, 283:573–588, 2005.
- [26] S. Chen and S. A. Billings. Neural networks for non- linear dynamic system modelling and identification. *International Journal of Control*, 56:319–346, 1992.
- [27] B. T. Chu. Stability of systems containing a heat source - the rayleigh criterion. Technical report, NACA-RM-56D27, Washington, D. C, 1956.
- [28] Comsol AB. *COMSOL FEMLAB 3.2 User's Guide*, 2005.
- [29] L. Crocco and S. Cheng. *Theory of combustion instability in liquid propellant rocket motors*. Butterworth Scientific Publications, 1956.
- [30] F. E. Culick. A note on rayleigh's criterion. *Combustion Science and Technology*, 56:159–166, 1987.
- [31] F. E. C. Culick. Non-linear growth and limiting amplitude of acoustic oscillations in combustion chambers. *Combust. Sci. and Tech.*, 3:1–16, 1971.
- [32] F. E. C. Culick. Nonlinear behavior of acoustic waves in combustion chambers. parts *i* and *ii*. *Acta Astronautica*, 3:715–734,735–757, 1976.

- [33] F. E. C. Culick. *Unsteady Motions in Combustion Chambers for Propulsion Systems*. RTO-AG-AVT-039, 2006.
- [34] A. E. Deane, I. G. Kevrekidis, G. E. Karniadakis, and S. A. Orszag. Low-dimensional models for complex geometry flows: application to grooved channels and circular cylinders. *J. Phys. Fluids A*, 10:2337–2354, 1991.
- [35] E. Deuker. *Ein Beitrag zur Vorausberechnung des akustischen Stabilitätsverhaltens von Gasturbinen-Brennkammern mittels theoretischer und experimenteller Analyse von Brennkammerschwingungen*. PhD thesis, RWTH Aachen, 1994.
- [36] A. P. Dowling. Nonlinear self-excited oscillations of a ducted flame. *J. of Fluid Mechanics*, 346:271–290, 1997.
- [37] A. P. Dowling and A. S. Morgans. Feedback control of combustion oscillations. *Annual Review of Fluid Mechanics*, 37:151–182, 2005.
- [38] A.P. Dowling. The calculation of thermoacoustic oscillations. *J of Sound and Vibration*, 180:557–581, 1995.
- [39] W. J. Dunstan, R. R. Bitmead, and S. M. Savaresi. Fitting nonlinear low-order models for combustion instability control. *Control Engineering Practice*, 9:1301–1317, 2001.
- [40] D. Durox, T. Schuller, and S. Candel. Combustion dynamics of inverted conical flames. *Proceedings of the Combustion Institute*, 30:1717–1724, 2005.
- [41] M. Ö. Efe. Low dimensional model-based boundary control of 2d heat flow utilizing root locus. *Transactions of the Institute of Measurement and Control*, 29:53–69, 2007.
- [42] M. Ö. Efe and H. Özbay. Low dimensional modelling and dirichlet boundary controller design for burgers equation. *Int. J. Control*, 77:895–906, 2004.

- [43] K. Engelborghs, T. Luzyanina, and D. Roose. Numerical bifurcation analysis of delay differential equations. *Journal of Computational and Applied Mathematics*, 125:265–275, 2000.
- [44] B. Entezam, W. K. Van Moorhem, and J. Majdalani. Two-dimensional numerical verification of the unsteady thermoacoustic field inside a rijke-type pulse combustor. *Numerical Heat Transfer*, 41:245–262, 2002.
- [45] S. Evesque and W. Polifke. Low-Order Acoustic Modelling for Annular Combustors: Validation and Inclusion of Modal Coupling. In *Int'l Gas Turbine and Aeroengine Congress & Exposition*, number ASME GT-2002-30064, Amsterdam, NL, 2002.
- [46] M. A. Ferreria and J. A. Carvalho. A simple derivation of the rayleigh criterion in integral form. *Journal of Sound and Vibration*, 203(5):889–893, 1997.
- [47] J. P. Flaherty, C. E. Seyler, and L. N. Trefethen. Large-amplitude transient growth in the linear evolution of equatorial spread f with a sheared zonal flow. *J. Geophys. Res.*, 104:6843–6857, 1999.
- [48] A. Fleifil, A.M. Annaswamy, Z. A. Ghoneim, and A. F. Ghoniem. Response of a laminar premixed flame to flow oscillations: A kinematic model and thermoacoustic instability results. *Combust. and Flame*, 106:487–510, 1996.
- [49] Fluent Inc., Lebanon, NH. *FLUENT User's Guide*, 2005.
- [50] S. Föllner, F. Selimefendigil, and W. Polifke. Linear identification of the unsteady heat transfer of a cylinder in pulsating crossflow. In *Int. Conf. on Jets, Wakes and Separated Flows*, 2008.
- [51] B. Galletti, C. H. Bruneau, L. Zannetti, and A. Iollo. Low-order modelling of laminar flow regimes past a confined square cylinder. *J. of Fluid Mechanics*, 503:161–170, 2004.
- [52] A. Gelb and W. E. V. Velde. *Multiple-Input Describing Functions and Nonlinear System Design*. McGraw Hill, 1968.

- [53] A. Gentemann and W. Polifke. Scattering and generation of acoustic energy by a premix swirl burner. In *Int'l Gas Turbine and Aeroengine Congress & Exposition*, 2007.
- [54] A. M. G. Gentemann, C. Hirsch, K. Kunze, F. Kiewewetter, T. Sattelmayer, and W. Polifke. Validation of flame transfer function reconstruction for perfectly premixed swirl flames. In *Int'l Gas Turbine and Aeroengine Congress & Exposition*, 2004.
- [55] K. Green and T. Wagenknecht. Pseudospectra and delay differential equations. *Journal of Computational and Applied Mathematics*, 196(2):567–578, 2006.
- [56] D. E. Gustafson and W. C. Kessel. Fuzzy clustering with a fuzzy covariance matrix. In *IEEE CDC*, 1978.
- [57] C. Hantschk and D. Vortmeyer. Numerical simulation of self-excited thermoacoustic instabilities in a rijke tube. *J. of Sound and Vibration*, 3(277):511–522, 1999.
- [58] N. Hasan and S. Sanghi. Proper orthogonal decomposition and low-dimensional modelling of thermally driven two-dimensional flow in a horizontal rotating flow. *J. of Fluid Mechanics*, 573:265–295, 2007.
- [59] A. Heckl. Non-linear acoustic effects in the rijke tube. *Acustica*, 72:63–71, 1990.
- [60] M. A. Heckl. Active control of the noise from a rijke tube. *Journal of Sound and Vibration*, 124:117–133, 1988.
- [61] R. Hilpert. Wärmeabgabe von geheizten drähten und rohren im luftstrom. *Forsch. Gebiete Ingenieurw.*, 4:215–224, 1933.
- [62] H. Hristova and S. Roch. Transient growth in taylor-couette flow. *Physics Of Fluids*, 14(10):567–578, 2002.
- [63] X. Huang and W. T. Baumann. Reduced-order modeling of dynamic heat release for thermoacoustic instability prediction. *Combust. Sci. and Tech*, 179:617–636, 2007.

-
- [64] A. Huber and W. Polifke. Dynamics of practical premix flames, part i: Model structure and identification. *Int. J. of Spray and Combustion Dynamics*, 1:199–229, 2009.
- [65] A. Huber and W. Polifke. Dynamics of practical premix flames, part ii: Identification and interpretation of cfd data. *Int. J. of Spray and Combustion Dynamics*, 1:229–250, 2009.
- [66] E. Jarlebring. *The spectrum of delay-differential equations: numerical methods, stability and perturbation*. PhD thesis, Technische Universität Carolo-Wilhelmina zu Braunschweig, Braunschweig, Germany, 2008.
- [67] A. Juditsky, H. Hjalmarsson, A. Beneviste, B. Delyon, L. Ljung, J. Sjoberg, and Q. Zhang. Nonlinear black-box models in system identification: mathematical foundations. *Automatica*, 31:1725—1750, 1995.
- [68] S. Karpov and A. Prosperetti. Nonlinear saturation of the thermoacoustic instability. *J. Acoust. Soc. Am.*, 107:3130–3147, 2000.
- [69] K. S. Kedia, S. B. Nagaraja, and R. I. Sujith. Impact of linear coupling on thermoacoustic instabilities. *Combust. Sci. and Tech.*, 180:1588–1612, 2008.
- [70] J. J. Keller. Thermoacoustic oscillations in combustion chambers of gas turbines. *AIAA Journal*, 33:2280–2287, 1995.
- [71] L. King. On the convection of heat from small cylinders in a stream of fluid: Determination of the convection constants of small platinum wires with applications to hot-wire anemometry. *Philosophical Transactions of the Royal Society*, pages 373–432, 1914.
- [72] M. J. Korenberg, S. B. Bruder, and P. J. McLlroy. Exact orthogonal kernel estimation from finite data records: Extending wiener’s identification of nonlinear systems. *Annals of Biomedical Eng.*, 16:201–214, 1998.
- [73] M.J. Korenberg. Parallel cascade identification and kernel estimation for nonlinear systems. *Annals of Biomedical Eng.*, 19:429–455, 1991.

- [74] U. Krüger, J. Hüren, W. Krebs, P. Flohr, and D. Bohn. Prediction and measurement of thermoacoustic improvements in gas turbines with annular combustion systems. *J. of Eng. for Gas Turbines and Power*, 123:557—565, 2001.
- [75] H. J. Landau. Loss in unstable resonators. *J. Opt. Soc. Amer.*, 66:525–529, 1976.
- [76] Z. Q. Lang and S. A. Billing. Energy transfer properties of nonlinear systems in the frequency domain. *International Journal of Control*, 78:345–362, 2005.
- [77] Y. W. Lee and M. Schetzen. Measurement of the wiener kernels of a non-linear system by cross-correlation. *International Journal of Control*, 2(3):237–254, 1965.
- [78] V. Lenaerts, G. Kerschen, and J. C. Golinval. Proper orthogonal decomposition for model updating of non-linear mechanical systems. *Mechanical Systems and Signal Processing*, 15(1):31–43, 2001.
- [79] L. M. Li and S. A. Billings. Discrete time subharmonic modelling and analysis. *Int. J. Control*, 78(16):1265–1284, 2005.
- [80] T. Lieuwen. Experimental investigation of limit-cycle oscillations in an unstable gas turbine combustor. *Journal of Propulsion and Power*, 18(1):61–67, 2002.
- [81] T. Lieuwen. Nonlinear kinematic response of premixed flames to harmonic velocity disturbances. In *Proceedings of the Combustion Institute*, 2005.
- [82] T. Lieuwen and V. Yang, editors. *Combustion Instabilities in Gas Turbine Engines: Operational Experience, Fundamental Mechanisms, and Modeling*. AIAA, 2006.
- [83] M. J. Lighthill. The response of laminar skin friction and heat transfer to fluctuations in the stream velocity. *Proceedings of the Royal Society A*, 224:1–23, 1954.

-
- [84] L. Ljung. *System Identification: Theory for the User*. Englewood Cliffs, 1987.
- [85] X. Ma and G. E. Karniadakis. A low-dimensional model for simulating 3d cylinder flow. *J. of Fluid Mechanics*, 458:181–190, 2002.
- [86] The Math Works Inc., Natick MA, USA. *Matlab: The Language of Technical Computing*, 2000.
- [87] K. I. Matveev. Energy consideration of the nonlinear effects in a rijke tube. *Journal of Fluids and Structures*, 18(6):783–794, 2003.
- [88] K. I. Matveev. *Thermoacoustic instabilities in the Rijke tube: experiments and modeling*. PhD thesis, California Institute of Technology, Pasadena, California, 2003.
- [89] K. R. McManus, T. Poinsot, and S.M. Candel. A review of active control of combustion instabilities. *J. Prog. Energy Combust. Sci.*, 19:1–29, 1993.
- [90] H. J. Merk. Analysis of heat-driven oscillations of gas flows. *Applied Scientific Research*, 8:1–27, 1959.
- [91] S. Nagaraja, K. Kedia, and R.I. Sujith. Characterizing energy growth during combustion instabilities: Singularvalues or eigenvalues? In *Proceedings of the Combustion Institute*, volume 32, pages 2933–2940, 2009.
- [92] K. Narendra and K. Parthasarathy. Identification and control of dynamical systems using neural networks. *IEEE Transactions on Neural Networks*, 1:4–27, 1990.
- [93] O. Nelles. *Nonlinear System Identification with Local Linear Neuro-Fuzzy Models*. PhD thesis, Darmstadt University of Technology, Darmstadt, Germany, 1999.
- [94] F. Nicoud, L. Benoit, and C. Sensiau and T. Poinsot. Acoustic modes in combustors with complex impedances and multidimensional active flames. *AIAA J.*, 45:426–441, 2007.

- [95] B. R. Noack, P. Papas, and P. A. Monkewitz. The need for a pressure-term representation in empirical galerkin models of incompressible shear flows. *J. of Fluid Mechanics*, 523:339–365, 2005.
- [96] N. Noiray, D. Durox, T. Schuller, and S. Candel. A unified framework for nonlinear combustion instability analysis based on the flame describing function. *J. of Fluid Mechanics*, 615:139–167, 2008.
- [97] R. D. Nowak. Nonlinear system identification. *Circuits, Systems, and Signal Processing*, 21:109–122, 2002.
- [98] M. Nørgaard, O. Ravn, and N.K. Poulsen. Nnsysid-toolbox for system identification with neural networks. mathematical and computer modelling of dynamical systems. *Mathematical and Computer Modelling of Dynamical Systems*, 8(1):1–20, 2002.
- [99] C. Pankiewitz. *Ein hybrides Berechnungsverfahren für Verbrennungsschwingungen in Ringbrennkammern*. PhD thesis, Technische Universität München, 2004.
- [100] C. Pankiewitz and T. Sattelmayer. Time domain simulation of combustion instabilities in annular combustors. In *ASME Turbo Expo*, Amsterdam, The Netherlands, 2002.
- [101] C. Pankiewitz and T. Sattelmayer. Hybrid methods for modelling combustion instabilities. In *Tenth International Congress on Sound and Vibration*, Stockholm, Sweden, 2003.
- [102] L. G. Papparizos and F. E. C. Culick. The two-mode approximation to nonlinear acoustics in combustion chambers i. exact solution for second order acoustics. *Combustion Science and Technology*, 65 (1):39–65, 1989.
- [103] C. O. Paschereit, B. B. H. Schuermans, W. Polifke, and O. Mattson. Measurement of transfer matrices and source terms of premixed flames. *J. Eng. Gas Turbines and Power*, 124:239–247, 2002.
- [104] C.O. Paschereit and W. Polifke. Investigation of the thermo-acoustic characteristics of a lean premixed gas turbine burner. In *Int'l Gas Turbine and Aeroengine Congress & Exposition*, 1998.

-
- [105] D. T. Pha. *Neural Networks for Identification, Prediction and Control*. Springer, 1995.
- [106] W. Polifke. *Advances in Aeroacoustics and Applications*, chapter Combustion Instabilities. Number ISBN 2-930389-54-0 in VKI LS 2004-05. Von Karman Institute, Brussels, BE, 2004.
- [107] W. Polifke. Numerical techniques for identification of acoustic multipoles. In *Advances in Aeroacoustics and Applications*, VKI LS 2004-05, Brussels, BE, March 15 - 19 2004. Von Karman Institute.
- [108] W. Polifke. System modelling and stability analysis. In *Basics of Aero-Acoustics and Thermo-Acoustics*, VKI LS 2007-02, Brussels, BE, Dec 3-7 2007. Von Karman Institute.
- [109] W. Polifke and A M. Gentemann. Order and realizability of impulse response filters for accurate identification of acoustic multi-ports from transient cfd. *J. of Acoustics and Vibration*, 9(3):139–148, 2004.
- [110] W. Polifke, A. Poncet, C. O. Paschereit, and K. Döbbeling. Reconstruction of acoustic transfer matrices by instationary computational fluid dynamics. *J. of Sound and Vibration*, 245:483–510, 2001.
- [111] W. Polifke, J. van der Hoek, and B. Verhaar. Basic equations and numerical tools for linear acoustics in gas turbines. Technical report, ABB Corporate Research, Baden, Switzerland, 1997.
- [112] E. A. Powell and B. T. Zinn. A single mode approximation in the solution of nonlinear combustion instability problems. *Combustion Science and Technology*, 3(3):121–132, 1971.
- [113] A. A. Putnam. *Combustion-driven oscillations in industry*. American Elsevier Pub. Co, New York, 1971.
- [114] A. A. Putnam and W. R. Dennis. Burner oscillations of the gauzestone type. *Journal of the Acoustical Society of American*, 26:716–725, 1954.
- [115] J. W. Rayleigh. *The theory of sound*. Dover, New York, 1945.

- [116] S. C. Reddy, P. J. Schmid, and D. S. Henningson. Pseudospectra of the Orr-Sommerfeld operator. *SIAM J. Appl. Math.*, 53:15–47, 1993.
- [117] M. Robbe and M. Sadkane. Discrete-time Lyapunov stability of large matrices. *J. Comput. Appl. Math.*, 115:479–494., 2000.
- [118] C. W. Rowley. *Modeling, Simulation and Control of Cavity Flow Oscillations*. PhD thesis, California Institute of Technology, 2002.
- [119] W. J. Rugh. *Nonlinear System Theory*. The Johns Hopkins University Press, 1981.
- [120] M. Schetzen. Measurement of the kernels of a non-linear system of finite order. *International Journal of Control*, 1(3):251–263, 1965.
- [121] M. Schetzen. *The Volterra and Wiener Theories of Nonlinear Systems*. John Wiley & Sons, 1980.
- [122] H. Schlichting. *Boundary-Layer Theory*. McGraw-Hill, 1955.
- [123] P. J. Schmid and D. S. Henningson. *Stability and Transition in Shear Flows*. Springer, 2001.
- [124] T. Söderström and P. Stoica. *System Identification*. Prentice-Hall International, Hemel Hempstead, UK, 1989.
- [125] L. Sirovich. Turbulence and the dynamics of coherent structures part i: Coherent structure. *Quart. Appl. XLV*, 3:561–571, 1986.
- [126] J. Sjöberg, Q. Zhang, L. Ljung, A. Benveniste, B. Delyon, P.Y. Glorennec, H. Hjalmarsson, and A. Juditsky. Nonlinear black-box modeling in system identification: a unified overview. *Automatica*, 31(12):1691–1724, 1995.
- [127] J. J. Slotine and W. Li. *Applied Nonlinear Control*. Prentice Hall, 1991.
- [128] S. R. Stow and A. P. Dowling. Low-order modelling of thermoacoustic limit cycles. In *ASME Turbo Expo Power for Land and Sea*, Vienna, Austria., 2004.

- [129] P. Subramanian and R. Sujith. Non-normality and nonlinearity in thermoacoustic interaction of ducted premixed flames. In *48th AIAA Aerospace Sciences Meeting*, Orlando, Florida, 2010.
- [130] T. Takagi and M. Sugeno. Fuzzy identification of systems and its application to modeling and control. *IEEE Transactions on Systems, Man and Cybernetics*, 15 (1):116–132, 1985.
- [131] K. Tanaka. *An introduction to Fuzzy Logic for Practical Applications*. Springer, 1996.
- [132] L. Tay Wo Chong, R. Kaess, T. Komarek, S. Föllner, and W. Polifke. Identification of flame transfer functions using LES of turbulent reacting flows. In *High Performance Computing in Science and Engineering, Garching 2009*, LRZ, Garching, Germany, 2009. Springer.
- [133] D. Telionis. *Unsteady Viscous Flows*. Springer, 1981.
- [134] E. C. Teran, S. Mohammed, and P. Ruffino. Hartman-grobman theorems along hyperbolic stationary trajectories. *Discrete and Continuous Dynamical Systems*, 17:281–292, 2007.
- [135] N. Trefethen. Computation of pseudospectra. *Acta Numerica*, pages 247–295, 1999.
- [136] N. Trefethen and M. Embree. *Spectra and Pseudospectra*. Princeton Univ. Press, 2005.
- [137] P. P. J. van den Bosch and A. C. van der Klauw. *Modeling, Identification and Simulation of Dynamical Systems*. CRC Press, 1994.
- [138] D. Veynante and T. Poinso. *Theoretical and Numerical Combustion*. R.T. Edwards, Inc., 2005.
- [139] J. Wray and G. G. R. Green. Calculation of the volterra kernels of non-linear dynamic systems using an artificial neural network. *Biological Cybernetics*, 71:187–195, 1994.

- [140] C. G. Wu, Y. C. Liang, W. Z. Lin, H.P. Lee, and S.P. Lim. A note on equivalence of proper orthogonal decomposition methods. *Journal of Sound and Vibration*, 265:1103–1110, 2003.
- [141] X. F. Wu, Z. Q. Lang, and S. A. Billings. Analysis of the output frequencies of nonlinear systems. *IEEE Trans on Signal Processing*, 55:3239–3246, 2007.
- [142] V. Yang, S. I. Kim, and F. E. C. Culick. Triggering of longitudinal pressure oscillations in combustion chambers. i: Nonlinear gasdynamics. *Combustion Science and Technology*, 72 (4):183–214, 1990.
- [143] H. Yuan, S. Karpov, and A. Prosperetti. A simplified model for linear and nonlinear processes in thermoacoustic prime movers. part ii. nonlinear oscillations. *J. Acou. Soc. Am.*, 102:3497–3506, 1997.
- [144] S. W. Yuen, A. M. G. Gentemann, and W. Polifke. Investigation of the influence of boundary conditions on system identifiability using real time system modeling. In *11th Int. Congress on Sound and Vibration (ICSV11)*, pages 3501–3508, Saint-Petersburg, Russia, July 5-8 2004. IIAV.
- [145] B. T. Zinn and M. E. Lores. Application of the galerkin method in the solution of non-linear axial combustion instability problems in liquid rockets. *Combust. Sci. and Tech.*, 14:269–278, 1971.

A System Properties

A.1 Linearity

The method of superposition is applied to a system operator L which is said to be linear.

$$y_k(t) = L(u_k(t)), \text{ for } k = 1, 2, \dots \quad (\text{A.1})$$

where u_k , and y_k are the inputs and outputs, respectively. For arbitrary coefficients b_k ,

$$L\left(\sum_{k=1}^N b_k u_k(t)\right) = \sum_{k=1}^N b_k L(u_k(t)) = \sum_{k=1}^N b_k y_k(t) \quad (\text{A.2})$$

A.2 Time Invariant

A translation of time for the input results in the same translation for the output. A linear/nonlinear operator P of a system acts on the input u as,

$$y(t) = P(u(t)). \quad (\text{A.3})$$

P is time invariant if for a time translation τ on input, $u(t + \tau)$ results in

$$P(u(t + \tau)) = y(t + \tau). \quad (\text{A.4})$$

A.3 Stability

It is sometimes called Bounded Input-Bounded Output (BIBO) stability. Bounded Input means there exists K such that $|u(t)| < K$ for all t .

Linear System

An LTI system, which can be represented with unit impulses (first order Volterra kernels),

$$y(t) = \int_{-\infty}^{\infty} h(\tau) u(t-\tau) d\tau, \quad (\text{A.5})$$

is stable if and only if

$$\int_{-\infty}^{\infty} |h(\tau)| d\tau < \infty. \quad (\text{A.6})$$

The sufficiency condition is checked as,

$$|y(t)| = \left| \int_{-\infty}^{\infty} h(\tau) u(t-\tau) d\tau \right| < K \int_{-\infty}^{\infty} |h(\tau)| d\tau < \infty. \quad (\text{A.7})$$

The necessary condition can be shown when the equation is not satisfied for the case for which a bounded input can be found such that the corresponding output is unbounded [121].

Let us assume the input to be

$$u(t-\tau) = 1, \text{ when } h(\tau) \geq 0, \text{ and} \quad (\text{A.8}) \\ -1, \text{ when } h(\tau) < 0.$$

The corresponding output then becomes,

$$y(t) = \int_{-\infty}^{\infty} |h(\tau)| d\tau = \infty. \quad (\text{A.9})$$

Volterra System

A system, which is represented by a Volterra series of order n ,

$$y(t) = \underbrace{\int_{-\infty}^{\infty} h_1(\tau_1) u(t - \tau_1) d\tau_1}_{\text{Impulse response}} + \int_{-\infty}^{\infty} \dots \int_{-\infty}^{\infty} \underbrace{h_n(\tau_1, \dots, \tau_n)}_{n^{\text{th}} \text{ order kernel}} u(t - \tau_1) \dots u(t - \tau_n) d\tau_1 \dots d\tau_n + \dots \quad , (A.10)$$

is stable if the k th order term of the above summation is

$$\int_{-\infty}^{\infty} \dots \int_{-\infty}^{\infty} |h_k(\tau_1, \dots, \tau_k)| d\tau_1 \dots d\tau_k < \infty, \text{ for } k = 1, 2, \dots, n. \quad (A.11)$$

This condition is sufficient but not necessary for the stability [121]. The sufficiency condition is formulated as,

$$\begin{aligned} & \left| \int_{-\infty}^{\infty} \dots \int_{-\infty}^{\infty} h_k(\tau_1, \dots, \tau_k) u(t - \tau_1) \dots u(t - \tau_k) d\tau_1 \dots d\tau_k \right| \leq \\ & \int_{-\infty}^{\infty} \dots \int_{-\infty}^{\infty} |h_k(\tau_1, \dots, \tau_k)| |u(t - \tau_1)| \dots |u(t - \tau_k)| d\tau_1 \dots d\tau_k < \\ & K^k \int_{-\infty}^{\infty} \dots \int_{-\infty}^{\infty} |h_k(\tau_1, \dots, \tau_k)| d\tau_1 \dots d\tau_k < \infty. \end{aligned} \quad (A.12)$$

A.4 Causality

If the system response does not depend on the future outputs, then the system is said to be casual.

Let us consider the Volterra series representation (it contains LTI system representation for the first order). The k th order component of the summation, which is represented as,

$$y_k(t) = \int_{-\infty}^{\infty} \dots \int_{-\infty}^{\infty} |h_k(\tau_1, \dots, \tau_k)| d\tau_1 \dots d\tau_k < \infty, \text{ for } k = 1, 2, \dots, n, \quad (\text{A.13})$$

is casual if the k th output, $y_k(t)$, does not depend on the future input, $u(t - \tau_i)$, for $\tau_i < 0$. This is possible when the corresponding k th kernel becomes equal to zero if any of its arguments is less than zero. The necessary and sufficient condition for the causality is then $h_k(\tau_1, \dots, \tau_k) = 0$ if any $\tau_i < 0$ for $i = 1, \dots, k$.

B Describing Function Table

Table B.1: Describing Function of Common Nonlinearities. The input to the nonlinear element is assumed to be a sinusoid of amplitude A and frequency ω [52].

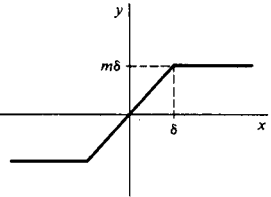
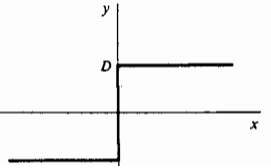
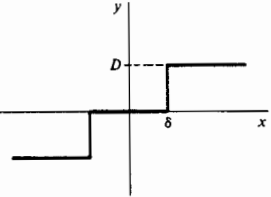
Nonlinearity	Describing Function
 <p data-bbox="209 1227 536 1261">saturation or limiter</p>	$N(A) = \frac{2m}{\pi} \left(\sin^{-1}\left(\frac{\delta}{A}\right) + \frac{\delta}{A} \sqrt{1 - \left(\frac{\delta}{A}\right)^2} \right), \quad A > \delta$
 <p data-bbox="288 1536 456 1570">ideal relay</p>	$N(A) = \frac{4D}{\pi A}$
 <p data-bbox="209 1883 536 1917">relay with dead zone</p>	$N(A) = \frac{4D}{\pi A} \sqrt{1 - \left(\frac{\delta}{A}\right)^2}, \quad A > \delta$

Table B.2: Describing Function of Common Nonlinearities (Continued)

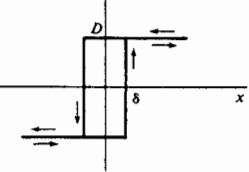
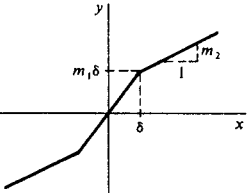
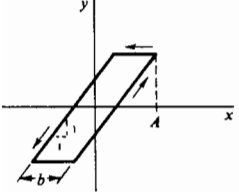
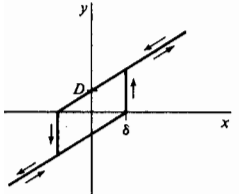
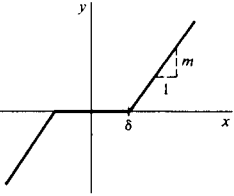
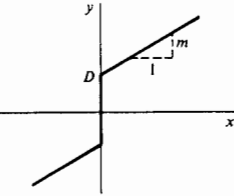
Nonlinearity	Describing Function
 <p data-bbox="212 763 507 797">rectangular hysteresis</p>	$N(A) = \frac{4D}{\pi A} \sqrt{1 - \left(\frac{\delta}{A}\right)^2} - j \frac{4D\delta}{\pi A^2}, \quad A > \delta$
 <p data-bbox="209 1106 510 1140">gain changing element</p>	$N(A) = \frac{2(m_1 - m_2)}{\pi} \left(\sin^{-1} \left(\frac{\delta}{A} \right) + \frac{\delta}{A} \sqrt{1 - \left(\frac{\delta}{A} \right)^2} \right) + m_2, \quad A > \delta$
 <p data-bbox="300 1453 419 1487">backlash</p>	$N(A) = \frac{1}{\pi} \left(\frac{\pi}{2} \sqrt{\frac{2b}{A} - \left(\frac{b}{A}\right)^2} - \frac{j}{\pi} \left(\frac{2b}{A} - \left(\frac{b}{A}\right)^2 \right) \right), \quad A > \frac{b}{2}$
 <p data-bbox="229 1823 489 1856">negative deficiency</p>	$N(A) = \frac{4D}{\pi A} \left(\frac{\pi}{2} \sqrt{1 - \left(\frac{\delta}{A}\right)^2} \right) + \frac{D}{\delta} - j \frac{D\delta}{\pi A^2}, \quad A > \delta$

Table B.3: Describing Function of Common Nonlinearities (Continued)

Nonlinearity	Describing Function
 <p data-bbox="336 992 475 1025">dead zone</p>	$N(A) = \frac{m}{\pi} \left(\pi - 2 \sin^{-1} \left(\frac{\delta}{A} \right) - 2 \frac{\delta}{A} \sqrt{1 - \left(\frac{\delta}{A} \right)^2} \right), \quad A > \delta$
 <p data-bbox="352 1373 459 1406">preload</p>	$N(A) = \frac{4D}{\pi A} + m$
<p data-bbox="363 1507 448 1541">$y = x^n$</p> <p data-bbox="209 1547 608 1581">$n = 3, 5, 7, \dots$ odd nonlinearity</p>	$N(A) = \frac{n(n-2)(n-4)\dots(3)}{(n+1)(n-1)(n-3)\dots(4)} A^{n-1}$
<p data-bbox="363 1675 448 1709">$y = x^{\frac{1}{3}}$</p>	$N(A) = 1.16A^{\frac{-2}{3}}$

C Nonlinear Network Model

Linear network models of thermo-acoustics have been developed [35, 38, 45, 70, 74, 111]. An extension to the nonlinear regime, for the case where the main source of nonlinearity is due to the heat source, is derived. heat source is expressed in terms of higher order transfer functions. A harmonic balancing approach in the frequency domain accounts for the coupling of the modes when acoustic pressure and velocity are written as the sum of the modes.

The equations are derived for a one-dimensional acoustic field inside a resonator tube of length L with a compact heat source located at position $x = x_f$. A schematic representation of a horizontally located tube at open-open boundary conditions is shown in Fig. C.1.

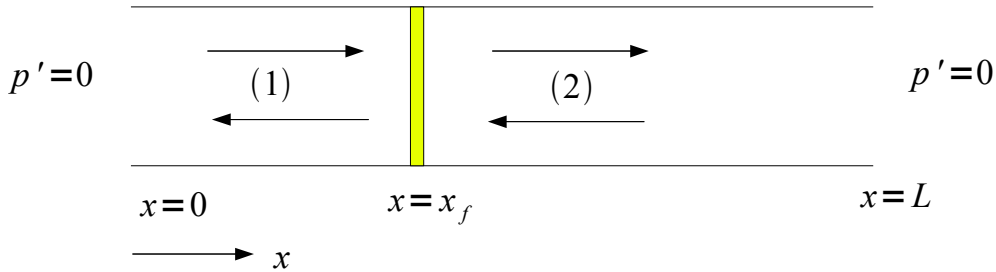


Figure C.1: Horizontally located resonator tube of length L at open-open boundary conditions with a concentrated heat source at position $x = x_f$

Acoustic pressure at section 1 and 2 :

$$p_1(x, t) = \sum_{r=1}^N \left(\begin{array}{l} A_r e^{-i(k_{1r}(x-x_f)-\omega_r t)} + A_{-r} e^{i(k_{1r}(x-x_f)-\omega_r t)} \\ + B_r e^{i(k_{1r}(x-x_f)+\omega_r t)} + B_{-r} e^{-i(k_{1r}(x-x_f)+\omega_r t)} \end{array} \right), \quad (\text{C.1})$$

$$p_2(x, t) = \sum_{r=1}^N \left(\begin{array}{l} C_r e^{-i(k_{2r}(x-x_f)-\omega_r t)} + C_{-r} e^{i(k_{2r}(x-x_f)-\omega_r t)} \\ + D_r e^{i(k_{2r}(x-x_f)+\omega_r t)} + D_{-r} e^{-i(k_{2r}(x-x_f)+\omega_r t)} \end{array} \right). \quad (\text{C.2})$$

The modal coefficients (A_r, A_{-r}) , (B_r, B_{-r}) , (C_r, C_{-r}) and (D_r, D_{-r}) are complex conjugate pairs, and the pressures at sections 1 and 2 with the given representation are already real numbers.

Acoustic velocity at section 1 and 2 :

$$u_1(x, t) = \frac{1}{\rho_1 c_1} \sum_{r=1}^N \left(\begin{array}{l} A_r e^{-i(k_{1r}(x-x_f)-\omega_r t)} + A_{-r} e^{i(k_{1r}(x-x_f)-\omega_r t)} \\ - B_r e^{i(k_{1r}(x-x_f)+\omega_r t)} - B_{-r} e^{-i(k_{1r}(x-x_f)+\omega_r t)} \end{array} \right), \quad (\text{C.3})$$

$$u_2(x, t) = \frac{1}{\rho_2 c_2} \sum_{r=1}^N \left(\begin{array}{l} C_r e^{-i(k_{2r}(x-x_f)-\omega_r t)} + C_{-r} e^{i(k_{2r}(x-x_f)-\omega_r t)} \\ - D_r e^{i(k_{2r}(x-x_f)+\omega_r t)} - D_{-r} e^{-i(k_{2r}(x-x_f)+\omega_r t)} \end{array} \right). \quad (\text{C.4})$$

Wave numbers k_1 and k_2 are defined as

$$k_{1r} = \frac{\omega r}{c_1}, \quad k_{2r} = \frac{\omega r}{c_2}. \quad (\text{C.5})$$

Heat source is expressed as a function of velocity at the heat source location in terms of Volterra kernels up to third order as :

$$\begin{aligned} Q'(t) = & \sum_{m_1=1}^L h_1(m_1) u(t - m_1 + 1) + \sum_{m_1=1}^L \sum_{m_2=1}^L h_2(m_1, m_2) u(t - m_1 + 1) u(t - m_2 + 1) \\ & + \sum_{m_1=1}^L \sum_{m_2=1}^L \sum_{m_3=1}^L h_3(m_1, m_2, m_3) u(t - m_1 + 1) u(t - m_2 + 1) u(t - m_3 + 1) \end{aligned} \quad (\text{C.6})$$

The following coefficients,

$$L_r = \frac{1}{\rho_1 c_1} (A_r - B_r), \quad L_{-r} = \frac{1}{\rho_1 c_1} (A_{-r} - B_{-r}), \quad (\text{C.7})$$

and linear/higher order transfer functions are defined as,

$$H_1(\omega) = \sum_{m_1=1}^L h_1(m_1) e^{-i\omega(m_1-1)\Delta t}, \quad (\text{C.8})$$

$$H_2(\omega_1, \omega_2) = \sum_{m_1=1}^L \sum_{m_2=1}^L h_2(m_1, m_2) e^{-i\omega_1(m_1-1)\Delta t} e^{-i\omega_2(m_2-1)\Delta t}, \quad (\text{C.9})$$

$$H_3(\omega_1, \omega_2, \omega_3) = \sum_{m_1=1}^L \sum_{m_2=1}^L \sum_{m_3=1}^L h_3(m_1, m_2, m_3) e^{-i\omega_1(m_1-1)\Delta t} e^{-i\omega_2(m_2-1)\Delta t} e^{-i\omega_3(m_3-1)\Delta t}. \quad (\text{C.10})$$

Then the nonlinear heat source is obtained as,

$$\begin{aligned}
Q'(t) = & \sum_{r_1=1}^N \left(L_{r_1} H_1(\omega r_1) e^{-i\omega r_1 t} + L_{-r_1} H_1(-\omega r_1) e^{i\omega r_1 t} \right) \\
& + \sum_{r_1=1}^N \sum_{r_2=1}^N \left(\begin{aligned} & L_{r_1} L_{r_2} H_2(\omega r_1, \omega r_2) e^{-i\omega(r_1+r_2)t} \\ & + L_{r_1} L_{-r_2} H_2(\omega r_1, -\omega r_2) e^{-i\omega(r_1-r_2)t} \\ & + L_{r_2} L_{-r_1} H_2(\omega r_2, -\omega r_1) e^{-i\omega(r_2-r_1)t} \\ & + L_{-r_1} L_{-r_2} H_2(-\omega r_1, -\omega r_2) e^{-i\omega(-r_1-r_2)t} \end{aligned} \right) \\
& + \sum_{r_1=1}^N \sum_{r_2=1}^N \sum_{r_3=1}^N \left(\begin{aligned} & L_{r_1} L_{r_2} L_{r_3} H_3(\omega r_1, \omega r_2, \omega r_3) e^{-i\omega(r_1+r_2+r_3)t} \\ & + L_{r_1} L_{-r_2} L_{r_3} H_3(\omega r_1, -\omega r_2, \omega r_3) e^{-i\omega(r_1-r_2+r_3)t} \\ & + L_{r_2} L_{-r_1} L_{r_3} H_3(\omega r_2, -\omega r_1, \omega r_3) e^{-i\omega(r_2-r_1+r_3)t} \\ & + L_{-r_1} L_{-r_2} L_{r_3} H_3(-\omega r_1, -\omega r_2, \omega r_3) e^{-i\omega(-r_1-r_2+r_3)t} \\ & + L_{r_1} L_{r_2} L_{-r_3} H_3(\omega r_1, \omega r_2, -\omega r_3) e^{-i\omega(r_1+r_2-r_3)t} \\ & + L_{r_1} L_{-r_2} L_{-r_3} H_3(\omega r_1, -\omega r_2, -\omega r_3) e^{-i\omega(r_1-r_2-r_3)t} \\ & + L_{r_2} L_{-r_1} L_{-r_3} H_3(\omega r_2, -\omega r_1, -\omega r_3) e^{-i\omega(r_2-r_1-r_3)t} \\ & + L_{-r_1} L_{-r_2} L_{-r_3} H_3(-\omega r_1, -\omega r_2, -\omega r_3) e^{-i\omega(-r_1-r_2-r_3)t} \end{aligned} \right) \quad (\text{C.11})
\end{aligned}$$

Boundary Conditions

For a tube at open-open boundary conditions,

$$p_1(0, t) = p_2(L, t) = 0. \quad (\text{C.12})$$

In terms of modal coefficients

$$A_r e^{ik_{1r}x_f} + A_{-r} e^{-ik_{1r}x_f} + B_r e^{ik_{1r}x_f} + B_{-r} e^{-ik_{1r}x_f} = 0, \quad (\text{C.13})$$

$$C_r e^{-ik_{2r}(L-x_f)} + C_{-r} e^{ik_{2r}(L-x_f)} + D_r e^{ik_{2r}(L-x_f)} + D_{-r} e^{-ik_{2r}(L-x_f)} = 0. \quad (\text{C.14})$$

Pressure Jump across the Heater

$$p_1(x_f, t) = p_2(x_f, t), \quad (\text{C.15})$$

in terms of modal coefficients

$$A_r + A_{-r} + B_r + B_{-r} = C_r + C_{-r} + D_r + D_{-r}. \quad (\text{C.16})$$

Velocity Jump across the Heater

$$u_2(x_f, t) - u_1(x_f, t) = \frac{(\gamma - 1)}{\rho_1 c_1^2} Q'(t). \quad (\text{C.17})$$

This is the most important part for the nonlinear modeling since the main source of nonlinearity originates from the local heat source. A harmonic balancing (equating the exponentials of the same order) is used for the right and left hand sides of Eq. (C.17)). The equation for the mode number s is drawn as,

$$\begin{aligned} & \frac{\rho_1 c_1^2}{(\gamma - 1)} \left(\frac{1}{\rho_2 c_2} (C_s - D_s) - \frac{1}{\rho_1 c_1} (L_s) \right) = \quad (\text{C.18}) \\ & L_s H_1(\omega s) + \sum_{s_1=1}^N \sum_{s_2=1}^N \left(\begin{aligned} & L_{s_1} L_{s_2} H_2(\underbrace{\omega s_1, \omega s_2}_{s_1+s_2=s}) + L_{s_1} L_{-s_2} H_2(\underbrace{\omega s_1, -\omega s_2}_{s_1-s_2=s}) \\ & + L_{s_2} L_{-s_1} H_2(\underbrace{\omega s_2, -\omega s_1}_{s_2-s_1=s}) \end{aligned} \right) \\ & + \sum_{s_1=1}^N \sum_{s_2=1}^N \sum_{s_3=1}^N \left(\begin{aligned} & L_{s_1} L_{s_2} L_{s_3} H_3(\underbrace{\omega s_1, \omega s_2, \omega s_3}_{s_1+s_2+s_3=s}) + L_{s_1} L_{-s_2} L_{s_3} H_3(\underbrace{\omega s_1, -\omega s_2, \omega s_3}_{s_1-s_2+s_3=s}) \\ & + L_{s_2} L_{-s_1} L_{s_3} H_3(\underbrace{\omega s_2, -\omega s_1, \omega s_3}_{s_2-s_1+s_3=s}) + L_{-s_1} L_{-s_2} L_{s_3} H_3(\underbrace{-\omega s_1, -\omega s_2, \omega s_3}_{-s_1-s_2+s_3=s}) \\ & + L_{s_1} L_{s_2} L_{-s_3} H_3(\underbrace{\omega s_1, \omega s_2, -\omega s_3}_{s_1+s_2-s_3=s}) + L_{s_1} L_{-s_2} L_{-s_3} H_3(\underbrace{\omega s_1, -\omega s_2, -\omega s_3}_{s_1-s_2-s_3=s}) \\ & + L_{s_2} L_{-s_1} L_{-s_3} H_3(\underbrace{\omega s_2, -\omega s_1, -\omega s_3}_{s_2-s_1-s_3=s}) \end{aligned} \right) \end{aligned}$$

In this representation the effects of the higher order modes on the fundamental harmonic and the energy transfer from the fundamental to the higher order modes is directly seen.

We have $2N$ equations based on the boundary conditions, N equations for the pressure jump and N equations for the velocity jump across the heater accounting for only the real parts. In total, the number of equations accounting for the imaginary parts is $8N$. The unknowns are the complex conjugate coefficients (A_r and A_{-r} , B_r and B_{-r} , C_r and C_{-r} , D_r and D_{-r}) and frequency (ω). Each coefficient has 2 unknowns (real and imaginary parts), and the corresponding complex conjugate part is determined from these unknowns. For example, if $A_r = a_r + jb_r$ with a_r and b_r being real numbers, the complex conjugate part will be $A_{-r} = a_r - jb_r$. The number of unknowns will then be $8N$ for the unknown modal coefficients and 1 for frequency ω . An additional equation is obtained for the frequency by assuming the imaginary part of one of the modal coefficients to be zero, i.e. $\Im(A_1) = 0$.